STUDIES RELATED TO RESERVOIR SEICHES, IMPACT OF DAM ON REGIONAL SCALE CIRCULATION, REVIEW OF DESIGN WATER LEVELS AND WAVES AND MODELLING OF DAM IN NTCPWC SIMULATOR

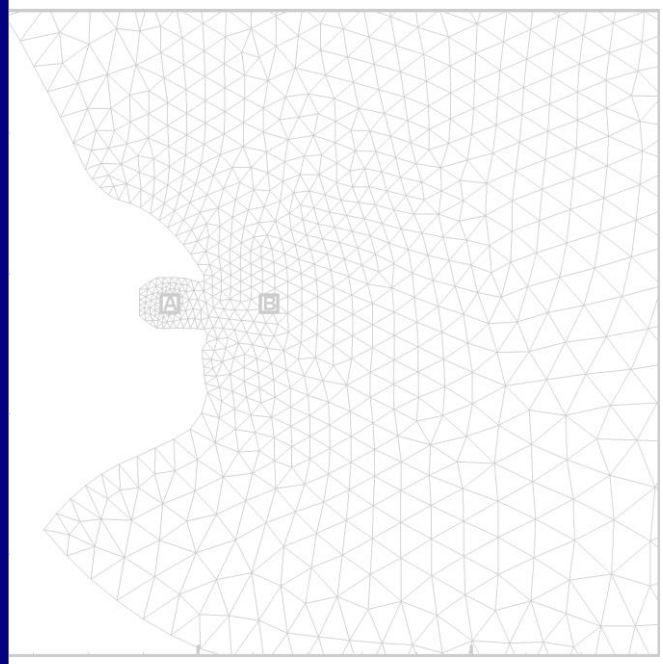

Draft Final Report

Client

National Centre for Coastal Research

National Technology Centre for Ports, Waterways and Coasts
Department of Ocean Engineering
Indian Institute of Technology Madras
Chennai – 600 036

March 2023

Contents

1 Introduction

The north-western regions of India are almost dry and India is considered as one of the most 'water-stressed' countries in the world (USAID Report). The primary objective of the Kalpasar Project is to ensure the adequate supply of fresh water by constructing a dam, approximately of 50 km length across the Gulf of Khambhat (GoK) by collecting the inflow of rivers Narmada, Sabarmati, Mahi and Dhadar. The scientific studies regarding this project dated back to 1969 till 2017, spans into three phases such as preliminary studies, pre-feasibility report leading to design studies and the feasibility report of the altered designs (Dhruv Rajeev, 2018). As far as the need of the fresh water storage is concerned, the most important functionality is the replacement of the saline water by the riverine water on closure of the dam. Coastal reservoirs are intended to store the riverine water discharging into the ocean during the monsoon period and to use it in the drought period. They are constructed across an estuary or a bay or in the sea to collect the riverine water during flooding and normal conditions. The major disadvantages of the conventional reservoirs are categorized into the disruption of the continuity of the river flow and the transport of sediments, geomorphological and hydrodynamic changes in the neighbouring ecosystems (Zhao et al, 2021).

The Gulf of Khambhat, also known as the Gulf of Cambay, is a bay on India's Arabian Sea coast, just north of Mumbai and Diu Island, bordering Gujarat. The Gulf of Khambhat is roughly 200 kilometres long, with a width of 20 kilometres in the north and up to 70 kilometres in the south. The Narmada, Tapti, Mahi, and Sabarmati are major rivers that drain Gujarat and produce estuaries in the Gulf. It separates the Kathiawar Peninsula from Gujarat's south-eastern region. The study area is geographically located between 22°24'32.64" and 20° 2'31.66" N latitude and 72°29'28.43" and 72° 3'18.76" E longitude. There is a proposal to construct a 30 km dam across India's Gulf of Khambhat in order to create a massive fresh water coastal reservoir for irrigation, drinking, and industrial reasons. The Kalpasar Project, also known as the Gulf of Khambhat Development Project, entails the construction of dam which will be able to store 10,000 million cubic metres of fresh water from rivers such as the Narmada, Mahi, Dhadhar, Sabarmati, Limbdi-Bhagovo, and two other minor rivers, amounting to 25% of Gujarat's average annual precipitation flow. Over the dam, a 10-lane road link will be built, considerably reducing the distance between Saurashtra and South Gujarat. The dam is located between 21° 48' 25.22"N, 72° 9' 2.02"E and 21° 48' 25.71"N, 72° 38' 51.17" E.

2 Scope and Objectives of the Study

The main objective of the project is to

1. Two-Dimensional CFD of reservoir with dam to assess the added mass and Studies related to Three-Dimensional reservoir sieche modeling.
2. Impact of the Kalpasar dam on the regional circulation.
3. Numerical modeling of hydrodynamics and morphodynamics.

3 Key observations

3.1 Two-dimensional CFD of reservoir with dam to assess the added mass and studies related to three-dimensional reservoir sieche modeling.

The study aimed to assess the added mass and consider the L/D ratio of the reservoir to visualize the seiches. CFD has advantages such as conducting studies in full scale, inclusion of free surface effects, and detailed investigation of flow behaviour. The study used FLUENTtm package as a solver with VOF model and k-ε turbulence model. The seismic data provided was of two types, Maximum credible earthquake simulation (MCES) and Design based earthquake simulation (DBES), used for 2D CFD simulations of the reservoir with the dam to find the forces and added mass on the dam. The results showed that the RMS value of force was 400KN for MCES data and 391KN for DBES data. The assessed added mass was 1.57X106 kg for MCES data and 2.6X106 kg for DBES data, which is close to the values with reference to P.M.V. Ribeiro and L.J. Pedroso's study. The details of investigation and results are presented in **Annexure-A.**

As a part of this study a three-dimensional reservoir sieche modeling approach to determine the forces acting on a dam wall during hydrostatic and hydrodynamic pressure conditions is conducted. Time series were extracted at different zones near the dam wall to measure the total pressure and pressure fluctuation during different sieche conditions. The simulation used a three-dimensional grid geometry file with 2637888 nodes, 4789048 elements, and 12 layers. The maximum total pressure across the domain was 221000 Pa during the initial condition and increased to 254290.06 Pa during sieche interaction with the dam wall. The results of the study are provided in **Annexure-A**. The results are analysed at different cross sections.

The modelling was done with respect to elevation value and total pressure value at different zones (top level, middle level and bottom level) in section A-A'. The figures and table show the pressure variation at the bottom, middle, and top zones over different times during sieche propagation. The total pressure predicted during three time frames of sieche propagation, sieche approaching the dam, sieche against the dam, and sieche while returning from the dam are shown to be 220000 Pa for all three scenarios. The findings suggest that the pressure is highest at the bottom level and gradually decreases towards the top surface. During sieche approaching the dam to sieche against the dam, the level of pressure fluctuation increases in all three zones due to the sieche hitting the dam wall. The pressure in the bottom and middle zones increases from sieche approaching the dam to sieche against the dam, while the pressure gradually decreases from sieche against the dam to sieche while returning from the dam.

At section B-B’, the pressure varies in different zones of the section, with the highest pressure at the bottom and gradually decreasing towards the top surface similar to section A-A’. During the sieche propagation from approaching the dam to against the dam, the pressure increases in the bottom and middle zones, while there is a fluctuation in the top surface zone, which increases by 89%. The pressure reaches its highest value of 234000 Pa while sieche hits the dam wall at the bottom, and the nature of fluctuation in the pressure gradually decreases while sieche is returning from the dam. The total pressure in the bottom and middle zones increases from sieche approaching the dam to sieche against the dam, while there is a gradual decrease in pressure from sieche against the dam to sieche while returning from the dam similar to section A-A’.

The characteristic of pressure fluctuations are similar to other sections in section C-C’. The results show that the pressure is highest at the bottom level and gradually decreases towards the top surface. The maximum pressure recorded during the event was 234000 Pa while the sieche was approaching the dam. The maximum pressure fluctuations in the top surface zone increased by 86%, middle surface by 14%, and the bottom surface by 6% from the sieche approaching the dam to the sieche against the dam, which is caused by the sieche hitting the dam wall.

The characteristic of pressure fluctuations are similar to other sections in section D-D’. At section D-D' the total pressure across the domain was found to be 170000 Pa at the bottom

level. The pressure fluctuation increased by 94% at the top surface, 17% at the middle surface, and 9% at the bottom surface during the sieche approaching to the sieche against the dam. However, during the sieche against the dam to the sieche while returning from the dam, the pressure fluctuation gradually decreased by 89% at the top surface, 10% at the middle surface, and 2% at the bottom surface with respect to time series.

The study examined the pressure variation in different zones of Section E-E' during sieche events approaching the dam, sieche against the dam, and sieche returning from the dam and the pressure fluctuation trends are similar to other sections. The total pressure across the domain was found to be 207000Pa. The nature of fluctuation in the top surface zone increases by 81%, the middle surface by 4%, and the bottom surface by 8% from the sieche approaching the dam to the sieche against the dam. The level of pressure fluctuation gradually decreases by 38% in the top surface, 5% in the middle surface, and 3% in the bottom surface from the sieche against the dam to the sieche while returning from the dam with respect to time series.

3.1.1 Conclusive remarks

In 2-Dimensional study, Root mean square (RMS) value of forces on the dam wall is approximately around 400KN for MCES acceleration data (horizontal shaking data) and 391KN for DBES acceleration data (horizontal shaking data) and the corresponding added mass for the RMS forces are 1.57x106 kg in case of MCES and 2.6x106 kg in case of DBES acceleration data. The total pressure acting on the wall is approximately 2.4x105pa for MCES and DBES data.

A numerical model was developed using TELEMAC-3D to design a reservoir at the Gulf of Khambhat, Gujarat and analyze the forces acting on the dam wall in a 3-dimensional study. The model utilized appropriate geometry and boundary conditions and the flexible mesh was used to arrive at accurate results and conclusions. The 3-dimensional model results were consistent with those obtained from the 2-dimensional model. The sieche formation after an earthquake causes oscillation of the reservoir water, and different slice locations were analyzed for each time frame in the domain to determine the impact of the sieche on the dam wall. To measure the total pressure exerted by the sieche in the domain, the sieche approaching the dam, sieche against the dam, and sieche returning from the dam were examined. The total pressure and pressure fluctuation in the domain were determined at different levels, including the bottom, middle, and top surface, for each slice or transect. Table A9 shows the percentage

change in pressure fluctuation at different zones in different sections. It was observed that the nature of pressure fluctuation changes more at the top surface than in the bottom zone, and the pressure is highest at the bottom compared to the top surface.

3.2 Impact of the Kalpasar dam on the regional circulation

The present study aimed to analyze the hydrodynamics in a region of the Arabian Sea with and without the presence of a dam using a 3D numerical model. The study area covered a large area ranging from 59.35 ^{O}E to 77.55 ^{O}E longitude and 5.5 ^{O}N to 25.5 ^{O}N latitude, including the Gulf of Kutch (GoK), which is characterized by shallow waters with a tidal range of 10 m or more and currents greater than 3 m/s. To model the hydrodynamics, the 3D domain was discretized into triangular elements using a Linux-based meshing package, with the horizontal resolution ranging from 10-12 km in the open boundary to 30-40 m near the project area. The Eulerian-Lagrangian Circulation (ELCIRC) model, which is a flexible open-source model capable of solving the momentum equations, continuity equation, and transport equation, was used to simulate the unsteady flow of water and the dispersion of temperature. The model was capable of handling different forcing regimes, such as tides, winds, currents, and river discharge, and could be fitted on unstructured grids. The shallow water equations were solved using finite difference/finite volume algorithms, and the density was computed as a function of temperature, salinity, and hydrostatic pressure using the equation of state. The study considered three cases: normal, monsoon, and extreme flood events, and the model was forced accordingly. The algorithmic procedure involved initialization, selection of model inputs, choice of turbulence scheme, solving required variables, and storing outputs in respective files. The model outputs could be stored periodically, and the net heat transfer across the air-water interface was accounted for as the combined effect of the downward heat flux, down welling solar radiative heat flux, and heat flux from precipitation. The details of the study are given in **Annexure-B**.

The computation is carried out for tidal activity in the Gulf of Khambat for a diurnal tidal cycle. During 0th hour, the tides retreat seaward in the southwest direction with a decreasing trend in elevation, but in the central parts of the gulf, the tides still advance in the northern direction due to reflection from land boundaries. During 2nd hour of the tidal course the northward arm is a little more localized above 21.5^{O} N latitude with a decreasing trend in speed, whereas the seaward movement is more rapid with an average velocity of 1 m/s, particularly at the mouth of the gulf. The tidal conditions in the 4th hour are similar to the previous case, with a slight

change in spatial orientation, and the horizontal extent is further diminished. During the 6th hour, the landward movement of the tide is more defined till 20.5^{O} N, whereas the regions above this experience seaward flow. The flow of the tides during the 8th hour resembles that in the previous case, but the tides begin to shoal due to the decreasing width of the gulf regions. During the 12th hour of the tidal cycle, there is a more prominent northward movement of the tide, but it undergoes damping due to bottom friction. The flat bottom regions of the gulf experience very little tidal flow in the 14th hour, and the seaward movement intensifies from 21.5^{O} N latitude, followed by a well-defined seaward motion in the subsequent hours, and asymmetric movement of the tide is visible in the final hours. The study describes the movement of the tides in subsequent hours and notes that the tidal activity in the central regions of the gulf is greatly enhanced by river discharge originating from the rivers Narmada, Tapi, and Mahi. Tidal currents in the southwest are 1.5 m/s while wind-driven currents oppose the tide, creating a barrier between two water masses northward of 20^{O} latitude.

The intrusion of saline water under the influence of tide and wind is investigated and notes that during the first half of the semidiurnal tidal cycle, the 32 PSU contour is completely occupied in the southwest regions of the mouth of the gulf. The spatial variation of temperature during a diurnal tidal cycle is also investigated, and the deterministic nature of salinity is revealed by the balance between evaporation and precipitation. The article concludes by highlighting that the numerical model of tidal activity and intrusion of saline water can help in understanding the dynamics of the Gulf of Khambat and provide insights into managing the coastal resources and environment.

Heat transfer across air-water interface is calculated by considering various factors such as heat flux, radiative flux, and turbulent fluxes and a parameterization scheme. Ocean water temperature varies with depth and season, and diurnal variation due to tides remains a research challenge. Mudflat regions retain heat during slack hours and distribute it during high tide, resulting in temperature collapse during the 4th hour of tidal cycle. Surface temperature distribution is affected by wind conditions, with a range of 2-3^{o}C diurnal variation. The temperature of ocean water varies with depth and season, and is affected by tidal cycles and interactions between different interfaces. The distribution of surface temperature in the water changes during the tidal cycle, with maximum variation during the flood tide and patchy appearance due to wind effects.

The dam acts as a non-penetrable wall boundary, reducing the computational domain by almost 50 km longitudinally and 25 km latitudinally, which shortens the area by approximately 1200 km^2. The dam reduces river discharge and increases tidal range by 1.3 m. The southern side of 21.8^O N latitude has an average tidal range of 6 m, while the north-western side of River Tapi has a maximum tidal range of 8 m without the dam. With the dam, the tidal range increases by more than 2 m in these regions and reaches up to 9 m near the dam wall, causing flooding and inundation. It can be seen that the surface profiles of tidal elevation with the dam keeps almost the same profile with its counterpart, except its magnitude in the vicinity of the dam wall. Similarly, the tidal current also hold the same behaviour in most of the time slots of the cycle, and slightly differing in their magnitudes during certain stages. The barrier formation is still visible further northward of 20^O N latitude, which results from the opposing water masses trying to cross each other. The wind driven circulation is oriented eastward and north-eastward.

Salinity profiles with the dam show different trends due to tidal and wind forcing. The dam keeps 20 PSU isohaline contours till 21°N latitude. Tides are dominant in salinity intrusion, and western Maharashtra and the Sourashtra Peninsula are now more prone to high salinity. The hydrodynamic setup with a dam causing a considerable increase in tidal range is expected. Tidal water moves north-eastward towards the land, increasing the possibility of inundation. The horizontal profiles show an average temperature increase of 0.5°C, likely due to intense vertical mixing from tidal activity and heat exchange from mud flats. However, further systematic testing and vertical temperature profile analysis is needed. Details are presented in **Annexure-B**

3.2.1 Conclusive remarks

A numerical model was developed to study the hydrodynamics in the region of interest is analysed with the help of a 3D circulation model capable of addressing the spatial and temporal changes of elevation, salinity and temperature with and without the dam during normal case. at the Gulf of Khambhat, Gujarat.

In conclusion, the study reveals the hydrodynamic behavior of the Gulf of Khambhat without and with the presence of a dam. Without the dam, the tides show complex patterns of movement due to the reflection from the lateral land boundaries. The tides experience a rapid change in direction and amplitude in the regions above the latitudinal belt 20.5^O N. The presence of the dam acts as a non-penetrable wall boundary, which shuts down the discharge of Mahi and

Sabarmati rivers, resulting in an increase in the tidal range by 1.3 m. The regions on the seaside of the dam are flooded and subsequently inundated, causing a maximum tidal range of 9 m in the vicinity of the dam wall. The study also highlights the uniform distribution of surface temperature during the flood tide due to mixing, and the collapse of the uniform distribution during the 4th hour of the tidal cycle.

3.3 Numerical modeling of hydrodynamics and morphodynamics.

The main objective of the project is to investigate the tidal hydrodynamics, seasonal circulation changes in the study area and analyse the seasonal morphodynamic changes. Demarcation of the study domain is done to set up the extent of the model domain. Hydrodynamic modelling is carried out for the study region by using Telemac 2d model. Modelling the bed evolution of the domain is performed using the morphodynamic routine of Ocirc. Both hydrodynamic and morphodynamic model is simulated for a two neap to neap condition, which covers all the astronomical aspects of tidal forcing. The siltation rate for the study area is calculated based on different seasons. The present study focused on analysing the circulation features and its effect on morphodynamic changes in the proposed dam area in Kalpassar, Gulf of Khambhat. Numerical models are used to predict the bed level changes based on the hydrodynamic. The hydrodynamic modelling study is carried out by establishing the hydrodynamic model for a detail understanding of the tidal hydrodynamics and in addition with the wind induced circulation for the two cases, which are without dam and with dam conditions. The model predict the flow field and it is used to compute the changes in the bed level using sediment load balance in the water column. The dam is located between 21° 48' 25.22"N, 72° 9' 2.02"E and 21° 48' 25.71"N, 72° 38' 51.17" E. The model domain is discretized with the triangular element to obtain numerical solution to the hydrodynamic equations. The final mesh has fine element coast and shallow water depth. The average mesh size is found to be 130-250 m near shore which is very fine for the large gulf such as GoK .The mesh is coarser near the offshore boundaries where the water depths are greater. A typical mesh that is used to discretize the domain and bathymetry of the domain used for two cases for the simulation along with the bathymetry used in with dam and without dam condition. The model is capable of capturing the details of the bathymetry significantly closer to reality**.** Several data including measurement of tide, wind, bathymetry covering seasonal variation of hydrodynamics are collected and used for calibration and validation. The bathymetry obtained by the measured data is interpolated into the mesh. Wind data for the year 2021 is obtained from ERA5 dataset from ECMWF with

the horizontal resolution of 0.25-degree x 0.25 degree and hourly temporal resolution. The wind data is interpolated into mesh using Telemac2d**.** The boundary of the model domain is forced with varying water level and velocity conditions using data from TPXO global tide model. The water level variation obtained near the dam area (21°47'40.35"N, 72°23'22.07"E). These data is fed into the numerical model that simulates hydrodynamics, tidal and wind-induced circulation, sediment transport, and siltation rate in the proposed site and its environs. The simulation findings reveal the impact of seasonal variation on sedimentation processes in great detail. The amount of silt is calculated based on the rate of siltation and the surrounding area. The results of 'Numerical modeling of hydrodynamic and morphodynamic' are attached in **Annexure-C.** The current study will be conducted using Telemac2d, a widely used industry-ready hydrodynamic setup, the details of which are discussed in **Annexure-D**. The morphodynamic routine of model OCIRC- IITM inbuilt model is used and the details of which are given in **Annexure- E.** In further without dam condition is described as **Case I** and with dam condition is described as **Case II**. The extreme condition in the simulation is characterised by higher river discharges.

Under the hydrodynamic study in the **Case I**, higher velocity observed in the domain with the maximum current speed in the order of 1.4 -3 m/s. less current speed is observed in the Ebbing period. The maximum current speed of 0.7 -1.4 m/s is observed in the offshore area. The maximum velocity during the ebbing is in the range of 1.4 m/s -2.1 m/s. Eddy formation is observed near the island in the north part of the domain during flooding. The increased velocity is due to the fact that, in the absence of the proposed structure there is more flows occurring from the estuaries. In the **Case I** the siltation behaviour is observed in the range of 0.01-0.09 m/2N-N cycle near the proposed dam area. Low amount of siltation in the range of 0.01-0.08 m/2N-N cycle is observed in the central area of the study domain. The less siltation happens because of the flushing from the rivers in the domain without any obstruction. In the Pre-Monsoon the siltation is 20% lesser than the Monsoon season. In the Post-Monsoon season the siltation is observed to be 30 % lesser than the same.

The hydrodynamic study in the **Case II** shows, an average of 0.3-2.4 m/s current speed is observed all over the considered domain during the flooding and less current speed is observed during the ebbing. The proposed dam will act as a wall which eliminate some circulation. The maximum current speed of 1 -1.5 m/s is observed in the offshore areas. During the ebbing the

current velocity is in the range of 0.3-1.2 m/s near the study area. The proposed dam's south side has currents that range from 0.3 to 0.9 m/s The Morphodynamic study under the **Case II** shows significant siltation observed in the jetty area near the river opening exactly in the northern part of the Narmada River Mouth in the range of 0.05-0.1m/2N-N cycle. Siltation behaviour is observed more near the proposed dam is in the range of 0.06-0.16 m/2N-N cycle. The significant siltation around 0.09-0.15 m/2N-N cycle observed in the central region of the domain. In the Pre-monsoon and Post-Monsoon, the siltation is observed 15% and 20% decrease respectively.

In the extreme event of the **Case I**, near the river mouth, the current can be seen more frequently when there is flooding. Near the island, some eddy formations may be seen. When taking into account the study region, the domain's average current speed is found to be in the range of 0.3-3.15 m/s. Near the island, a speed of 2.8 -3.15 m/s has been recorded. The proposed dam's south side has currents that range from 1.4 to 2.8 m/s. The siltation in the extreme event of **Case I** is between 0.08 and 0.18 m/2N-N in the river area closest to the jetty. The amount of siltation close to the dam is between 0.01-0.08 m/2N-N. Erosion is also visible in the same location. The siltation in the domain's centre region ranges from 0.04-0.08 m/2N-N. The siltation in the vicinity of the jetty is between 0.004-0.08 m/2N-N.

In the extreme event of **Case II,** During the time of flooding, the current is observed more near the river mouth. The current speed in the order of 0.3-2.1 m/s is observed in the domain. The current speed of 1.2 -2.5 m/s is observed near the island .In the south side of the proposed dam the current have a range of 0.9-1.5 m/s .During ebbing the maximum current speed of 0.3 -2.1 m/s is observed in the domain. The southern side of the dam experience the velocity in the range of 0.3-0.9 m/s. In the **Case II** extreme event, more erosion persists close to the river's mouth. The river mouth contains silt with a range of 0.16-0.19 m/2N-N. The proposed dam is surrounded by siltation that ranges from 0.04-0.17 m/2N-N. The central region has siltation that ranges from 0.08 to 0.12 m/2N-N. The siltation in the jetty region ranges from 0.01 to 0.08 m/2N-N.

3.3.1 Conclusive remarks

In the presence of the dam, the siltation rate is higher with the range of 0.06-0.16 m/2N-N cycle near the dam. The lack of flushing from the estuaries on the northern side is the cause of the increased siltation. This causes significant siltation in the area, particularly near the Narmada

river mouth at the jetty and near to the proposed dam. In Case I eroding patches are seen in the jetty area when compared with Case-II. The range of siltation observed in Case II seems to be slightly high compared to Case-I with the siltation rate of 0.05-0.1m/2N-N cycle.

In the vicinity of the proposed dam, eddy can be seen with the local circulation. The velocity in the area is between 0.4 and 0.6 m/s in average. A volume of silt nearly 18 Mm^3/14 days is anticipated to amass in the reservoir region as a result of the siltation. This can be the cause of 1.5-3% annual storage capacity reduction.

ANNEXURE-A
TWO DIMENSIONAL CFD OF RESERVOIR WITH DAM TO ASSESS THE ADDED MASS AND STUDIES RELATED TO THREE-DIMENSIONAL RESERVOIR SIECHE MODELING

EXECUTIVE SUMMARY

IIT Madras has carried out Two Dimensional Computational fluid dynamics (CFD) analyses for Kalpasar dam along with reservoir to estimate the forces acting on the dam wall and calculate the added mass. The modelling challenge includes mainly, to give input as the seismic data provided by CSIR and sponsored by National Centre for Coastal Research to the CFD simulation. The data provided is of two types one is Maximum credible earthquake simulations (MCES) and other is Design based earthquake simulations (DBES) and in this considering only horizontal shaking for 2D simulations. The study was based on solution of fluid-dynamics equations for simulation of flow. A volume of fluids method is used for investigating free surface effects. As a result, the RMS value of forces on the dam wall for MCES and DBES acceleration data (horizontal shaking data) and the assessment of added mass.

Based on the study and detailed analysis of results, it is seen that,

1 Root mean square (RMS) value of forces on the dam wall is approximately around 400KN for MCES acceleration data (horizontal shaking data) and 391KN for DBES acceleration data (horizontal shaking data) and the corresponding added mass for the RMS forces are $1.57x10^6$ kg in case of MCES and $2.6x10^6$ kg in case of DBES.
2 The total pressure acting on the wall is approximately $2.4x10^5$pa.
3 The seiches in the simulation is unable to predict and visualise due to the L/D ratio of reservoir.

1.1 Introduction

Department of Ocean Engineering, IIT Madras to investigate the forces acting on the dam wall for a given seismic data. The length of the reservoir is approximately around 52km and the maximum depth is around 20m. A 2D computational fluid dynamics (CFD) modelling approach is adopted here to find the forces acting on dam wall and considering the L/D ratio of the reservoir unable to visualise the seiches. CFD has advantages such as the ability to conducts

studies in full scale, inclusion of free surface effects and detailed investigation of flow behaviour. This report details the studies conducted by IIT Madras under this project.

1.2 Project Methodology

A Profile of reservoir is shown in **Figure A1**. Considering BB' for the 2D CFD simulations. BB' is of length 52km and maximum depth is of 20m. The specific objectives of the project could be achieved by means of giving the acceleration time series as input to the whole domain. The domain the mesh configurations are shown **Figure A2**. The scaling is done only in y direction to visualise the domain and mesh. Mesh generation details are given in **Error! Reference source not found.**.

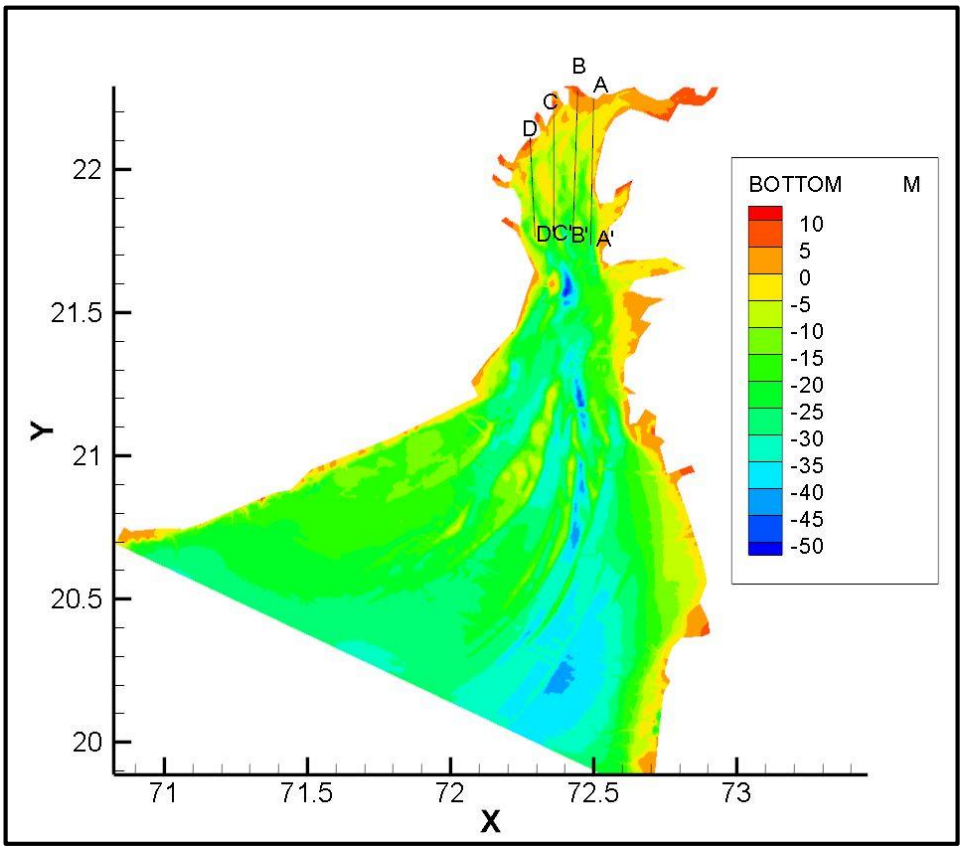

Figure A1: Profile of the reservoir bottom

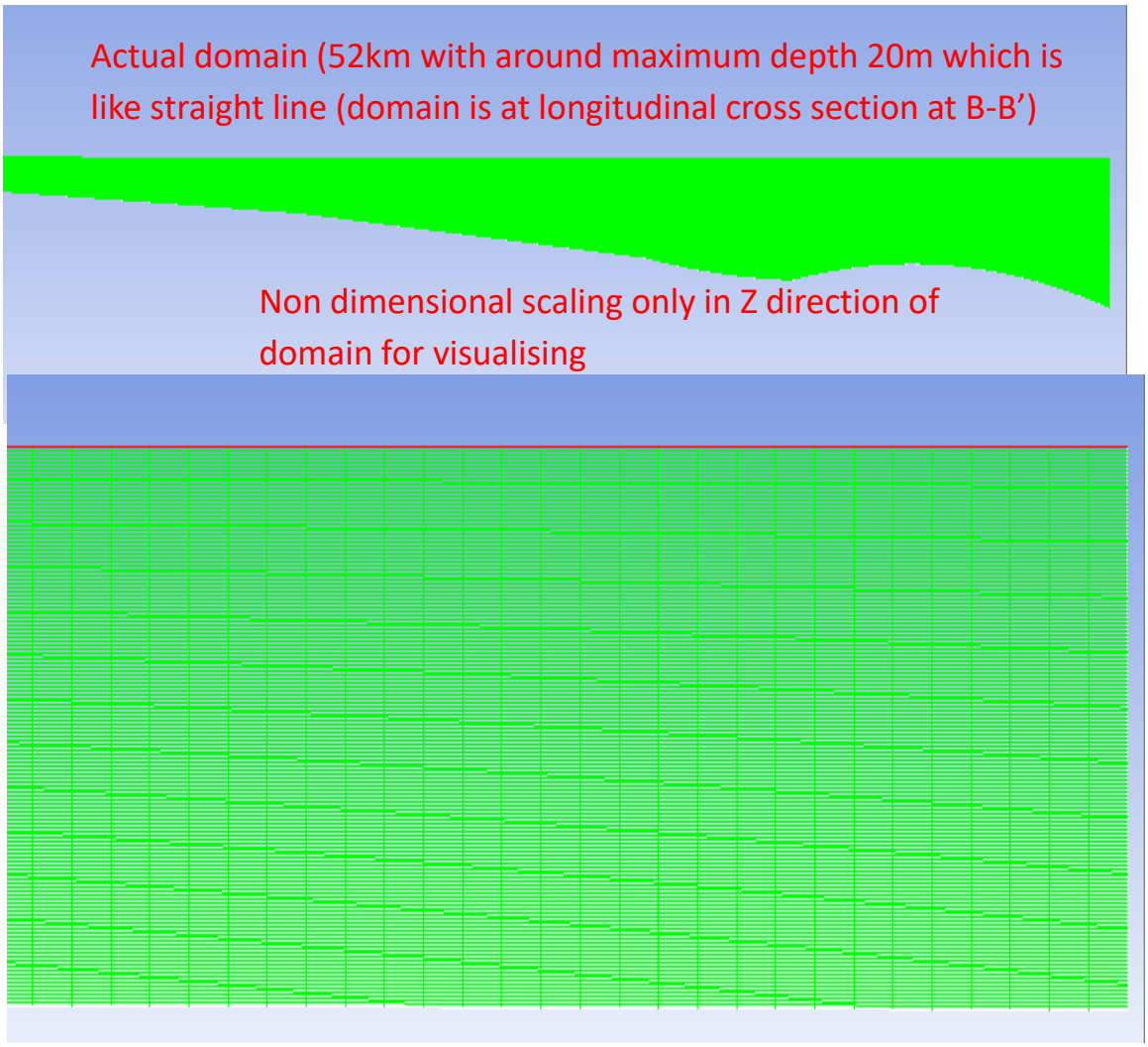

Figure A2: Mesh generation and profile of BB'

Domain Extents:

X-coordinate: 0 - 52km

Z-coordinate: min (m) = -20m to 9m

Mesh Generation Details

Quadrilateral mesh with 1 in 5m in x direction and 1 in 0.06m in y direction

Table A1: Mesh details

Cells	Faces	Nodes

2292759	4601262	2308504

1.3 Solvers and Boundary Conditions

The CFD based analysis is carried out using industry standard FLUENT^{tm} package. The CFD studies are conducted in prototype scale. The solver parameters, material properties, boundary conditions and other parameters considered for 3D analysis is detailed in **Table A1** to **Table A3**. The VOF model with implicit scheme and *k-ε* turbulence model is used for studying the forces acting on dam wall.

Table A2: Solver parameters

2d Dimensional Model
Unsteady RANS with shock capturing
Standard K-∈ Standard Wall Function
Multi-Phase VOF
Constant Density
Segregated Flow

Table A3: Boundary conditions

Domain Interior	**Acceleration In X Direction Given As Udf table (User Defined Function)**
Dam Wall	Wall
Reservoir Bed	Wall
Outlet	Pressure Outlet
Free surface	Pressure Outlet

1.4 Input data provided by CSIR:

The seismic data provided is of two types, one is Maximum credible earthquake simulation (MCES) and other is Design based earthquake simulation (DBES). For 2D CFD simulation of reservoir with dam the following MCES and DBES input acceleration data varying from 0 to 45s at an interval of 0.005s used to find the forces and added mass on the dam.

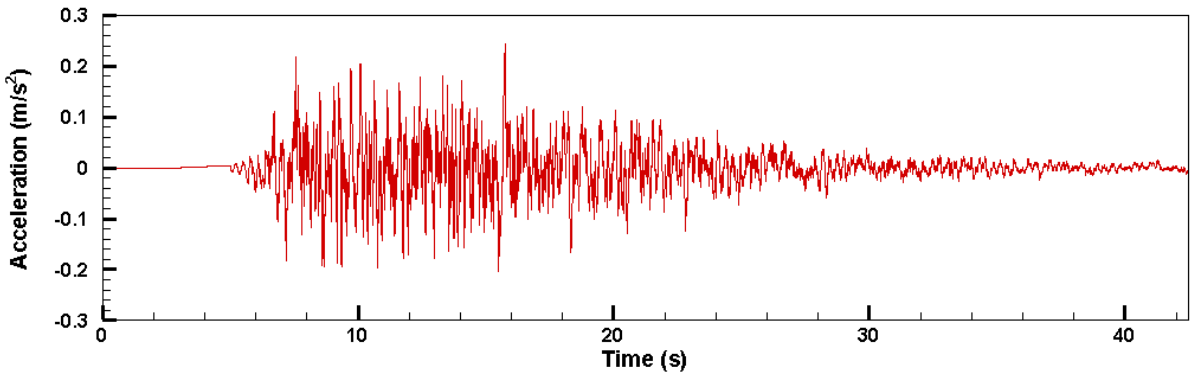

Figure A3: MCES data (X accelerations)

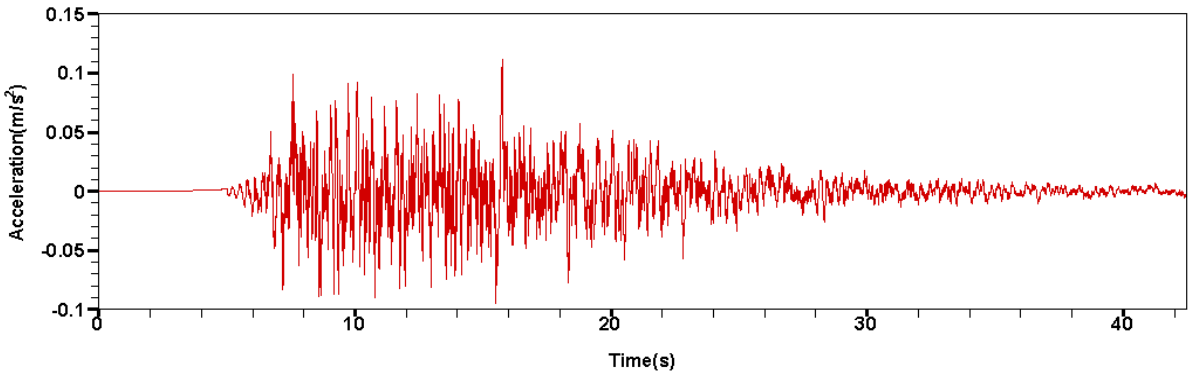

Figure A4: DBES seismic data (X accelerations)

1.5 Results and Discussions

To run the simulations, the domain is initialized with acceleration input data. The acceleration data (horizontal shaking) is varying from 0 to 45s at an interval of 0.005s. Therefore, the simulations are carried out as transient flow for the input data given. The contours, forces, total pressure and the calculated added mass are presented in **Figures A5** to A**11**. The pressure contour scaled in z direction is shown in **Figure A5** and the volume fraction of water scaled in z direction for visualising is shown in Error! Reference source not found. . The force on the dam wall for MCES data is shown in **Figure A7** and the RMS value of the force is 400KN and the assessed added mass is $1.57X10^6$ kg. **Figure A8** shows the peak-to-peak comparison of force and input

acceleration data. The total pressure acting on the dam wall is shown in Error! Reference source not found. for the MCES acceleration data. Similarly, **Figure A10** shows the peak-to-peak comparison of force and input acceleration data for DBES acceleration data and the RMS of value of the force is 391KN and the assessed added mass is $2.6X10^6$ kg, the assessed added mass through CFD simulations is close to the values with reference to P.M.V. Ribeiro and L.J. Pedroso (Dynamic Response of Dam-Reservoir Systems: Review and a Semi-Analytical Proposal). Error! Reference source not found. Shows the total pressure acting on the dam wall for DBES acceleration data.

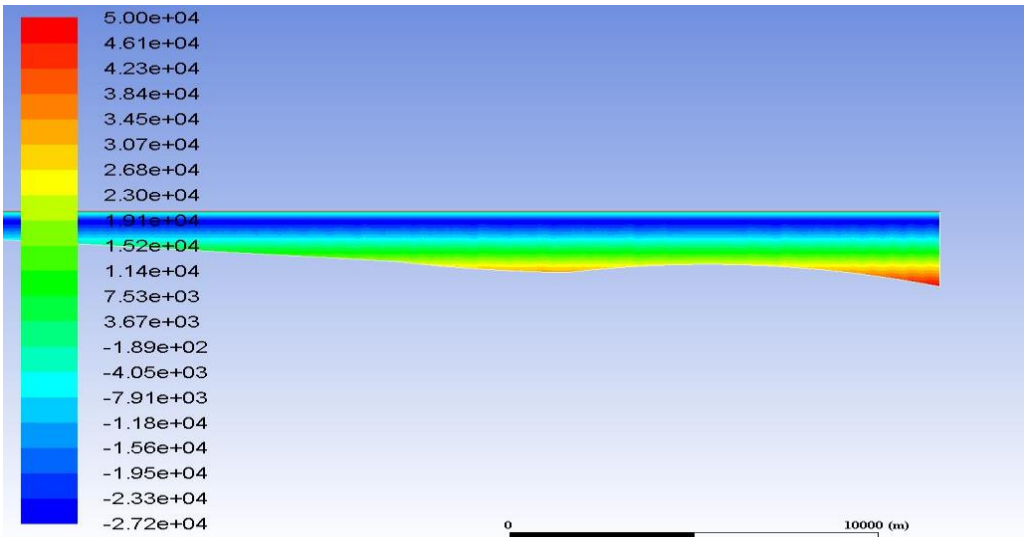

Figure A5: Pressure contour (scaling only in Z direction for visualizing)

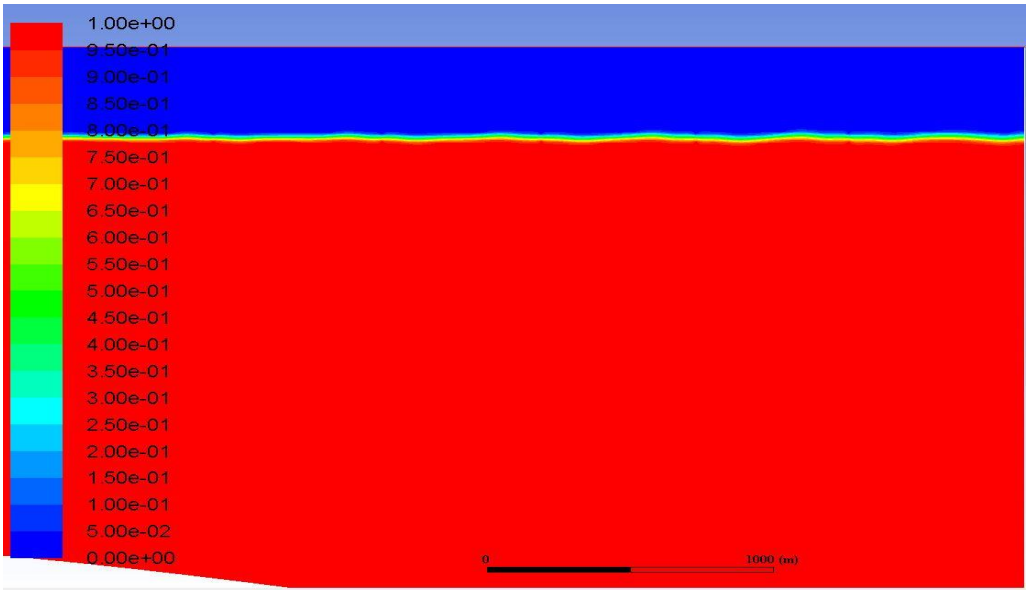

Figure A6: Volume fraction of water scaling in direction to visualise

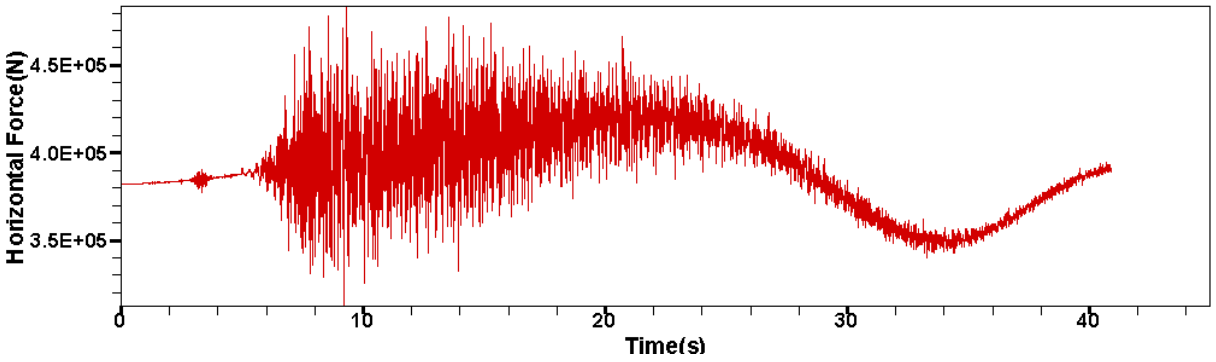

Figure A7: Forces on dam wall for Whole Acceleration Time Series (MCES)

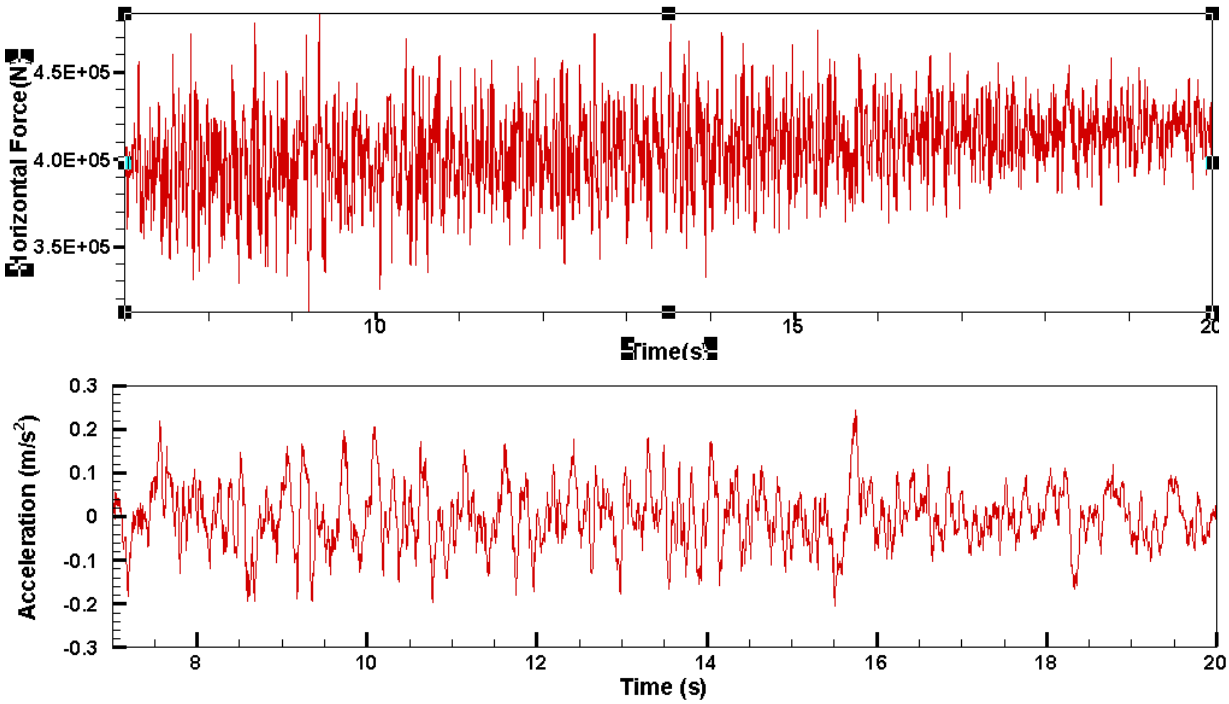

Figure A8: Forces at peak amplitude of Accelerations (MCES)

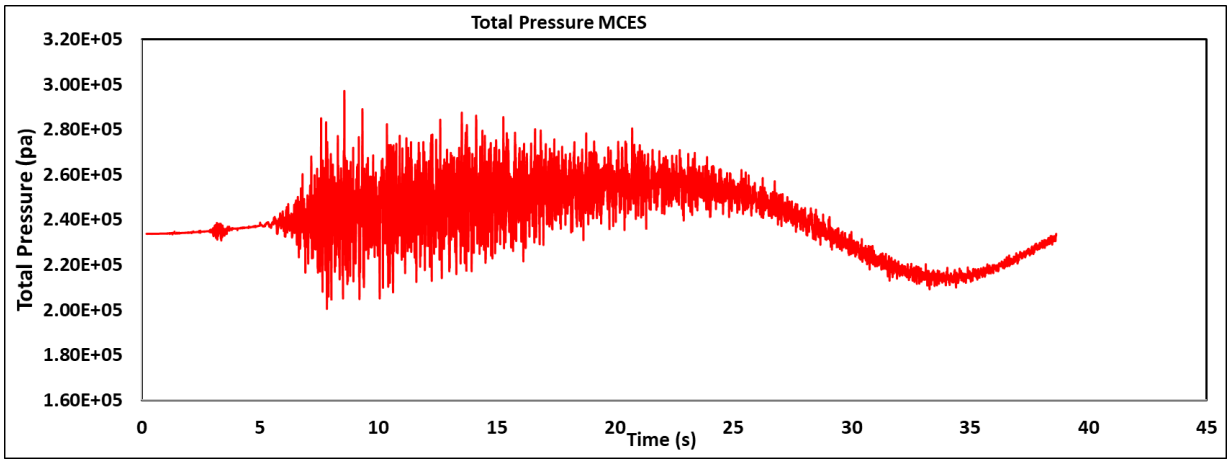

Figure A9: Total Pressure acting on dam wall for Acceleration Time Series (MCES)

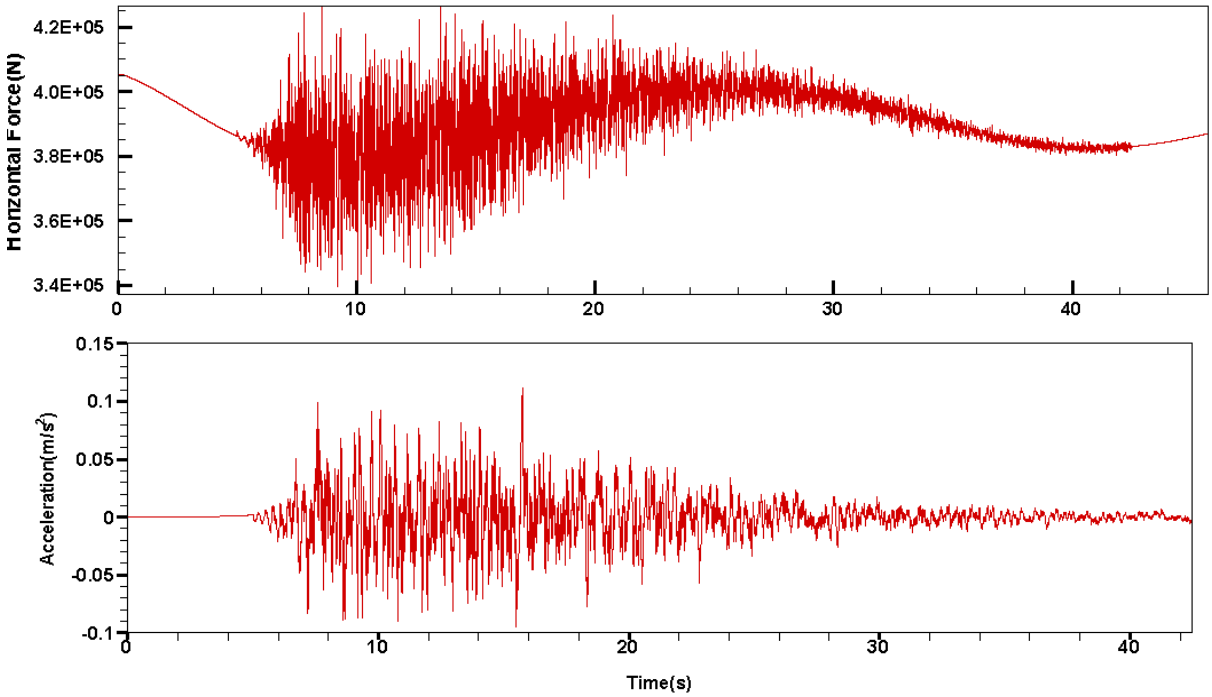

Figure A10: Forces on dam wall for Whole Acceleration Time Series (DBES)

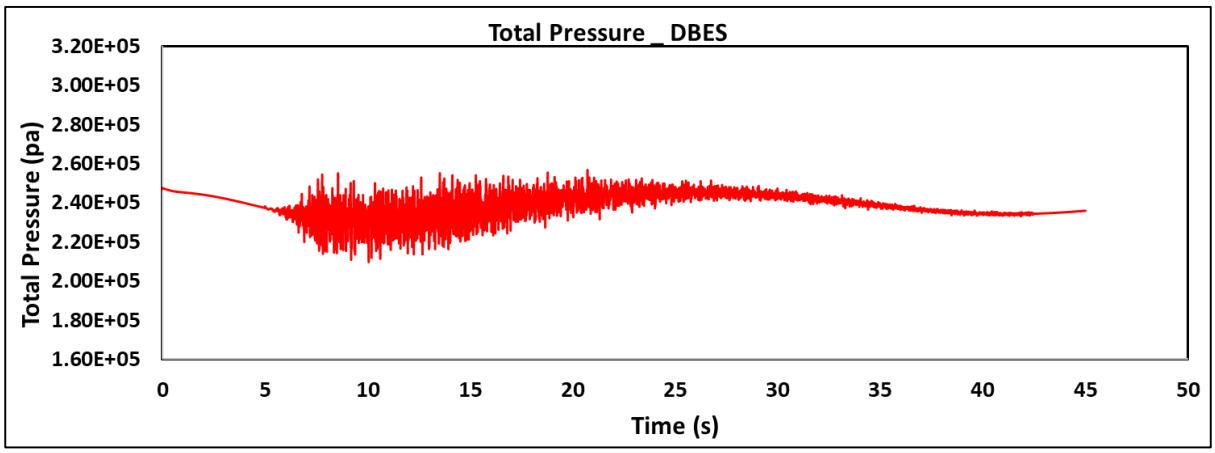

Figure A11: Total Pressure acting on dam wall for Acceleration Time Series

1.6 STUDIES RELATED TO THREE-DIMENSIONAL RESERVOIR SIECHE MODELING

The Kalpasar Project, also known as the Gulf of Khambhat Development Project, entails building a dam that can hold 10,000 million cubic metres of fresh water from rivers like the Narmada, Mahi, Dhadhar, Sabarmati, Limbdi-Bhagovo, and two other minor rivers, or 25% of Gujarat's average annual precipitation flow. A three-dimensional reservoir sieche modelling approach is used to determine the forces acting on the dam wall while considering hydrostatic, and hydrodynamic pressure plots. The three-dimensional elevation and sieche plots are initially

taken. After an earthquake, the reservoir water will oscillate and a sieche will form. For each time frame in the domain, a different slice location is chosen, such as A-A', B-B', C-C', D-D', and E-E'. To measure the total pressure exerted by the sieche in the domain, three-time frames are used: the sieche approaching the dam, the sieche against the dam, and the sieche returning from the dam are each represented in **Figure A12**, **A13**, and **A14**, respectively. Acceleration in Y direction is induced to capture the critical impact on dam wall.

Time series were extracted at three different slice locations at various zones of:

1. Pressure at the bottom
2. Pressure in the middle
3. Pressure at the top surface

To determine the total pressure and pressure fluctuation in the domain during different sieche conditions. The locations were selected near the dam wall at different zones in order to extract the time series plot.

In the present study, a simulation related to three-dimensional reservoir sieche modelling is been conducted, and the three-dimensional grid geometry file contained 2637888 Nodes, 4789048 Elements, and 12 Layers. The maximum total pressure across the domain is 221000 Pa during the initial condition before initiation of earthquake forcing and this maximum pressure raises to 254290.06 Pa at the time of sieche interaction with the dam wall.

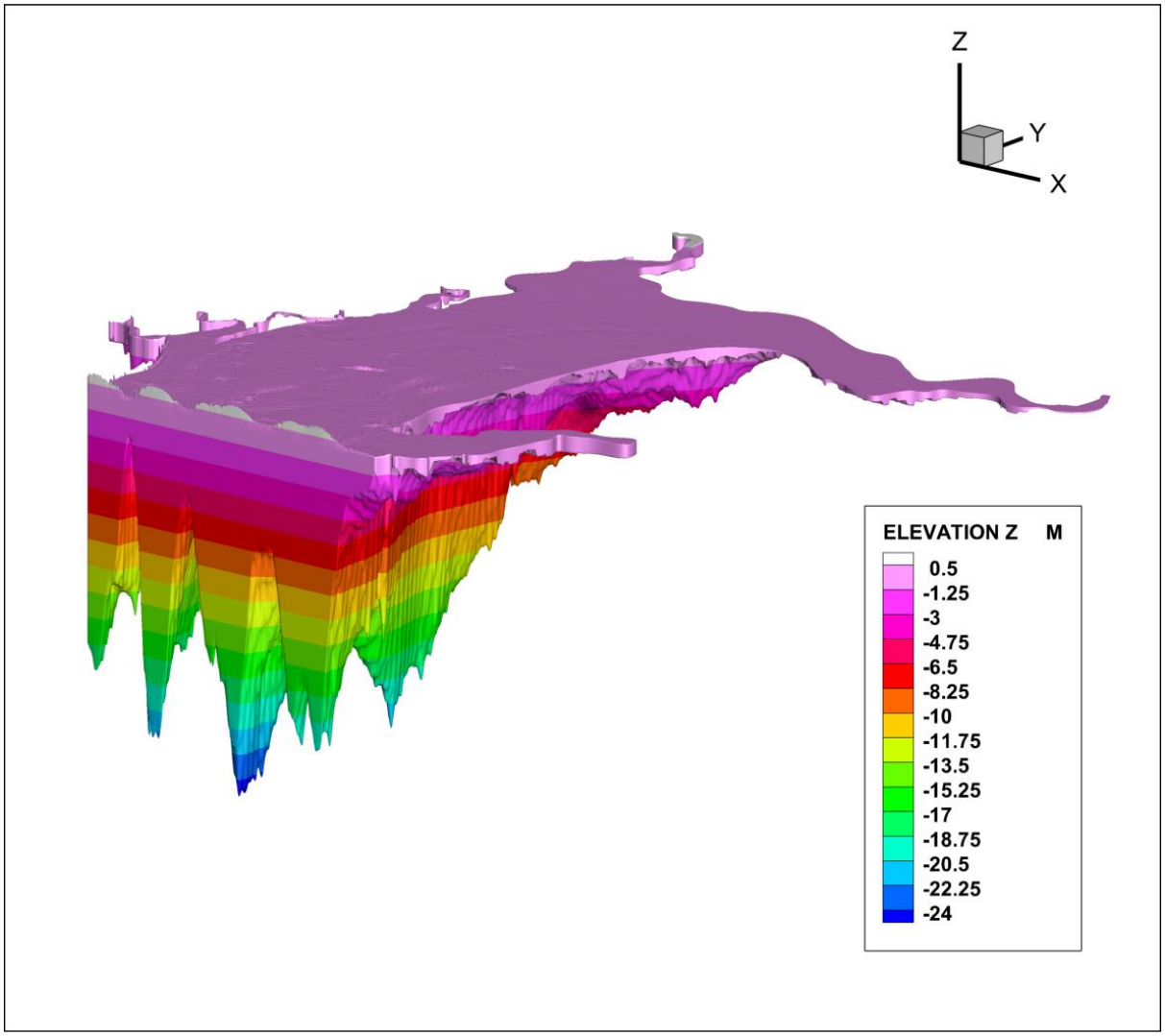

Figure A12: Sieche approaching the Dam

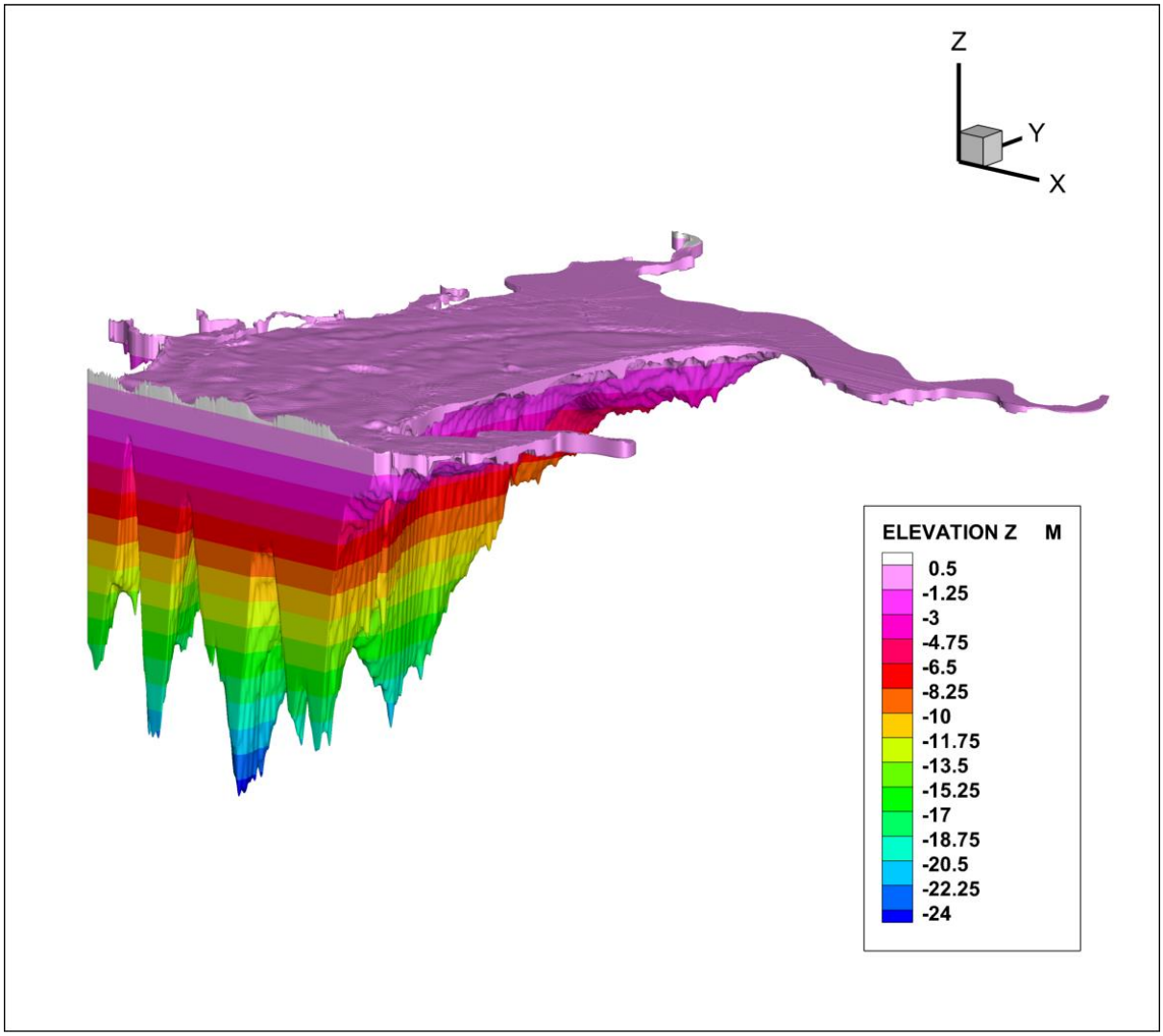

Figure A13: Sieche against the Dam

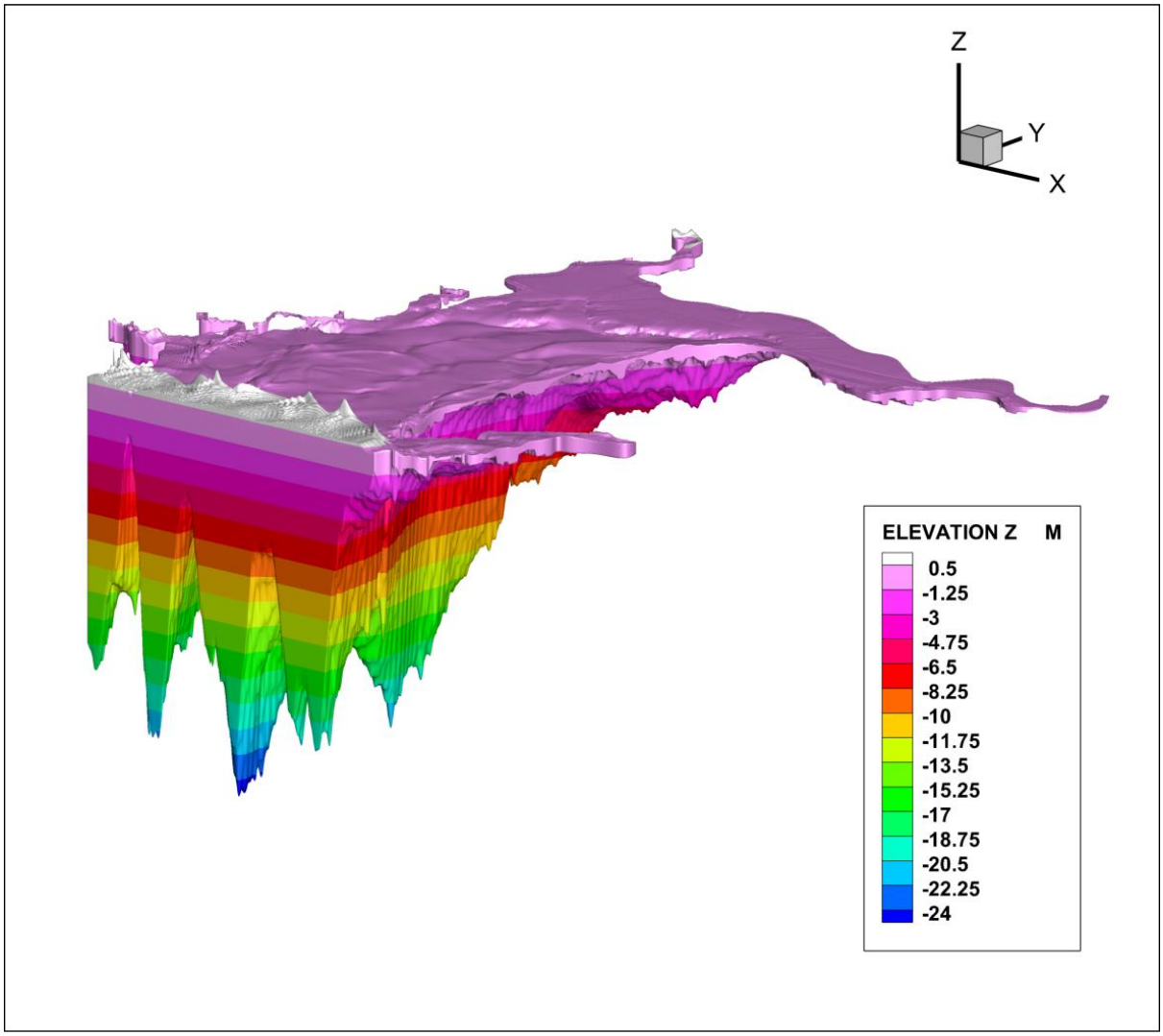

Figure A14: Sieche while returning from the Dam

1.6.1 Studies related to three-dimensional reservoir sieche modeling in section A-A'

Based on reservoir sieche modelling with respect to elevation value, the sieche approaching the dam at **section A-A'** is shown in **Figure A15**. The maximum total pressure predicted is 223000 Pa.

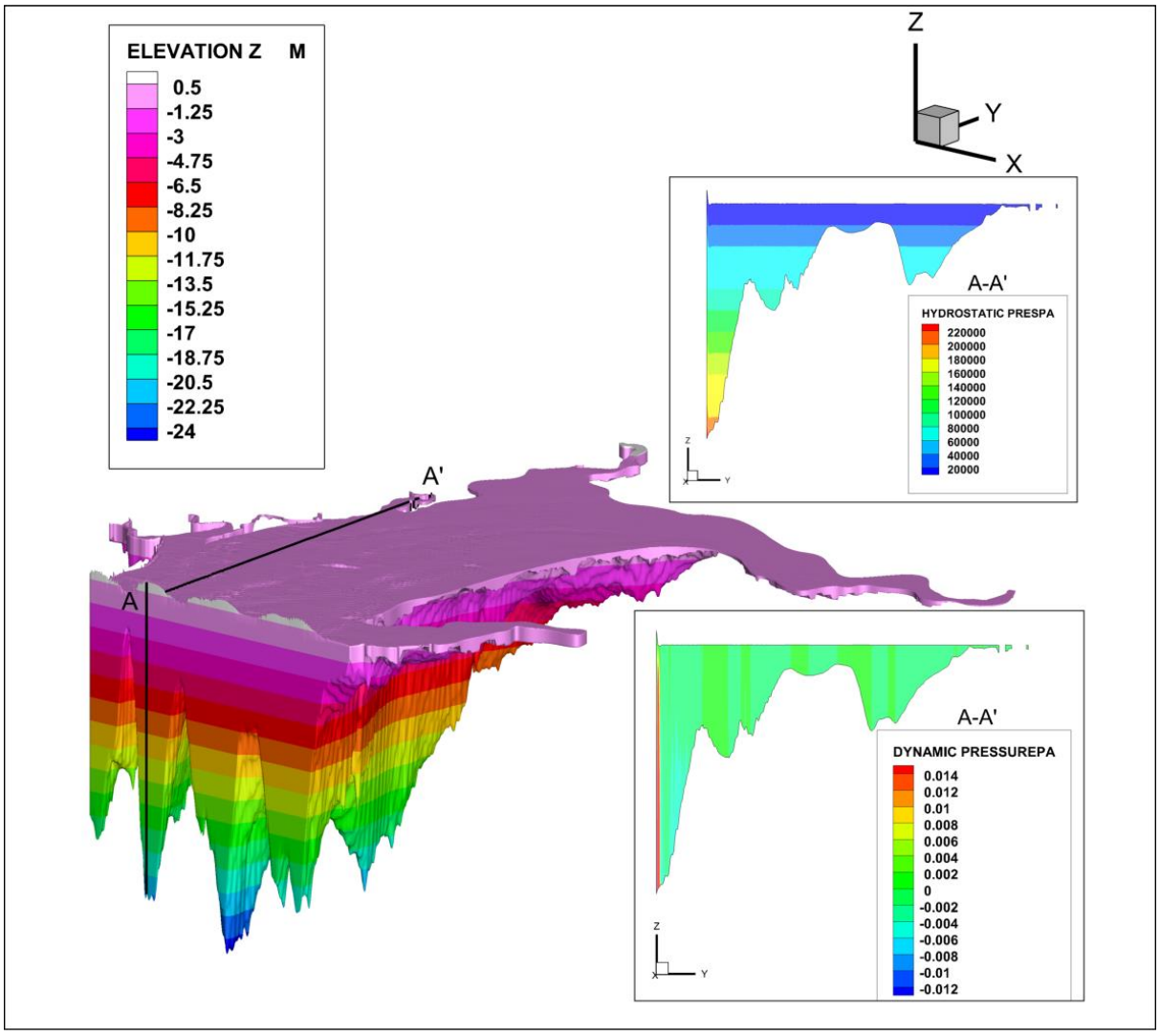

Figure A15: Sieche approaching the Dam at section A-A'

Based on reservoir sieche modelling with respect to the total pressure value at the bottom zone of **section A-A'** is shown in **Figure A16**. During the initial solution time, the total pressure was approximately 208000 Pa up to the solution time of 86400 sec (initiation of earthquake forcing). While the total pressure at the time of sieche approaching the dam is 206000 Pa. 223000 Pa of total pressure is predicted while sieche against the dam, and 218000 Pa is predicted while sieche returning.

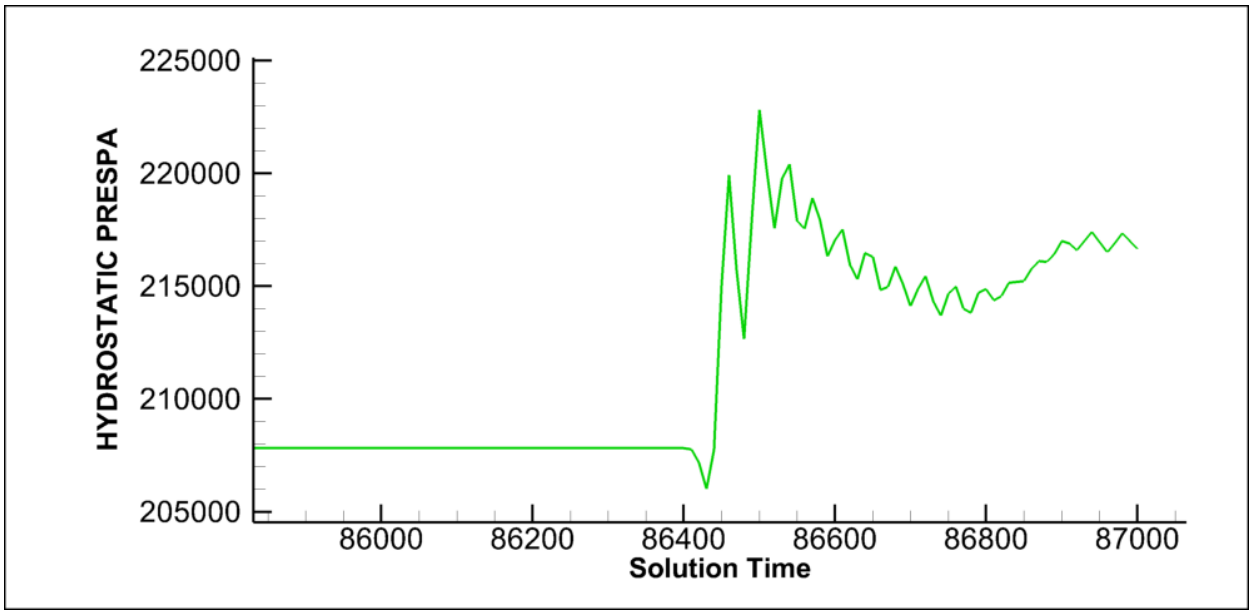

Figure A16: Total Pressure at bottom for section A-A'

Based on reservoir sieche modelling with respect to elevation value, the sieche against the dam at section A-A' is shown in **Figure A17**.

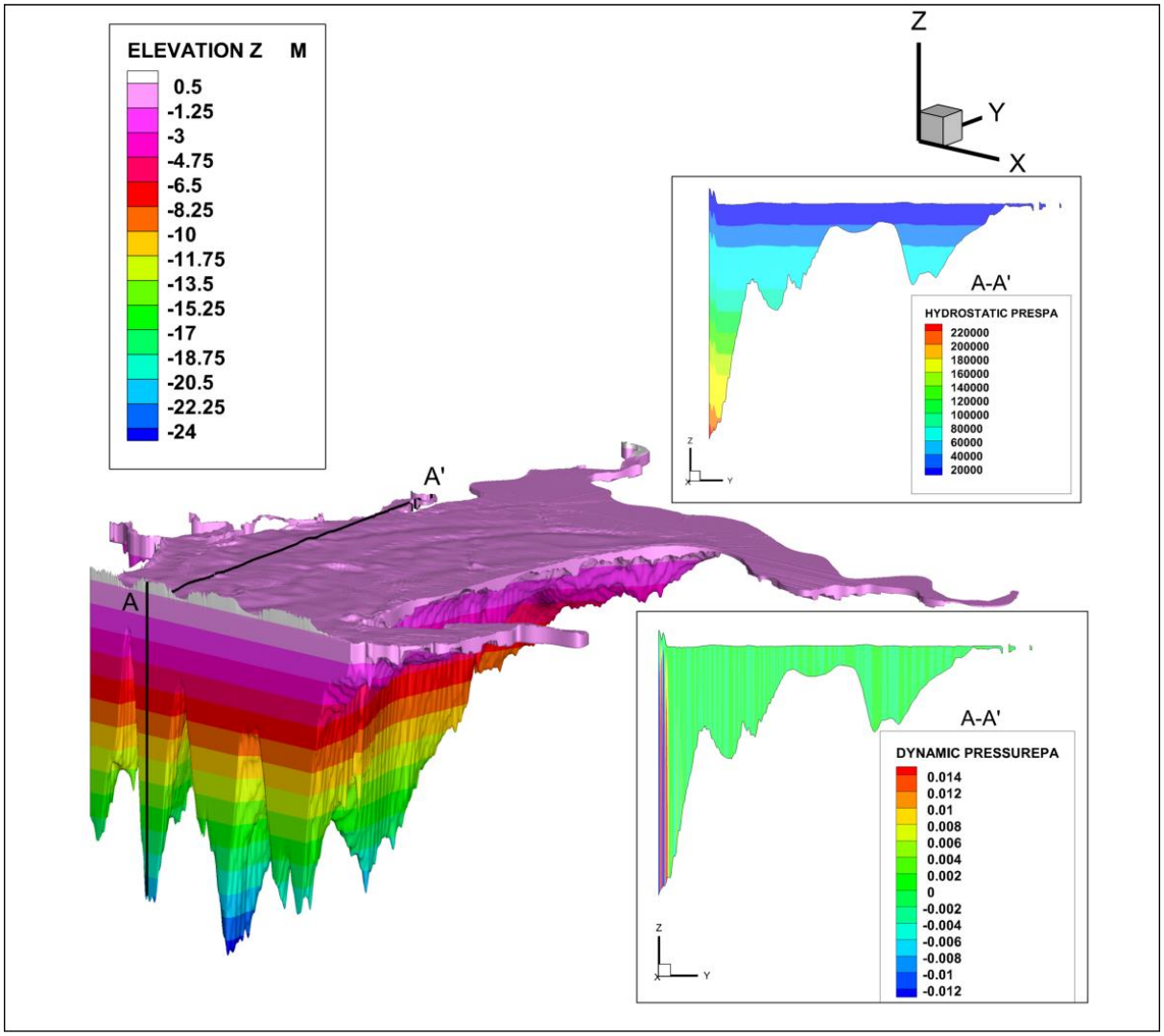

Figure A17: Sieche against the Dam at section A-A'

Based on reservoir sieche modelling with respect to total pressure value at the middle zone of the **section A-A'** is shown in **Figure A18**. During the initial solution time, the total pressure was approximately 104500 Pa up to the solution time of 86400 sec (initiation of earthquake forcing). While the total pressure at the time of sieche approaching the dam is 103500 Pa. 119000 Pa of total pressure is predicted while sieche against the dam, and 113000 Pa is predicted while sieche returning.

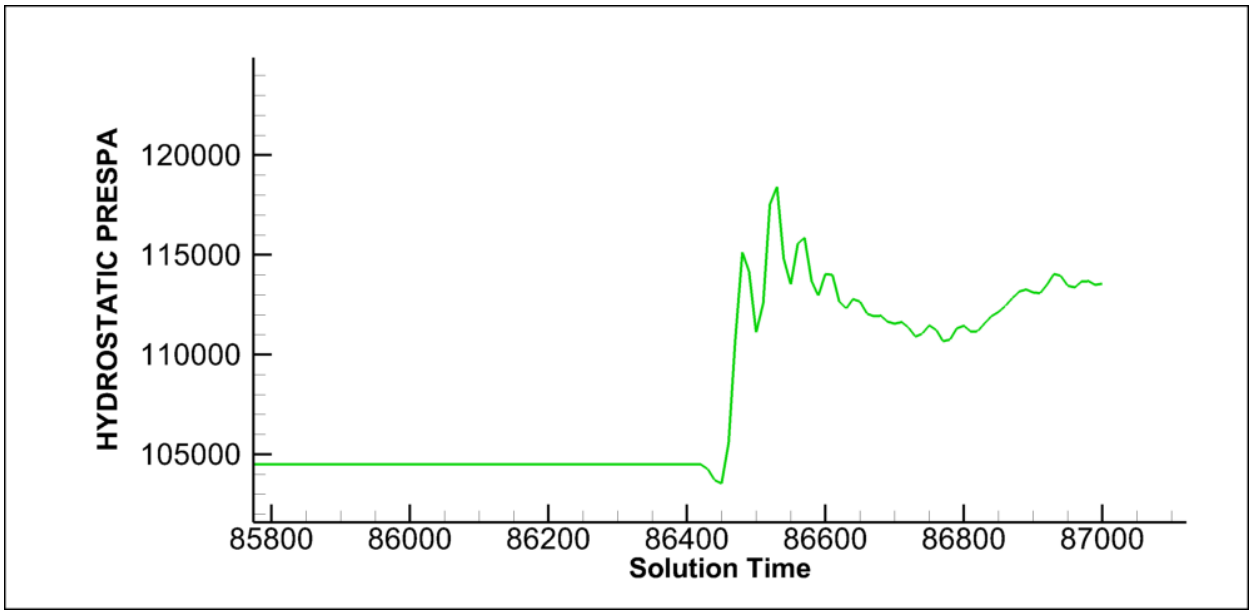

Figure A18: Pressure at the middle of dam at section A-A'

Based on reservoir sieche modelling with respect to elevation value, the sieche while returning from the dam at **section A-A'** is shown in **Figure A19**. The total pressure predicted is 220000 Pa.

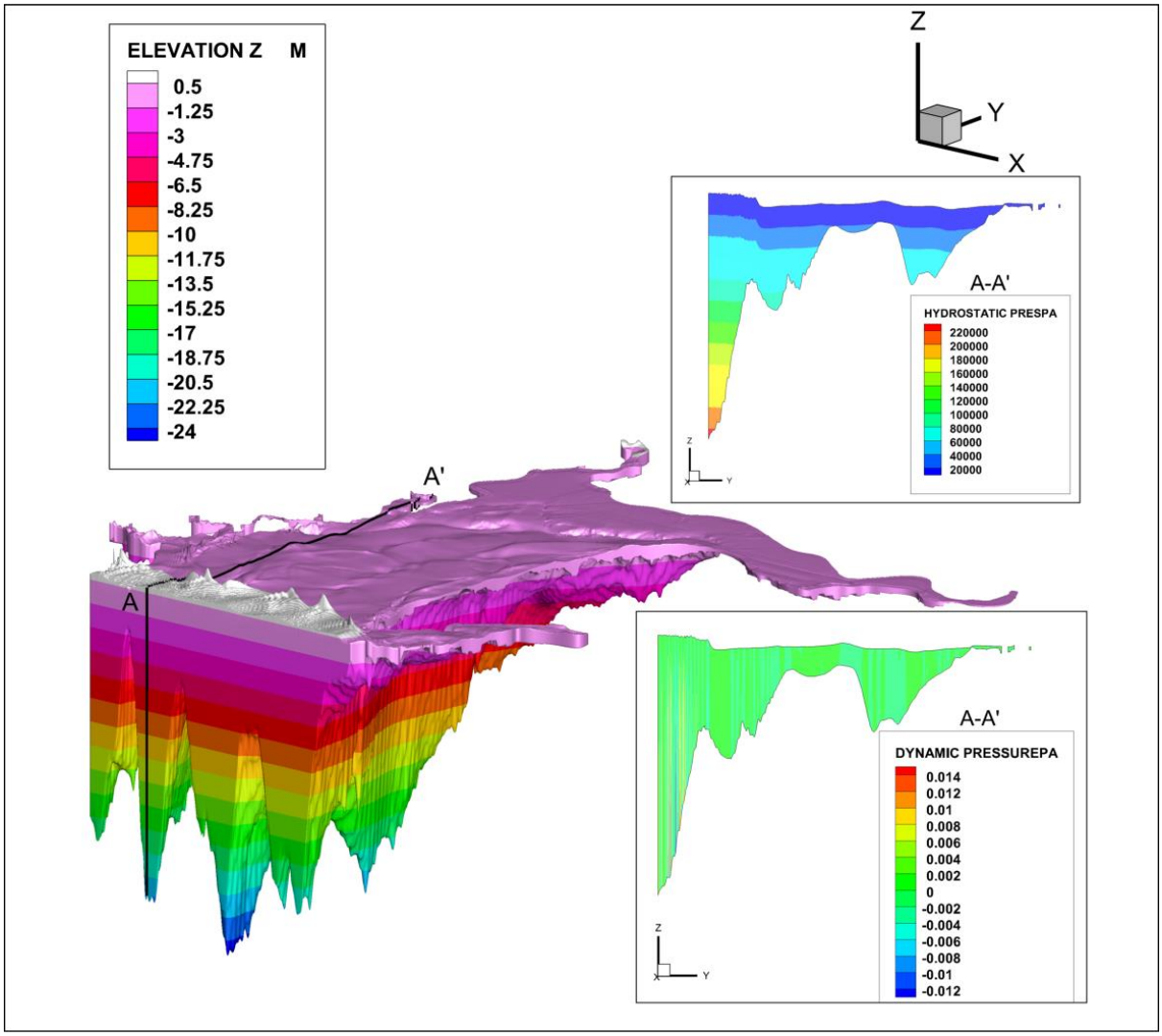

Figure A19: Sieche while returning from the Dam at section A-A'

Based on reservoir sieche modelling with respect to total pressure value at the top surface zone of **section A-A'** is shown in **Figure A20**. During the initial solution time, the total pressure was approximately 4800 Pa up to the solution time of 86400 sec (initiation of earthquake forcing). While the total pressure at the time of sieche approaching the dam is 4000 Pa. 18000 Pa of total pressure is predicted while sieche against the dam, and 14000 Pa is predicted while sieche returning.

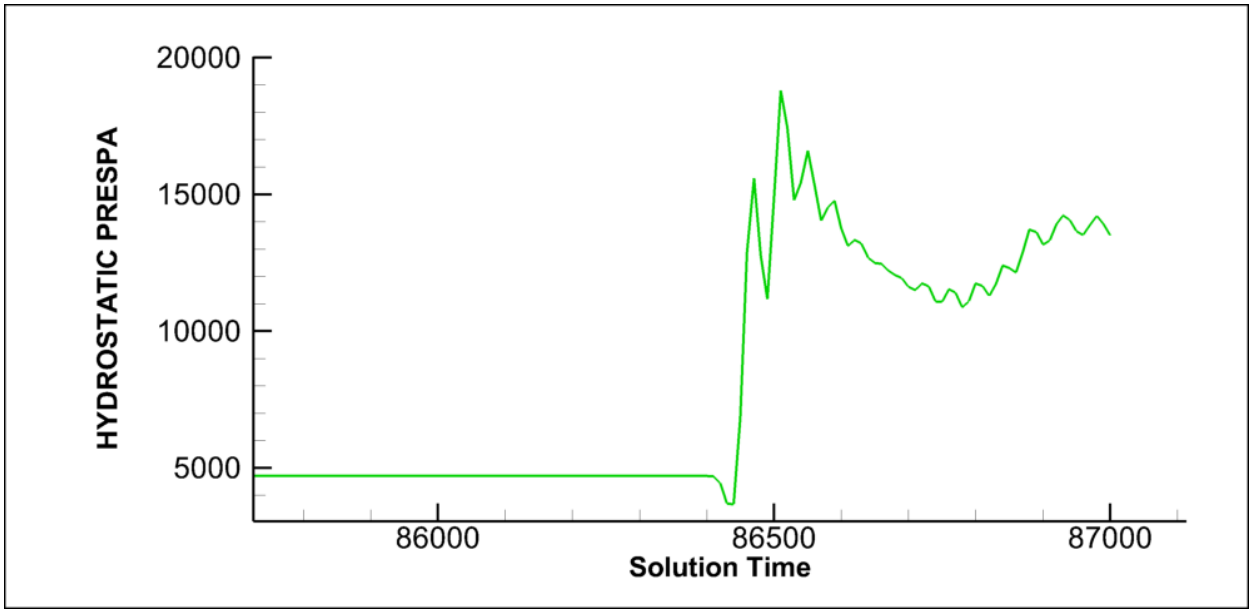

Figure A20: Pressure at the top of dam at section A-A'

Table A4 shows the pressure variation at various zones, including the bottom, middle, and top, over different time pf sieche propagation in **Section A-A'**. According to the findings of this study, the pressure is highest at the bottom level and gradually decreases towards the top surface. According to **Table A4**, the nature of fluctuation in the top surface zone increases by 78% (4000 Pa to 18000 Pa), the middle surface by 13% (103500 Pa to 119000 Pa), and the bottom surface by 8% (206000 Pa to 223000 Pa) during the sieche approaching the dam to the sieche against the dam, which is caused by the sieche hitting the dam wall. The level of pressure fluctuation gradually decreases by 29% (18000 Pa to 14000 Pa) in the top surface, the middle surface by 5% (119000 Pa to 113000 Pa) and the bottom surface by 2% (223000 Pa to 218000 Pa) during the sieche against the dam to the sieche while returning from the dam. The total pressure in the bottom and middle zones increases from sieche approaching the dam to sieche against the dam, and there is a gradual decrease in pressure from sieche against the dam to sieche while returning from the dam.

It is found that the change in total pressure is maximum at the top surface when compared to the bottom zone and the pressure is maximum at bottom as compared to top surface. It is clear that the sieche in the reservoir has a greater impact on the top surface.

Table A4: Pressure at different zone for section A-A'

SL. No	Zone	Sieche approaching Dam (Pa)	Sieche against Dam (Pa)	Sieche while returning from Dam (Pa)
1	Bottom	206000	223000	218000
2	Middle	103500	119000	113000
3	Top	4000	18000	14000

1.6.2 Studies related to three-dimensional reservoir sieche modeling at section B-B'

Based on reservoir sieche modelling with respect to elevation value, the sieche approaching the dam at **section B-B'** is shown in **Figure A21**. The maximum total pressure across the section is 234000 Pa.

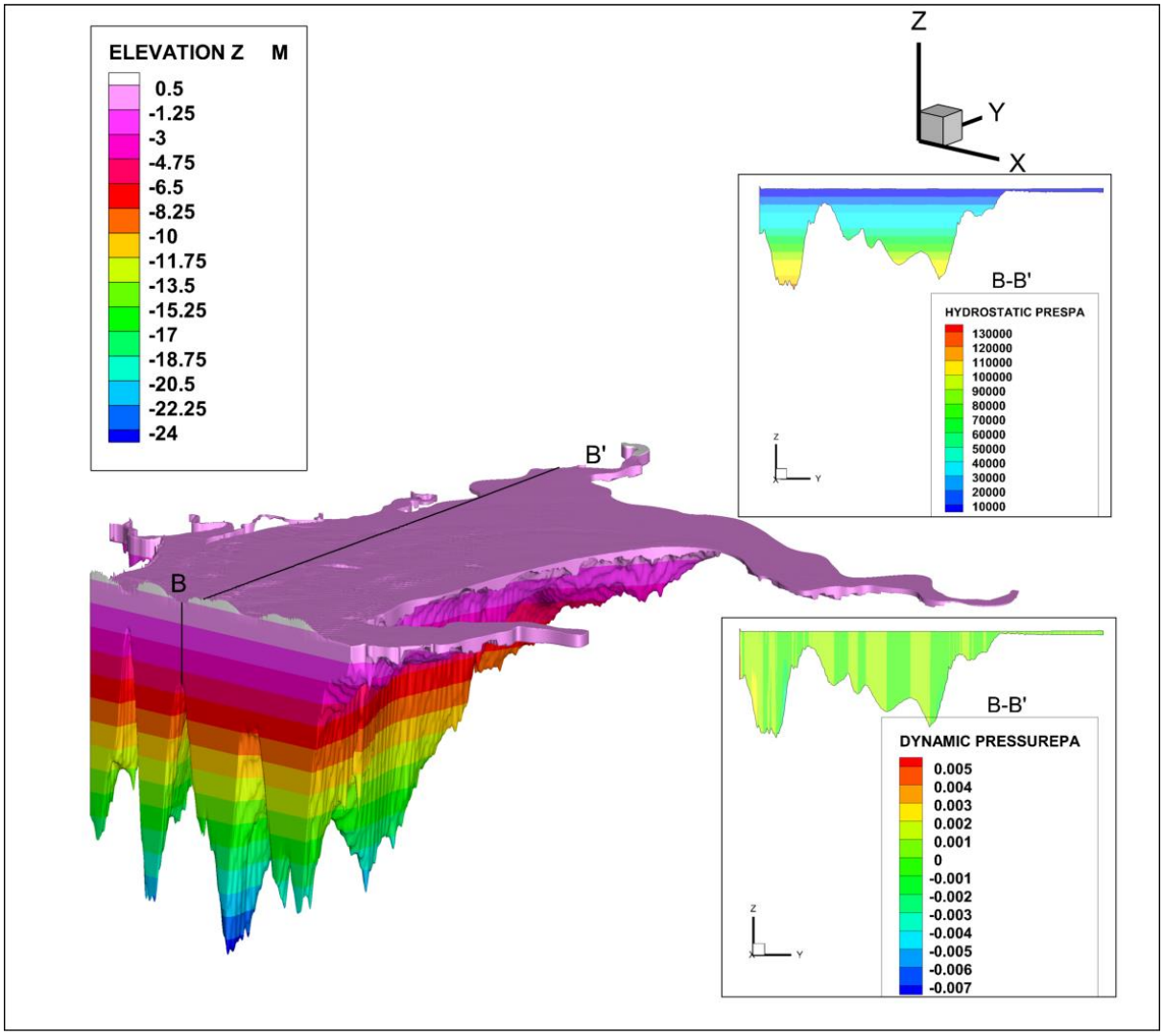

Figure A21: Sieche approaching the Dam at section B-B'

Based on reservoir sieche modelling with respect to total pressure value at the bottom zone of the section B-B' is shown in **Figure A22**. During the initial solution time, the total pressure was approximately 221000 Pa up to the solution time of 86400 sec (initiation of earthquake forcing). While the total pressure at the time of sieche approaching the dam is 218000 Pa. At about 234000 Pa is predicted while sieche against the dam, and 230000 Pa is predicted while sieche returning.

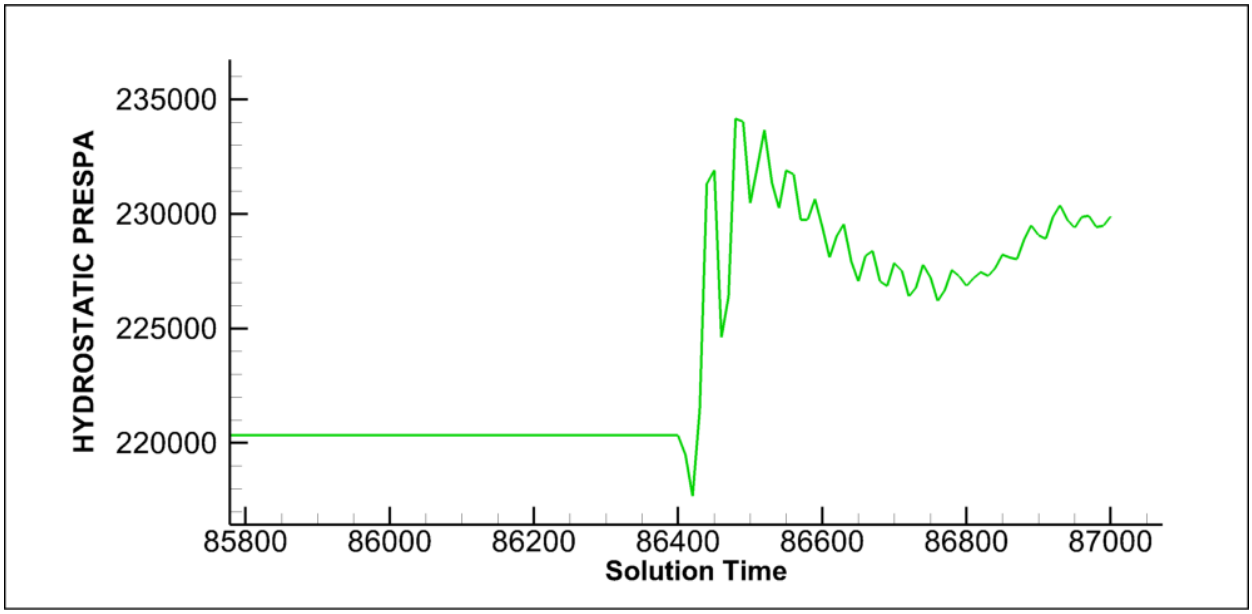

Figure A22: Pressure at the bottom of dam at section B-B'

Based on reservoir sieche modelling with respect to elevation value, the sieche against the dam at **section B-B'** is shown in **Figure A23**.

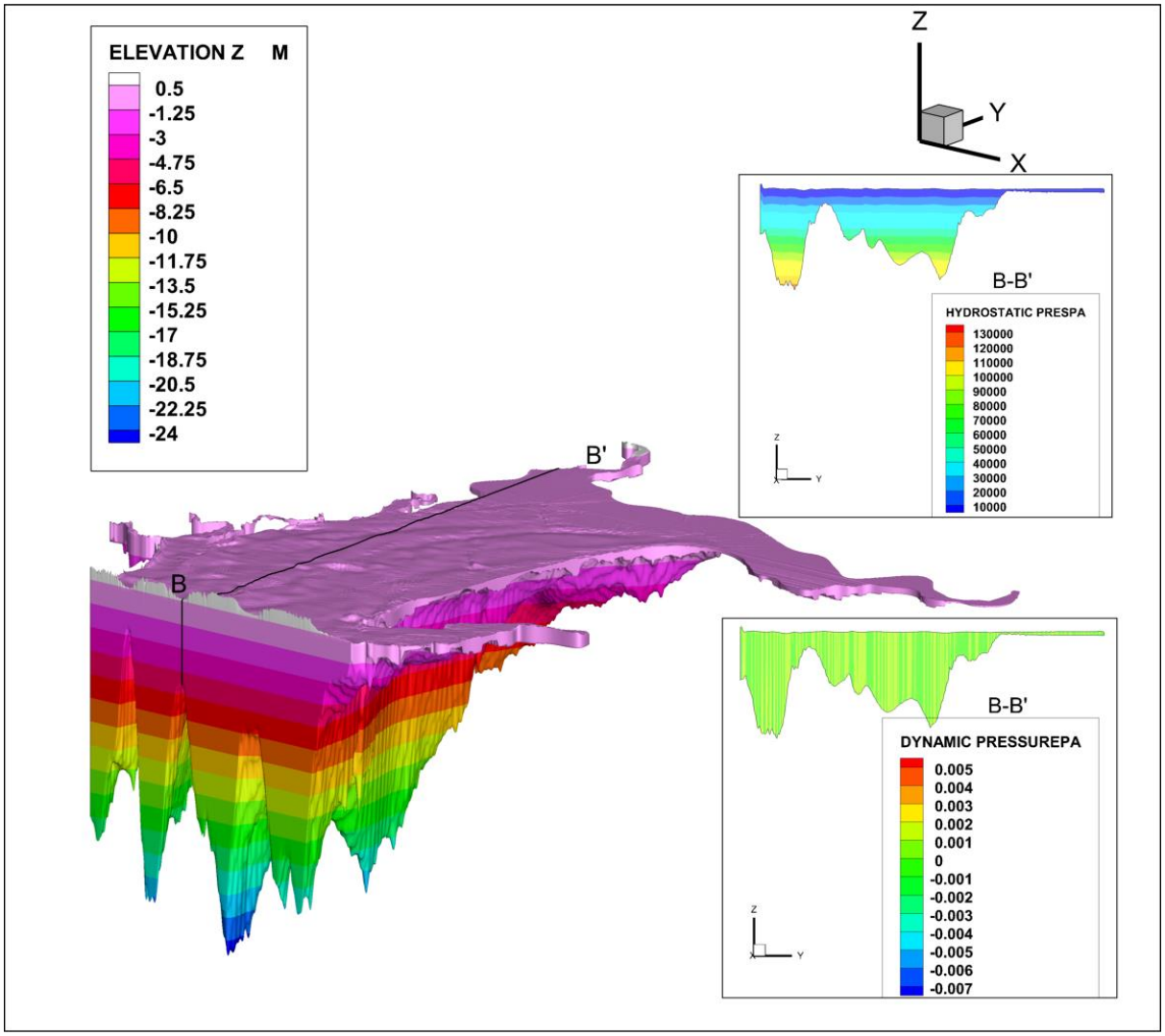

Figure A23: Sieche against the Dam at section B-B'

Based on reservoir sieche modelling with respect to total pressure value at the middle zone of the **section B-B'** is shown in **Figure A24**. During the initial solution time, the total pressure was approximately 101000 Pa up to the solution time of 86400 sec (initiation of earthquake forcing). While the total pressure at the time of sieche approaching the dam is 99000 Pa. 116000 Pa of total pressure is predicted while sieche against the dam, and 111000 Pa is predicted while sieche returning.

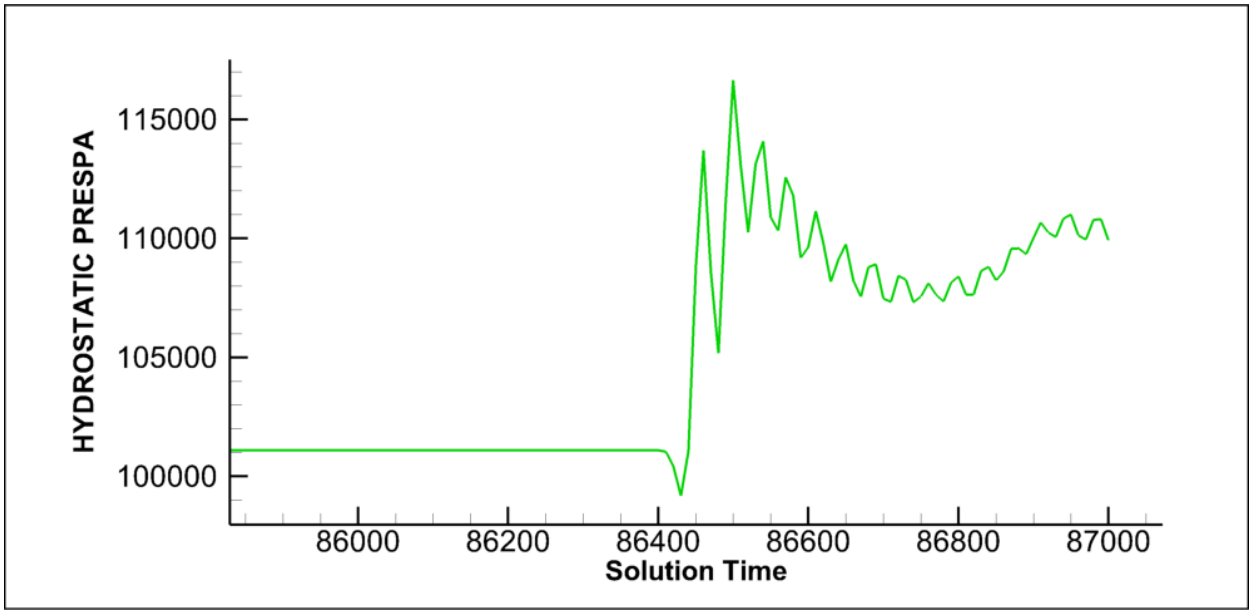

Figure A24: Pressure at the middle of dam at section B-B'

Based on reservoir sieche modelling with respect to elevation value, the sieche while returning from the dam at **section B-B'** is shown in **Figure A25**. The total pressure across the domain is 130000.005 Pa

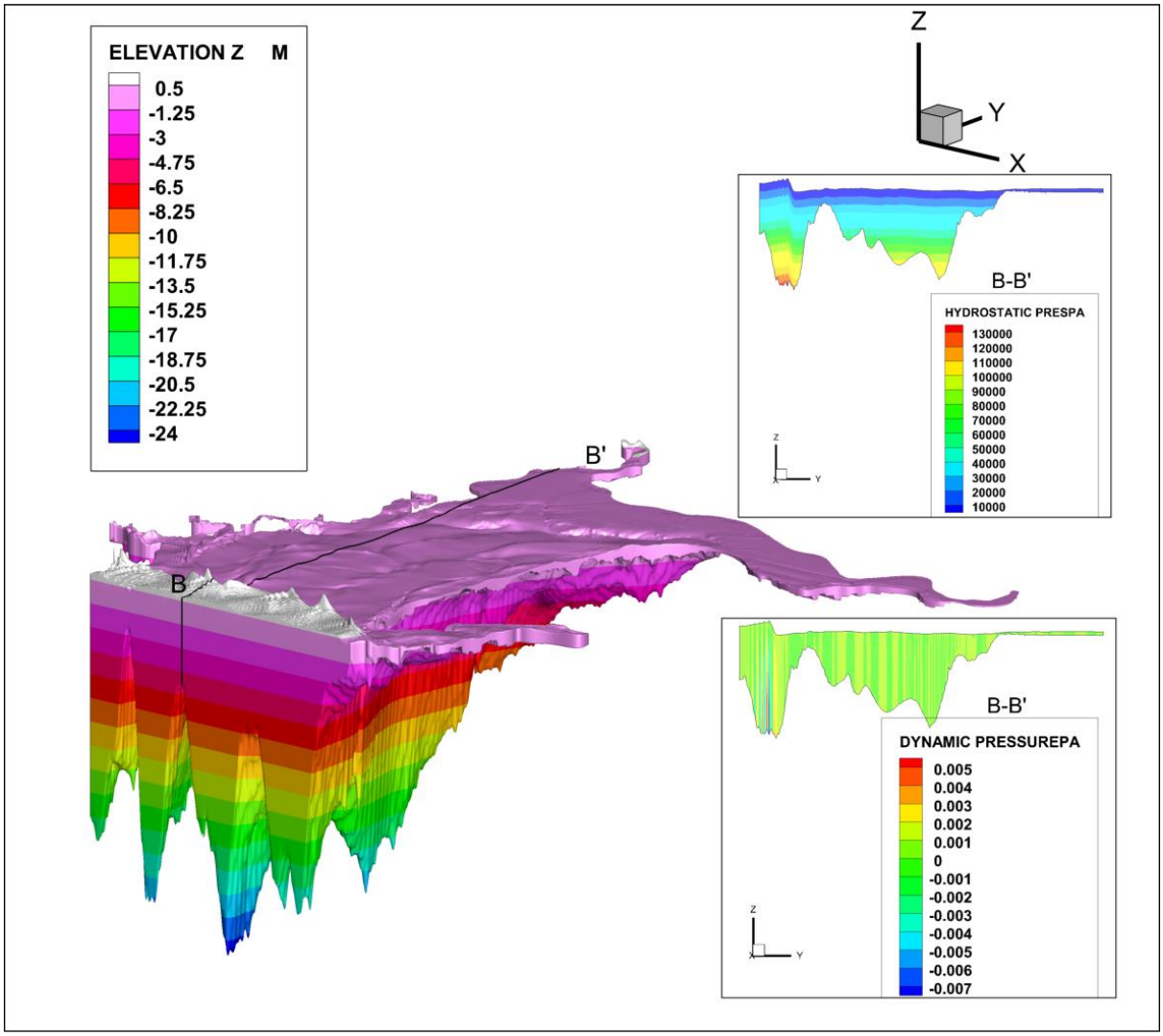

Figure A25: Sieche while returning from the Dam at section B-B'

Based on reservoir sieche modelling with respect to total pressure value at the top surface zone of **section B-B'** is shown in **Figure A26**. During the initial solution time, the total pressure was approximately 3500 Pa up to the solution time of 86400 sec (initiation of earthquake forcing). While the total pressure at the time of sieche approaching the dam is 2000 Pa. At about 18000 Pa is predicted while sieche against the dam, and 14000 Pa is predicted while sieche returning.

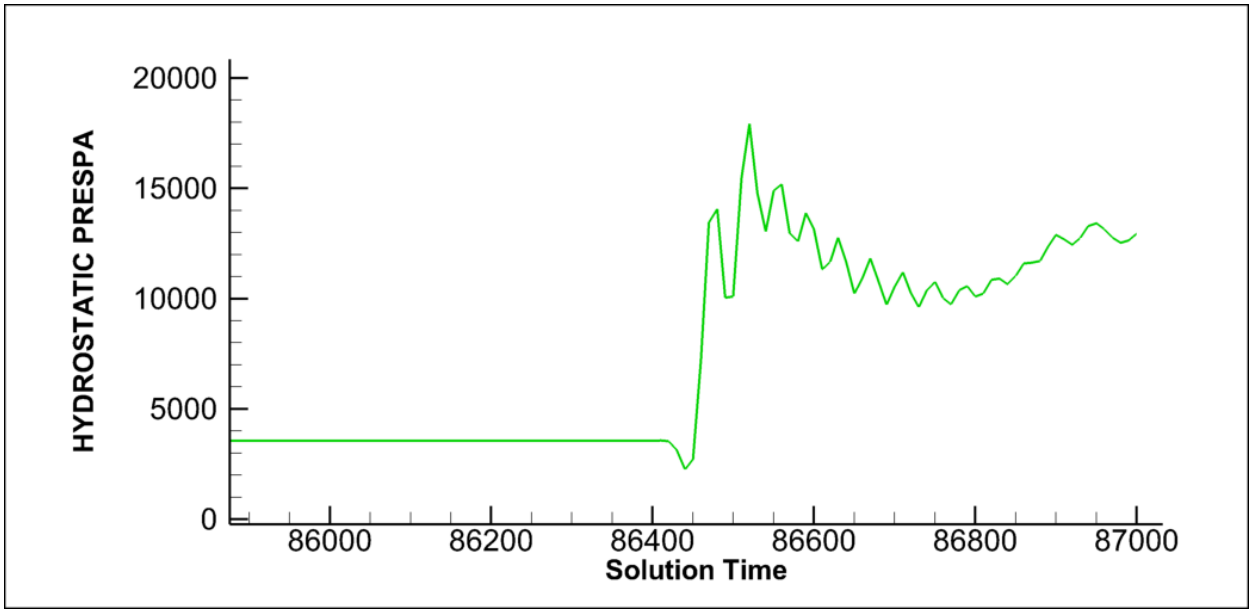

Figure 26: Pressure at the top of dam at section B-B'

Table A5 shows the pressure variation at various zones, including the bottom, middle, and top, over different time of sieche propagation in **Section B-B'**. According to the findings of this study, the pressure is highest at the bottom level and gradually decreases towards the top surface. According to **Table A5**, the nature of fluctuation in the top surface zone increases by 89% (2000 Pa–18000 Pa), the middle surface by 15% (99000 to 116000), and the bottom surface by 7% (218000 Pa to 234000 Pa) during the sieche approaching the dam to the sieche against the dam, which is caused by the sieche hitting the dam wall. The level of pressure fluctuation gradually decreases by 29% (18000 Pa to 14000 Pa) in the top surface, the middle surface by 4% (116000 Pa to 111000 Pa) and the bottom surface by 2% (234000 Pa to 230000 Pa) from the sieche against the dam to the sieche while returning from the dam. The total pressure in the bottom and middle zones increases from sieche approaching the dam to sieche against the dam, and there is a gradual decrease in pressure from sieche against the dam to sieche while returning from the dam.

It is found that the change in nature of pressure fluctuation is maximum at the top surface when compared to the bottom zone and the pressure is maximum at bottom as compared to top surface. The value makes it clear that the sieche that happens in the reservoir has a greater impact on the top surface.

Table A5: Pressure at different zone for section B-B'

SL. No	Zone	Sieche approaching Dam (Pa)	Sieche against Dam (Pa)	Sieche while returning from Dam (Pa)
1	Bottom	218000	234000	230000
2	Middle	99000	116000	111000
3	Top	2000	18000	14000

1.6.3 Studies related to three-dimensional reservoir sieche modeling at section C-C'

Based on reservoir sieche modelling with respect to elevation value, the sieche approaching the dam at **section C-C'** is shown in **Figure A27**. The total pressure across the section is 234000 Pa.

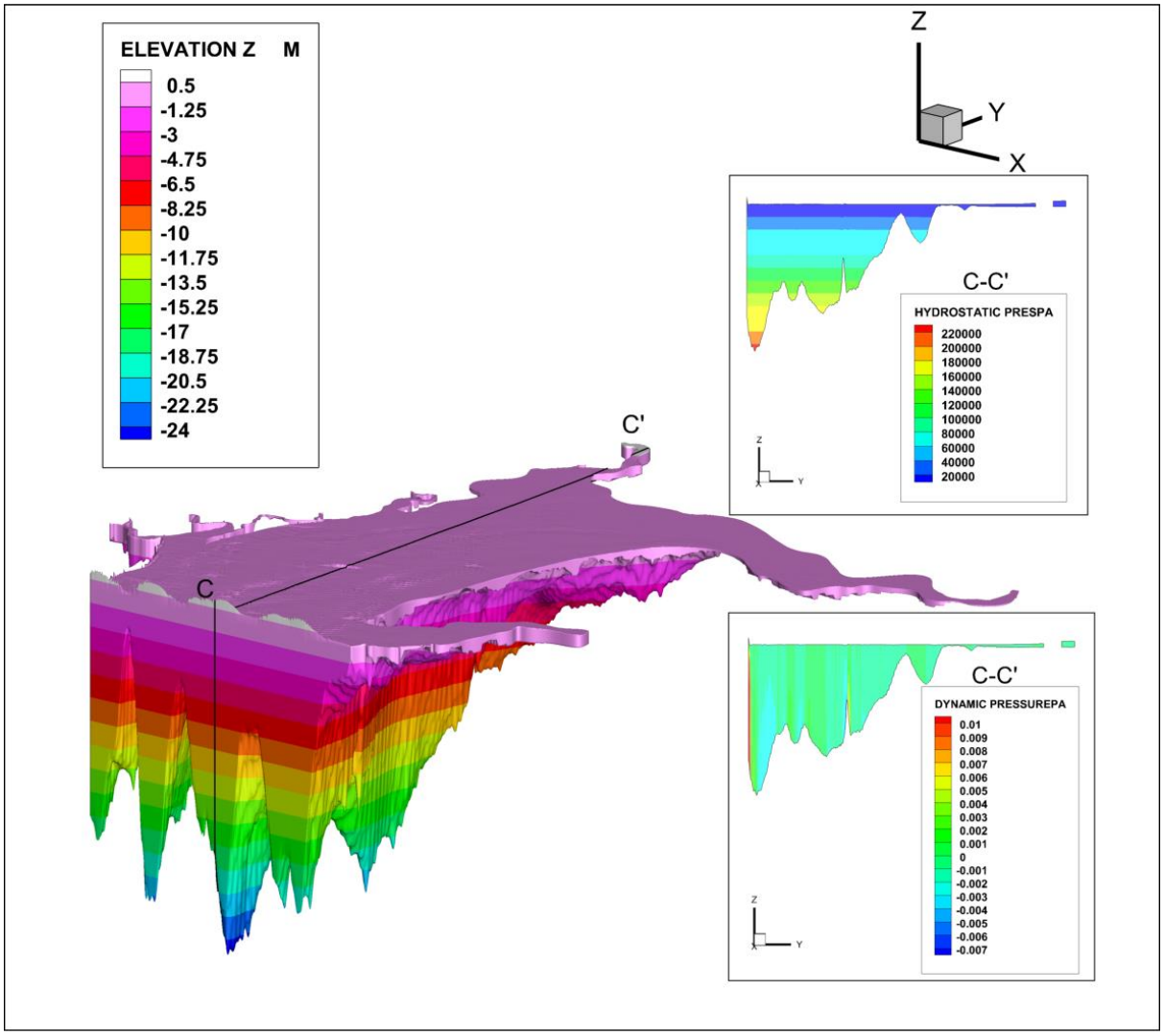

Figure A27: Sieche approaching the Dam at section C-C'

Based on reservoir sieche modelling with respect to total pressure value at the bottom zone of the **section C-C'** is shown in **Figure A28**. During the initial solution time, the total pressure was approximately 220500 Pa up to the solution time of 86400 sec (initiation of earthquake forcing). While the total pressure at the time of sieche approaching the dam is 221000 Pa. 234000 Pa is predicted while sieche against the dam, and 230000 Pa is predicted while sieche returning.

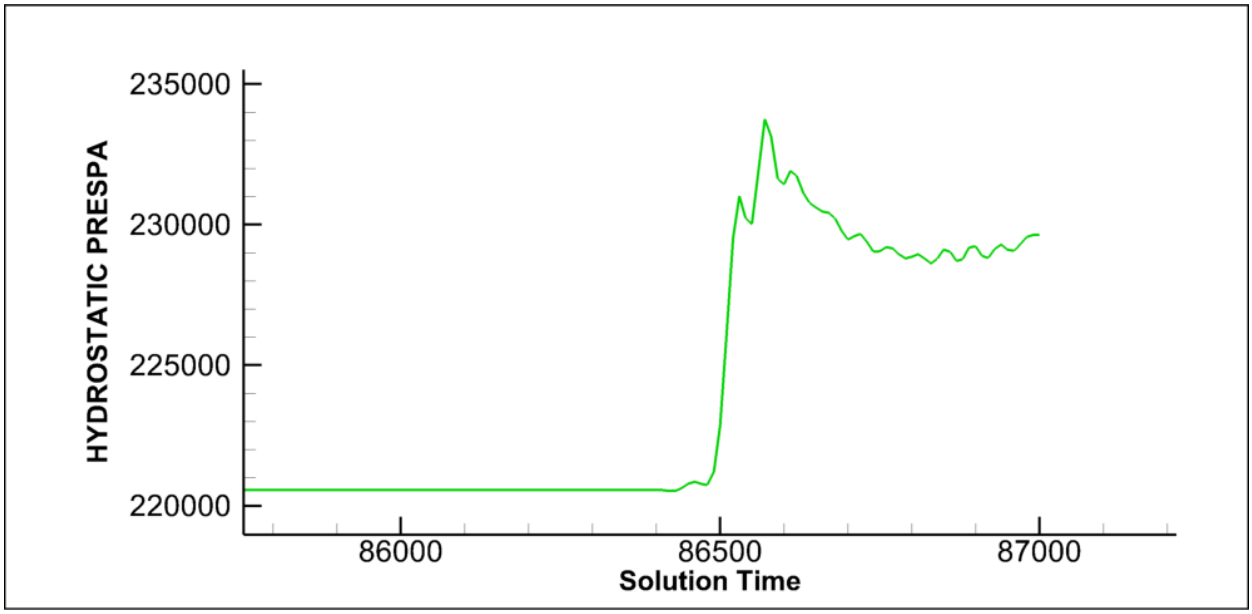

Figure A28: Pressure at the bottom of dam at section C-C'

Based on reservoir sieche modelling with respect to elevation value, the sieche against the dam at **section C-C'** is shown in **Figure A29**.

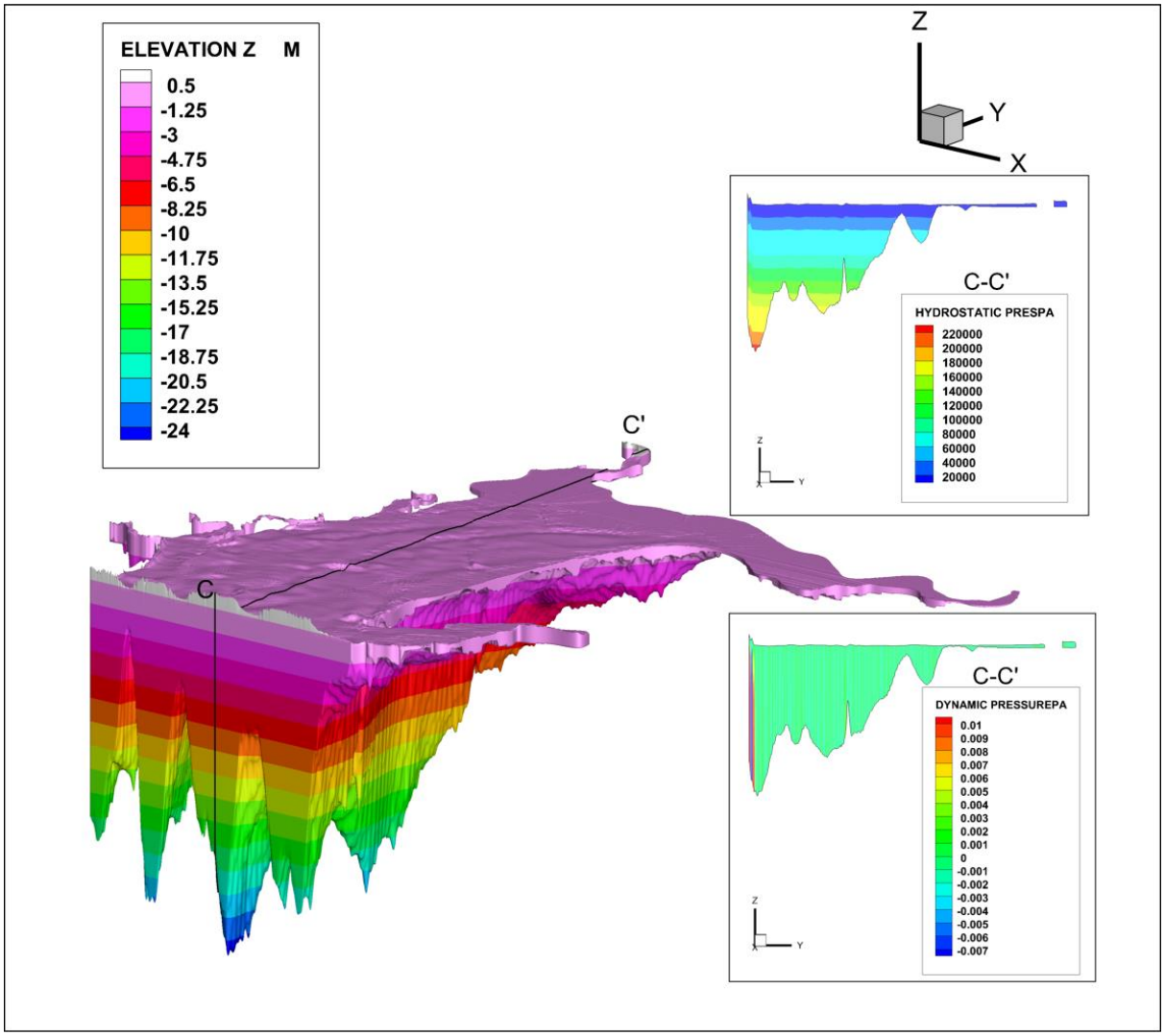

Figure A29: Sieche against the Dam at section C-C'

Based on reservoir sieche modelling with respect to total pressure value at the middle zone of the **section C-C'** is shown in **Figure A30**. During the initial solution time, the total pressure was approximately 102000 Pa up to the solution time of 86400 sec (initiation of earthquake forcing). While the total pressure at the time of sieche approaching the dam is 101000 Pa. 117000 Pa is predicted while sieche against the dam, and 112000 Pa is predicted while sieche returning.

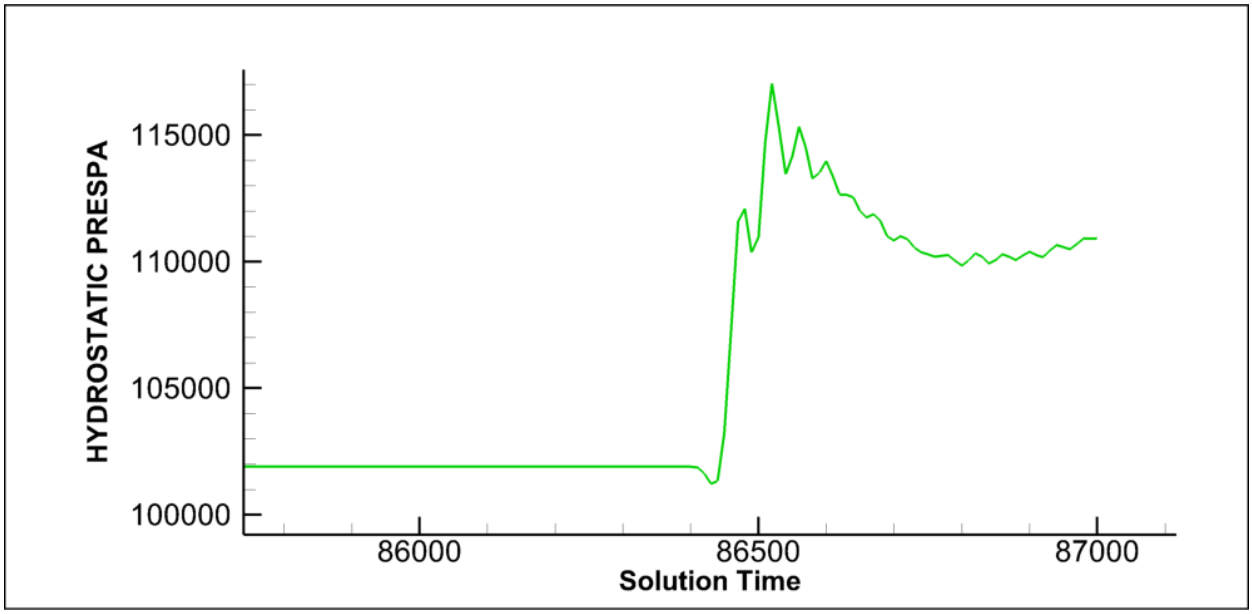

Figure A30: Pressure at the middle of dam at section C-C'

Based on reservoir sieche modelling with respect to elevation value, the sieche while returning from the dam at **section C-C'** is shown in **Figure A31.**

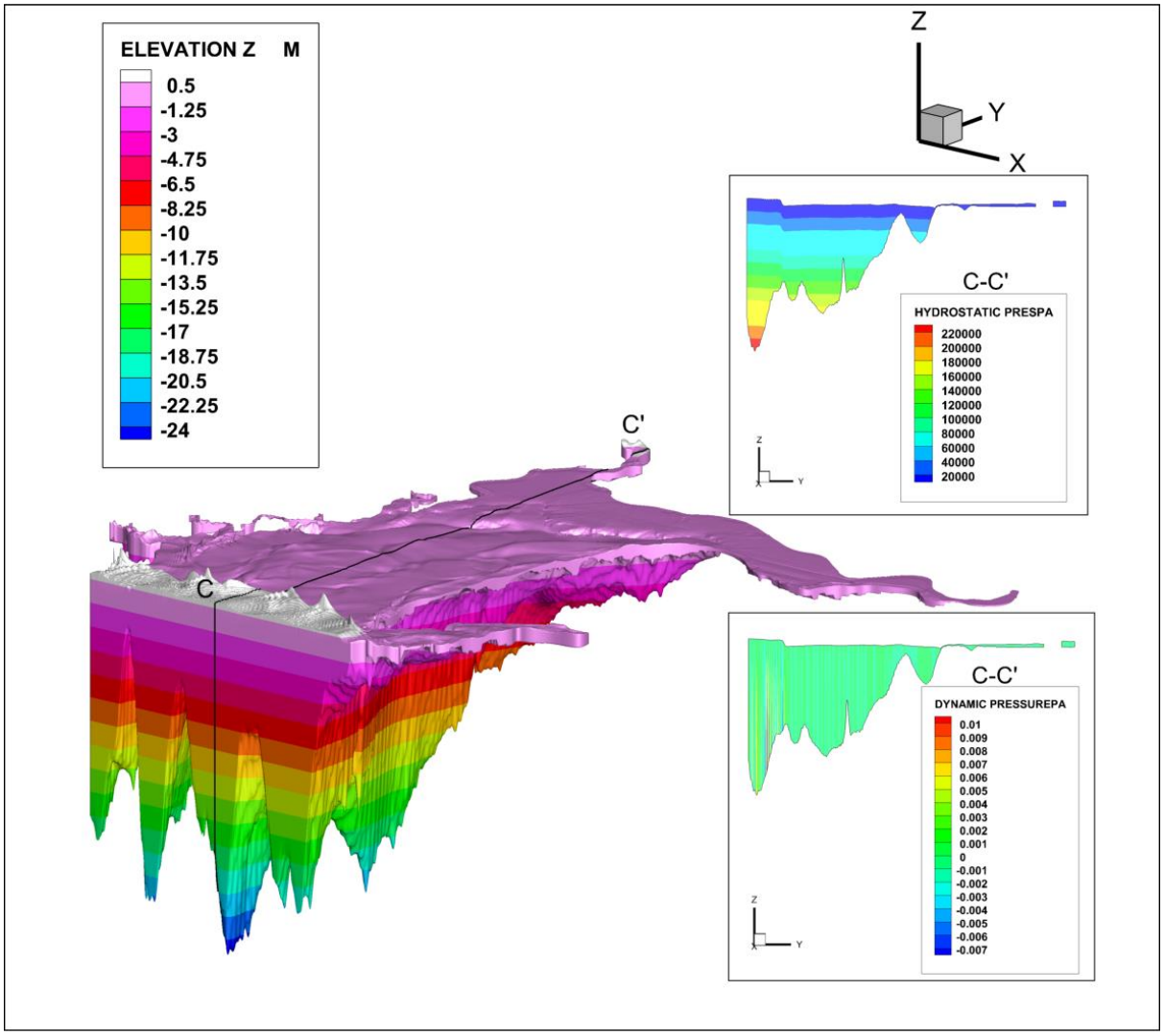

Figure A31: Sieche while returning from the Dam at section C-C'

Based on reservoir sieche modelling with respect to total pressure value at the top surface zone of **section C-C'** is shown in **Figure A32**. During the initial solution time, the total pressure was approximately 3100 Pa up to the solution time of 86400 sec (initiation of earthquake forcing). While the total pressure at the time of sieche approaching the dam is 2400 Pa. At about 17000 Pa is observed while sieche against the dam, and 13000 Pa is predicted while sieche returning.

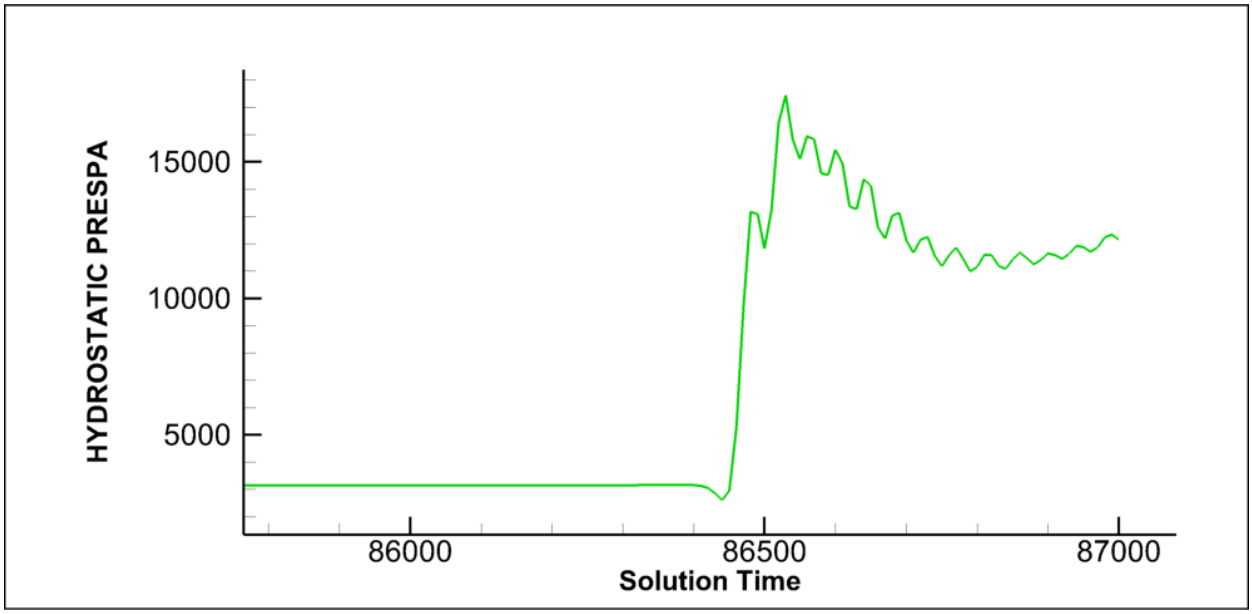

Figure A32: Pressure at the top of dam at section C-C'

Table A6 shows the pressure variation at various zones, including the bottom, middle, and top, over different times of sieche propagation in **Section C-C'**. According to the findings of this study, the pressure is highest at the bottom level and gradually decreases towards the top surface. According to **Table A6**, the nature of fluctuation in the top surface zone increases by 86% (2400 Pa–17000 Pa), the middle surface by 14% (101000 Pa to 117000 Pa), and the bottom surface by 6% (221000 Pa to 234000 Pa) from the sieche approaching the dam to the sieche against the dam, which is caused by the sieche hitting the dam wall. The level of pressure fluctuation gradually decreases by 31% (17000 Pa–13000 Pa) in the top surface, the middle surface by 4% (117000 Pa to 112000 Pa) and the bottom surface by 2% (234000 Pa to 230000 Pa) from the sieche against the dam to the sieche while returning from the dam with respect to time series. The total pressure in the bottom and middle zones increases from sieche approaching the dam to sieche against the dam, and there is a gradual decrease in pressure from sieche against the dam to sieche while returning from the dam.

It is found that the change in nature of pressure fluctuation is maximum at the top surface when compared to the bottom zone and the pressure is maximum at bottom as compared to top surface. The value makes it clear that the sieche that happens in the reservoir has a greater impact on the top surface.

Table A6: Pressure at different zone for section C-C'

SL. No	Zone	Sieche approaching Dam	Sieche against Dam	Sieche while returning from Dam
1	Bottom	221000	234000	230000
2	Middle	101000	117000	112000
3	Top	2400	17000	13000

1.6.4 Studies related to three-dimensional reservoir sieche modeling at section D-D'

Based on reservoir sieche modelling with respect to elevation value, the sieche approaching the dam at **section D-D'** is shown in **Figure A33**. The total pressure across the section is 170000 Pa.

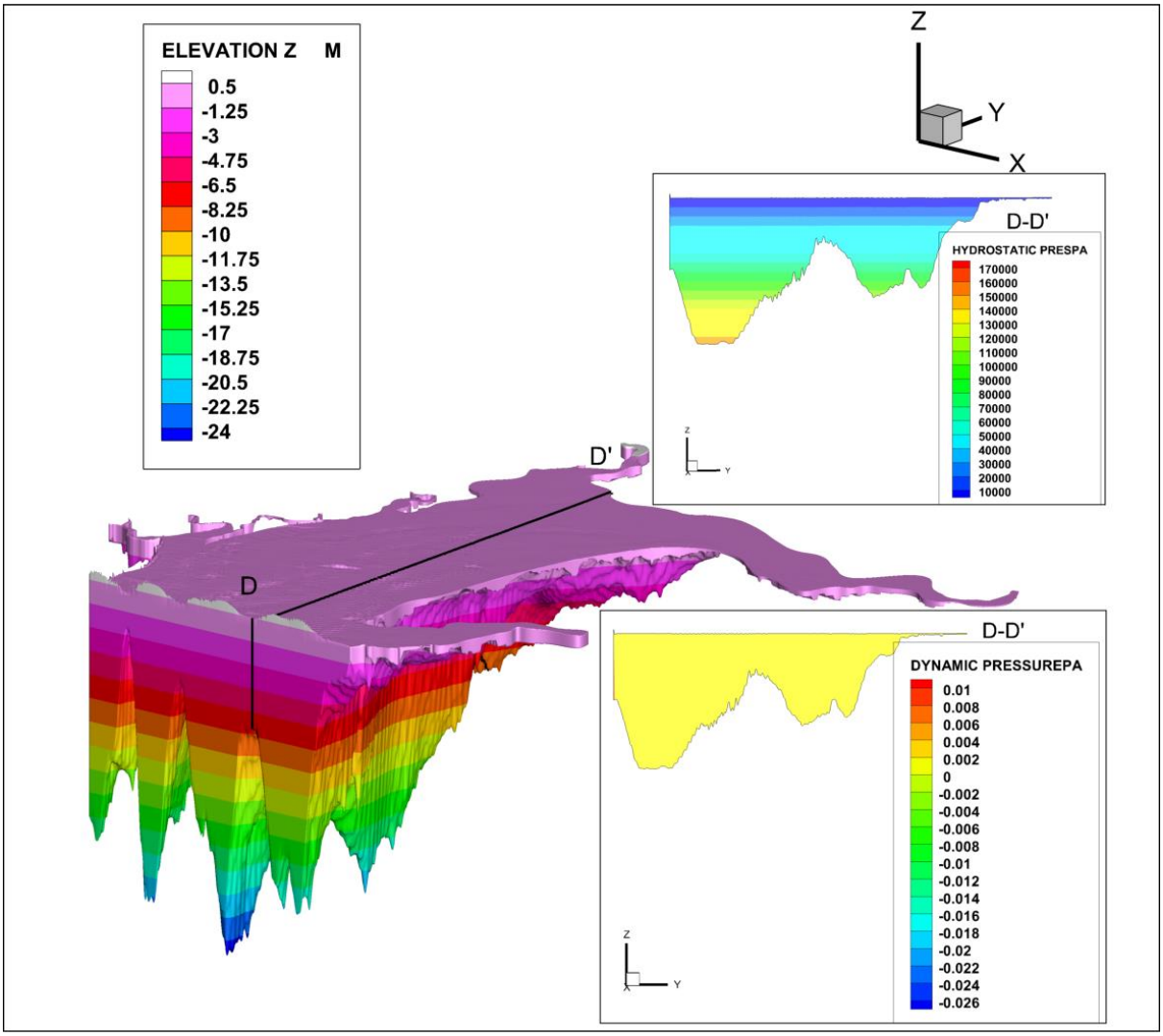

Figure A33: Sieche Approaching the Dam at section D-D'

Based on reservoir sieche modelling with respect to total pressure value at the bottom zone of the **section D-D'** is shown in **Figure A34**. During the initial solution time, the total pressure was approximately 152300 Pa up to the solution time of 86400 sec (initiation of earthquake forcing). While the total pressure at the time of sieche approaching the dam is 151500 Pa. At about 167000 Pa is predicted while sieche against the dam, and 163000 Pa is predicted while sieche returning.

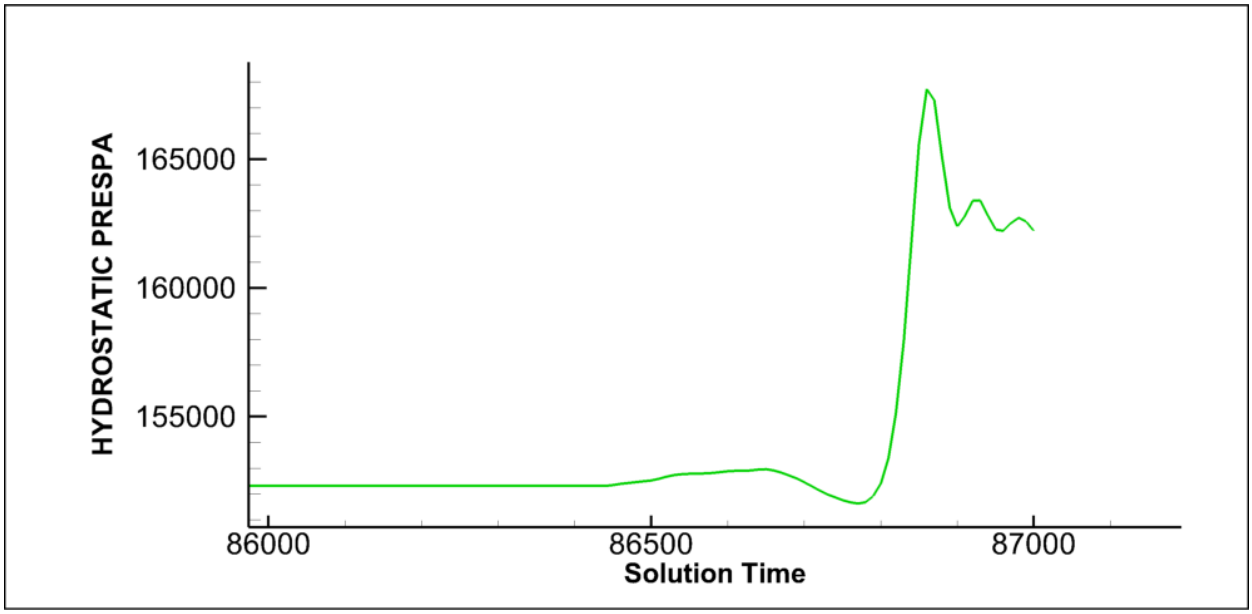

Figure A34: Pressure at the bottom of dam at section D-D'

Based on reservoir sieche modelling with respect to elevation value, the sieche against the dam at **section D-D'** is shown in **Figure A35**.

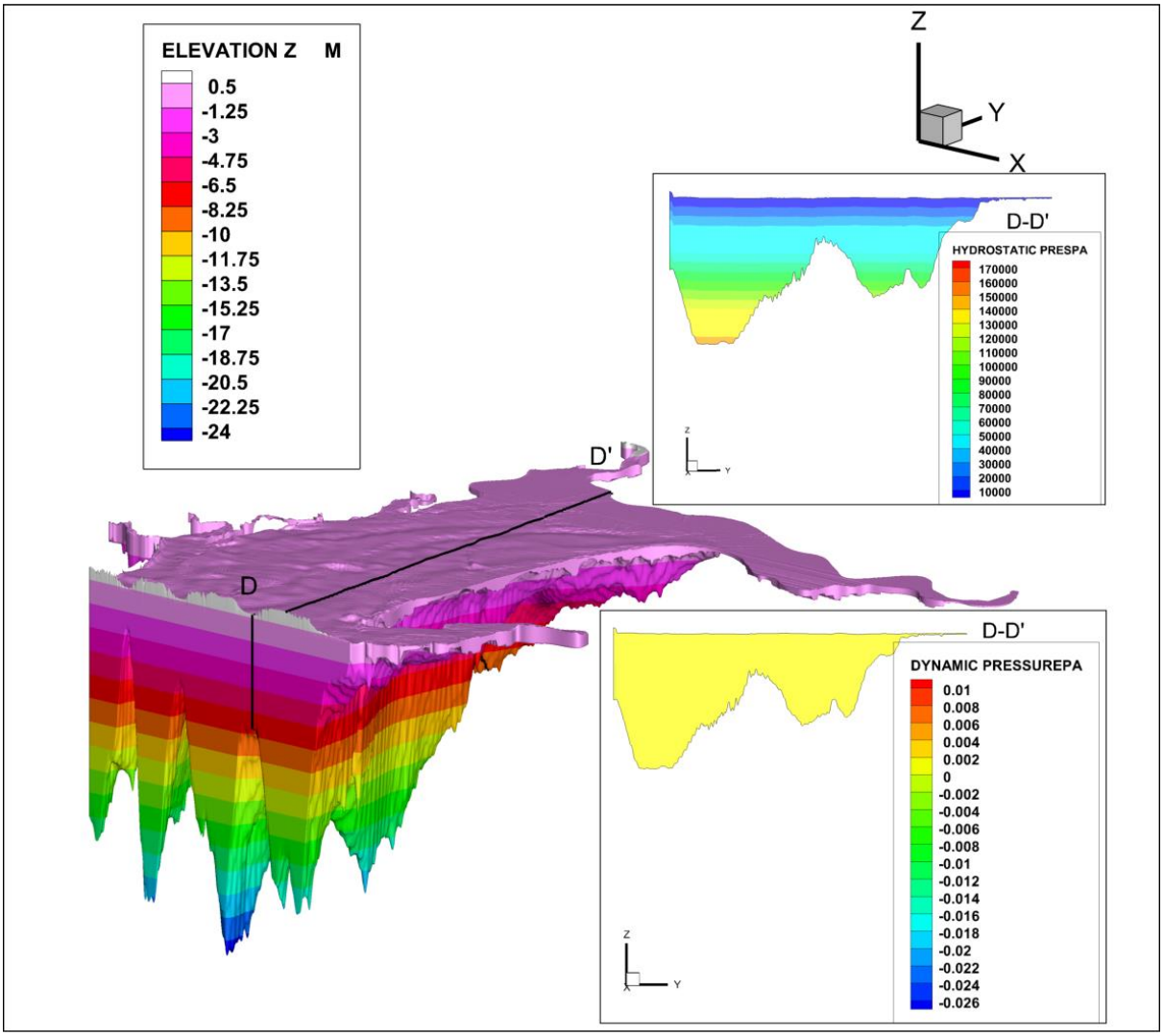

Figure A35: Sieche against the Dam at section D-D'

Based on reservoir sieche modelling with respect to total pressure value at the middle zone of the **section D-D'** is shown in **Figure A36**. During the initial solution time, the total pressure was approximately 71000 Pa up to the solution time of 86400 sec (initiation of earthquake forcing). While the total pressure at the time of sieche approaching the dam is 70900 Pa. At about 85000 Pa is predicted while sieche against the dam, and 77000 Pa is predicted while sieche returning.

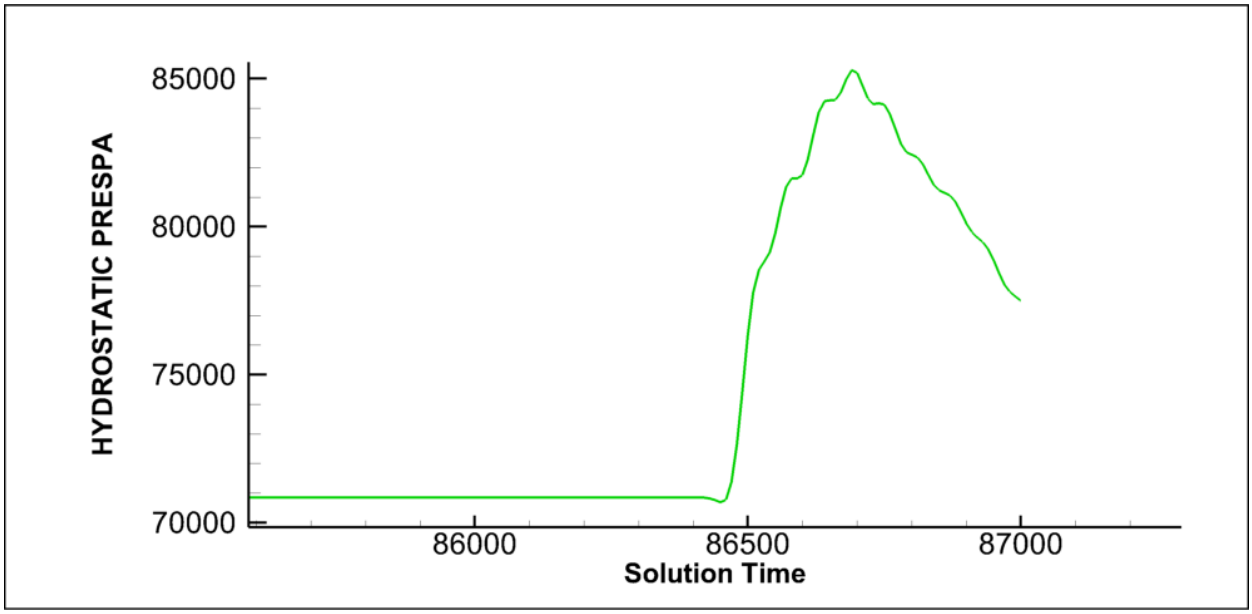

Figure A36: Pressure at the middle of dam at section D-D'

Based on reservoir sieche modelling with respect to elevation value, the sieche while returning the dam at **section D-D'** is shown in **Figure A37**.

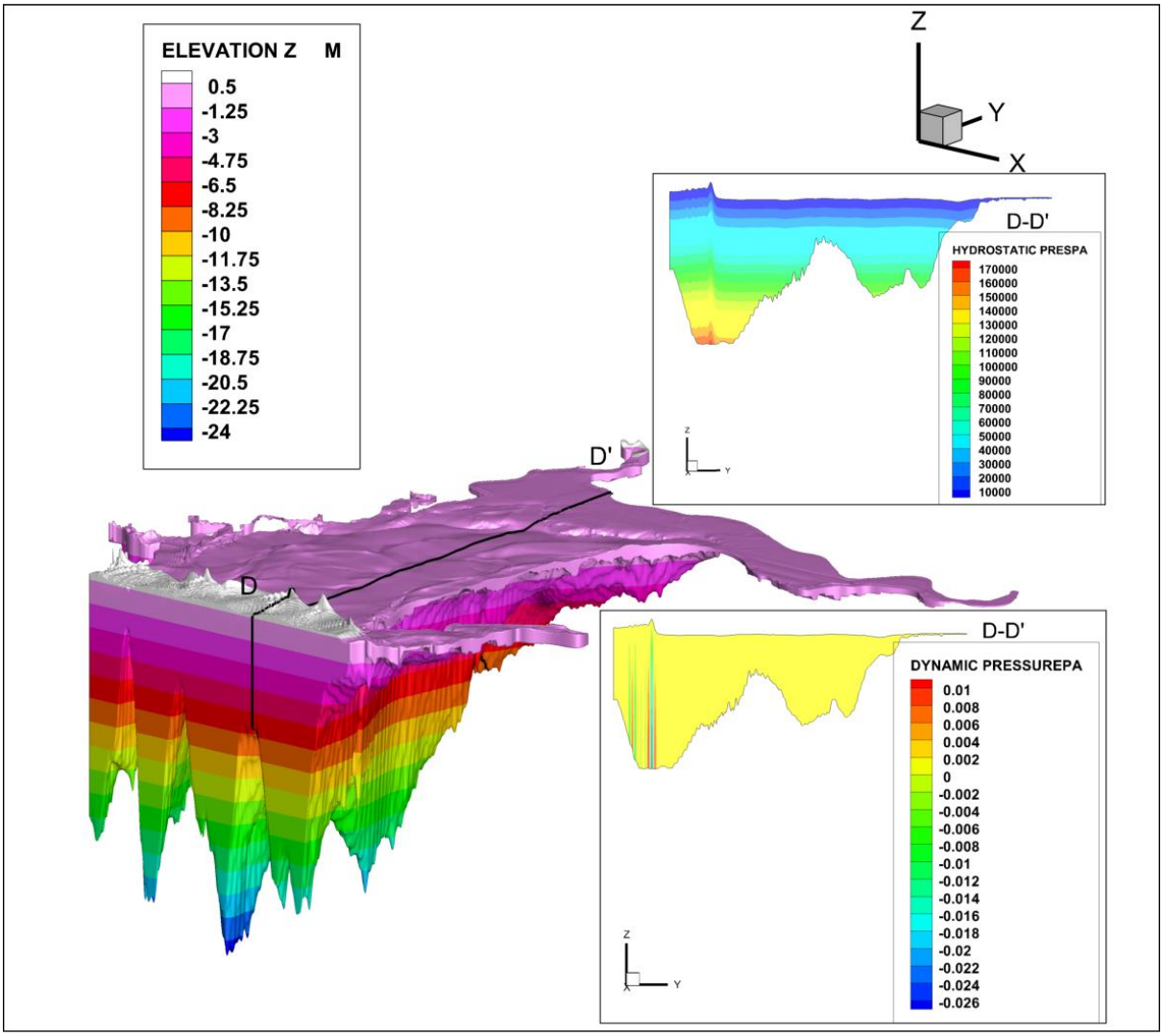

Figure A37: Sieche while returning from the Dam at section D-D'

Based on reservoir sieche modelling with respect to total pressure value at the top surface zone of the domain, the sieche at **section D-D'** is shown in **Figure A38**. During the initial solution time, the total pressure was approximately 1800 Pa up to the solution time of 86400 sec. While the total pressure at the time of sieche approaching the dam is 1100Pa. At about 17000 Pa is measured while sieche against the dam, and 9000 Pa is measured while sieche returning.

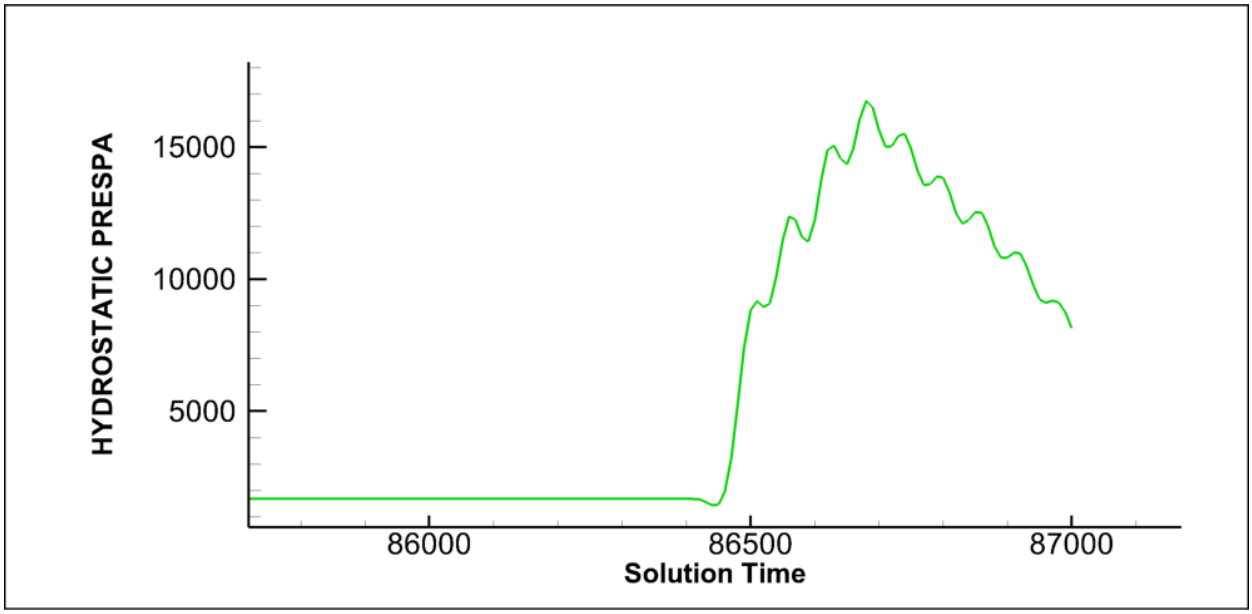

Figure A38: Pressure at the top of dam at section D-D'

Table A7 shows the pressure variation at various zones, including the bottom, middle, and top, over different times series in **Section D-D'**. According to the findings of this study, the pressure is highest at the bottom level and gradually decreases towards the top surface. According to **Table A7**, the nature of fluctuation in the top surface zone increases by 94% (1100 Pa to 17000 Pa), the middle surface by 17% (70900 Pa to 85000 Pa), and the bottom surface by 9% (151500 Pa-167000 Pa) from the sieche approaching the dam to the sieche against the dam, which is caused by the sieche hitting the dam wall. The level of pressure fluctuation gradually decreases by 89% (17000 Pa–9000 Pa) in the top surface, the middle surface by 10% (85000 Pa to 77000 Pa) and the bottom surface by 2% (167000 Pa to 163000 Pa) during the sieche against the dam to the sieche while returning from the dam with respect to time series. The total pressure in the bottom and middle zones increases from sieche approaching the dam to sieche against the dam, and there is a gradual decrease in pressure from sieche against the dam to sieche while returning from the dam.

It is found that the change in nature of pressure fluctuation is maximum at the top surface when compared to the bottom zone and the pressure is maximum at bottom as compared to top surface. The value makes it clear that the sieche that happens in the reservoir has a greater impact on the top surface.

Table A7: Pressure at different zone for section D-D'

SL. No	Zone	Sieche approaching Dam (Pa)	Sieche against Dam (Pa)	Sieche while returning from Dam (Pa)
1	Bottom	151500	167000	163000
2	Middle	70900	85000	77000
3	Top	1100	17000	9000

1.6.5 Studies related to three-dimensional reservoir sieche modeling at section E-E'

Based on reservoir sieche modelling with respect to elevation value, the sieche approaching the dam at **section E-E'** is shown in **Figure A39**. The total pressure across the section is 200000 Pa.

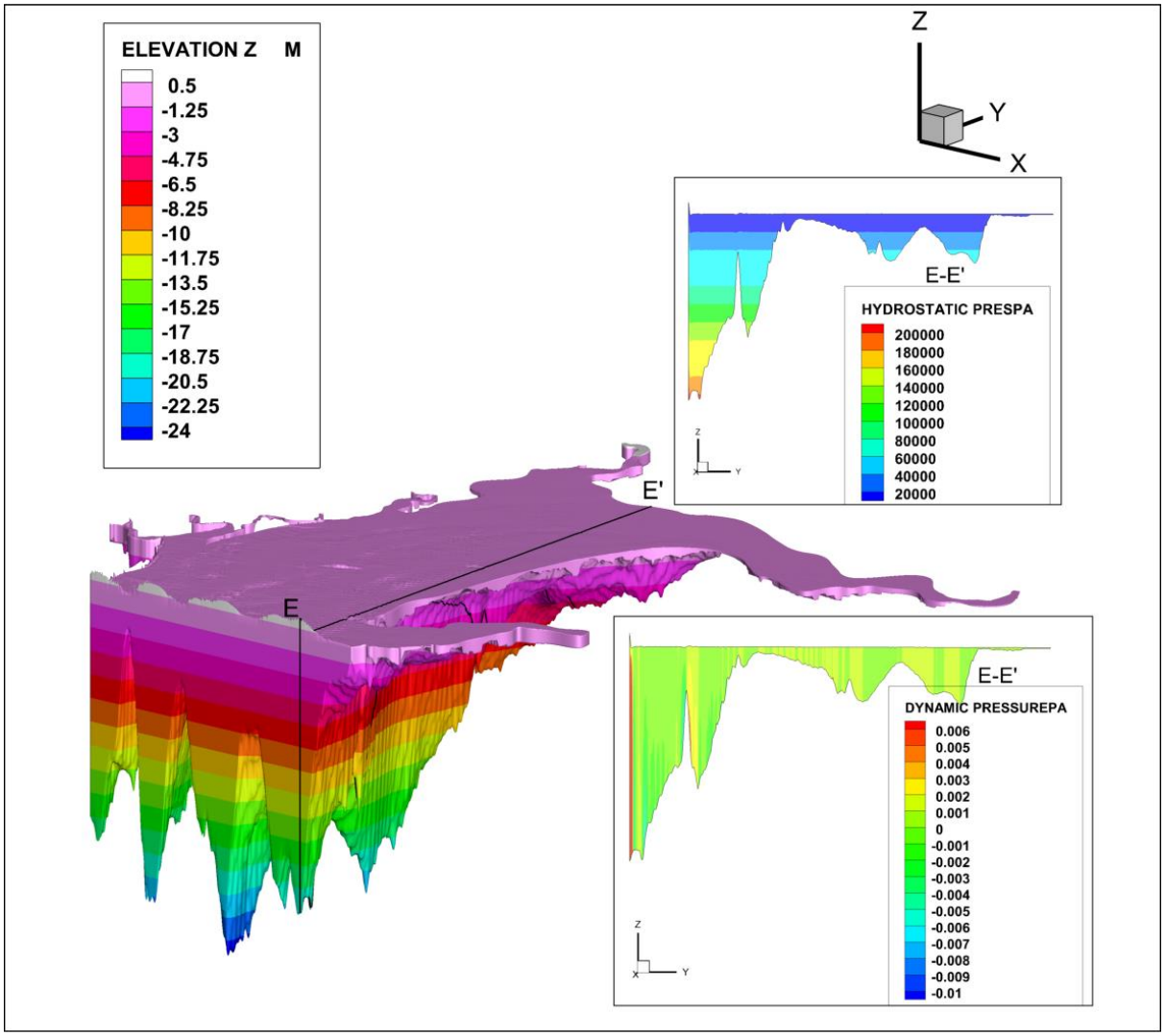

Figure A39: **Sieche approaching the Dam at section E-E'**

Based on reservoir sieche modelling with respect to total pressure value at the bottom zone of the **section E-E'** is shown in **Figure A40**. During the initial solution time, the total pressure was approximately 193100 Pa up to the solution time of 86400 sec (initiation of earthquake forcing). While the total pressure at the time of sieche approaching the dam is 191000 Pa. At about 207000 Pa is predicted while sieche against the dam, and 201000 Pa is predicted while sieche returning.

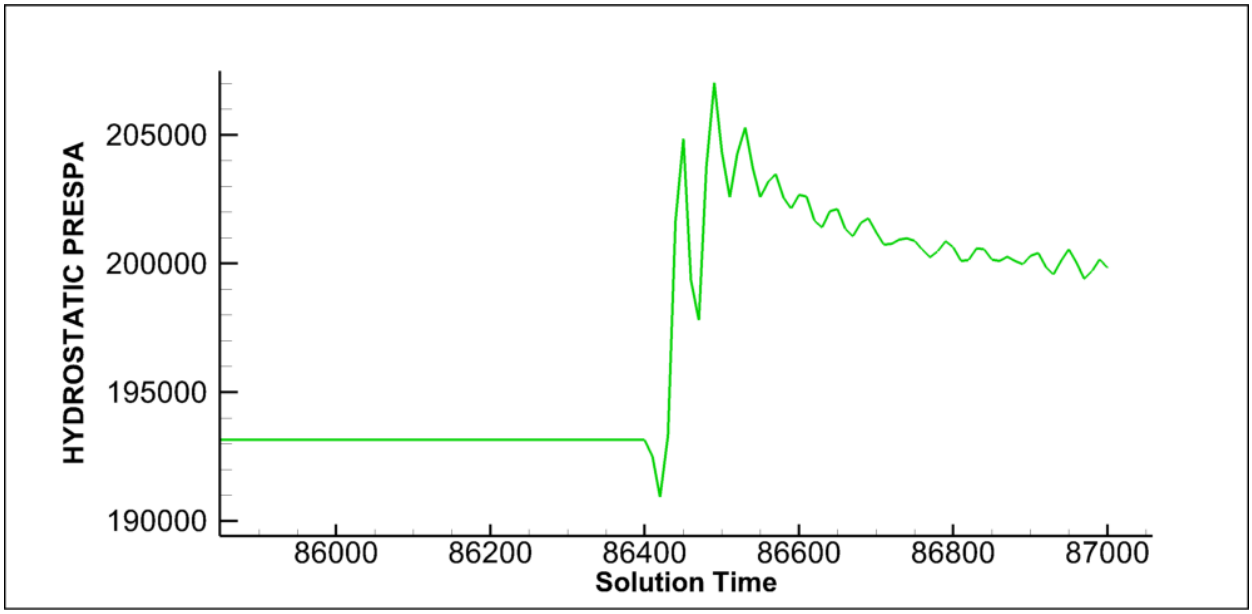

Figure A40: Pressure at the bottom of dam at section E-E'

Based on reservoir sieche modelling with respect to elevation value, the sieche against the dam at **section E-E'** is shown in **Figure A41**.

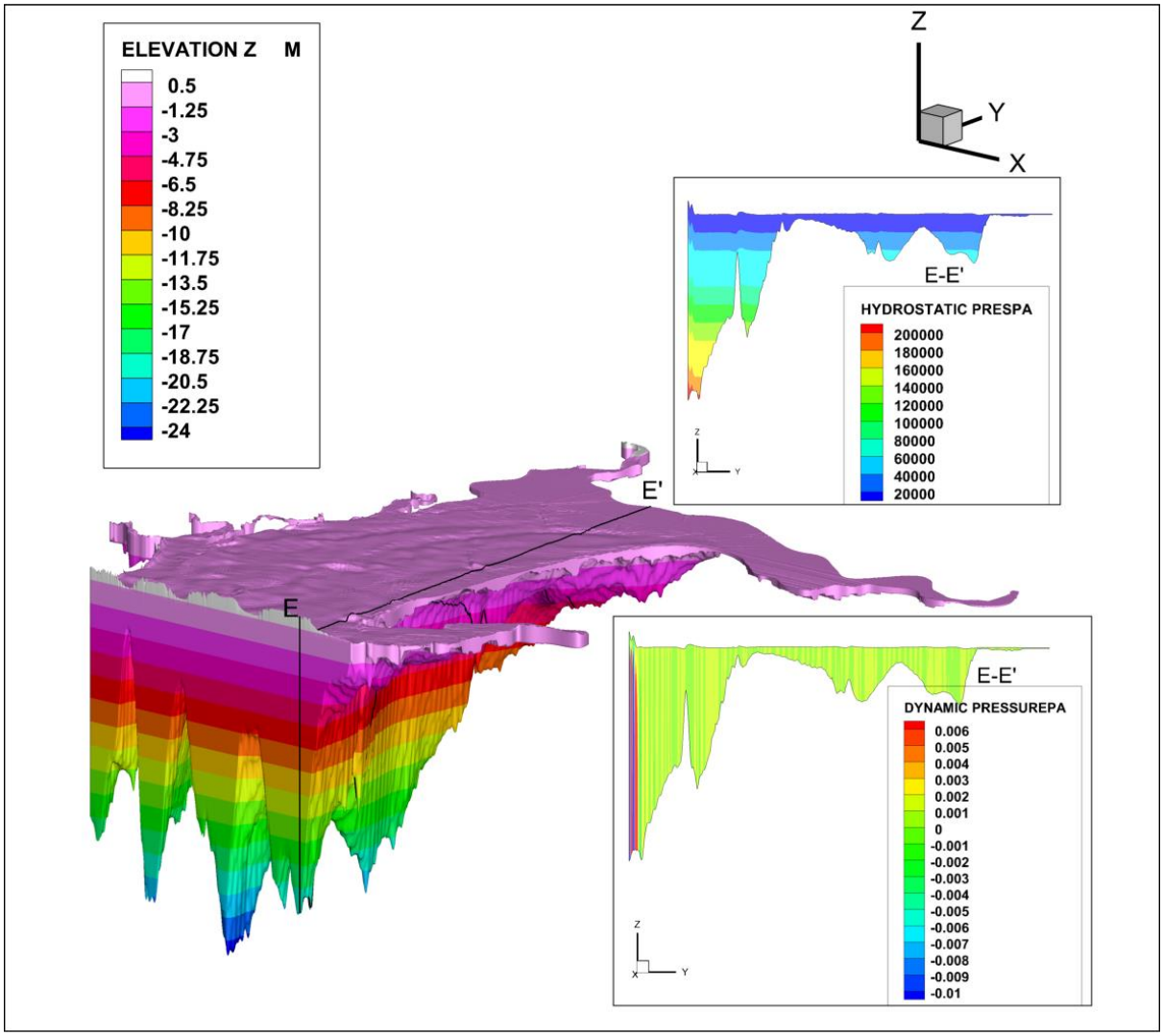

Figure A41: **Sieche against the Dam at section E-E'**

Based on reservoir sieche modelling with respect to total pressure value at the middle zone of the **section E-E'** is shown in **Figure A42**. During the initial solution time, the total pressure was approximately 97200 Pa up to the solution time of 86400 sec (initiation of earthquake forcing). While the total pressure at the time of sieche approaching the dam is 96500 Pa. At about 100000 Pa is predicted while sieche against the dam, and 95000 Pa is predicted while sieche returning.

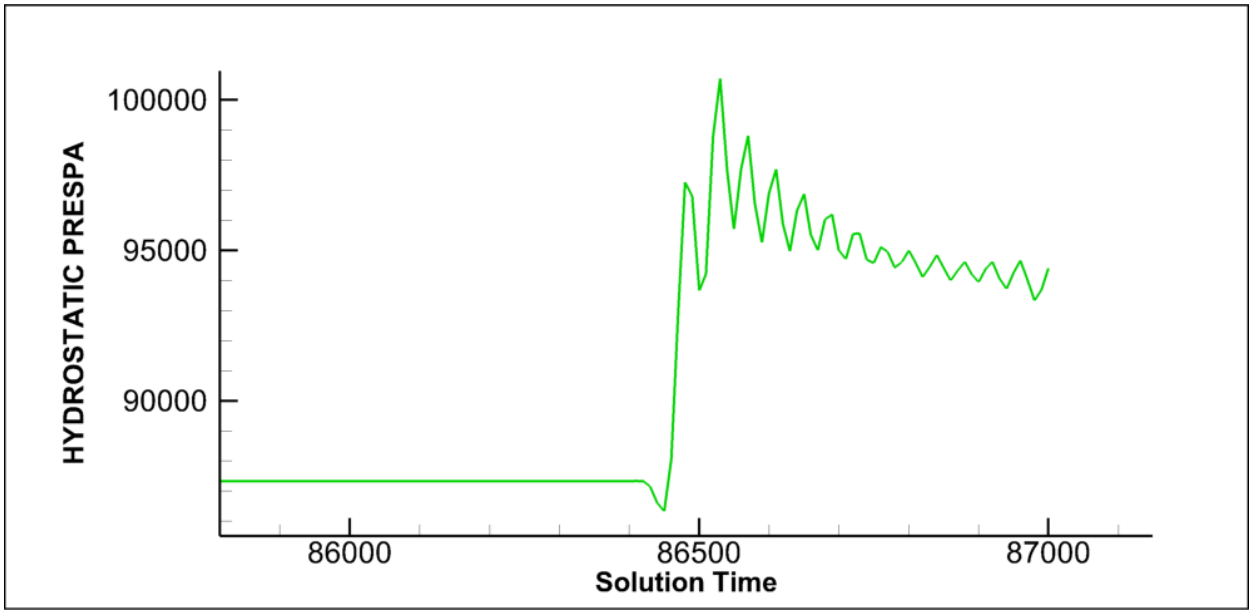

Figure 42: Pressure at the middle of dam at section E-E'

Based on reservoir sieche modelling with respect to elevation value, the sieche while returning the dam at **section E-E'** is shown in **Figure A43**.

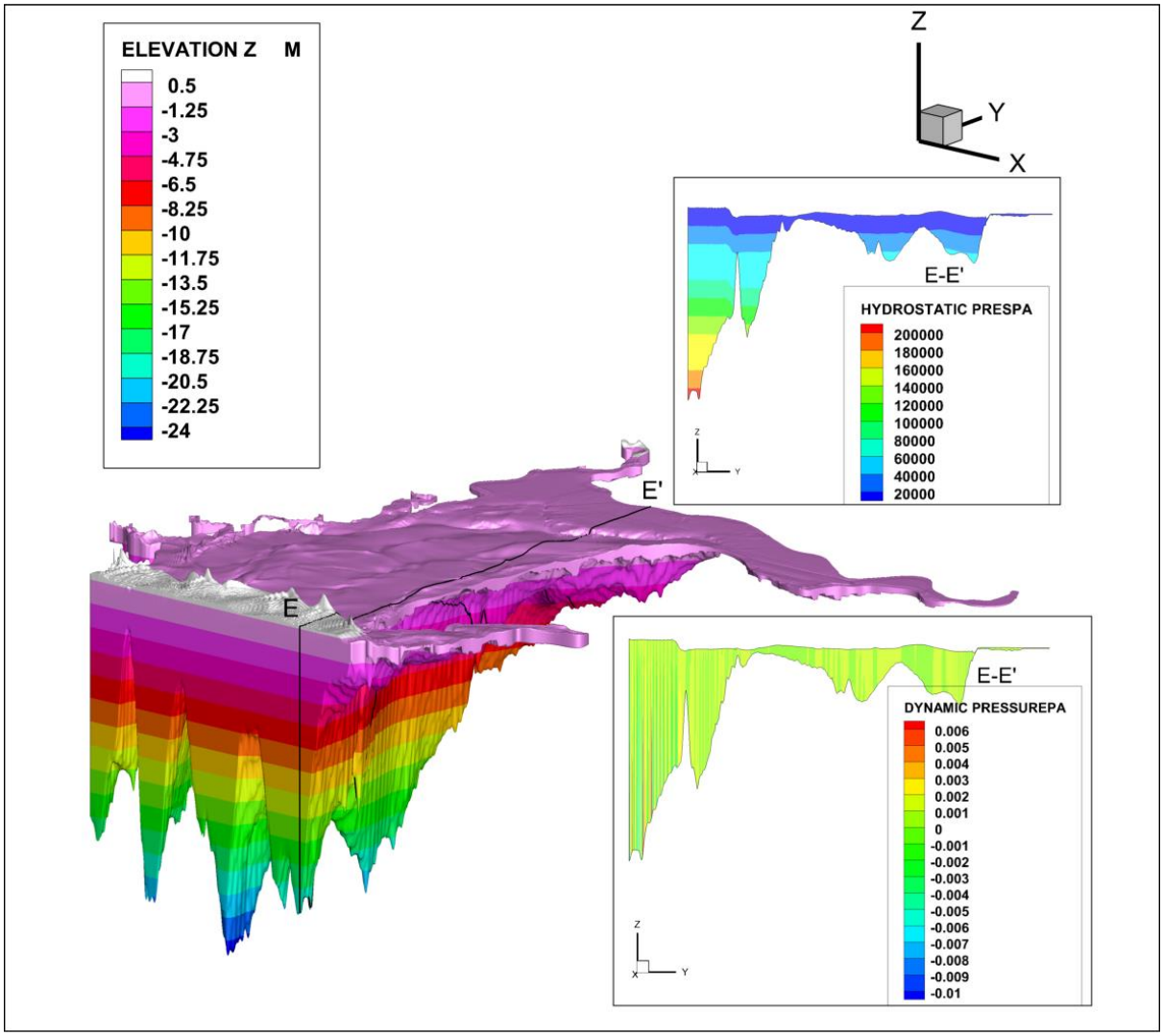

Figure 43: Sieche while returning from the Dam at section E-E'

Based on reservoir sieche modelling with respect to total pressure value at the top zone of the **section E-E'** is shown in **Figure A44**. During the initial solution time, the total pressure was approximately 4500 Pa up to the solution time of 86400 sec (initiation of earthquake forcing). While the total pressure at the time of sieche approaching the dam is 3500 Pa. At about 18000 Pa is predicted while sieche against the dam, and 13000 Pa is predicted while sieche returning.

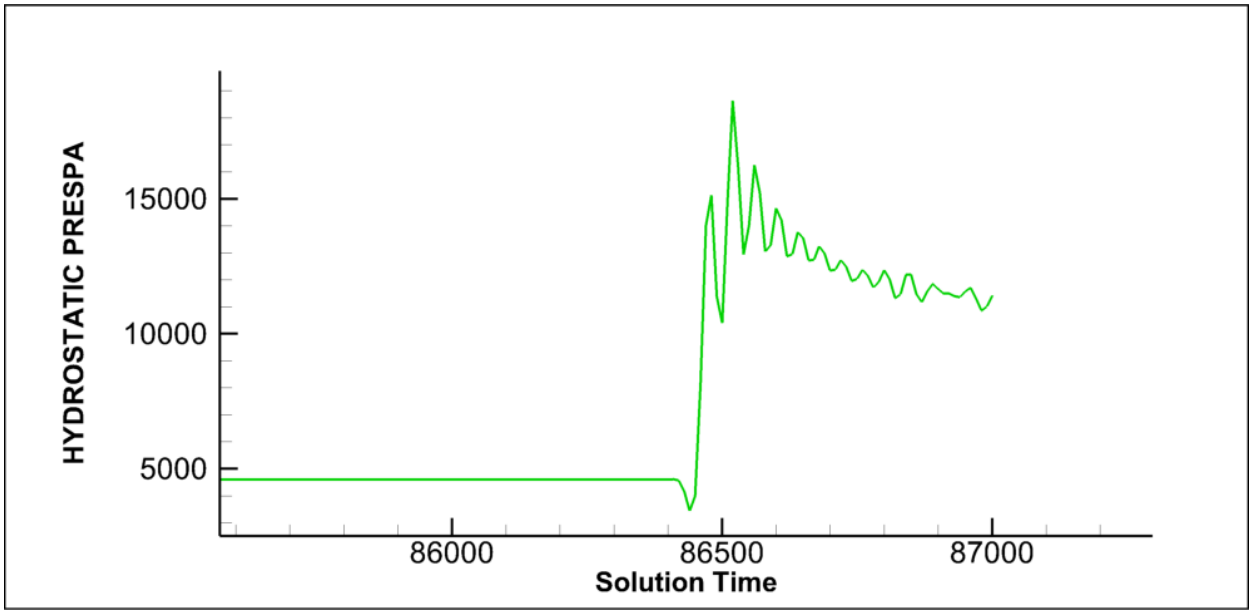

Figure 44: Pressure at the top of dam at section E-E'

Table A8 shows the pressure variation at various zones, including the bottom, middle, and top, over different times series in **Section E-E'**. According to the findings of this study, the pressure is highest at the bottom level and gradually decreases towards the top surface. According to **Table A8**, the nature of fluctuation in the top surface zone increases by 81% (3500 Pa to 18000 Pa), the middle surface by 4% (96500 Pa to 100000 Pa), and the bottom surface by 8% (191000 Pa to 207000 Pa) from the sieche approaching the dam to the sieche against the dam, which is caused by the sieche hitting the dam wall. The level of pressure fluctuation gradually decreases by 38% (18000 Pa to 13000 Pa) in the top surface, the middle surface by 5% (100000 Pa to 95000 Pa) and the bottom surface by 3% (207000 Pa to 201000 Pa) from the sieche against the dam to the sieche while returning from the dam with respect to time series. The total pressure in the bottom and middle zones increases from sieche approaching the dam to sieche against the dam, and there is a gradual decrease in pressure from sieche against the dam to sieche while returning from the dam.

Table 8: Total Pressure at different zone for section E-E'

SL. No	Zone	Sieche approaching Dam (Pa)	Sieche against Dam (Pa)	Sieche while returning from Dam (Pa)
1	Bottom	191000	207000	201000

2	Middle	96500	100000	95000
3	Top	3500	18000	13000

1.7 Concluding remarks

1.7.1 Remarks on 2D study

1. Root mean square (RMS) value of forces on the dam wall is approximately around 400KN for MCES acceleration data (horizontal shaking data) and 391KN for DBES acceleration data (horizontal shaking data) and the corresponding added mass for the RMS forces are $1.57x10^6$ kg in case of MCES and $2.6x10^6$ kg in case of DBES acceleration data.
2. The total pressure acting on the wall is approximately $2.4x10^5$pa for MCES and DBES data.

1.7.2 Remarks on 3D study

3. An attempt is made to design a reservoir in the location of Gulf of Khambhat, Gujarat to investigate the forces acting on the dam wall, with the help of numerical model. A three-dimensional model with a flexible mesh was created using the TELEMAC-3D, assuming appropriate geometry and boundary conditions. Model output was analysed to arrive at the appropriate results and conclusions. The results are agreeing with the 2-D model predictions.
4. After an earthquake, the reservoir water will oscillate and a sieche will form. For each time frame in the domain, a different slice location is chosen, such as A-A', B-B', C-C', D-D', and E-E' and analyse the sieche impact on dam wall. To measure the total pressure exerted by the sieche in the domain, three-time frames are used: the sieche approaching the dam, the sieche against the dam, and the sieche returning from the dam. Time series were extracted for three different levels at the bottom, Pressure in the middle and Pressure at the top surface in each slices or transects, to determine the total pressure and pressure fluctuation in the domain during different sieche conditions. **Table A9** showing the percentage of pressure fluctuation change in different sections at different zones.

Table A9: Percentage of pressure fluctuation change in different sections

Section	Sieche approaching dam - against the dam			Sieche against the dam - returning from the dam		
	Top	Middle	Bottom	Top	Middle	Bottom
	%			%		
A-A’	78	13	8	29	5	2
B-B’	89	15	7	29	4	2
C-C’	86	14	6	31	4	2
D-D’	94	17	9	89	10	2
E-E’	81	4	8	38	5	3

5. It is found that the change in nature of pressure fluctuation is maximum at the top surface when compared to the bottom zone and the pressure is maximum at the bottom as compared to the top surface.

ANNEXURE-B
IMPACT OF THE KALPASAR DAM ON THE REGIONAL CIRCULATION

1.8 INTRODUCTION

In terms of the human living standard, perhaps the most important resource may be adequate supply of fresh water. Human civilization has been flourished in the river valleys, where economy and developments advanced with the help of power generation, irrigation, industrial production etc, and all these happened by ensuring the availability of the most valuable 'element'- the fresh water. The north-western regions of India are almost dry and India is considered as one of the most 'water-stressed' countries in the world (USAID Report). The primary objective of the Kalpasar Project is to ensure the adequate supply of fresh water by constructing a dam, approximately of 50 km length across the Gulf of Khambhat (GoK) by collecting the inflow of rivers Narmada, Sabarmati, Mahi and Dhadar. The scientific studies regarding this project dated back to 1969 till 2017, spans into three phases such as preliminary studies, pre-feasibility report leading to design studies and the feasibility report of the altered designs (Dhruv Rajeev, 2018). As far as the need of the fresh water storage is concerned, the most important functionality is the replacement of the saline water by the riverine water on closure of the dam. Coastal reservoirs are intended to store the riverine water discharging into the ocean during the monsoon period and to use it in the drought period. They are constructed across an estuary or a bay or in the sea to collect the riverine water during flooding and normal conditions. The major disadvantages of the conventional reservoirs are categorized into the disruption of the continuity of the river flow and the transport of sediments, geomorphological and hydrodynamic changes in the neighbouring ecosystems (Zhao et al, 2021). On an international view, many countries have constructed coastal reservoirs to address the fresh water need. The sea-based Marina Barrage of Singapore, dividing the Marina Bay reservoir and the South China Sea is expected to control the flood and enhance the water supply to Singapore. Reclamation of very large costal area is envisaged in the full-fledged functioning of the Saemangeum Project in South Korea by enclosing the tidal mudflats. Other coastal reservoirs are Sihwa of South Korea, Shek pik, Plover cove, and High land of Hong Kong, China's Qingcaosha, Chenhang, Baogang etc. Cardiff Project of United Kingdom, is a long tidal excursion barrage constructed across the mouth of Cardiff Bay for land regeneration and the creation of a large fresh water lake. The largest mud regulator in India, the Thanneermukkom Bund, dividing the Vembanad Lake into the fresh water lake and brackish water lake, is operational since 1976. To date, no major environmental hazards have been reported in connection

with the coastal reservoirs, except those resulted due to the wrong operational principles, such as, the propagation of the water hyacinth in the fresh water areas of the Vembanad Lake (Kolathayar et al, 2018). However, the circulation changes must be studied properly, and the changes in the distribution of salinity and temperature as well. In the present study the hydrodynamics in the region of interest is analysed with the help of a 3D circulation model capable of addressing the spatial and temporal changes of elevation, salinity and temperature with and without the dam.

1.9 MATERIALS AND METHODS

1.9.1 Study Area

Since the prime analysis has to be progressed by considering the changes in circulation, that may arise due to the presence of the dam, a large area is selected in the Arabian Sea ranging from 59.35 ^{O}E to 77.55 ^{O}E longitude and 5.5 ^{O}N to 25.5 ^{O}N latitude. Kalpasar Project is a multidisciplinary task holding various objectives in fixing the performance of the dam. One of the major challenges in the ongoing analysis of the project is of environmental concern in nature, in which, the circulation plays a major role. It is evident that the closure of the proposed dam will result to have several hundreds of kilometres of the oceanic regions enclosed by physical barriers. The GoK joins the land regions of Gujarat and its peninsular extent by forming a funnel shaped indentation, with an average width of 80 km at the mouth, and diminished to 25 km on traversing a longitudinal distance of 140 km further northward (Mitra et al, 2020). The shallow regions of GoK (water depth ~ 30 m) are peculiar in nature, resulting a very large tidal range of 10 m or more, with tidal currents greater than 3 m/s, which makes the water column always turbid (Giardino et al, 2013). The bathymetry of the region of study and the major rivers discharging into the domain are shown in **Figure B1**. Bathymetry was obtained from the ETOPO2 world database using GEODAS Grid Translator utility developed by NOAA-National Geophysical Data Center. For coastal areas the bathymetry is corrected by the modified ETOPO2 data (Sindhu et al. 2007), and for the very shallow regions of GoK, bathymetric corrections are applied with the help of the measured data.

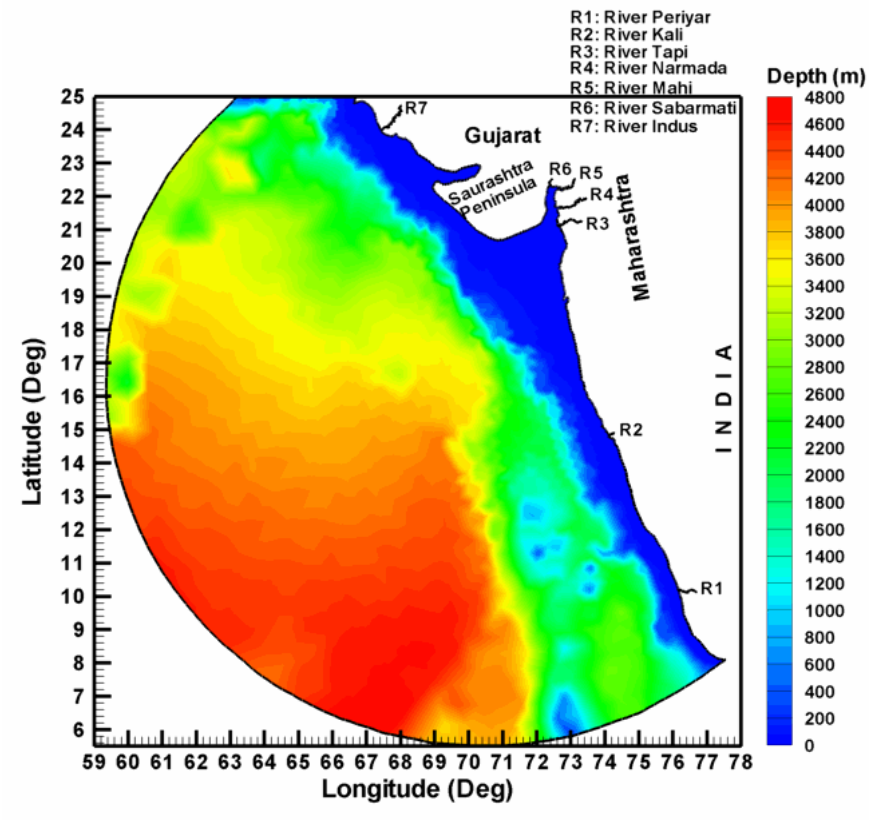

Figure 45: Bathymetric Map of the Study Region with Major Rivers

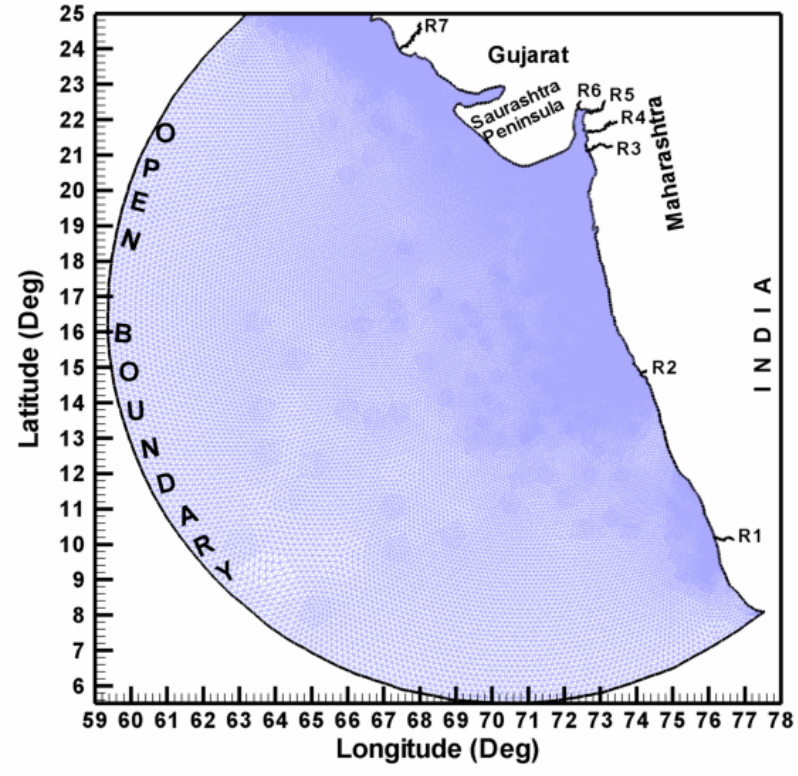

Figure 46: Computational Domain

The 3D domain is discretised into series of triangular elements having 94383 nodes and 180016 elements with the help of a Linux based meshing package XmGredit (**Figure B2**). Finely resolved triangular elements are placed near the project area with the horizontal resolution of order of 30 to 40 m, and in the open boundary where the domain is forced with the tidal data, is given 10-12 km resolution. The 3D modelling system is flexible enough to accommodate a varying horizontal resolution as per the choice of the physical situation. In the open boundary tidal elevation data is given from the TPXO model, which is a global tidal model fitting the Laplacian tidal equations and the altimetry data, developed by Egbert and Erofeeva (2002).

1.9.2 Three Dimensional Numerical Model

The unsteady flow of water and the dispersion of the temperature is investigated with the help of a 3D numerical model capable of solving the momentum equations, continuity equation and the transport equation under different forcing regimes such as tides, winds, currents, river discharge etc. The Eulerian-Lagrangian Circulation (ELCIRC) model is an open source circulation model (Zhang et al., 2004) and can be easily fitted on unstructured grids. The model was initially designed for the simulation of baroclinic tidal dynamics and is flexible enough to handle river-to-ocean scales. The shallow water equations are solved by finite difference/finite volume algorithm. The solution algorithm is efficiently written to address a wide range of oceanic processes with the inclusion different forcing mechanisms. Plume dynamics can be studied numerically if the model is capable of preserving the dynamic balance between inertia, vertical mixing, stratification and Coriolis force (Zhang et al., 2004). The density is computed as a function temperature, salinity and hydrostatic pressure by using the equation of state. The model can also provide different turbulence closure methodologies; thus, the system of equations can be mathematically solved by adopting proper numerical techniques enhanced by the initial conditions and the boundary conditions. The model uses a series of vertical layers starting from the bottom to the water surface, and the horizontal discretization of the computational domain is achieved by the triangular elements. This way the model can solve the variables of interest in both horizontal and vertical aspects. A spatially varying wind field obtained from ERA5 owned by the Asia Pacific Data Research Center (APDRC) is applied over the domain at every six hours (**Figure B3**). At the surface boundary the internal Reynold's stress is balanced by the wind stress, whereas at the bottom, frictional stress is accounted for balancing the internal stress. No salt flux is assumed at the surface and bottom, but heat exchange is allowed at the surface through a boundary condition. At the bottom the heat flux is zero. The model is integrated forward in time so as to account the

dynamics of the model variables corresponding to the physical situations under consideration. Since circulation is the most important phenomenon to be simulated, the whole modelling work is divided into three cases, namely the normal case, monsoon and the extreme event analysis- a flooded condition; and the model forced accordingly. The initial and the boundary conditions used in the numerical simulations are summarized in the **Tables B1** and **B2**, depending on the simulation event.

Table 10: Initial and boundary conditions used in the model study: Normal Case

Model parameter															
Temperature (°C)								Salinity (PSU)							
	Rivers								Rivers						
Initial Data*	R_1	R_2	R_3	R_4	R_5	R_6	R_7	Initial Data*	R_1	R_2	R_3	R_4	R_5	R_6	R_7
25.7-29.3	28.5	27.5	28.0	28.0	29.1	28.0	29.0	1.0-36.7	1.5	2.0	2.0	1.0	1.5	1.0	2.0

*Spatially varying data, remaining are constant values

R_1: Periyar, R_2: Kali, R_3: Tapi, R_4: Narmada, R_5: Mahi, R_6: Sabarmati, R_7: Indus

Table B2: River boundary conditions used in the model study: Normal Case

Discharge (m^3/s)						
Periyar	Kali	Tapi	Narmada	Mahi	Sabarmati	Indus
163	128	564	1216	383	33	2684

1.9.3 General Modeling Strategy

The general programming strategy of the model is described in this section. The algorithmic procedure for solving the model equations in a general perspective involves initialization, proper selection of the model inputs, choice of the turbulence scheme, solving the required variables and storing the outputs in respective files. The model initialization can be done either in the starting level (cold start) or with a pre-defined set of model variables (hot start), if available. The choice of turbulence closure methodologies simplifies the computation of eddy viscosity and diffusivity. Next, the solution of the horizontal velocities is performed followed by the realization of the vertical velocity. Once the velocities are obtained the free surface is then updated for computing the sea surface elevation. The next step in the computation sequence is the solution of the transport quantities for obtaining the temperature and salinity. These are the various operations involved in a single time step in the whole simulation effort, and, the same procedure is repeated until the simulation is completed. The model outputs can be stored periodically and can be written in the respective output files as per the choice. The net heat transfer across the air-water interface is accounted as the combined effect of the downward heat flux (net transport of heat energy in the

downward direction) at the surface, the down welling solar radiative flux (downward solar component) and the down/upwelling infrared radiative flux (down/up component in the infrared region of the spectrum). The computation is again enhanced by including the turbulent fluxes corresponding to the sensible and latent heat fluxes. The turbulent fluxes of heat and momentum are further modified by a parameterization scheme. This parameterization is designed for improving the accuracy under moderate and high wind regimes.

1.9.4 Model Forcing

The main forcing agents in the present study include tides, winds and discharge- the model dynamics is capable of representing the coastal currents derived from these parameters. The effect of waves is neglected in the hydrodynamic model as they impart practically zero fluid transport, and the turbulent mixing is well accounted in the tidal dynamics. The model can accommodate a spatially varying wind field, which will eventually interpreted as the surface stress responsible for the coastal currents. Although the dominant tidal constituent is the principal lunar tide M_2, since it accommodates large tidal volume, the other constituents (S_2, N_2, K_2, K_1, O_1, P_1, Q_1, M_4, MS_4 and MN_4), are also included in the model. Tidal heights are specified at the open boundary by the amplitudes and phases of these constituents.

1.10 RESULTS AND DISCUSSION

1.10.1 Model Validation

As measurements were not available for the locations of GoK, comparison between the simulated tidal elevations and those obtained from the global tidal model FES2014 (Carrere et al, 2015) are used for the purpose of validating the model. The results are summarized in **Figure B4**, and the statistical error analysis, in terms of the correlation coefficient (r) and the root mean square error (RMSE), are given in **Table B3**. Three location are chosen for the analysis, one is at the mouth of GoK, namely Pipavev, and two more such as Daman and Diu situated at a distance of 51.3 km and 73 km from the mouth. Locations inside the GoK are not considered, as FES2014 elevations will not be accurate for the shallow regions. It is evident that a very good agreement is ensured between the present model and FES2014, and hence the present model is capable of representing the tidal hydrodynamics in the domain of interest. The correlation coefficient estimates good amount of accuracy, and there exists strong linear relationship between simulated and FES2014 values.

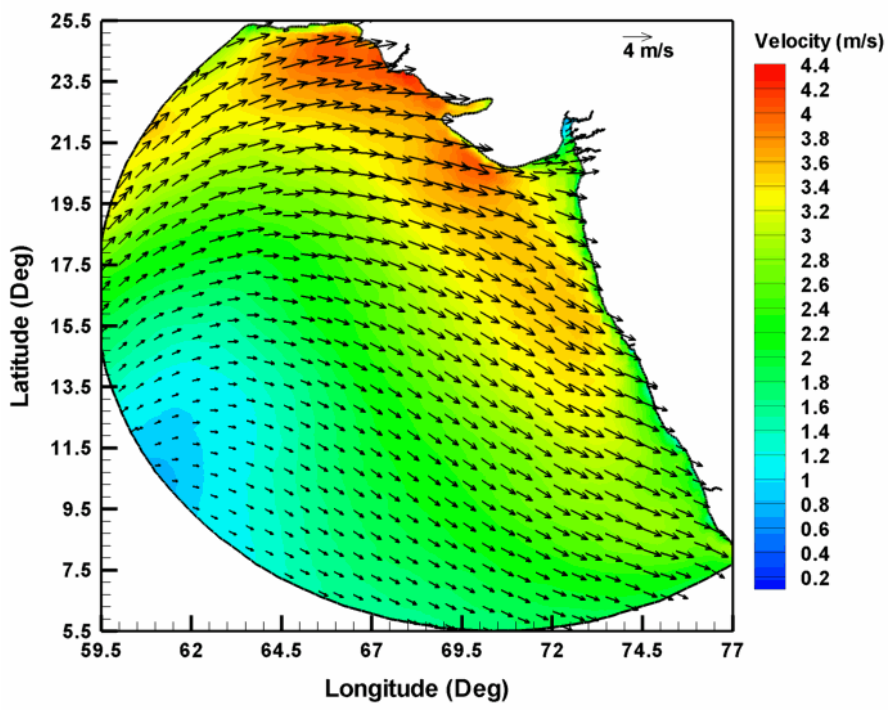

Figure B3: Typical Wind Field in the Study Region

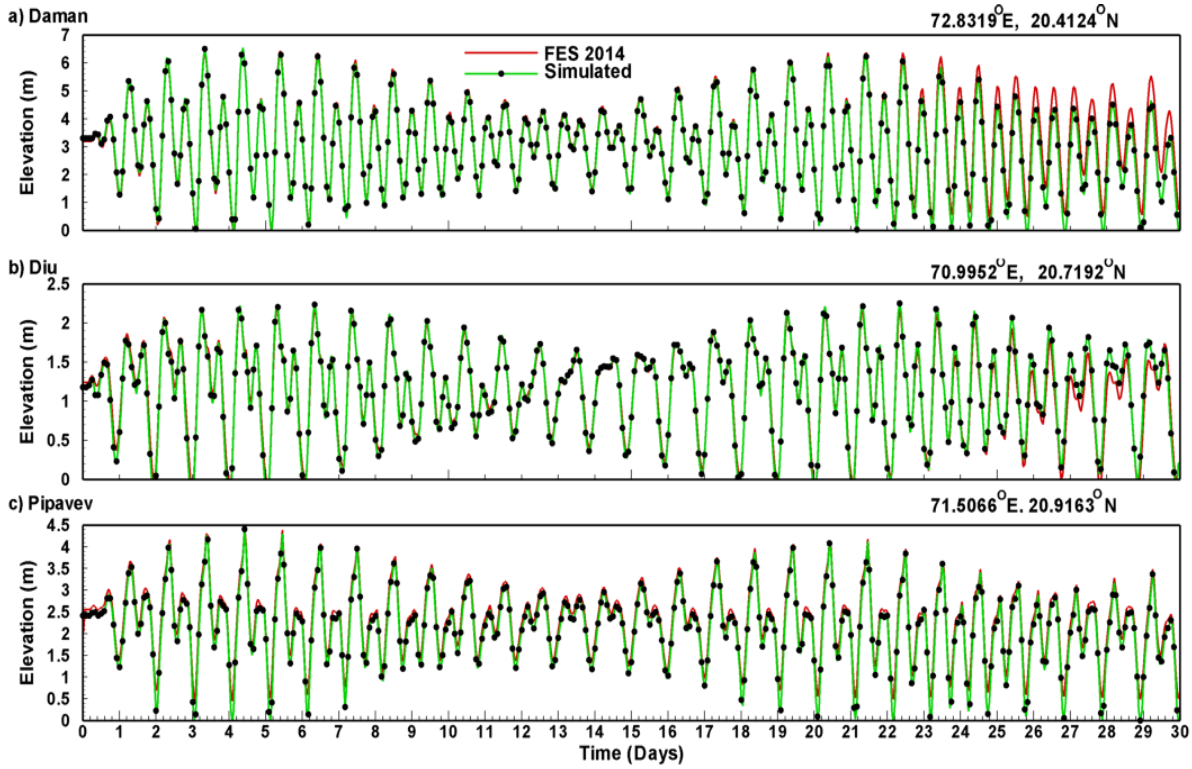

Figure B4: Comparison of Tidal Elevation

Table B3: Statistical error analysis for tidal elevation

Location	Correlation Coefficient	RMSE (m)
Pipavev	0.9966	0.0135
Daman	0.9825	0.0038
Diu	0.9871	0.0022

1.10.2 Normal Case: Without Dam

1.10.2.1 Spatial distribution of tidal elevation

The horizontal spreading of the tidal elevation for a diurnal tidal cycleis depicted in the **Figures B5** and **B6** with a time slot of 2 hours for the successive events. Here 0 hour is considered as the beginning of the tidal cycle. During this time the tides begin to retreat seaward in the southwest direction with a decreasing trend in elevation. But in the central parts of the gulf the tides still advance in the northern direction appearing like a standing wave, and this must be predominantly due to the reflection from the land boundaries in the lateral direction. The horizontal distribution of the tidal current vectors is shown in **Figures B7** and **B8**. During 2^{nd} hour of the tidal course the northward arm is a little more localized above 21.5^{O} N laititude with a decreasing trend in speed, whereas the seaward movement is more rapid with an average velocity of 1 m/s, particularly at the mouth of the gulf. Tidal condtions in the 4^{th} hour is almost same as that in the previous case, with a slight change in the spatial orientation and the horizontal extent is further diminished. During the 6^{th} hour of the tidal cycle landward movement of the tide is more defined till the latitudinal belt 20.5^{O} N, whereas the regions above this experiences seaward flow, and the amplitude is quickly diminished due to the strong landward flow of water. The flow of the tides during 8^{th} hour of the cycle resembles that in the previous case, but the tides begin to shoal due to the decreasing width of the gulf regions. The condition in the 10^{th} hour substantiates this statement with more rapid change in tidal elevation in the southwest direction, whereas some amount of partially reflected tidal water flows seaward in the exterme north of the gulf. The northward movement of the tide is a little more prominent in the 12^{th} hour but the velocity vectors undergo the damping effect due to the bottom friction. In the 14^{th} hour the flat bottom regions of the gulf experiences very less tidal flow, and the seaward movement gets intensified starting from 21.5^{O} N latitude. In the subsequent hours (16^{th} and 18^{th} hour), the tides show a well defined pattern of seaward motion, but in the subsequent hours (20^{th} and 22^{nd}) landward motion is established and asymmetric movement of the tide, characteristic to the convergent land boundaries, is clearly visible.

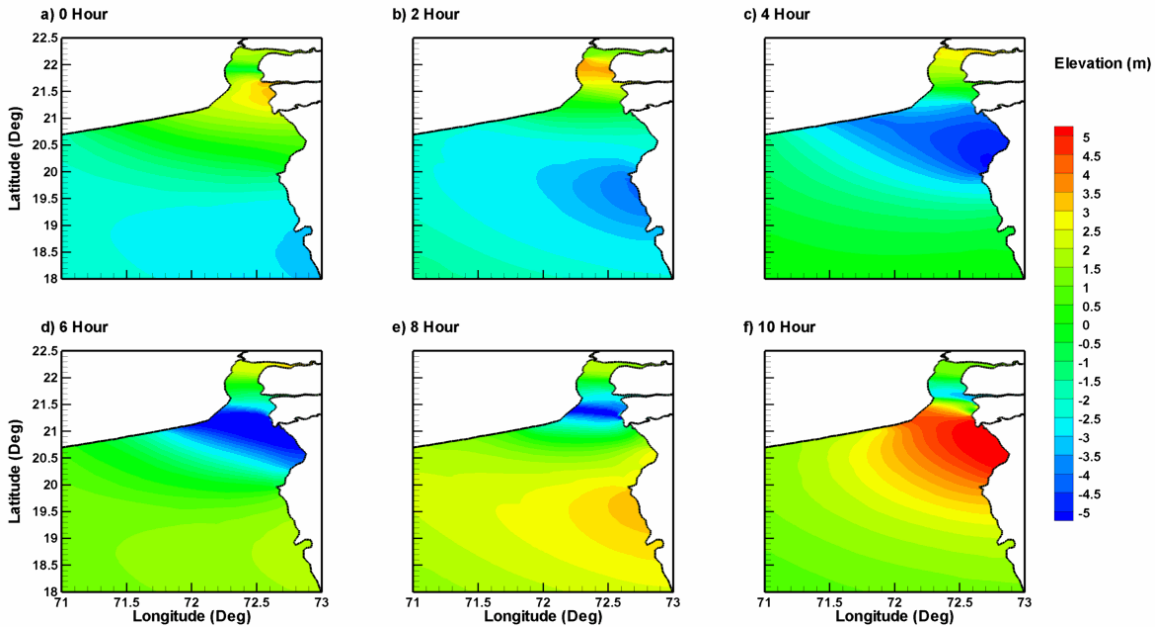

Figure B5: Spatial Distribution of Tidal Elevation (0 to 10 Hours)

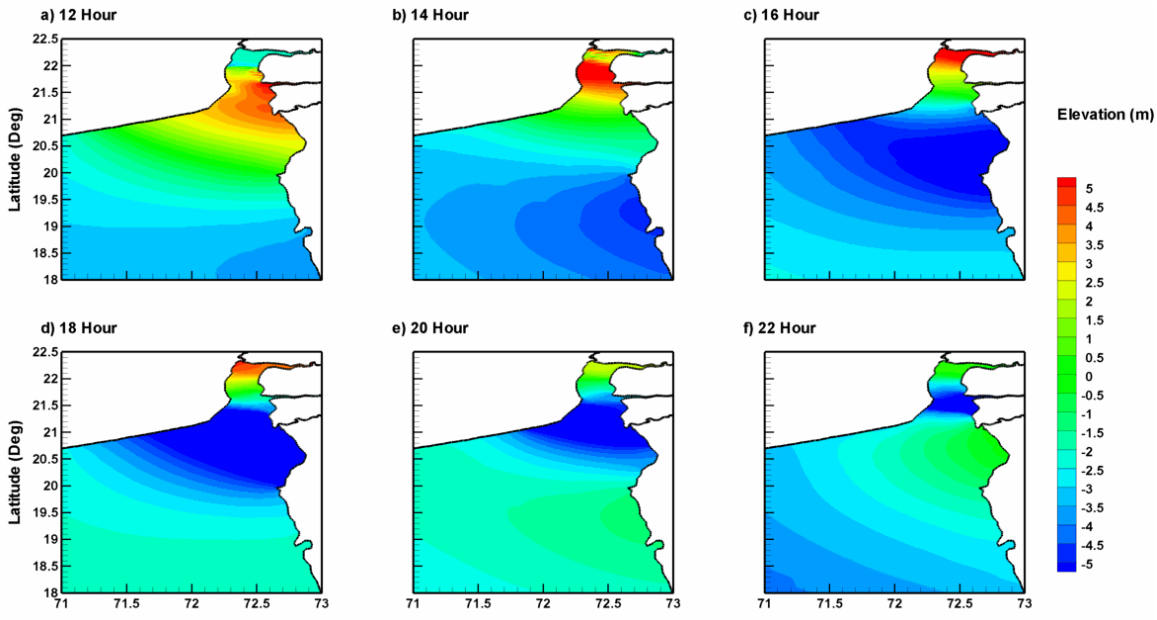

Figure B6: Spatial Distribution of Tidal Elevation (12 to 22 Hours)

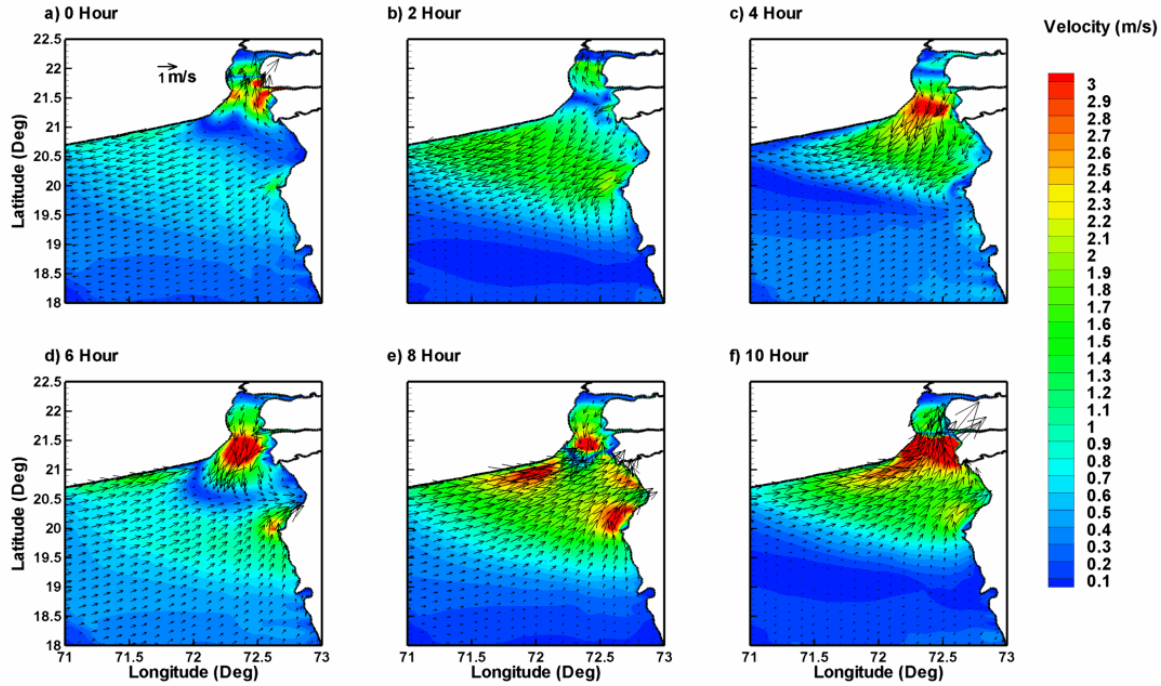

Figure B7: Spatial Distribution of Tidal Current Vectors (0 to 10 Hours)

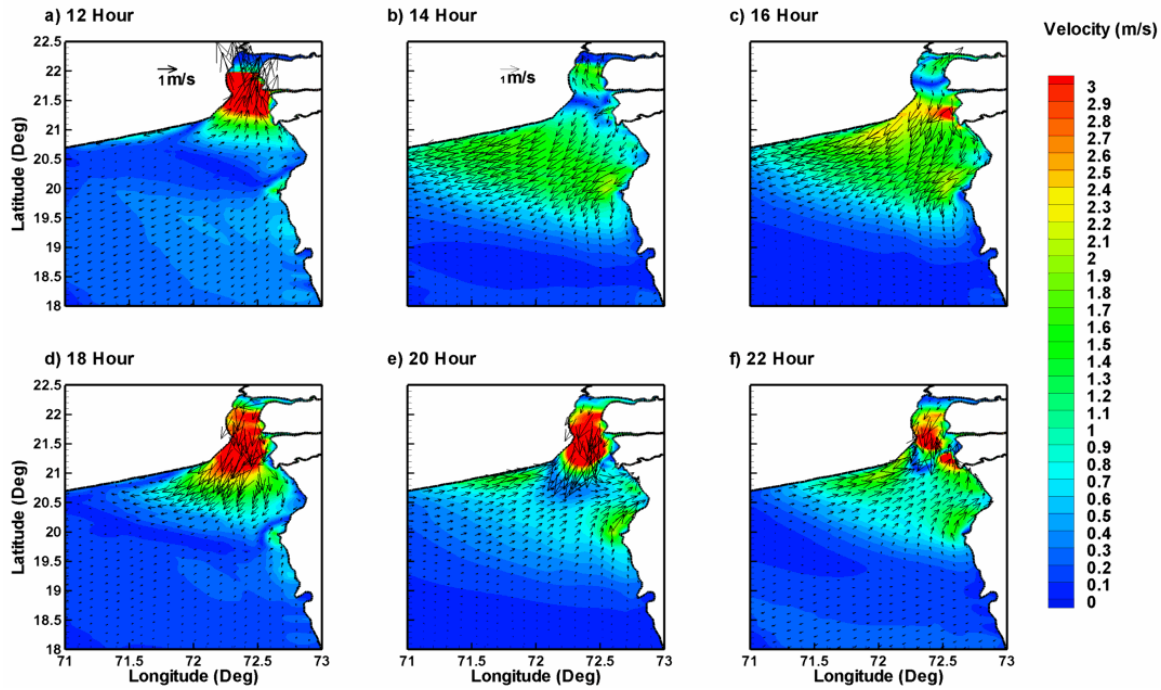

Figure B8: Spatial Distribution of Tidal Current Vectors (12 to 22 Hours)

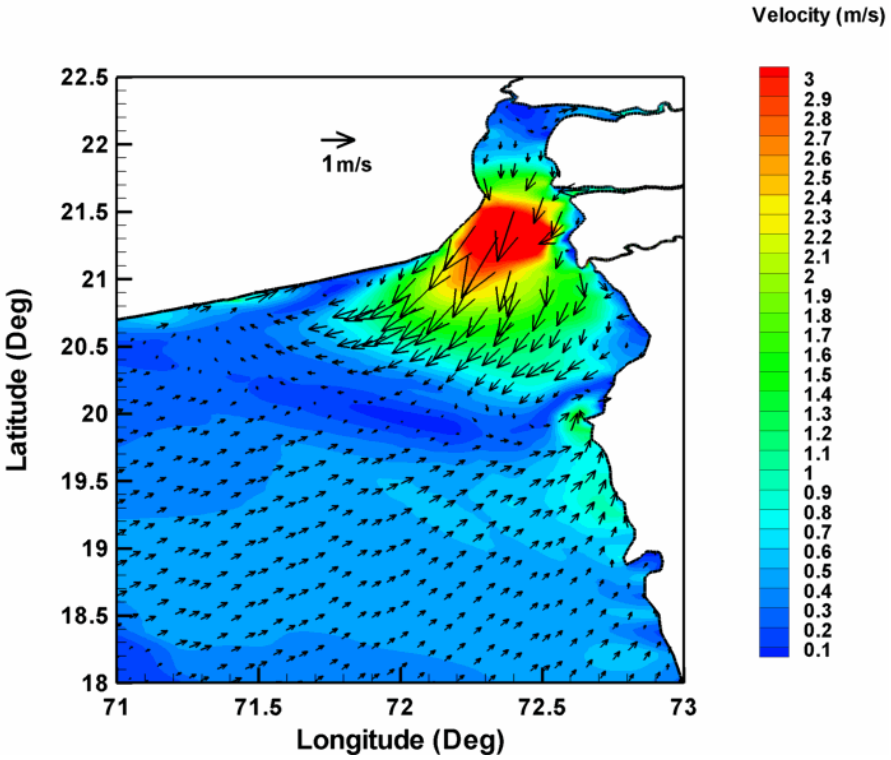

Figure B9: General Circulation Pattern

1.10.2.2 General circulation

The model is run for the combined action wind, tide and the river discharge events and the result is summarized in the **Figure B9**. The tidal activity in the central regions of the gulf is greatly enhanced by river discharge originating from the rivers Narmada, Tapi and Mahi. The tidal currents in these regions are around 1.5 m/s and directed along southwest trajectory. The wind driven circulation is oriented eastward and north-eastward and the current vectors are distributed so as to oppose the tidal flow. There is a clear demarcation between these two water masses ranging northward of 20^{O} latitude, extending longitudinally till the eastern land regions. Due to the combined action of the tide and wind, a barrier formation is developed in this region which makes the water masses to keep certain distance from each other.

1.10.2.3 Spatial distribution of salinity

The intrusion of saline water under the influence of the tide and wind is numerically simulated and the results are presented in the **Figures B10** and **B11**. During the first half of the semidiurnal tidal cycle (0 hour to 6 hour) the 32 PSU contour is completely occupied in the southwest regions of the mouth of the gulf. The 12 PSU contour is almost localised, tends to move in the northeast direction during the 6^{th} hour of the tidal cycle and reaches till the mouth of River Narmada. During

the next two phases of the tide (8th and 10th hour) the 32 PSU contour is further migrated in the southeast direction and embraces the Sourashtra Peninsula, as it does in the initial hours of the tidal action.

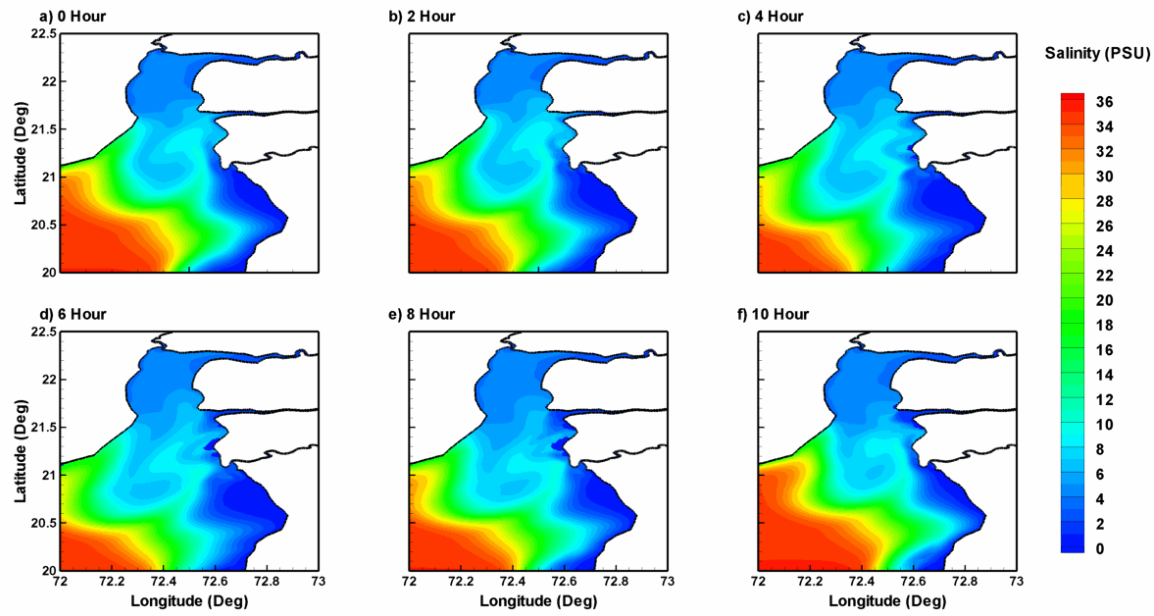

Figure B10: Spatial Distribution of Salinity (0 to 10 Hours)

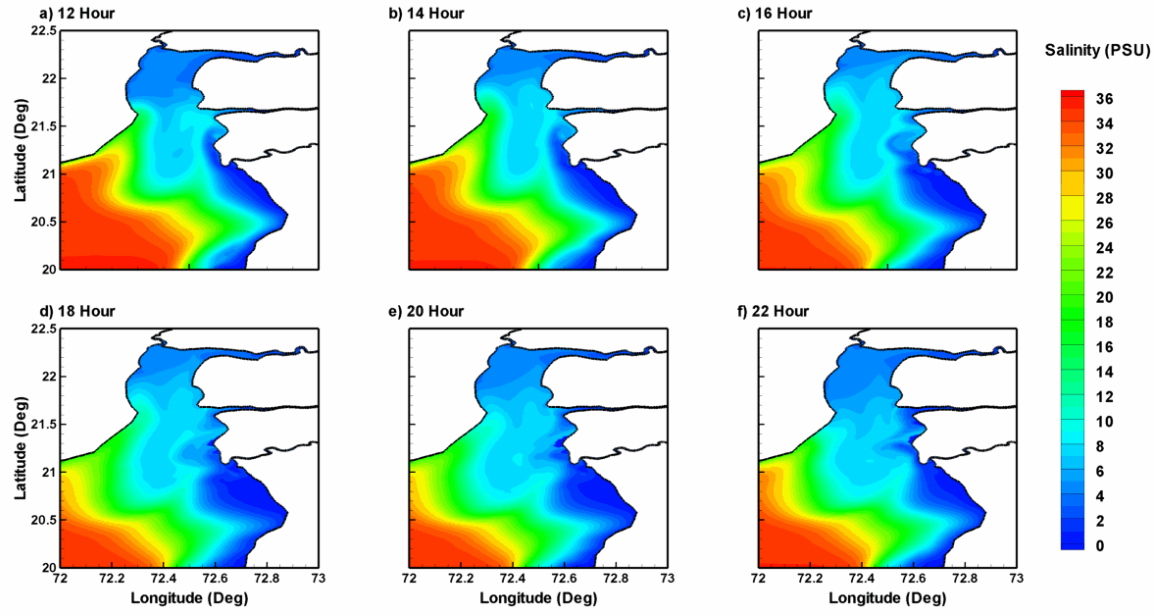

Figure B11: Spatial Distribution of Salinity (12 to 22 Hours)

1.10.2.4 Spatial distribution of temperature

The spatial variation of temperature during a diurnal tidal cycles is investigated and presented in **Figures B12** and **B13**. Unlike the salinity, temperature shows spatial disparities more rapidly. The deterministic nature of salinity is revealed by the balance between evaporation and precipitation. It is to be mentioned that no direct involvement of precipitation is considered in the model, whereas the effect of precipitation is exclusively adjusted by the river discharge. Computation of temperature is included in the model in a unique manner.

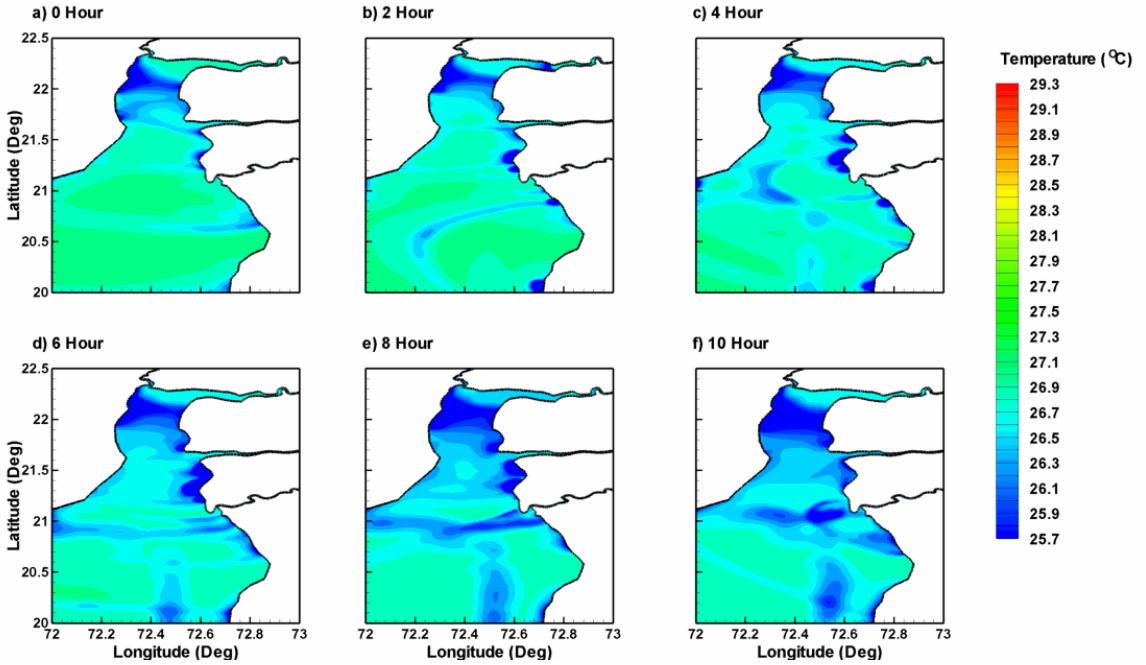

Figure B12: Spatial Distribution of Temperature (0 to 10 Hours)

The net heat transfer across the air-water interface is accounted as the combined effect of the downward heat flux at the surface, the down welling solar radiative flux and the down/upwelling infrared radiative flux. The computation is again enhanced by including the turbulent fluxes corresponding to the sensible and latent heat fluxes. The turbulent fluxes of heat and momentum are further modified by a parameterization scheme. This parameterization is designed for improving the accuracy under moderate and high wind regimes. It is quite evident that oceanic water shows variation in temperature as per the water depth and the seasonal changes as well. The diurnal variation of temperature caused by the oceanic tides is still considered as an unrevealed research problem as it involves complicated interactions between the air-water interface and the mudflat-water interface. The surface temperature shows maximum spatial variation during the daytime flood tide (0 to 4 hours) due to the inflow of heated water from the shallow coastal regions.

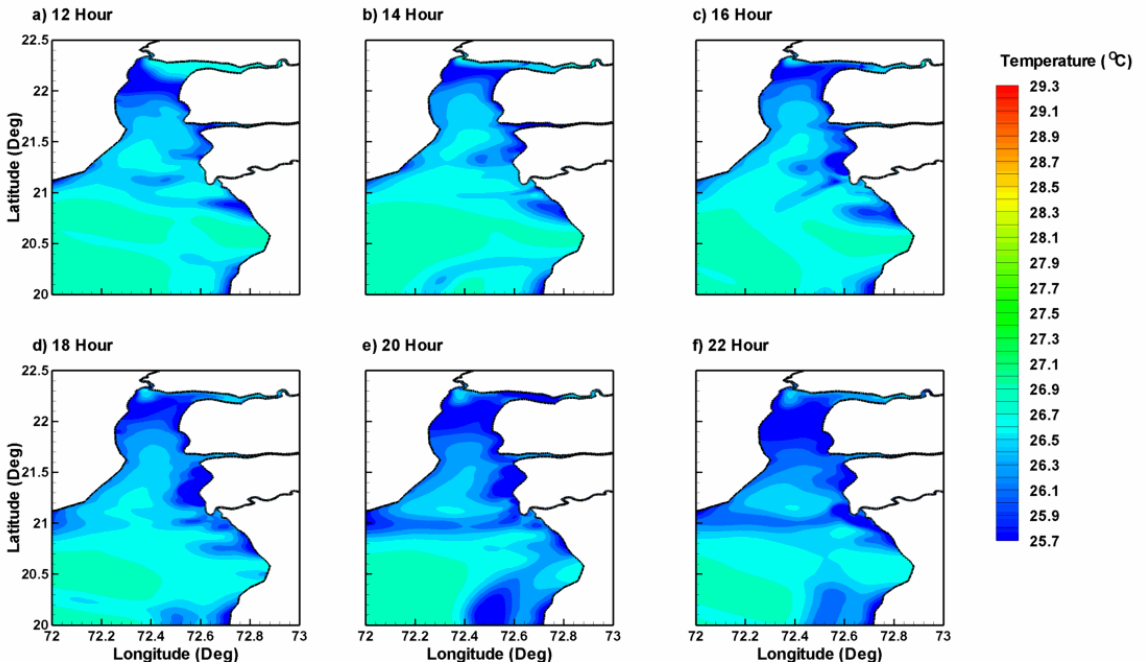

Figure B13: Spatial Distribution of Temperature (12 to 22 Hours)

During the slack hours the exposed mudflat regions retain large amount of heat originating from the solar heat flux, and this being quickly transferred to the subsequent high tide inundation. It is seen that the uniform distribution of surface temperature is suddenly collapsed during the 4th hour of the tidal cycle. During the flood tide the temperature is almost equally distributed by the tide due to mixing, and during the subsequent semidiurnal tidal cycles the surface distribution shows a decreasing trend. During the next semidiurnal tidal cycle the surface temperature follows the same behaviour as that of the preceding tidal conditions. It is to be mentioned that the diurnal variation exhibits a range of 2 to 3^{O} C, and the patchy appearance of the temperature is attributed to the effects of wind conditions in the domain.

1.10.3 Normal Case: With Dam

The computational domain for the normal case with dam is given in **Figure B14**, assuming that the dam is physically constructed as per the longitudinal and latitudinal positions proposed for the project. The physical barrier formation offered by the dam now acts as a non-penetrable wall boundary, which makes the computational domain diminished in extent, thereby shutting down the discharge (~400 m^3/s) of Mahi and Sabarmati rivers. There is a reduction of almost 50 km in the longitudinal direction and 25 km in the latitudinal direction, which makes roughly 1200 km^2 area of the rectangular part of the initial computational domain, shortened. This might be a

considerable area, as the total estuarine length is approximately 150 km till the mouth from the point where the discharge of River Sabarmati joins the computational domain.

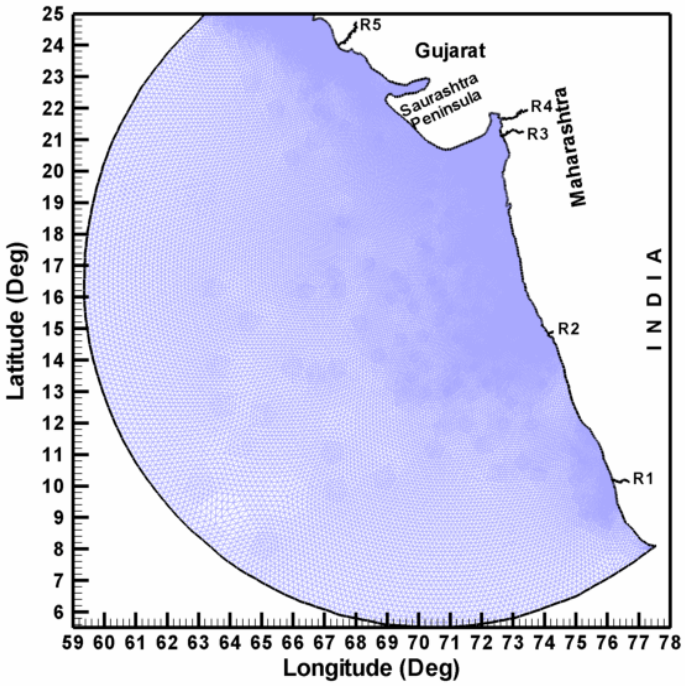

FigureB14: Computational Domain for the Proposed Site with Dam

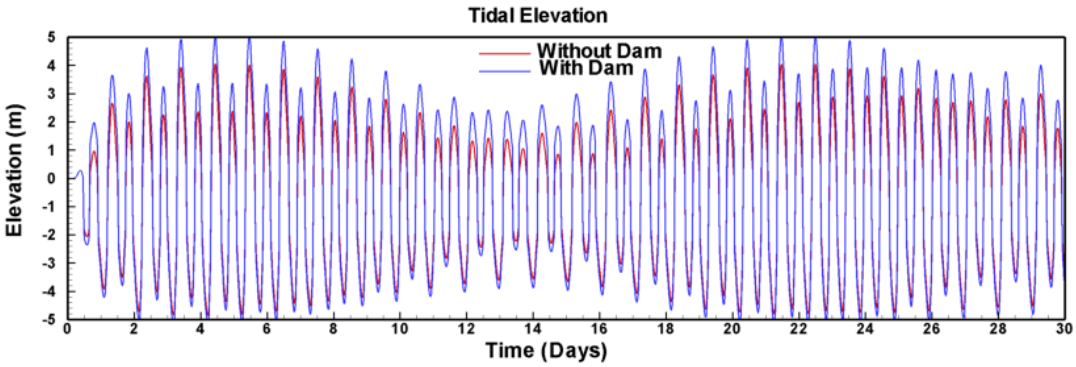

Figure B15: Comparison of the Tidal Elevation: With and Without the Dam

The initial and boundary conditions remain fixed, except the reduction in river discharge as mentioned, and simulation has been once again performed. In order to analyse change in tidal elevation a point (72.3931^{O} E, 21.7786^{O} N) is selected, which is almost equidistant from both the ends of the dam, situated at distance of 5 to 6 km from the dam wall. The time series of the extracted tidal elevations is compared with that derived from the simulation event in which the dam is absent. The result shows the tidal range is increased by 1.3 m due to the presence of the dam. On the seaside of the dam the tidal range projects a different pattern, which qualifies the

investigation made in time series analysis of tidal elevation. The tidal range given in the figure is the difference between the lowest low water line and the highest high water line possible with the present conditions of the simulation event. Without the dam, the average tidal range towards the southern side of 21.8^{O} N latitude is 6 m till 21.4^{O} N latitude. The maximum tidal range of the order of 8 m is seen in the north-western side of River Tapi. The comparative study suggests that more than 2 m increment in tidal range is observed in the regions mentioned above when the dam is present. Maximum tidal range of 9 m is observed in the vicinity of the dam wall. The hydrodynamic situation described here is well accepted, as the physical barrier offered by the dam makes the regions on the seaside of the dam flooded and subsequently inundated.

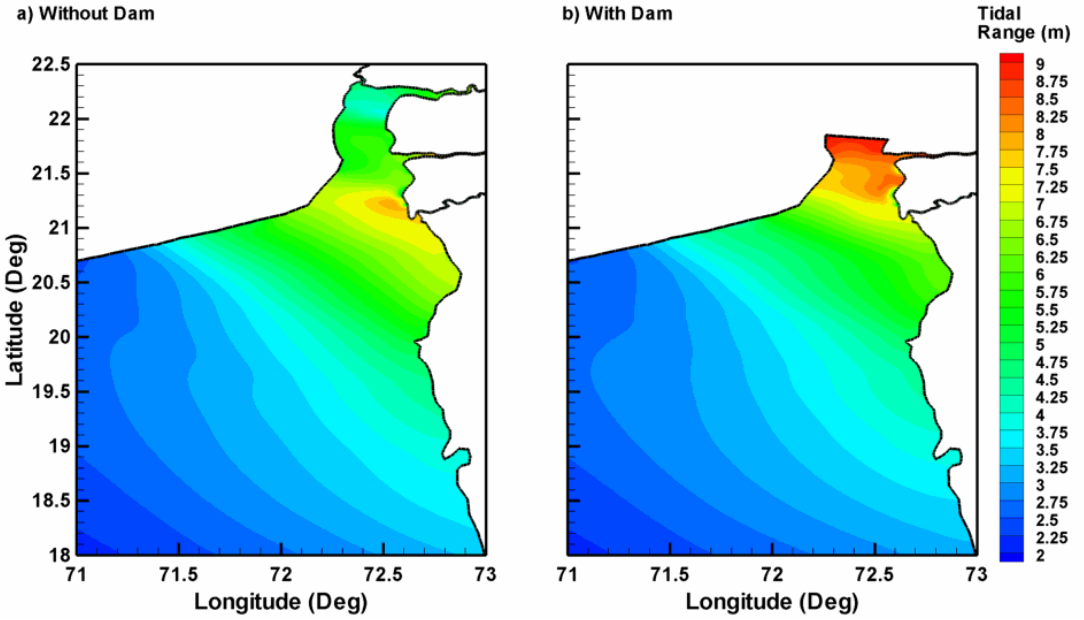

Figure B16 Spatial Distribution of Tidal Range

1.10.3.1 Spatial distribution of tidal elevation

As before, the horizontal spread of the tide is studied and represented in **Figures B17** and **B18**. On regional scale, vertically erected man-made structures for coastal protection have influenced the mean sea level and the landward reach of the spreading of water (Pickering et al., 2017). It can be seen that the surface profiles of tidal elevation with the dam keeps almost the same profile with its counterpart, except its magnitude in the vicinity of the dam wall. Similarly, the tidal current vectors (**Figures B19** and **B29**) also hold the same behaviour in most of the time slots of the cycle, and slightly differing in their magnitudes during certain stages.

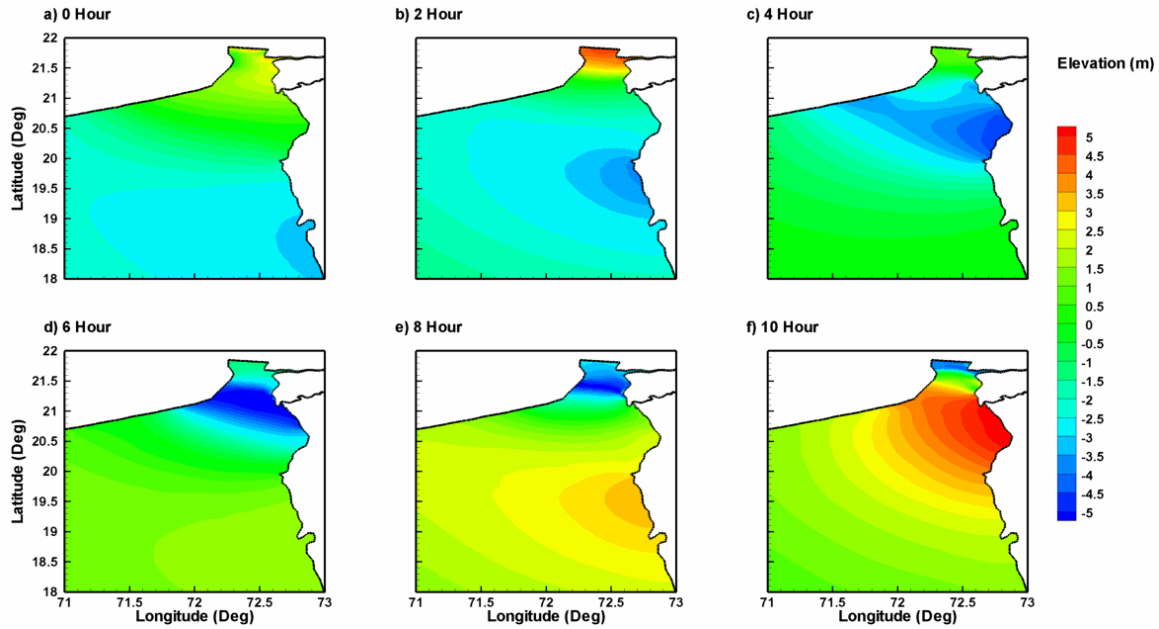

Figure B19: Spatial Distribution of Tidal Elevation (0 to 10 Hours)

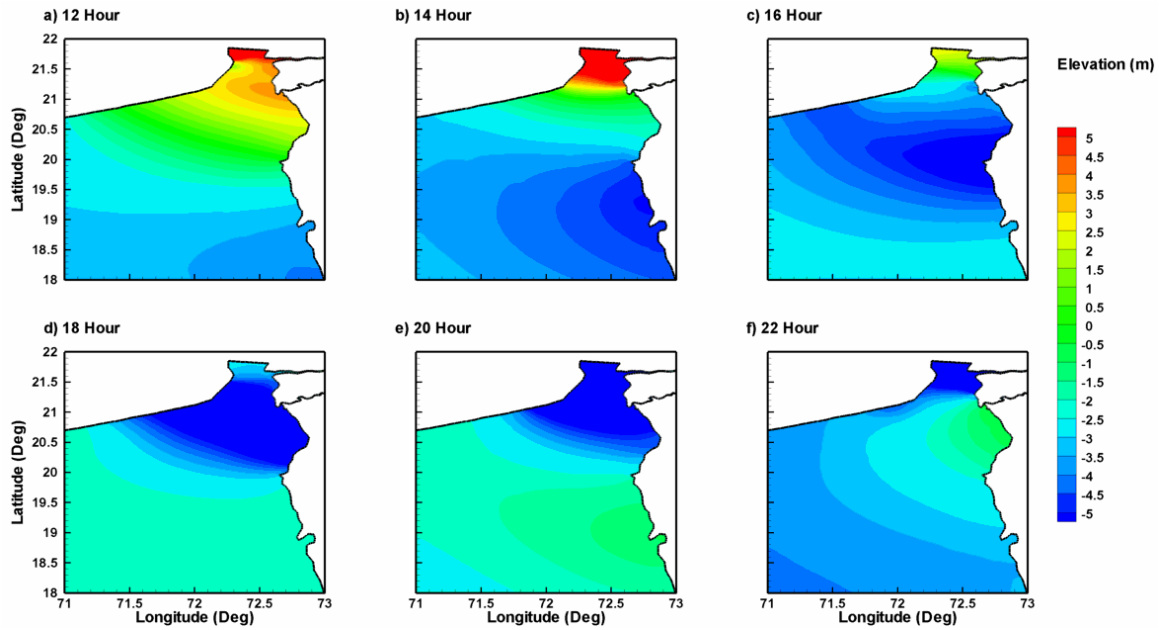

Figure B18: Spatial Distribution of Tidal Elevation (12 to 22 Hours)

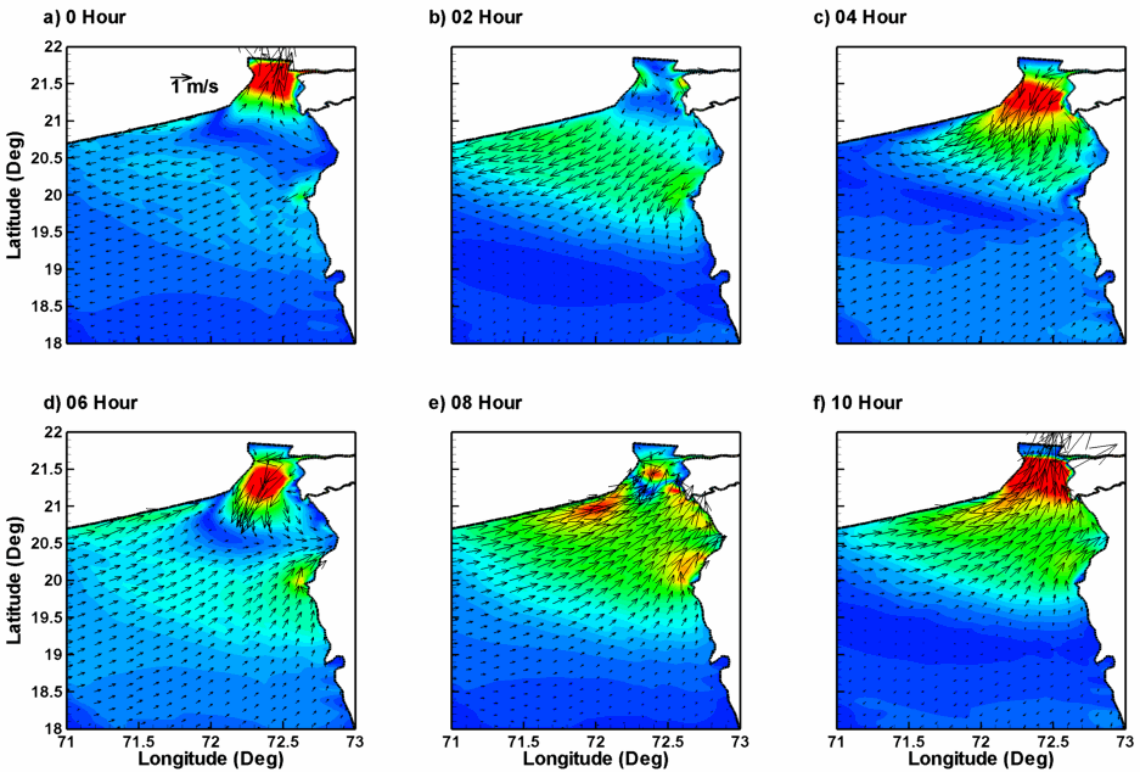

Figure B19: Spatial Distribution of Tidal Current Vectors (0 to 10 Hours)

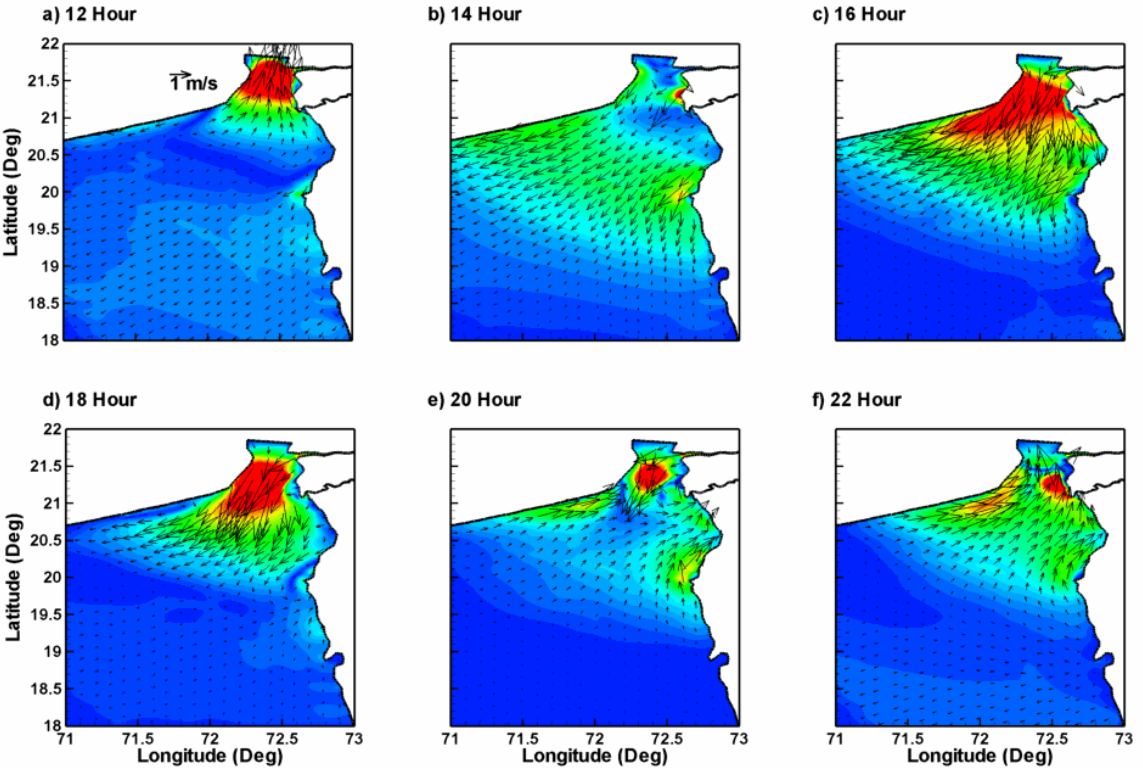

Figure B20: Spatial Distribution of Tidal Current Vectors (12 to 22 Hours)

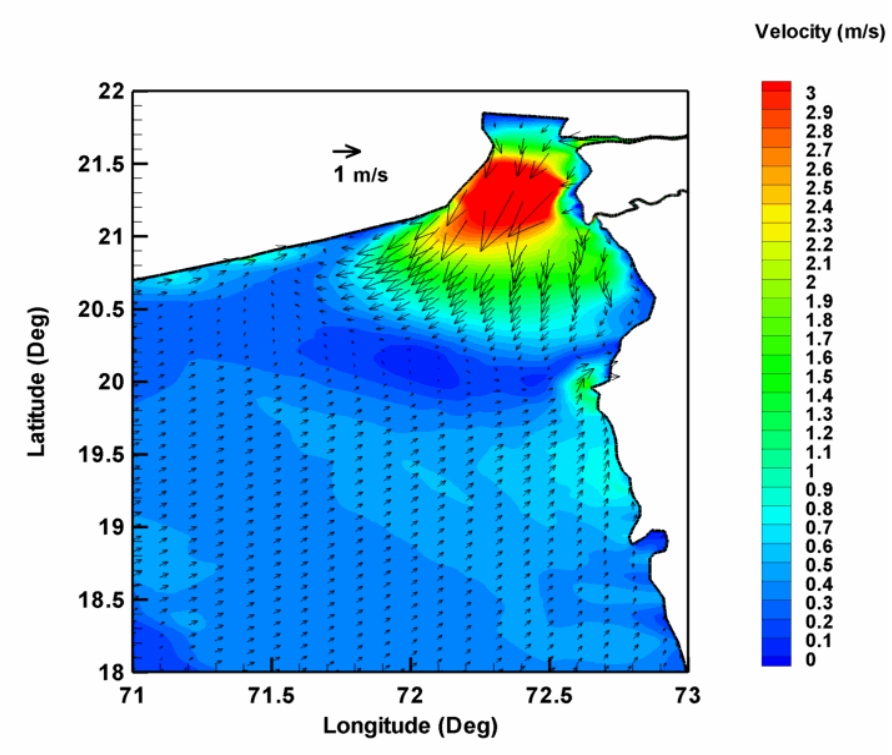

Figure B21: General Circulation Pattern

1.10.3.2 General circulation

The spatial distribution of general circulation pattern (**Figure B21**) with the presence of the dam does not deviate much from the corresponding distribution we have described in **section 2.3.2.2**. The barrier formation is still visible further northward of 20^{O} N latitude, which results from the opposing water masses trying to cross each other. The wind driven circulation is oriented eastward and north-eastward.

1.10.3.3 Spatial distribution of salinity

The horizontal profiles of salinity with the presence of the dam is portrayed in **Figures B22** and **B23**. The general trend of the salinity intrusion under tidal and wind forcing differs from its counterpart. The regions given in the figures can be considered well-mixed due to the intense tidal activity, the effect of wind also can be a factor, but not deterministic as the wind regime remains the same in both the simulation scenarios. The seaside of the dam preserves the isohaline contours of 20 PSU till 21^{O} N latitude during the entire slots of the tidal cycle. The oscillatory profiles of salinity distribution reconfirms the dominant nature of tides in fixing the hydrodynamics of the salinity intrusion. The western sides of Maharashtra and the Sourashtra Peninsula, which have

been almost safe from being intruded by the high saline water when the dam was absent, are now prone to be more salty.

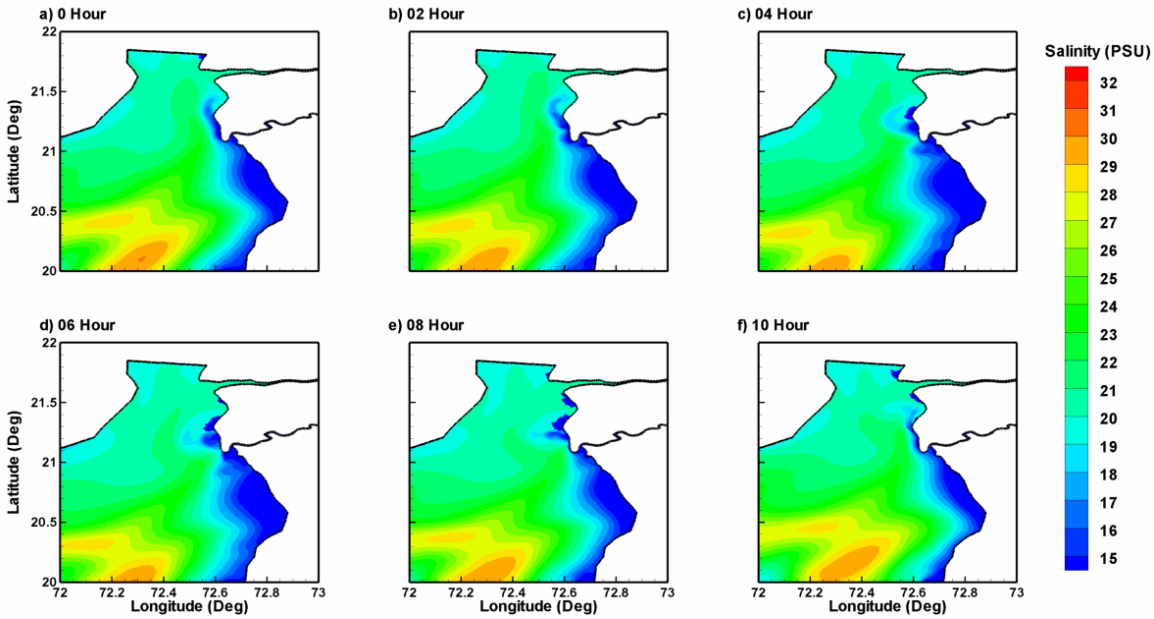

Figure B21: Spatial Distribution of Salinity (0 to 10 Hours)

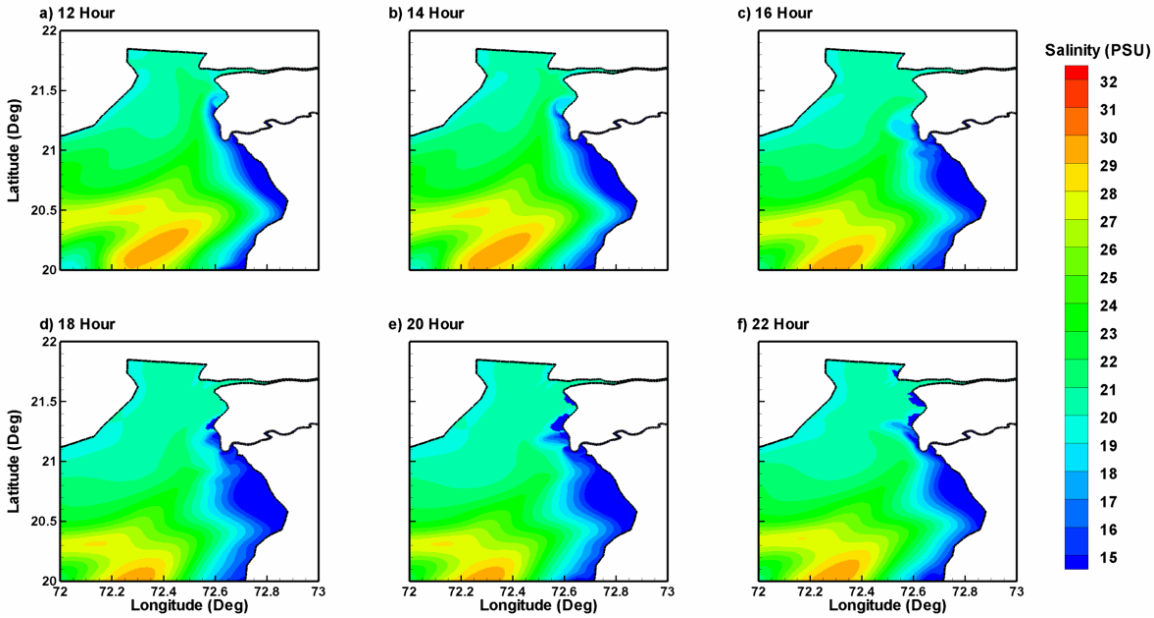

Figure B23: Spatial Distribution of Salinity (12 to 22 Hours)

This type of hydrodynamic setup is quite expected when there is considerable increment in the tidal range, and the reduction in the area makes the tidal prism much more confined in the available space. It is seen that tidal water gets migrated north-eastward to a considerable extent towards the land regions, indicating the possibility of the regions get inundated.

1.10.3.4 Spatial distribution of temperature

The spatial variation of temperature with the presence of the dam is presented in **Figures B24** and **B25**. These horizontal distributions also show much dissimilarities as compared to their counterparts described in **section 2.3.2.4**.

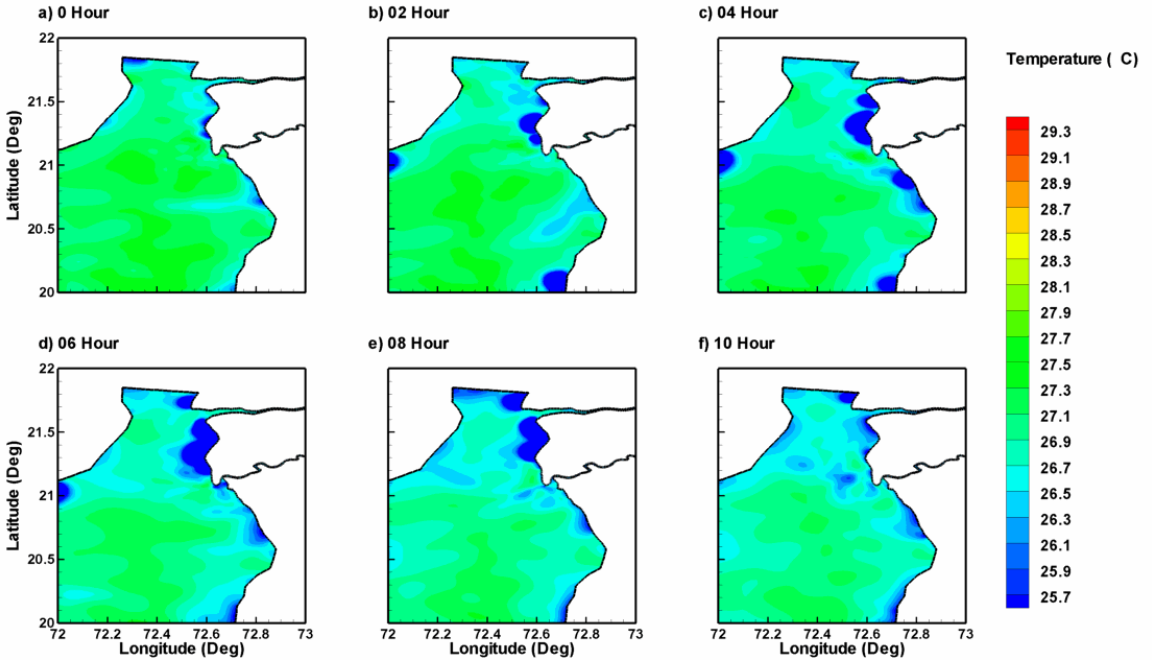

Figure B24: Spatial Distribution of Temperature (0 to 10 Hours)

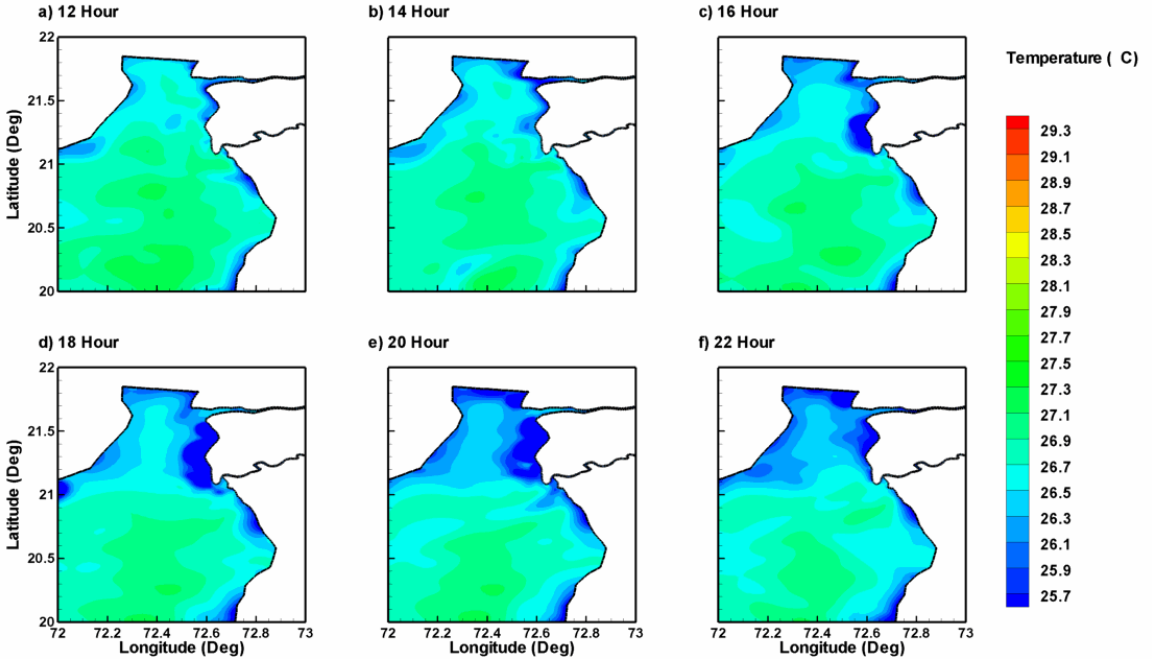

Figure B25: Spatial Distribution of Temperature (12 to 24 Hours)

On an average there is an increment of 0.5^{O} C in the horizontal profiles. This might be attributed to the intense vertical mixing caused by the tidal activity which imparts large quantities of momentum into the water column, thereby heat energy is increased. Another possibility is the presence of the mud flats in the region, which also makes the heat exchange to the water column. Since the region is experiencing more tidal range this explanation is satisfactory, but must be tested more systematically, and the vertical profiles of temperature need to be analysed.

ANNEXURE-C
NUMERICAL MODELING OF HYDRODYNAMICS AND MORPHODYNAMICS

1.11 Background

The Gulf of Khambhat, also known as the Gulf of Cambay, is a bay on India's Arabian Sea coast, just north of Mumbai and Diu Island, bordering Gujarat. The Gulf of Khambhat is roughly 200 kilometres long, with a width of 20 kilometres in the north and up to 70 kilometres in the south. The Narmada, Tapti, Mahi, and Sabarmati are major rivers that drain Gujarat and produce estuaries in the Gulf. It separates the Kathiawar Peninsula from Gujarat's south-eastern region. The study area is geographically located between 22°24'32.64" and 20° 2'31.66" N latitude and 72°29'28.43" and 72° 3'18.76" E longitude.

There is a proposal to construct a 30 km dam across India's Gulf of Khambhat in order to create a massive fresh water coastal reservoir for irrigation, drinking, and industrial reasons. The Kalpasar Project, also known as the Gulf of Khambhat Development Project, entails the construction of dam which will be able to store 10,000 million cubic metres of fresh water from rivers such as the Narmada, Mahi, Dhadhar, Sabarmati, Limbdi-Bhagovo, and two other minor rivers, amounting to 25% of Gujarat's average annual precipitation flow. Over the dam, a 10-lane road link will be built, considerably reducing the distance between Saurashtra and South Gujarat. The dam is located between 21° 48' 25.22"N, 72° 9' 2.02"E and 21° 48' 25.71"N, 72° 38' 51.17" E shown in the **Figure C1.**

Figure C1: Location Map of the study region

1.12 Scope and Objectives of the Study

The main objective of the project is to

1. Investigate the tidal hydrodynamics and the seasonal circulation changes in the study area.
2. Analyse the seasonal morphodynamic changes

1.13 Methodology

Demarcation of the study domain is done to set up the extent of the model domain. Hydrodynamic modelling is carried out for the study region by using Telemac 2d model. Modelling the bed evolution of the domain is performed using the morphodynamic routine of Ocirc. Both hydrodynamic and morphodynamic model is simulated for a two neap to neap condition, which covers all the astronomical aspects of tidal forcing. The siltation rate for the study area is calculated based on different seasons.

1.14 Modelling the Study Area

The present study focused on analysing the circulation features and its effect on morphodynamic changes in the proposed dam area in Kalpassar, Gulf of Khambhat. Numerical models are used to predict the bed level changes based on the hydrodynamic. The hydrodynamic modelling study is carried out by establishing the hydrodynamic model for a detail understanding of the tidal hydrodynamics and in addition with the wind induced circulation for the two cases, which are without dam and with dam conditions. The model predict the flow field and it is used to compute the changes in the bed level using sediment load balance in the water column. The model domain is discretized with the triangular element to obtain numerical solution to the hydrodynamic equations. The final mesh has fine element coast and shallow water depth. The average mesh size is found to be 130-250 m near shore which is very fine for the large gulf such as this .The mesh is coarser near the offshore boundaries where the water depths are greater. A typical mesh that is used to discretize the domain and bathymetry of the domain used for two cases for the simulation along with the bathymetry used in with dam and without dam condition are shown in **Figure C2** and **Figure C3.** The model is capable of capturing the details of the bathymetry significantly closer to reality**.** Typical bathymetry and computational mesh for the cases are shown in the **Figure C4.**

Several data including measurement of tide, wind, bathymetry covering seasonal variation of hydrodynamics are collected and used for calibration and validation. The bathymetry obtained by the measured data is interpolated into the mesh. Wind data for the year 2021 is obtained from ERA5 dataset from ECMWF with the horizontal resolution of 0.25-degree x 0.25 degree and hourly temporal resolution. The wind data is interpolated into mesh using Telemac2d**.** The boundary of the model domain is forced with varying water level and velocity conditions using data from TPXO global tide model. The water level variation obtained near the dam area (21°47'40.35"N, 72°23'22.07"E) is given in **Figure C5.**

These data is fed into the numerical model that simulates hydrodynamics, tidal and wind-induced circulation, sediment transport, and siltation rate in the proposed site and its environs. The simulation findings reveal the impact of seasonal variation on sedimentation processes in great detail. The amount of silt is calculated based on the rate of siltation and the surrounding area. The current study will be conducted using Telemac2d, a widely used industry-ready hydrodynamic setup, the details of which are discussed in **Annexure - A**. The morphodynamic routine of model

OCIRC- IITM inbuilt model is used and the details of which are given in **Annexure - .** In further without dam condition is described as **Case I** and with dam condition is described as **Case II**.

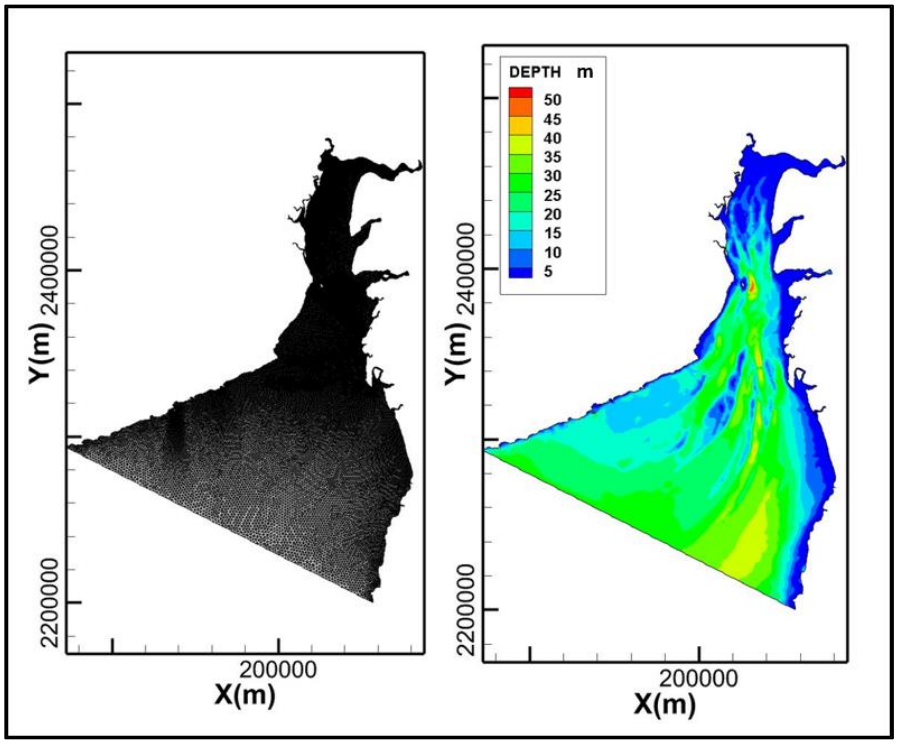

Figure C2 computational mesh and bathymetry for Case I

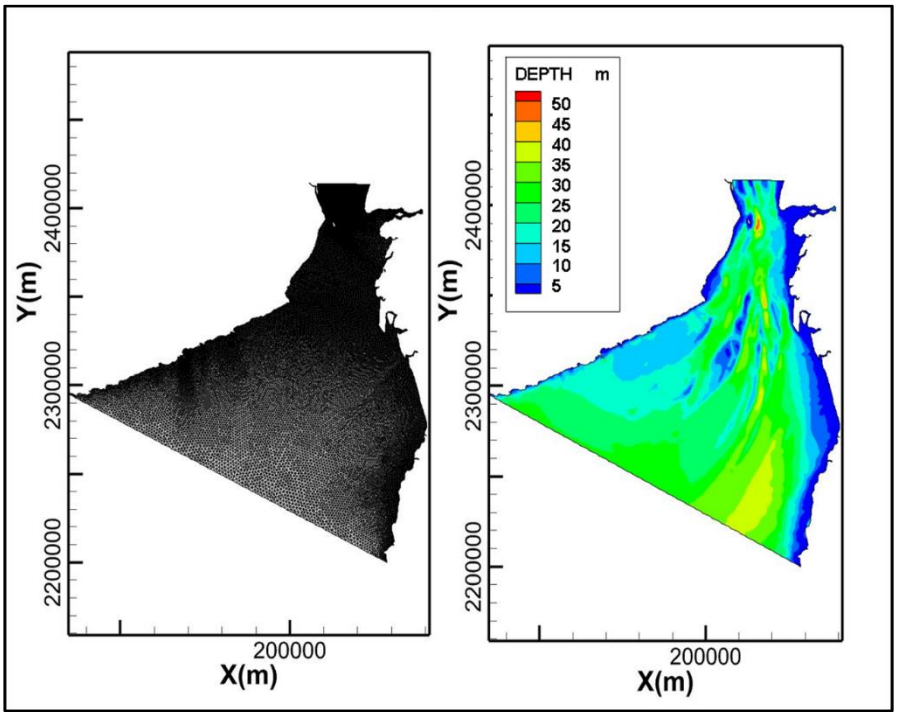

Figure C3: computational mesh and bathymetry for Case II

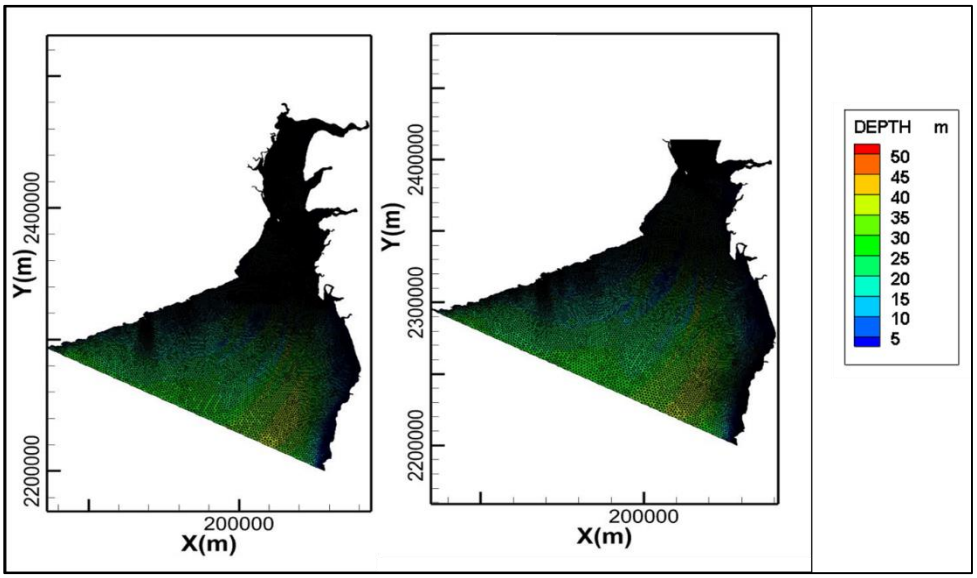

Figure C4: Computational mesh and bathymetry interpolated for Case I and cases II

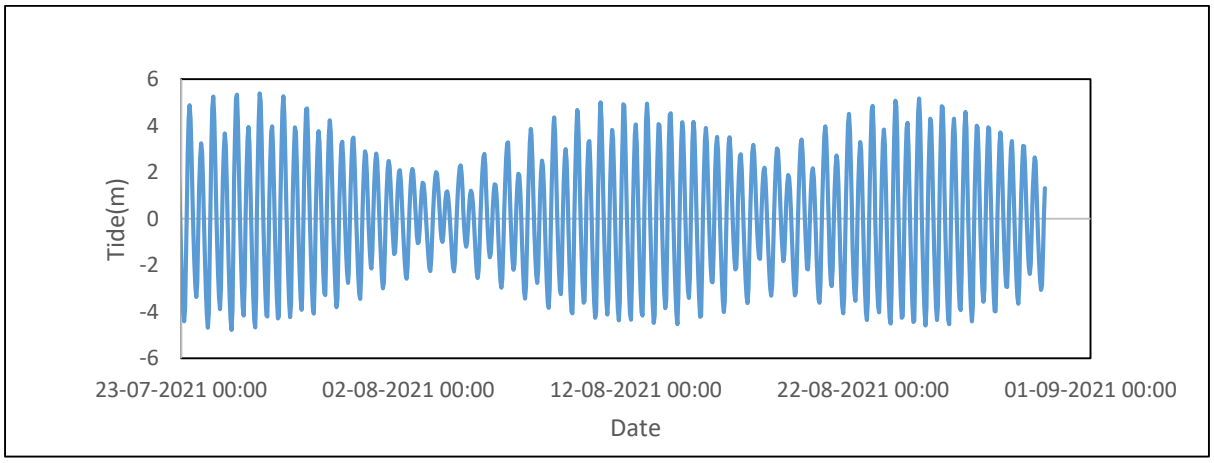

Figure C5: Tidal values near the proposed dam for Monsoon season

1.15 Results and Discussions

1.15.1 General

Accurate simulation of the tidal hydrodynamics in the study area depends on the kind of computational mesh generated for the simulations. An unstructured meshing scheme was selected in order to accurately capture the adjoining shoreline.

An unstructured meshing scheme is capable of resolving all the boundary and bathymetry details in the study area. This typical computational mesh depicts the ability of the meshing algorithm to exactly discretize the study area.

1.15.2 Hydrodynamic Study

1.15.2.1 Simulated Tidal Conditions

The present tidal hydrodynamic conditions at the site are mainly characterized by alternating northerly and southerly flow in the open sea. The direction of flow is north-easterly during flooding and south-westerly during ebbing. For the purpose of easy referencing of the hydrodynamics with the tide levels, typical time instances at which flow patterns have been extracted, are shown in The origin is at mean sea level.

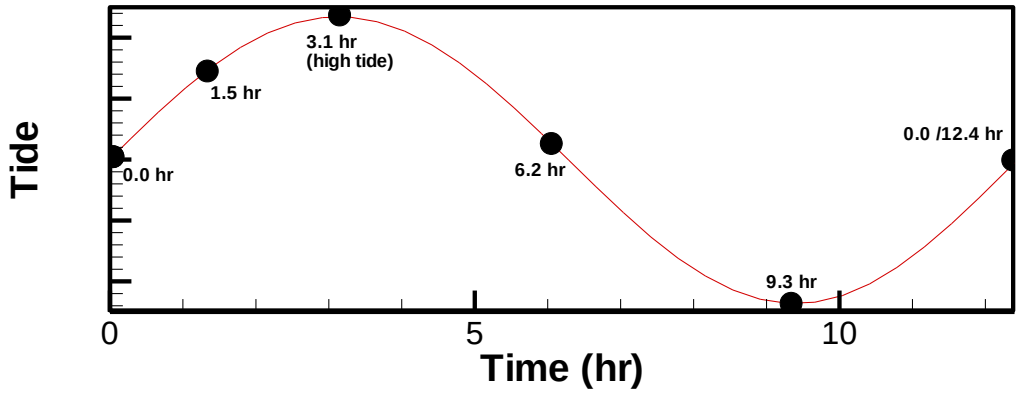

Figure C6: Times of tide at which the results are plotted

1.15.2.2 Hydrodynamic study of Without Dam Condition (Case I)

Flooding

The flow patterns during flooding condition in the domain is shown in **Figure C7** and **Figure C8**. The figures show a typical flow situation during the rising tide (at about 0 hr.) from which, the magnitudes of current at various locations in the study area can be deduced. The flooding phase of the tide is characterized with flow in the north-east. The tide will be entering the bay from the south direction and leaving back during ebbing tide. During the time of flooding, the current is observed more near the river mouth in the range of 1.4-2 m/s. considering the study area, the maximum current speed in the order of 1.4 -3 m/s is observed in the domain. The maximum current speed of 0.7 -1.4 m/s is observed in the offshore areas. According to the orientation of coast, current speed varies such as sheltered places are devoid of currents. The above currents are disappearing during the high tide event in the study area as shown in **Figure C9.**

Ebbing

The flow patterns during ebbing condition near the project site shown in **Figure C10**. The figure shows a typical flow situation during the falling tide (at about 6.2 hr.) from which, the magnitudes of current at various locations in the study area can be deduced. During the ebbing phase of the tide, which is followed by the occurrence of high tide, the tide starts to recede and reversal of flow start to occur towards back into open sea. During ebbing, the maximum current speed of 1.4 -2.1 m/s is observed in the offshore areas. Near the island the current velocity is in the range of 2.4-2.8 m/s. Generally, the coast is observed to experience low circulation dynamics during low tide. The flooding of water into the domain from offshore region follows the low tide which is observed in **Figure C11.**

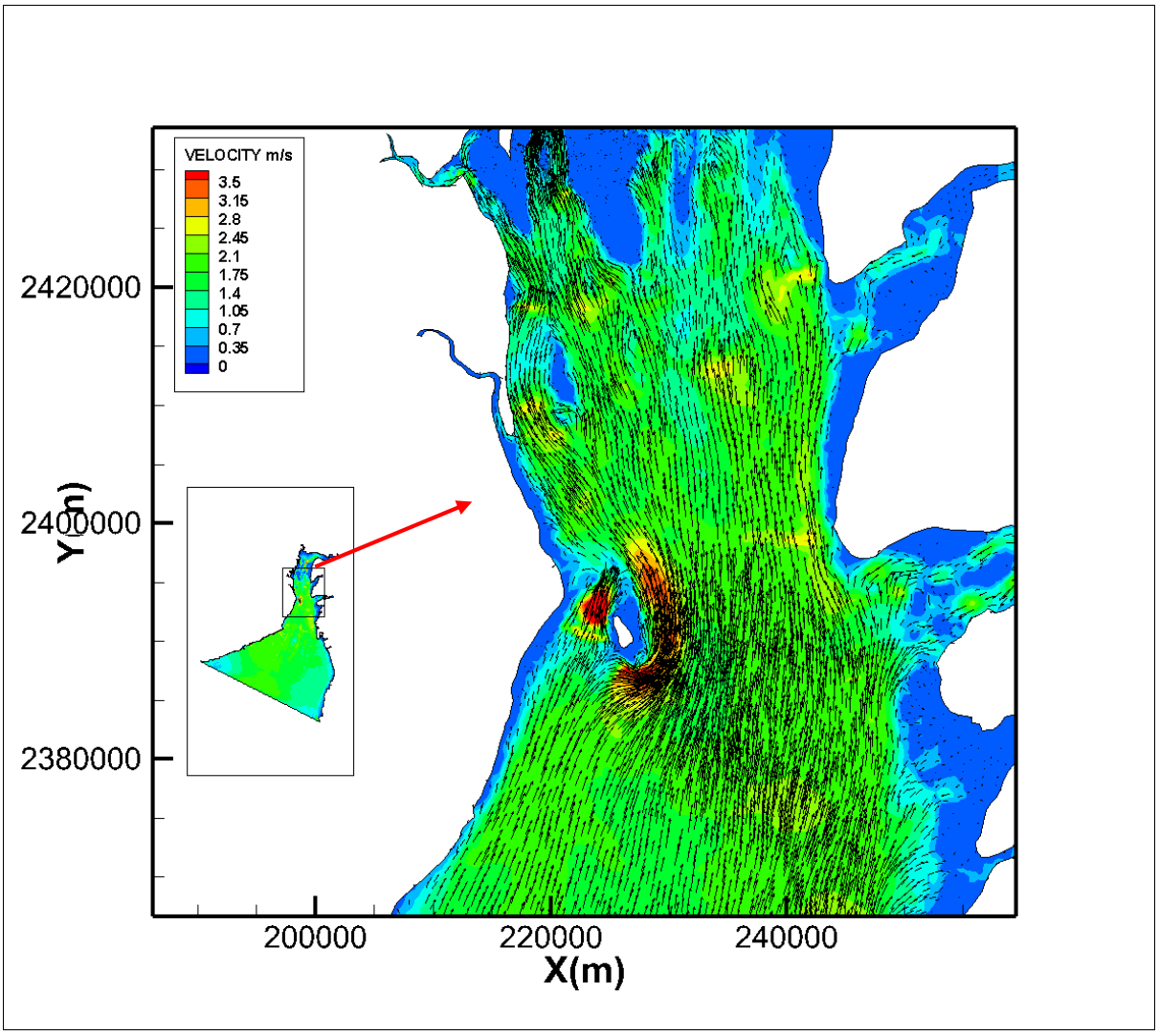

Figure C7: Velocity vectors and contour plots during flooding time at 0 hours in Case I

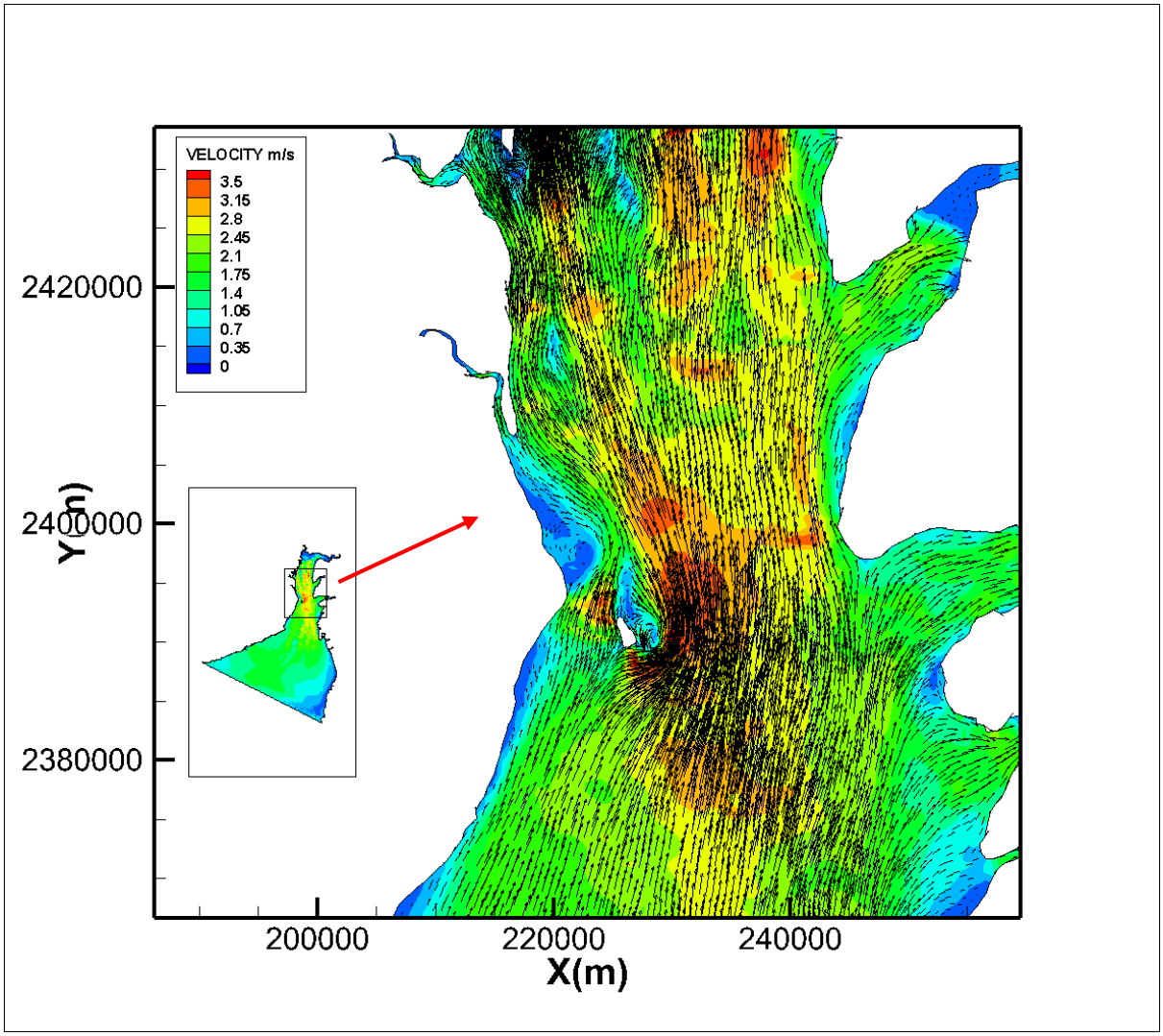

Figure C8: Velocity vectors and contour plots during flooding time at 1.5 hours in Case I

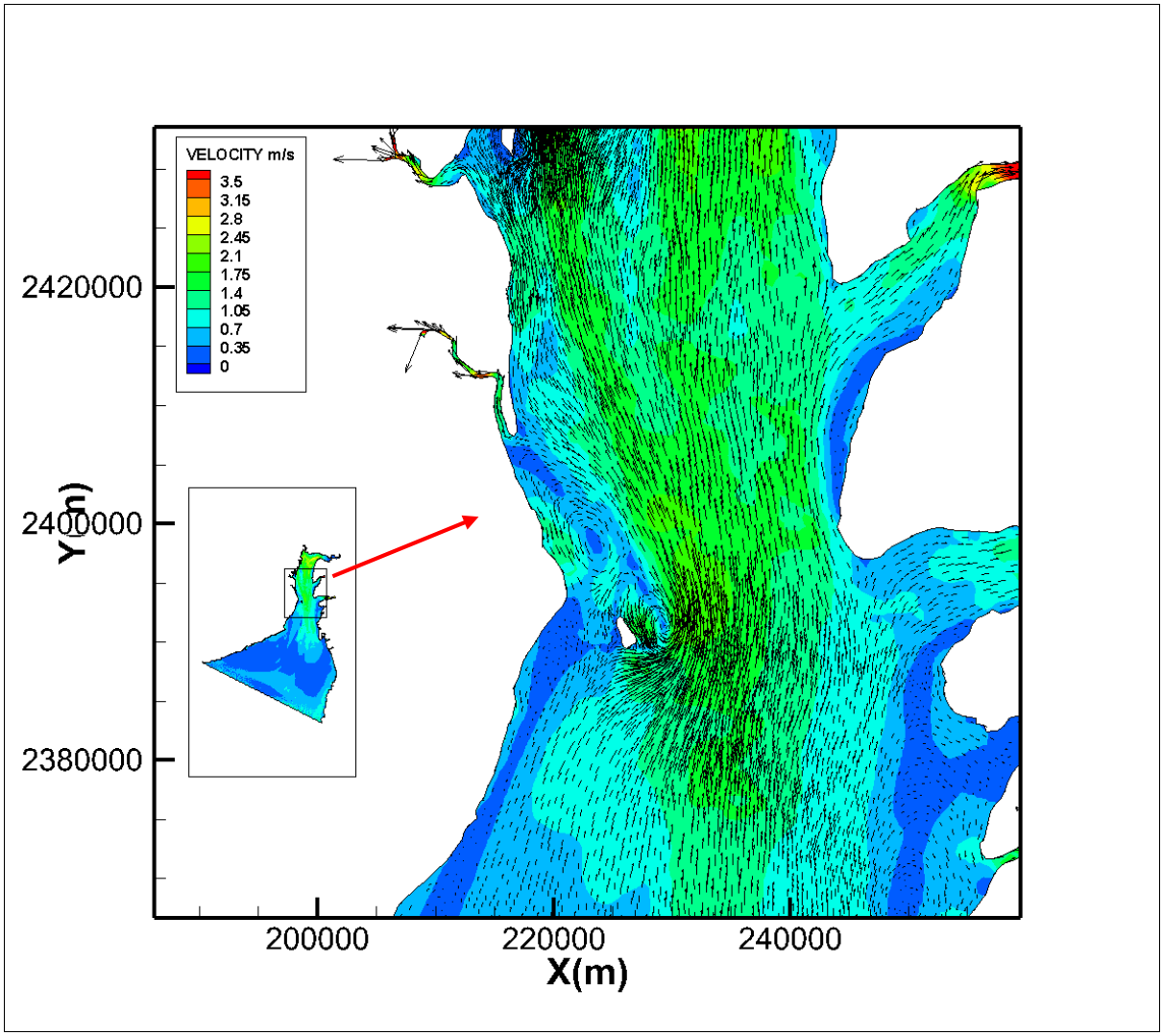

Figure C9: Velocity vectors and contour plots during High tide time at 3.1 hours in Case I

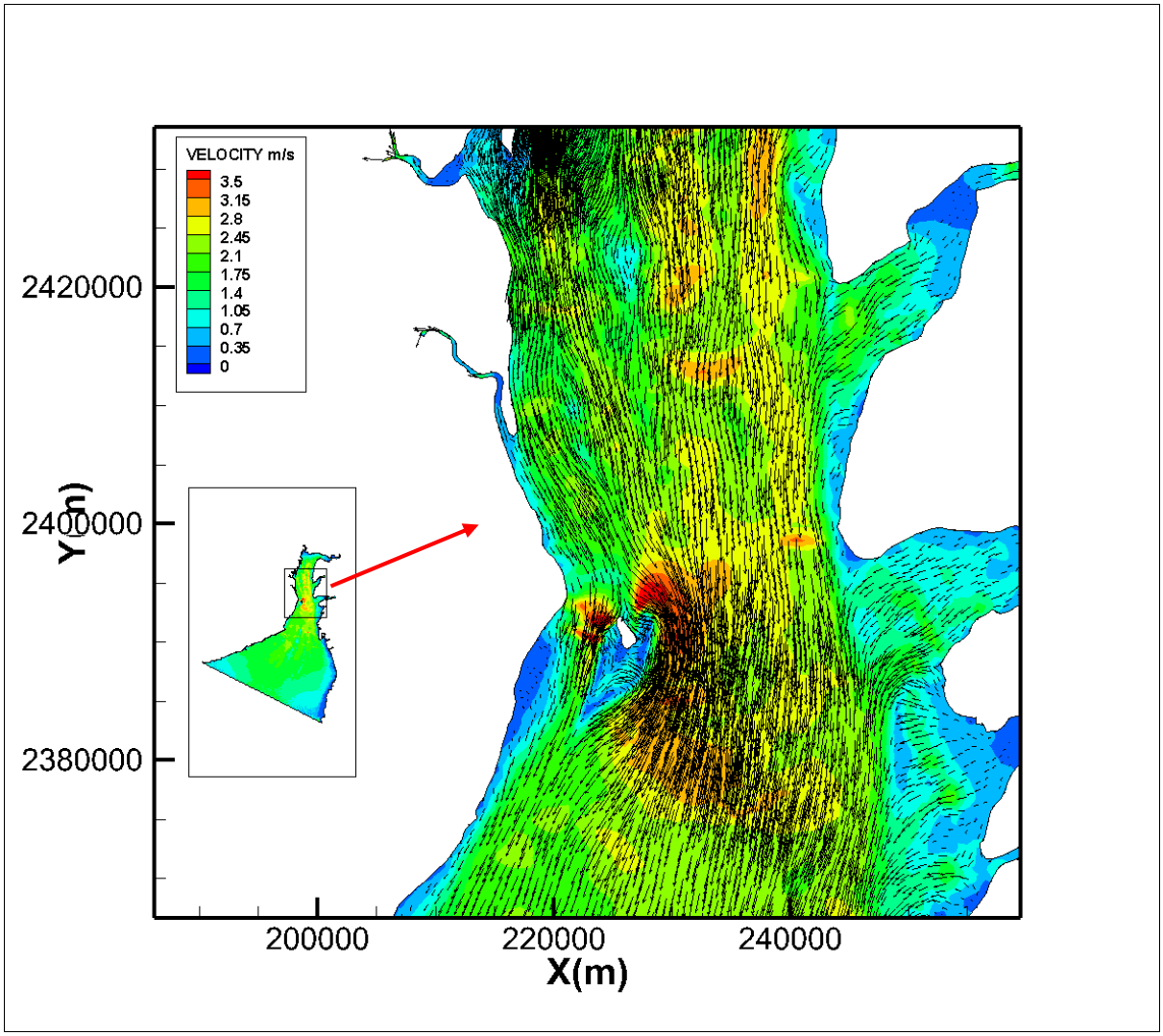

Figure C10: Velocity vectors and contour plots during Ebbing time at 6.2 hours in Case I

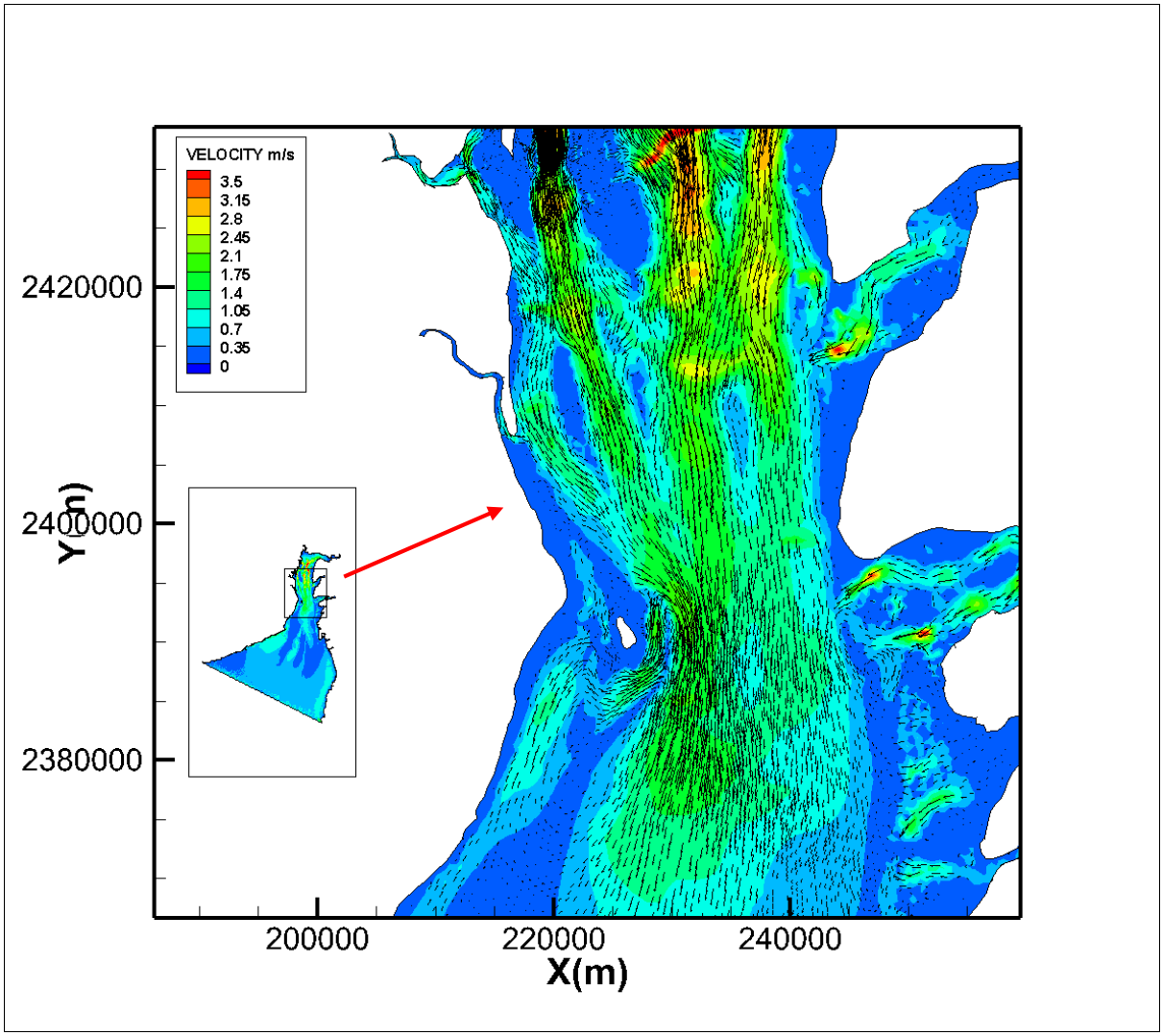

Figure C11: Velocity vectors and contour plots during low tide at 9.3 hours for Case I

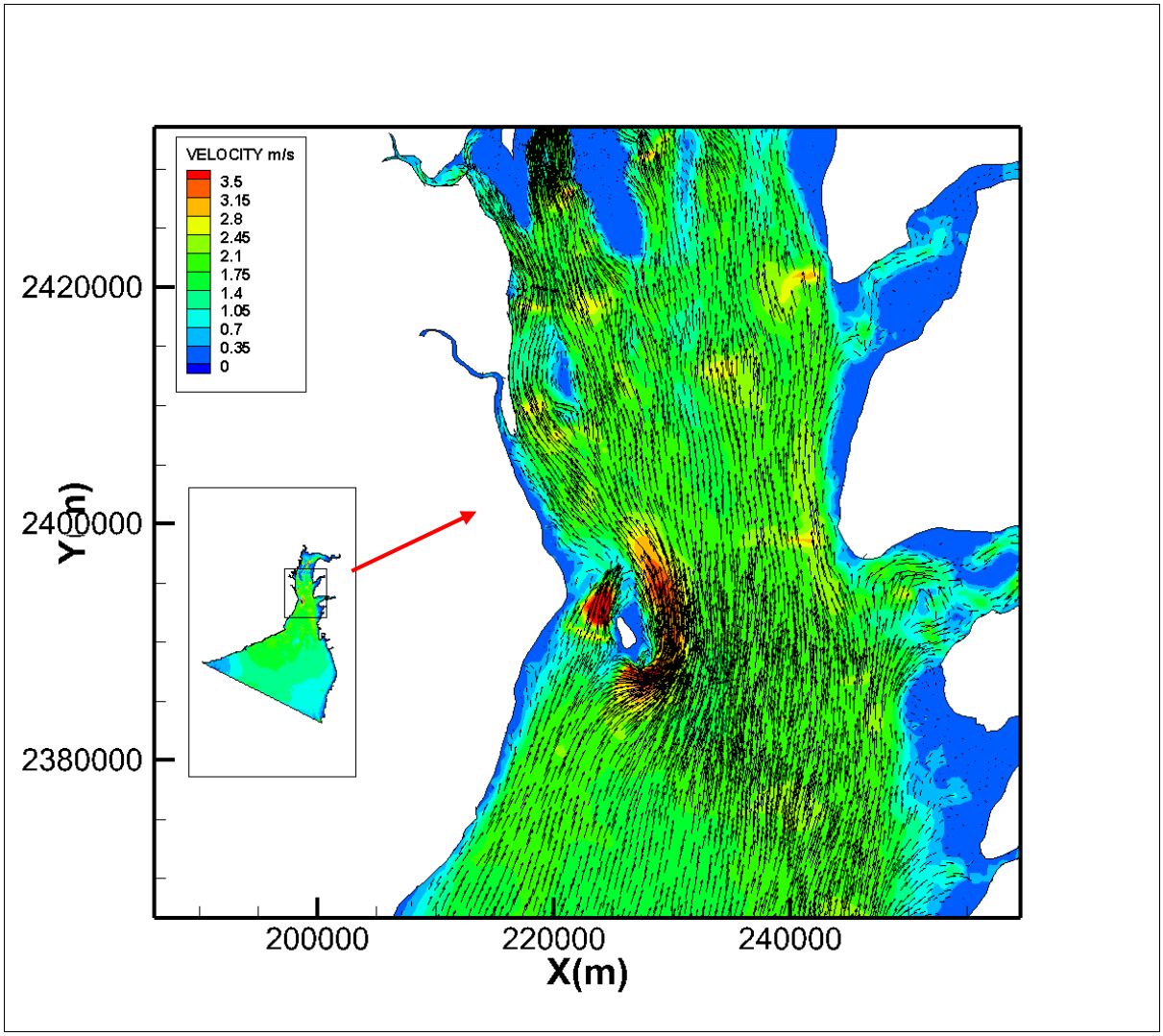

Figure C12: Velocity vectors and contour plots during flooding time at 12.4 hours for Case I

1.15.2.3 Hydrodynamic Study for With dam Condition (Case II)

Flooding

The flow patterns during flooding condition in the domain is shown in **Figure C13** and **Figure C14**. The figures show a typical flow situation during the rising tide (at about 0 hr.) from which, the magnitudes of current at various locations in the study area can be deduced. The flooding phase of the tide is characterized with flow in the north-east. The tide will be entering the bay from the south direction and leaving back during ebbing tide. During the time of flooding, the current is observed more near the river mouth. Considering the study area, the current speed in the order of 0.3-2.4 m/s is observed in the domain. The velocity of the current near the dam is 0.3-0.5 m/s. The proposed dam will act as a wall which eliminate some circulation. The current speed of

1 -1.5 m/s is observed in the offshore areas. According to the orientation of coast, current speed varies such as sheltered places are devoid of currents. Eddy formation is observed in the area south to proposed dam near the island. The above currents are disappearing during the high tide event in the study area as shown in **Figure C15**.

Ebbing

The flow patterns during ebbing condition near the project site shown in **Figure C16**. The figure shows a typical flow situation during the falling tide (at about 6.2 hr.) from which, the magnitudes of current at various locations in the study area can be deduced. During the ebbing phase of the tide, which is followed by the occurrence of high tide, the tide starts to recede and reversal of flow start to occur towards back into open sea. During ebbing, the maximum current speed of 0.3 -1.2 m/s is observed in the offshore areas. Near the dam the current velocity is in the range of 0.3-0.6 m/s. Generally, the coast is observed to experience low circulation dynamics during low tide especially at the proposed dam area. The flooding of water into the domain from offshore region follows the low tide which is observed in **Figure C17**.

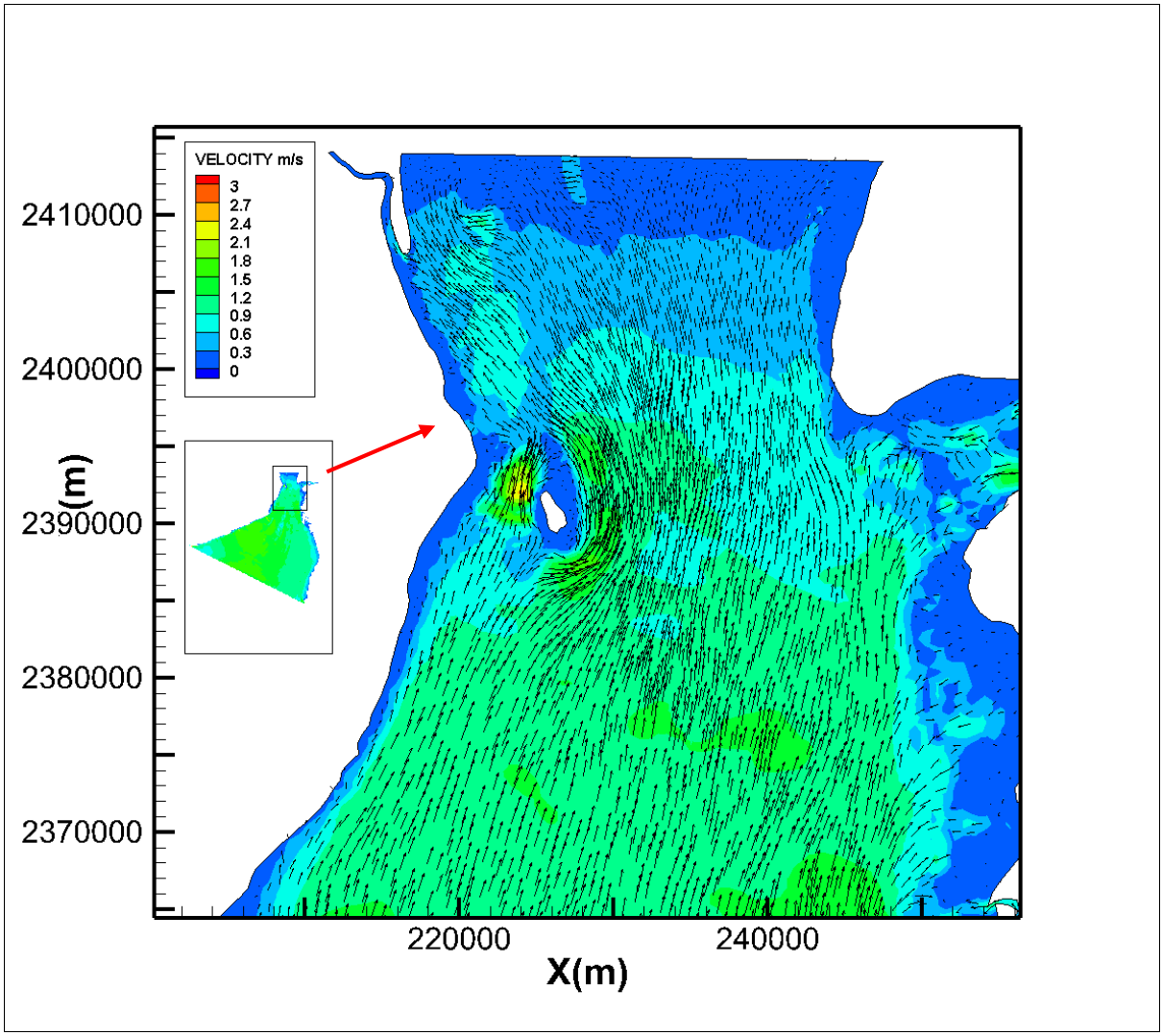

Figure C13: Velocity vectors and contour plots during flooding time at 0.0 hours for Case II

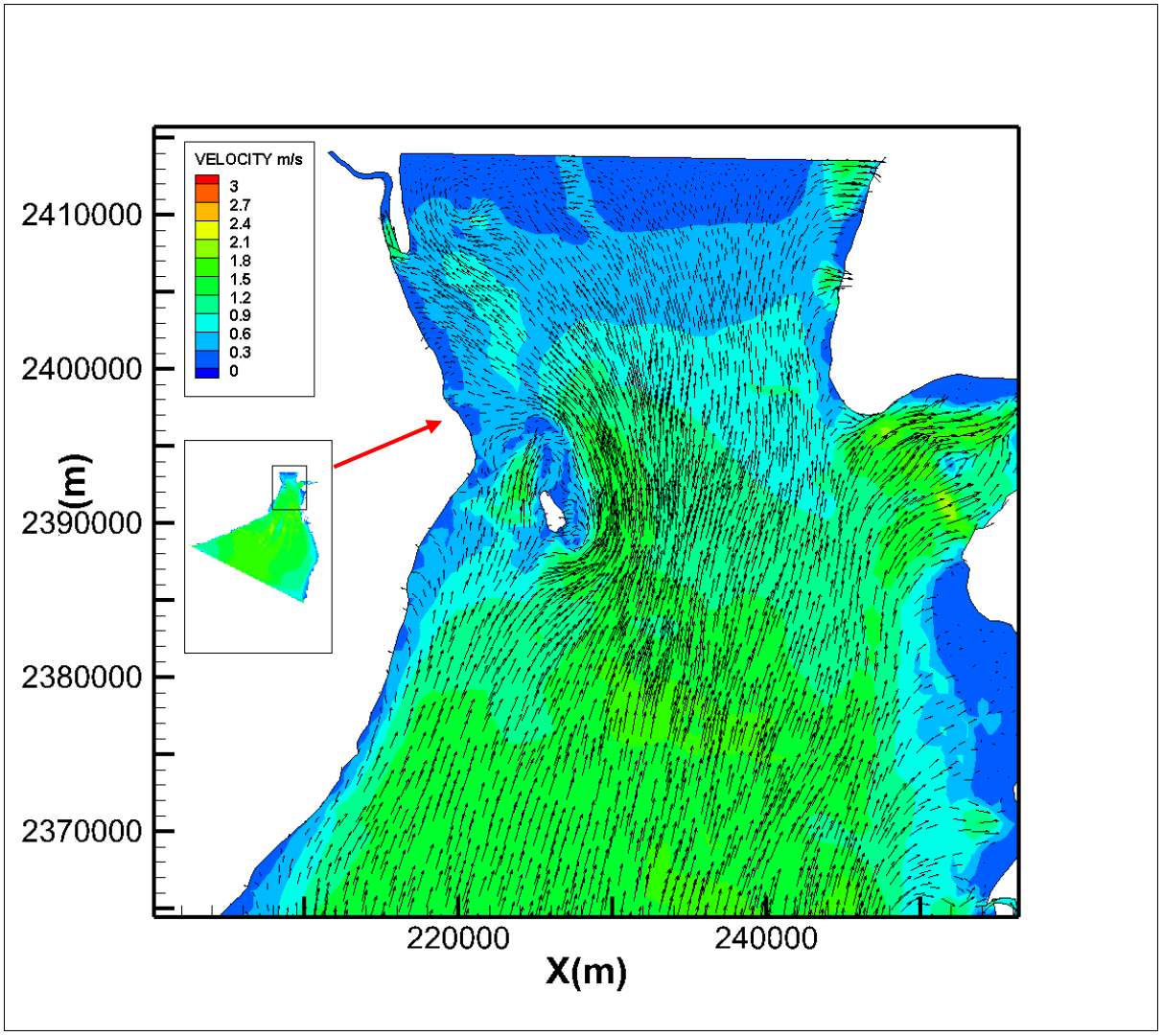

Figure C14: Velocity vectors and contour plots during flooding time at 1.5 hours for Case II

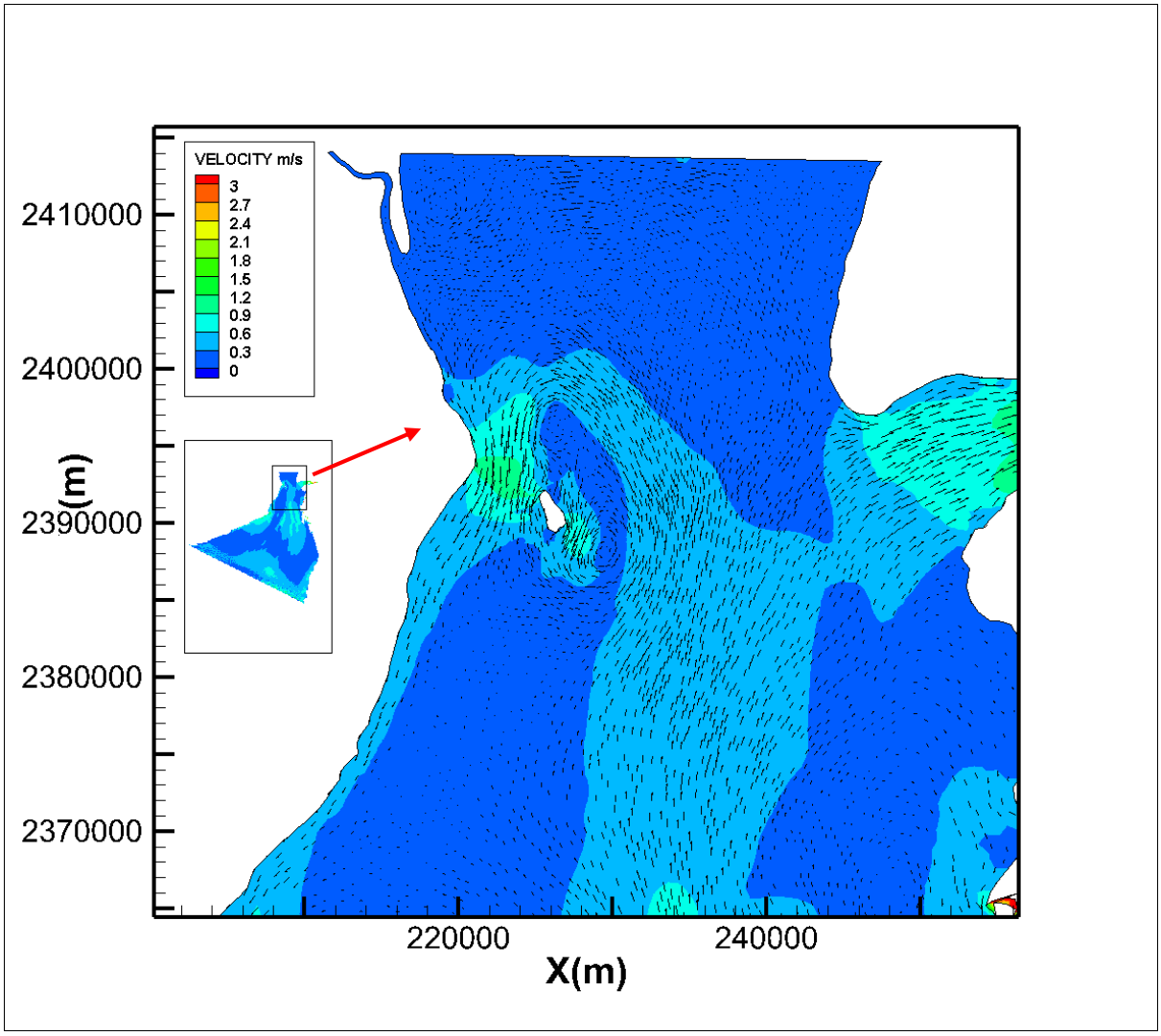

Figure C15: Velocity vectors and contour plots during high tide at 3.1 hours for Case II

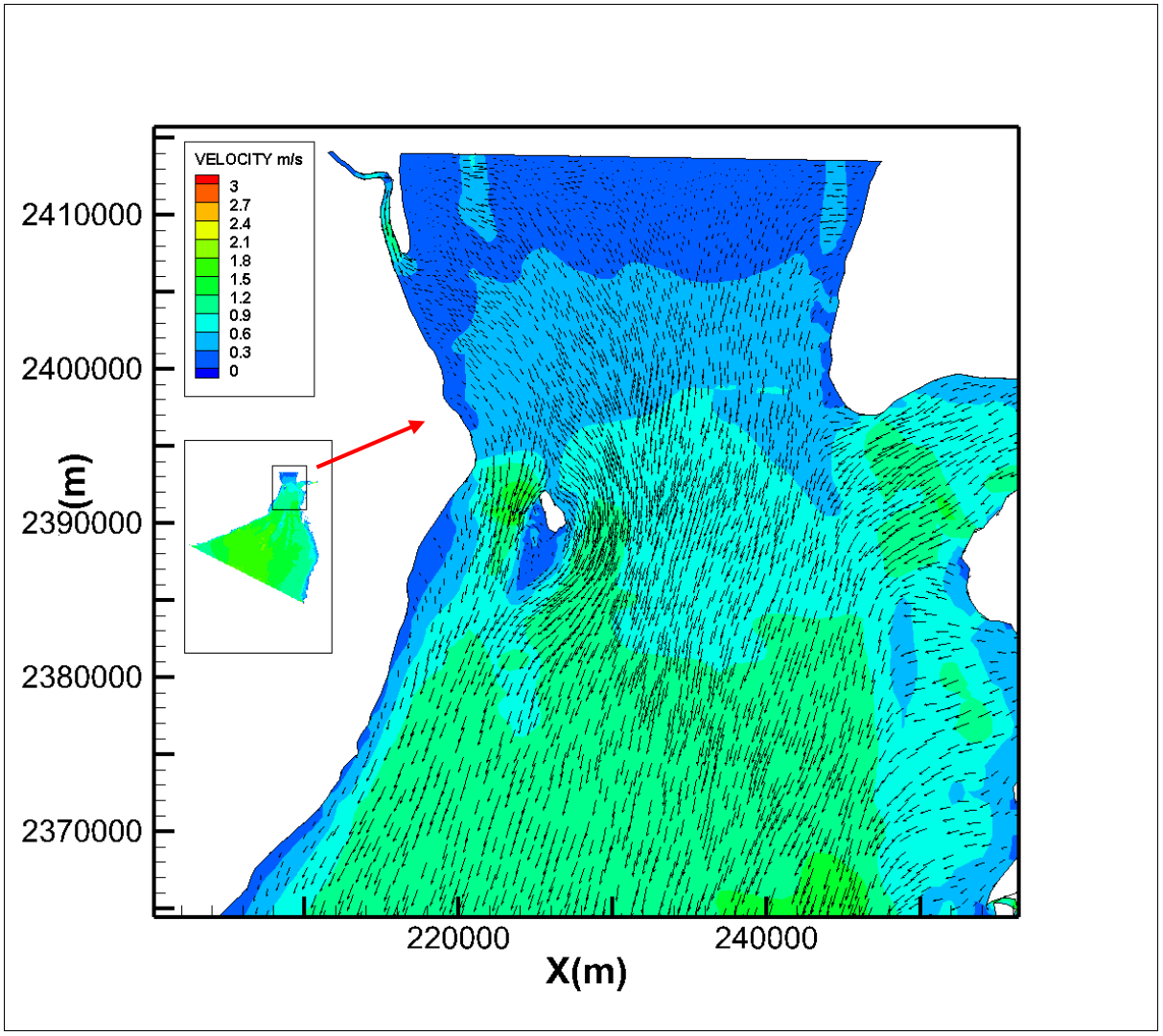

Figure C16: Velocity vectors and contour plots during ebbing time at 6.2 hours for Case II

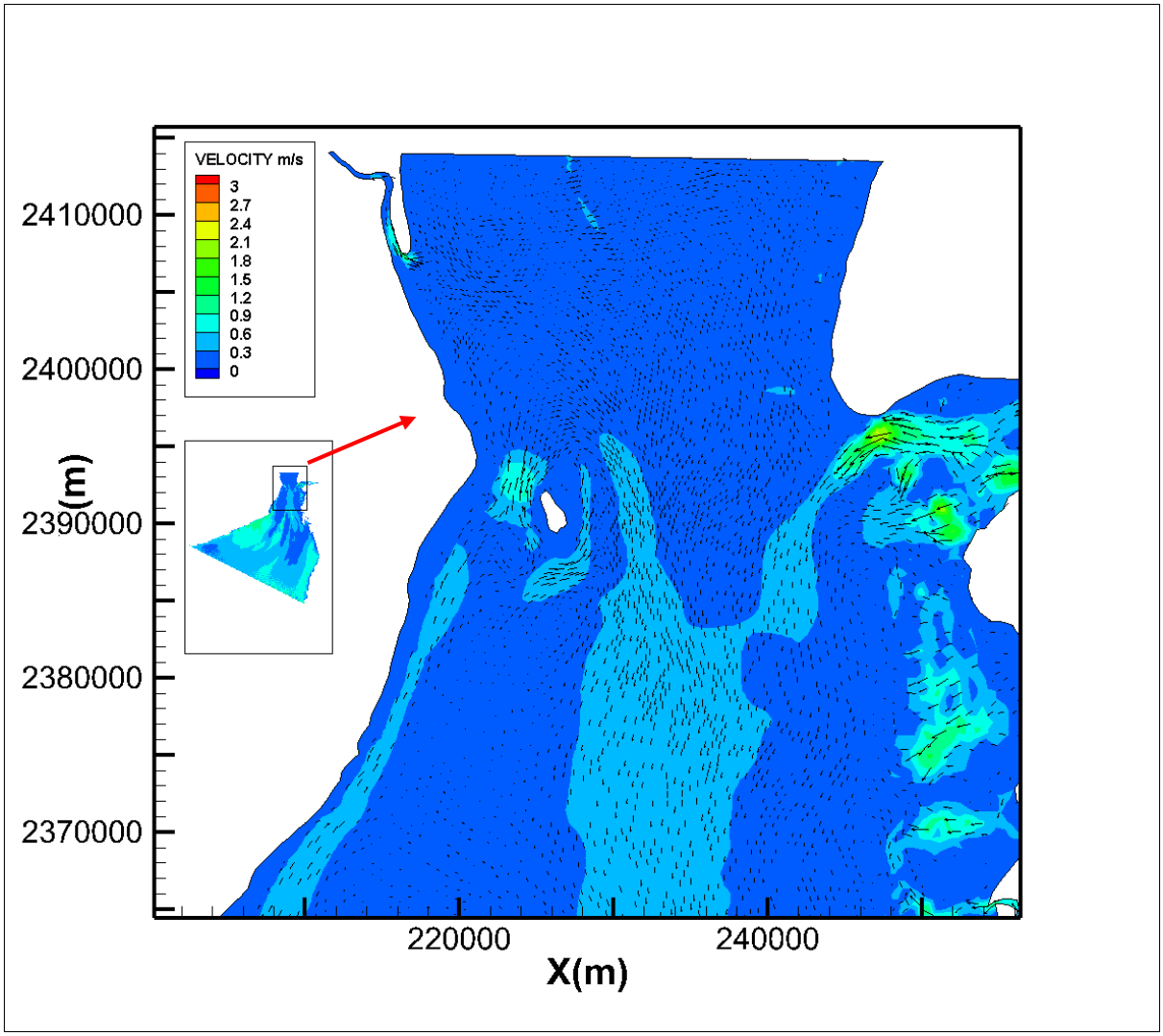

Figure C17: Velocity vectors and contour plots during low tide at 9.3 hours for Case II

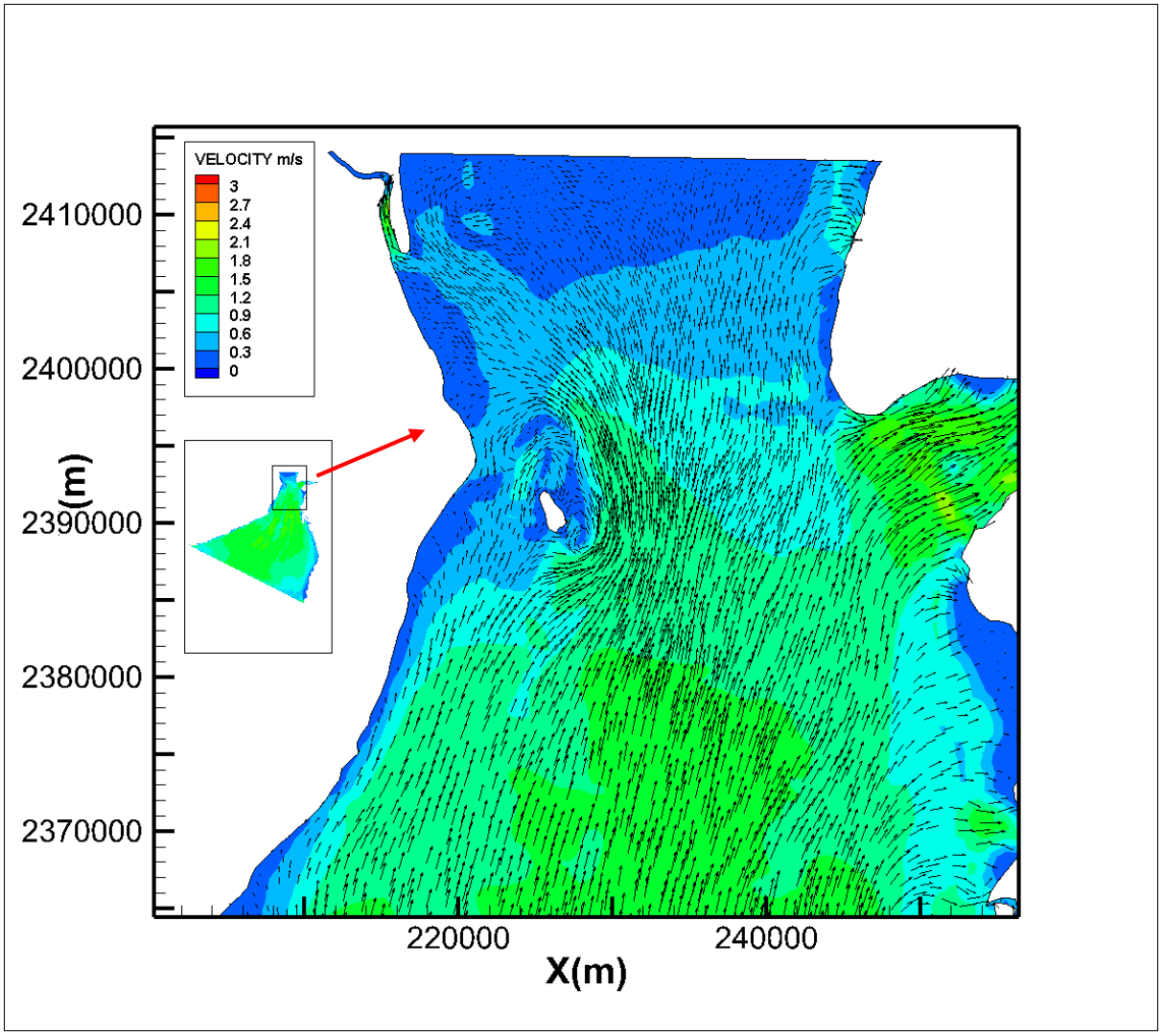

Figure C18: Velocity vectors and contour plots during flooding time at 12.4 hours for Case II

1.15.2.4 Hydrodynamic study in extreme event case for without dam condition (Case I)

Flooding

The flow patterns during flooding condition in the domain is shown in **Figure C19** and **Figure C20**. The figures show a typical flow situation during the rising tide (at about 0 hr.) from which, the magnitudes of current at various locations in the study area can be deduced. The flooding phase of the tide is characterized with flow in the north-east. The tide will be entering the bay from the south direction and leaving back during ebbing tide. During the time of flooding, the current is observed more near the river mouth. Some eddy formation can be seen near the island. Considering the study area, the current speed in the order of 0.3-3 m/s is observed in the domain. The current speed of 2.8 -3.15 m/s is observed near the island .In the south side of the proposed dam the current have a range of 1.4-2.8 m/s according to the orientation of coast, current speed varies such as sheltered places are devoid of currents. The above currents are disappearing during the high tide event in the study area as shown in **Figure C21**.

Ebbing

The flow patterns during ebbing condition near the project site shown in **Figure C22**. The figure shows a typical flow situation during the falling tide (at about 6.2 hr.) from which, the magnitudes of current at various locations in the study area can be deduced. Presence of eddy current can be seen in the southern side of the island. During the ebbing phase of the tide, which is followed by the occurrence of high tide, the tide starts to recede and reversal of flow start to occur towards back into open sea. During ebbing, the maximum current speed of 0.3 -2.8 m/s is observed in the domain. The southern side of the dam experience the velocity in the range of 1.4-2.8 m/s. Generally, the coast is observed to experience low circulation dynamics during low tide especially at the proposed dam area. The flooding of water into the domain from offshore region follows the low tide which is observed in **Figure 23**.

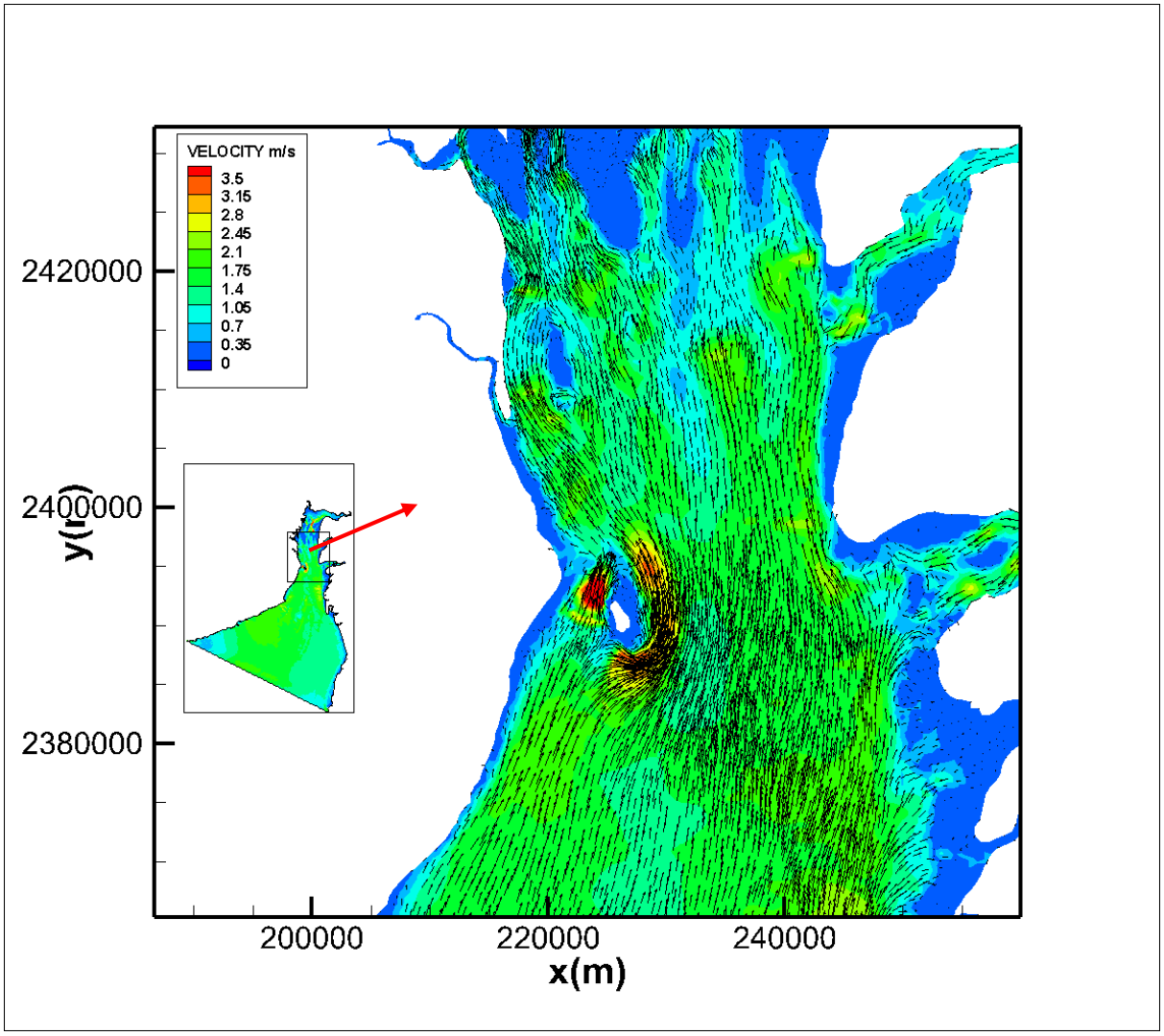

Figure C19: Velocity vectors and contour plots during flooding time at 0 hours for Case I

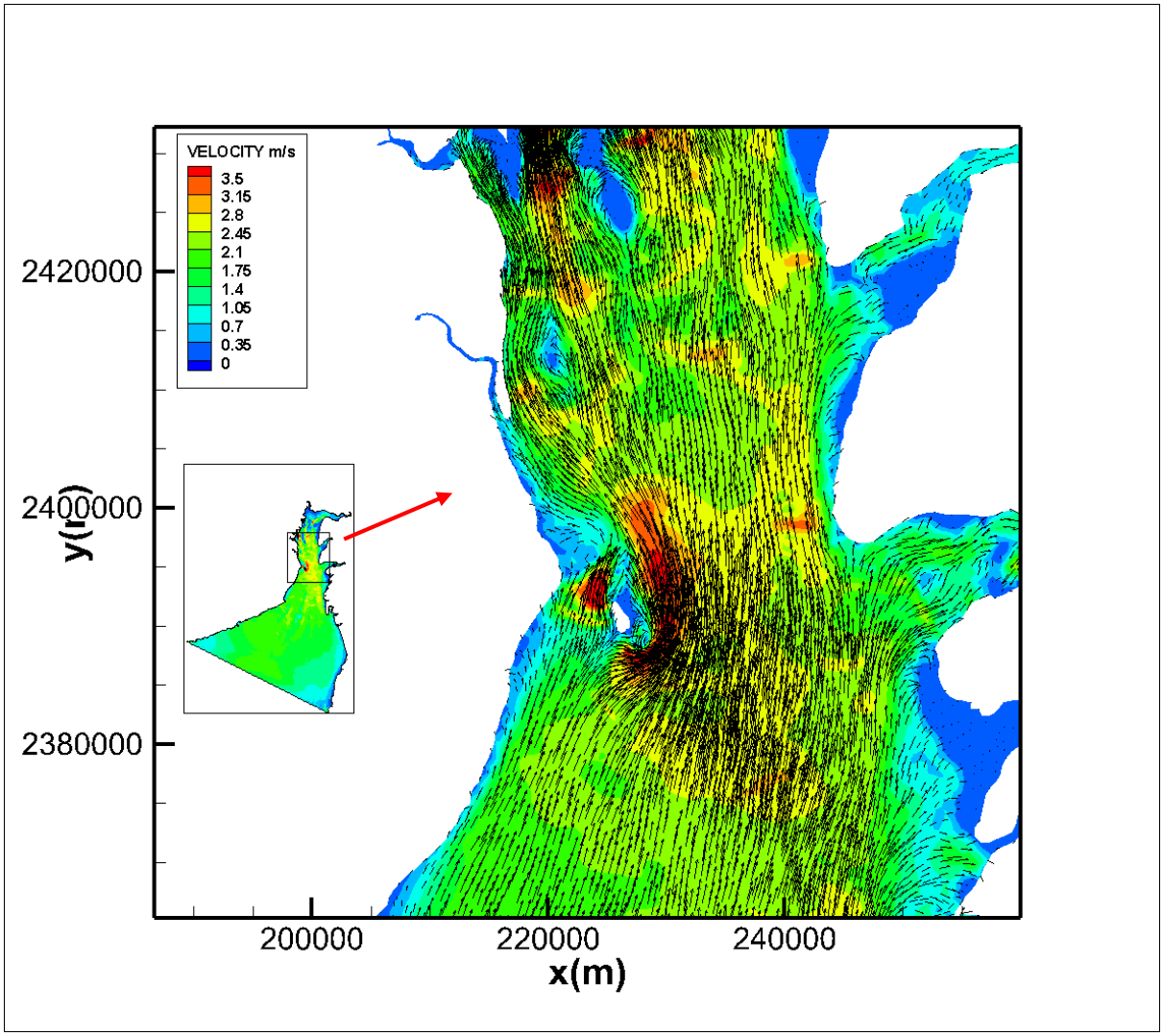

Figure C20: Velocity vectors and contour plots during flooding time at 1.5 hours for Case I

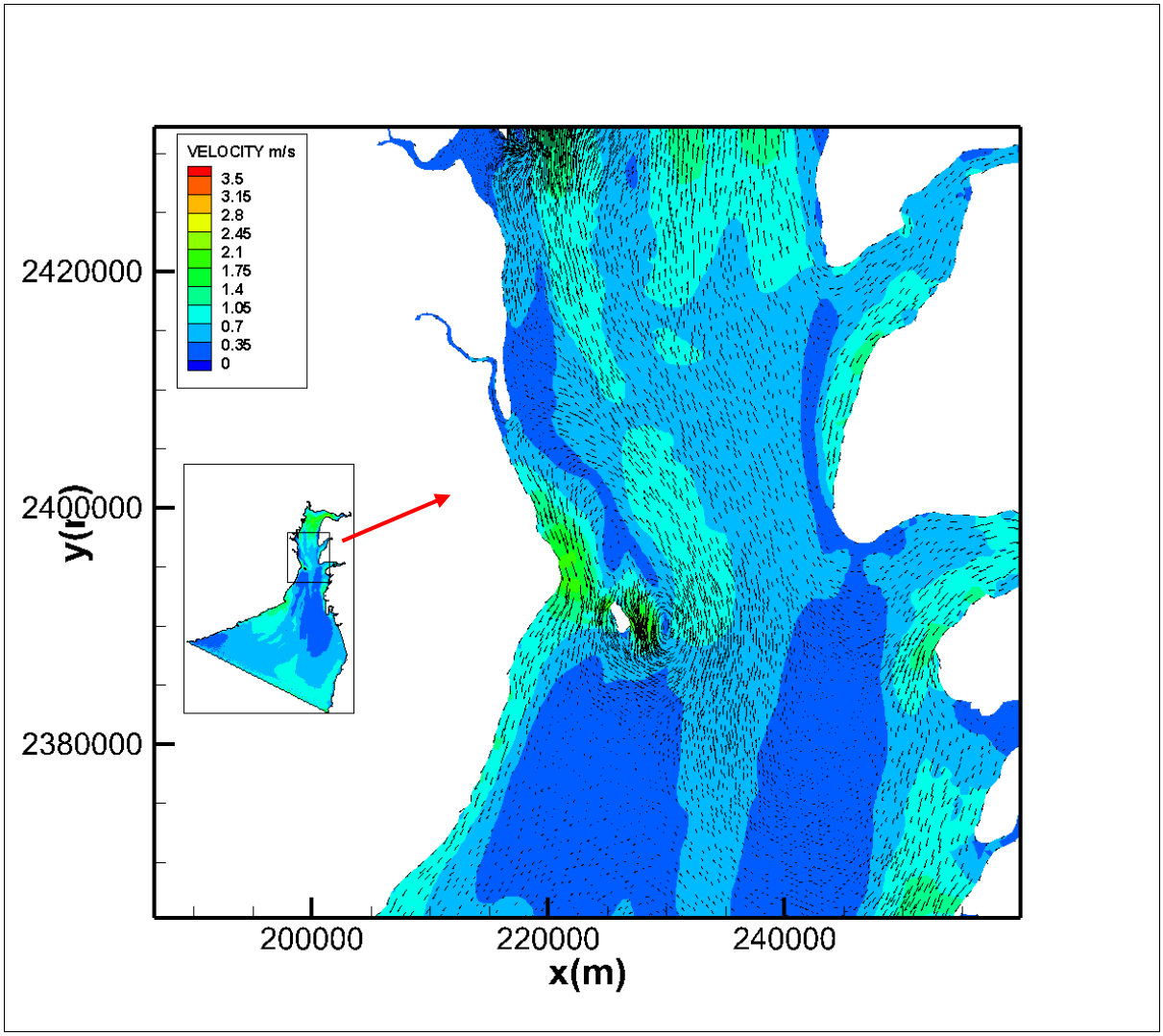

Figure C21: Velocity vectors and contour plots during High tide time at 3.1hours for Case I

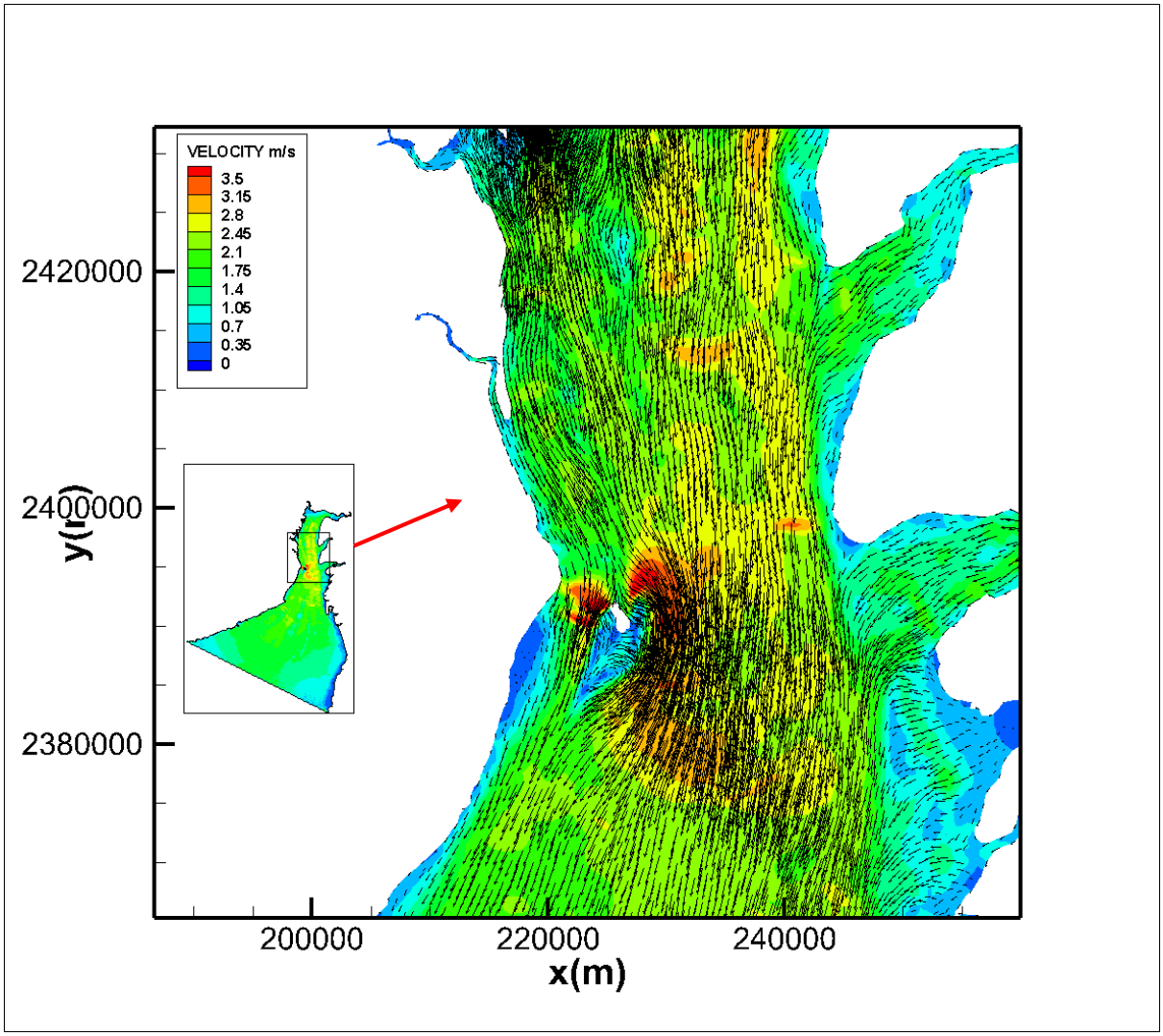

Figure C22: Velocity vectors and contour plots during Ebbing time at 6.2 hours for Case I

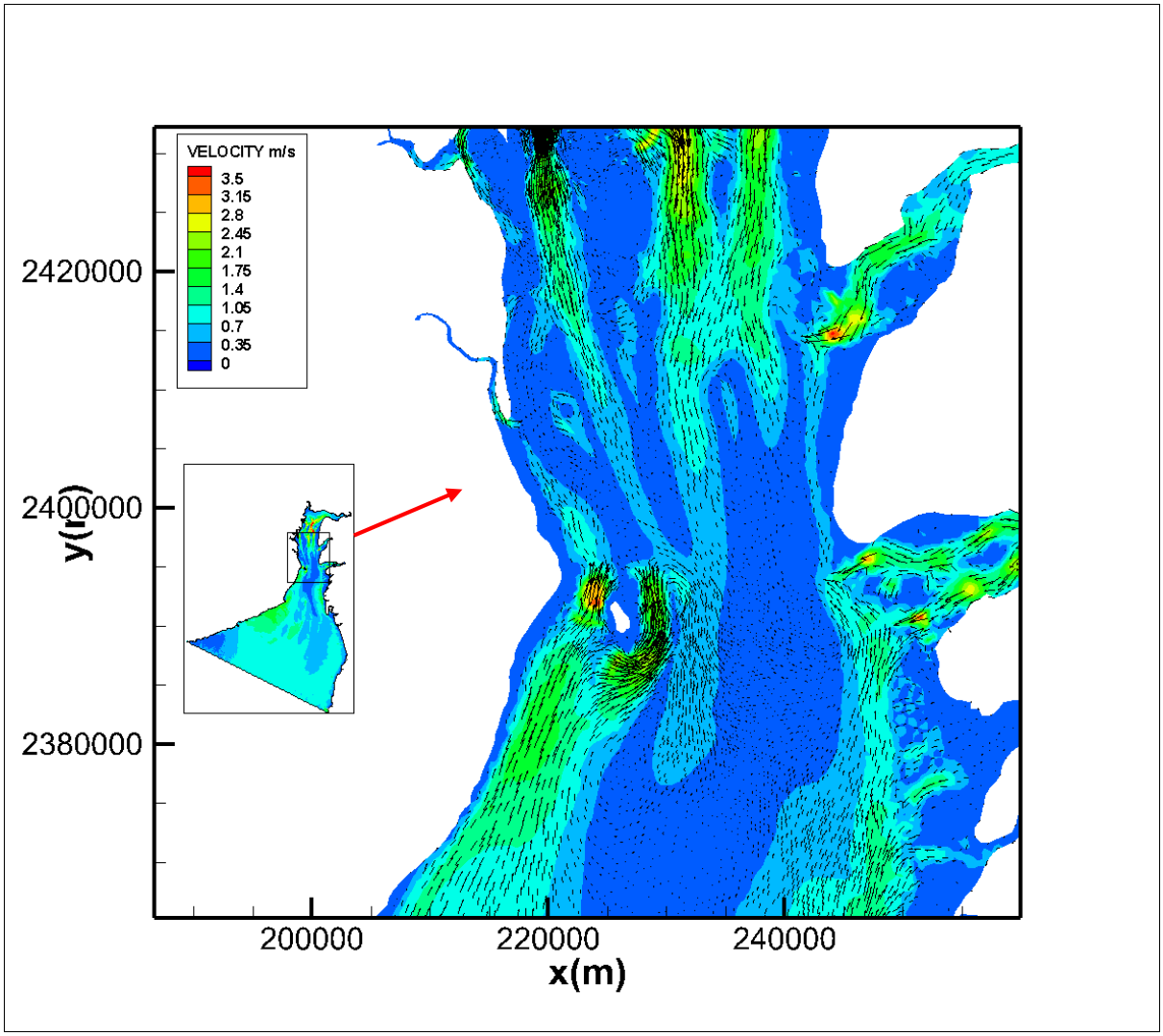

Figure C23: Velocity vectors and contour plots during Low tide time at 9.3 hours for Case I

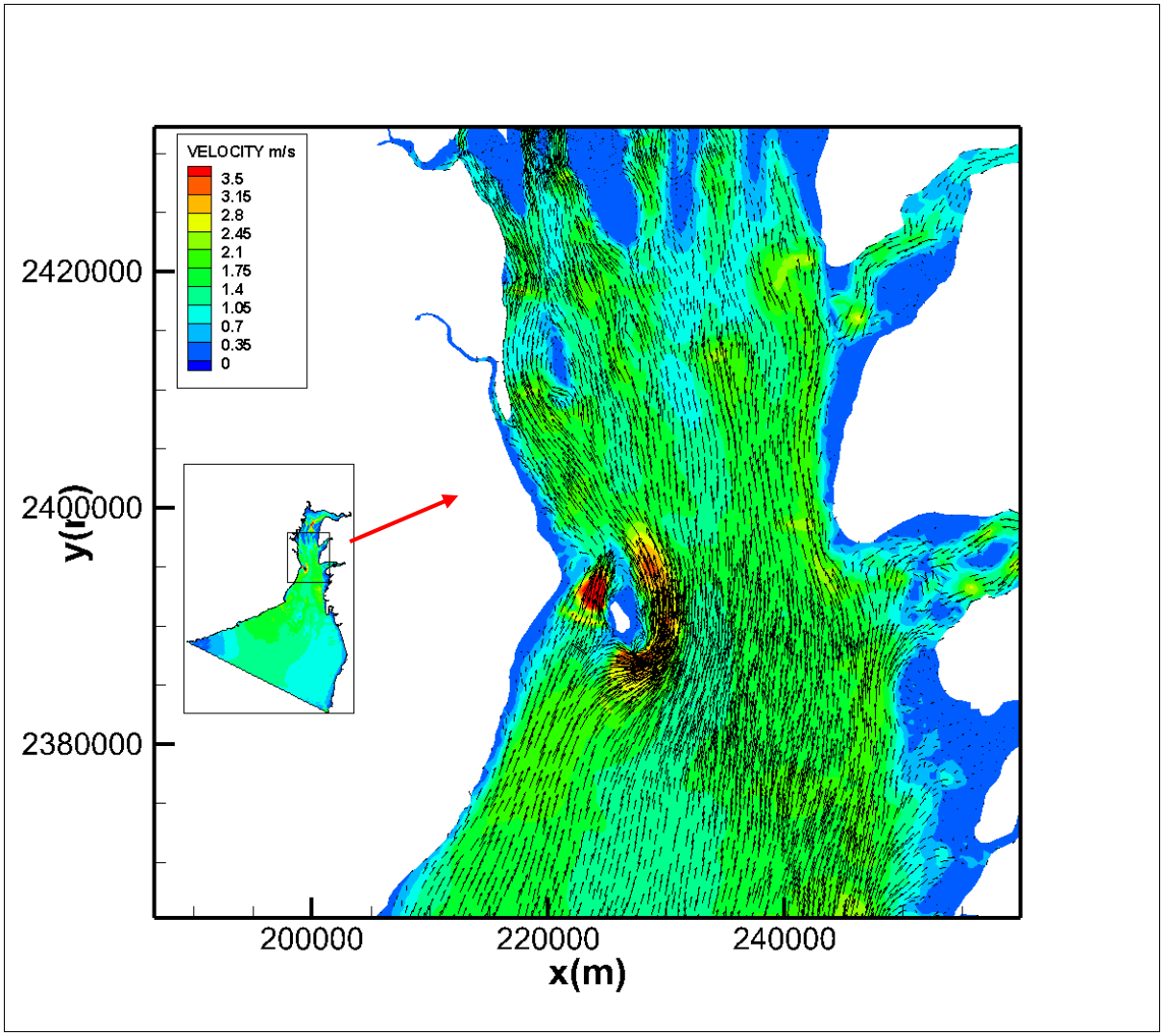

Figure C24: Velocity vectors and contour plots during flooding time at 12.4 hours for Case I

1.15.2.5 Hydrodynamic study for extreme event case for with dam condition (Case II)

Flooding

The flow patterns during flooding condition in the domain is shown in **Figure C25 and Figure C26**. The figures show a typical flow situation during the rising tide (at about 0 hr.) from which, the magnitudes of current at various locations in the study area can be deduced. The flooding phase of the tide is characterized with flow in the north-east. The tide will be entering the bay from the south direction and leaving back during ebbing tide. During the time of flooding, the current is observed more near the river mouth. Considering the study area, the current speed in the order of 0.3-2.1 m/s is observed in the domain. The current speed of 1.2 -2.5 m/s is observed near the island .In the south side of the proposed dam the current have a range of 0.9-1.5 m/s according

to the orientation of coast, current speed varies such as sheltered places are devoid of currents. The less velocity of the current is due to the presence of the dam in the domain which blocks the flushing from the north side of the dam. The above currents are disappearing during the high tide event in the study area as shown in **Figure C27**.

Ebbing

The flow patterns during ebbing condition near the project site shown in **Figure C28**. The figure shows a typical flow situation during the falling tide (at about 6.2 hr.) from which, the magnitudes of current at various locations in the study area can be deduced. Presence of eddy current can be seen in the southern side of the island. During the ebbing phase of the tide, which is followed by the occurrence of high tide, the tide starts to recede and reversal of flow start to occur towards back into open sea. During ebbing, the maximum current speed of 0.3 -2.1 m/s is observed in the domain. The southern side of the dam experience the velocity in the range of 0.3-0.9 m/s. Generally, the coast is observed to experience low circulation dynamics during low tide especially at the proposed dam area. The flooding of water into the domain from offshore region follows the low tide which is observed in **Figure C29**.

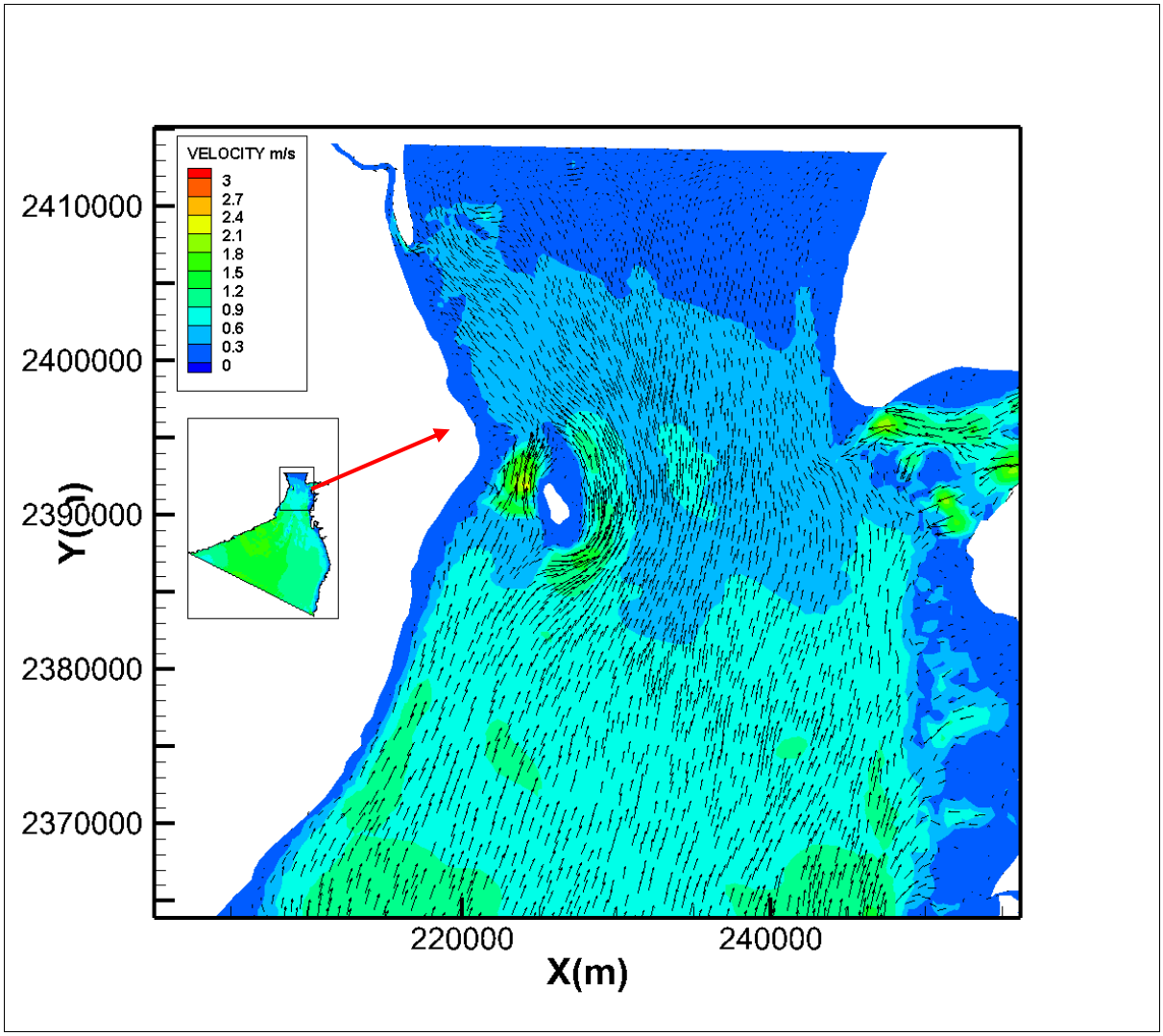

Figure C25: Velocity vectors and contour plots during flooding time at 0 hours for Case II

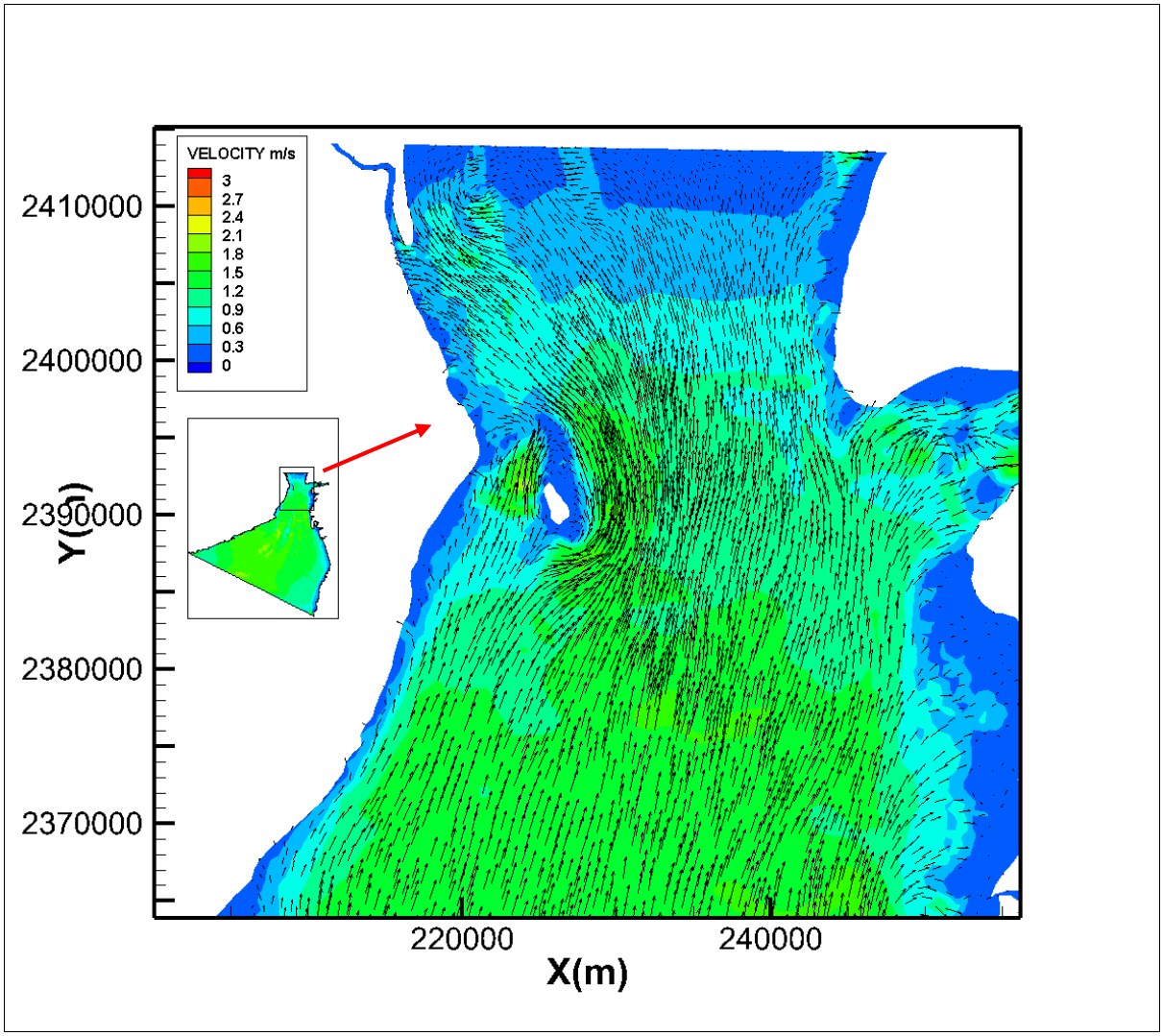

Figure C26: Velocity vectors and contour plots during flooding time at 1.5 hours for Case II

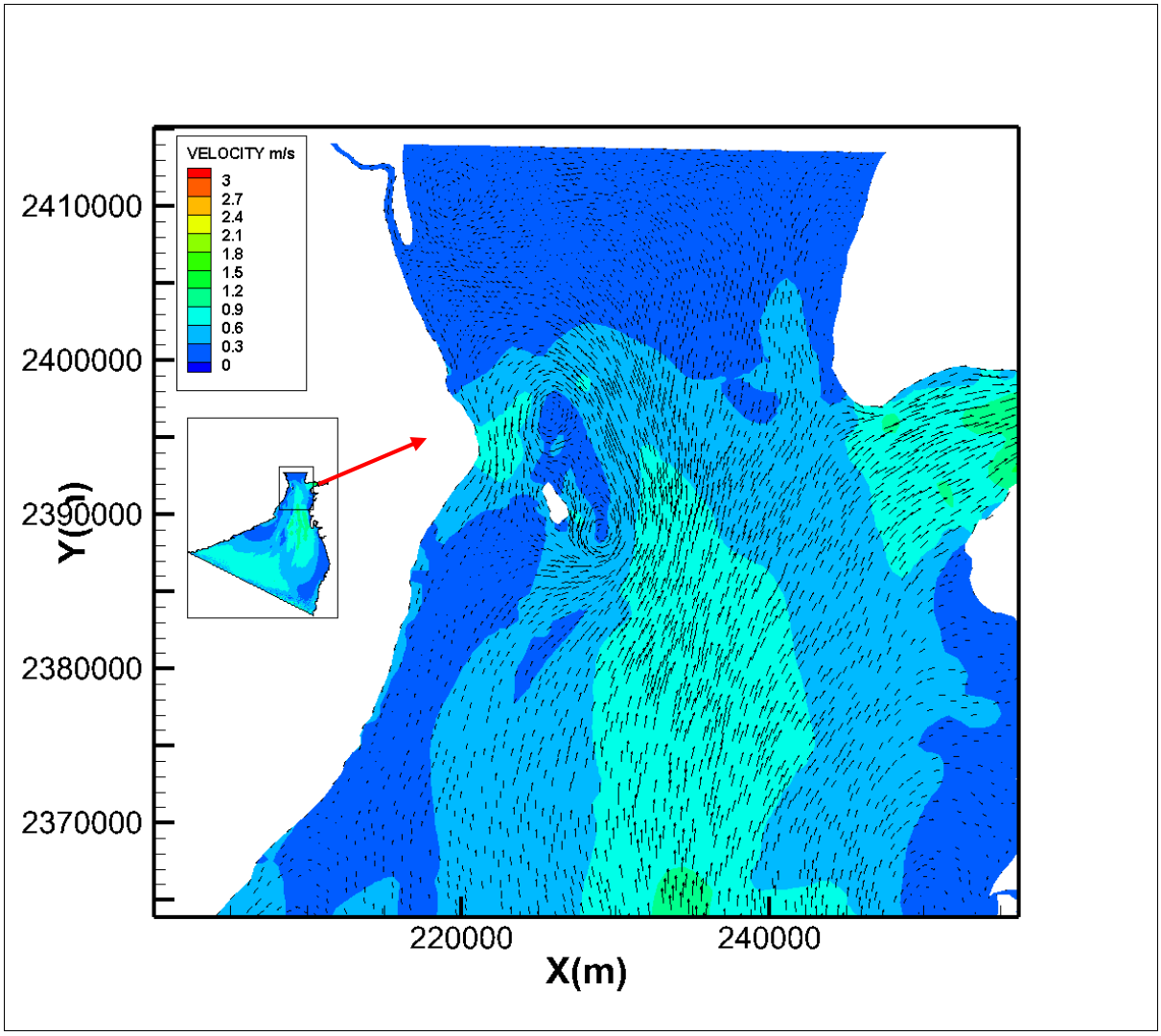

Figure C27: Velocity vectors and contour plots during High tide time at 3.1 hours for Case II

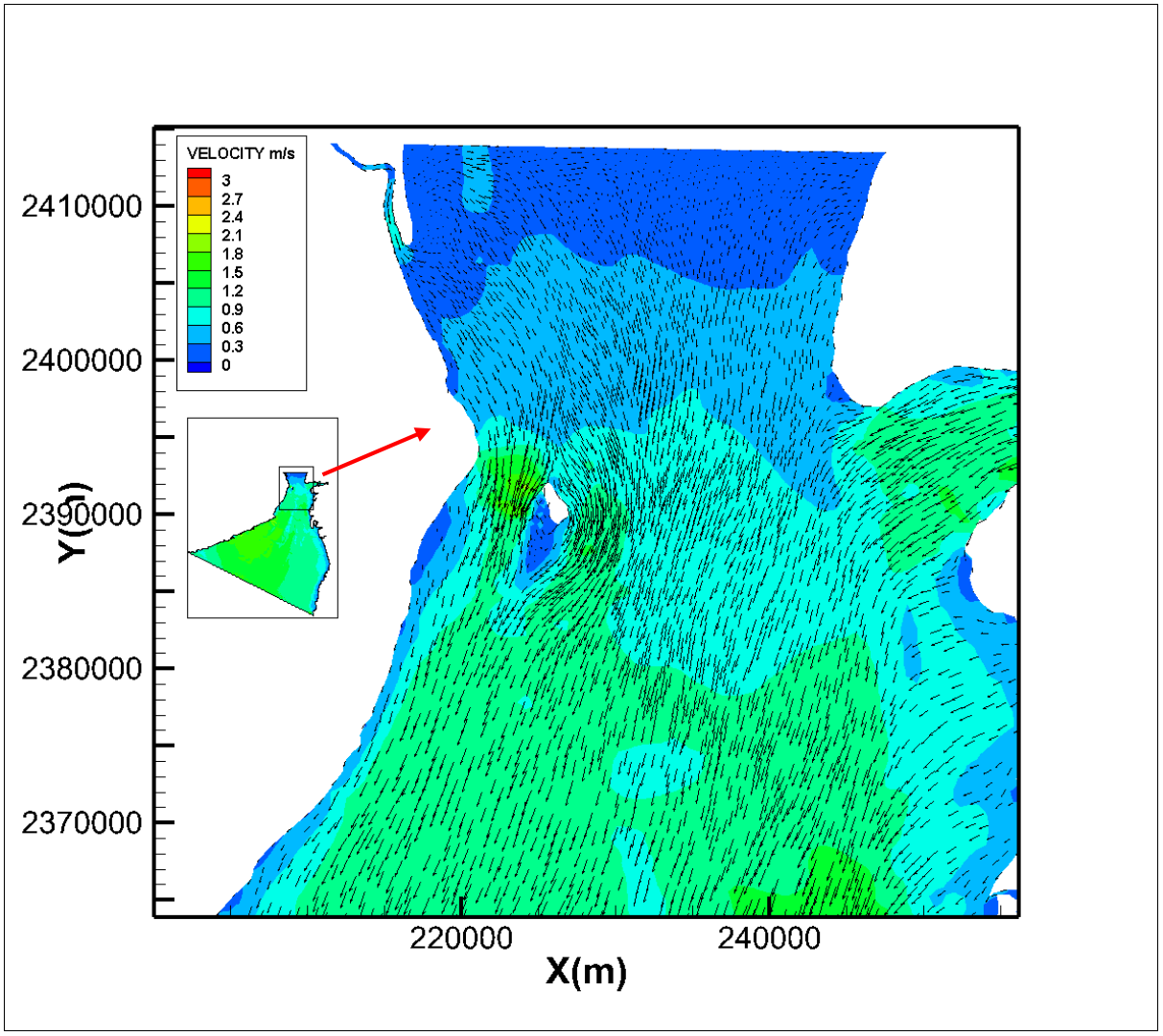

Figure C28: Velocity vectors and contour plots during Ebbing time at 6.2 hours for Case II

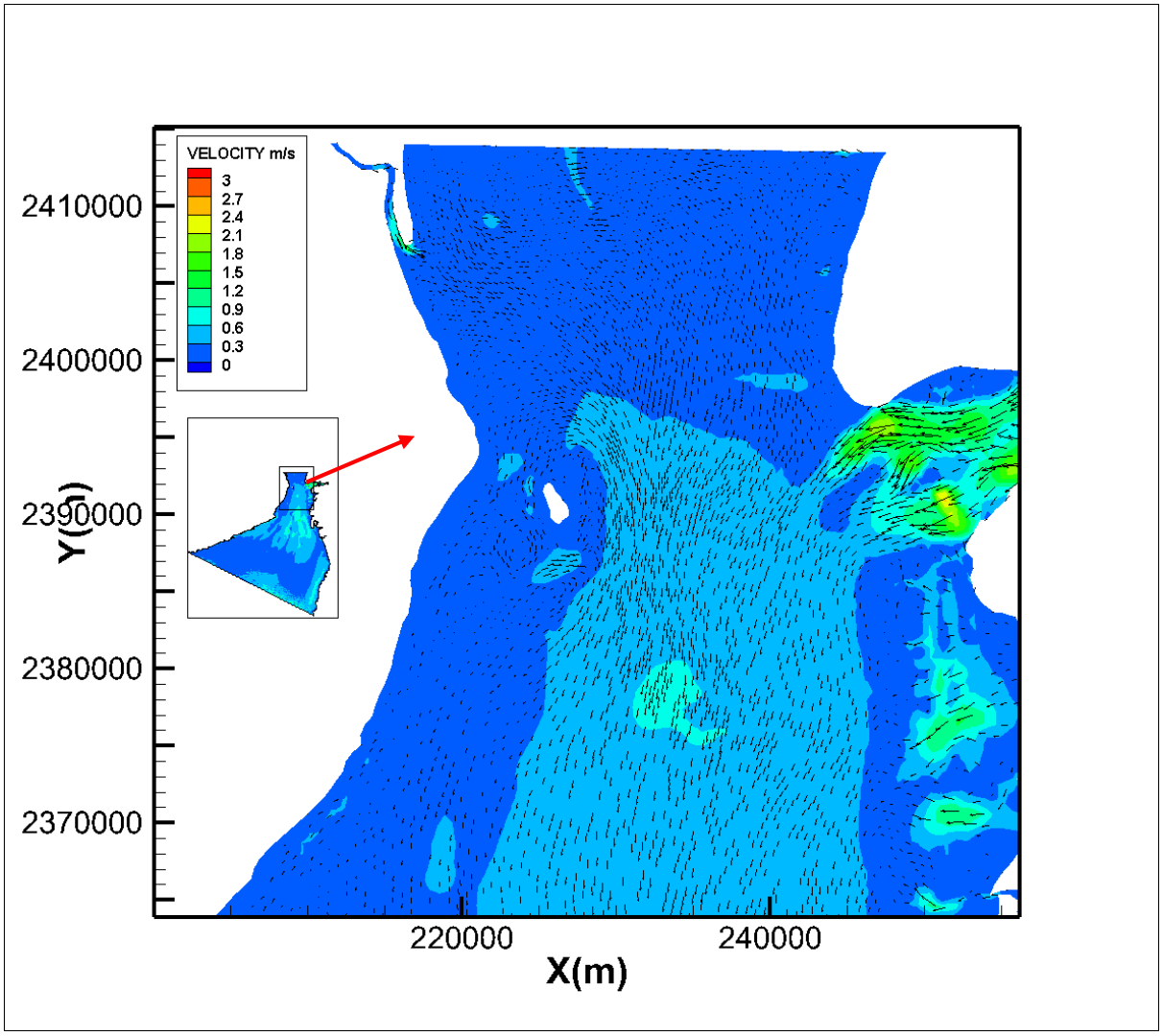

Figure C29: Velocity vectors and contour plots during Low tide time at 9.3 hours for Case II

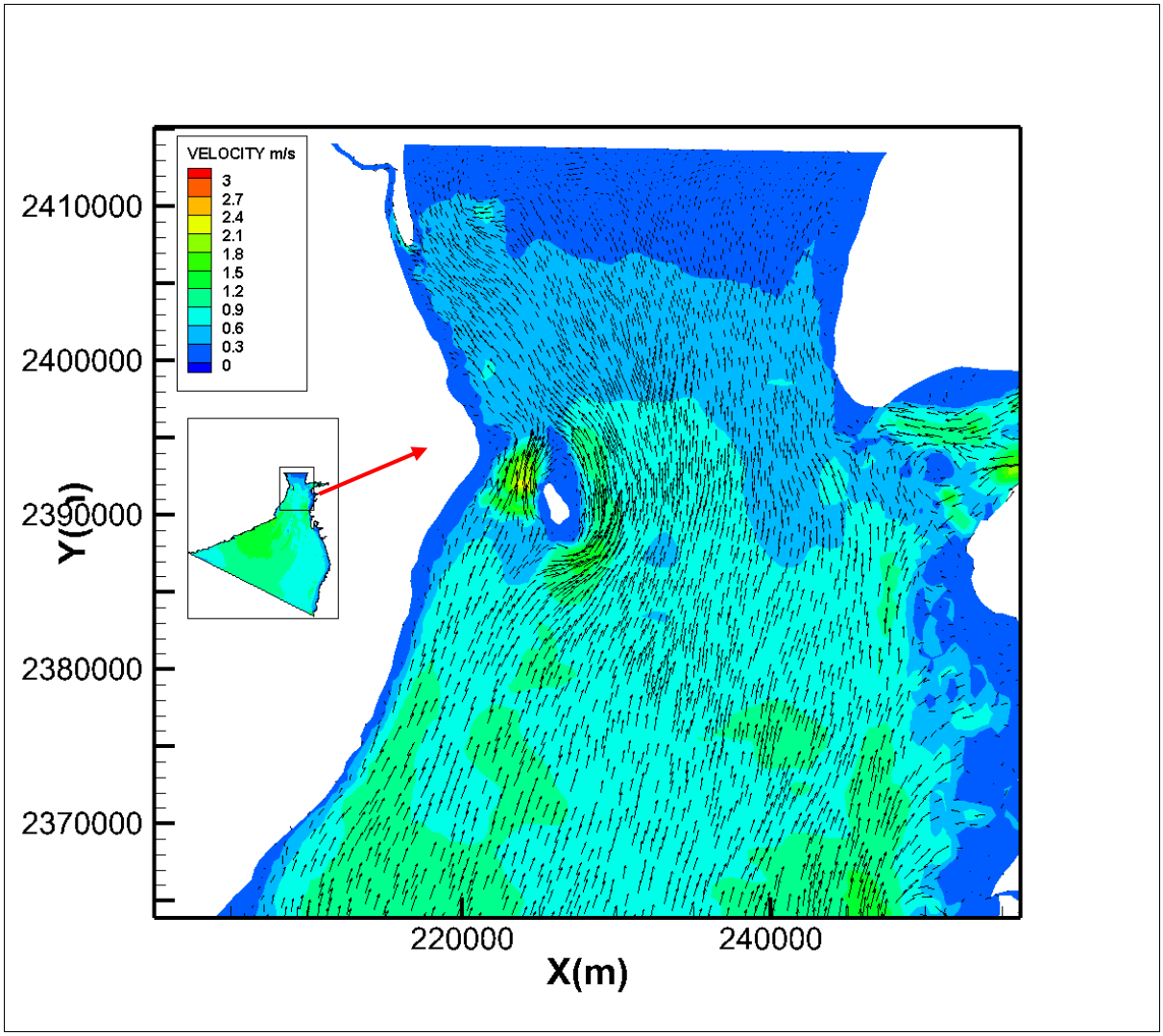

Figure C30: Velocity vectors and contour plots during flooding time at 12.4 hours for Case II

1.16 Morphodynamic Modeling

1.16.1 General

The present study is focused on analysing the circulation features and its effect on morphodynamic changes in the proposed dam area. Numerical models are used to predict the bed level change based on the hydrodynamics. The average mesh size is found to be about 130-250 m which is very fine around the region of interest. The mesh is coarser near the offshore boundaries where the water depths are greater. A typical mesh of with dam and without dam condition that will be used to discretize the domain is shown earlier. Detailed numerical modelling studies have been carried out to investigate the hydrodynamics of tides as explained in the previous section. With flow pattern and current velocity, the sediment transport model is simulated and the silt that gets settled in patches all over the domain is modelled.

1.16.2 Seasonal Morphodynamic Analysis

The research area's siltation rate is calculated throughout the year for three different seasons: pre-monsoon, monsoon, and post-monsoon. The effect of changing wind patterns and tidal circulations affects circulation in the research area, resulting in morphodynamic differences across seasons. Because the region is governed by tidal currents, the siltation pattern is dominated by them. As a result, throughout the year, a similar trend of bed level fluctuation was observed. For **Case I** and **Case II**, the magnitude of siltation rate is observed to be slightly high in the monsoon season compared to all other seasons.

In **Case I**, the siltation predicted during pre-monsoon, Monsoon and Post Monsoon season for 2N-N cycle is represented in the **Figure C31**, **Figure C32 and Figure C33.** In the Monsoon season siltation behaviour near the proposed dam is in the range of 0.01-0.09 m/2N-N cycle. The significant siltation around 0.01-0.08 m/2N-N cycle observed in the central region of the domain In **Case I**, near the jetty area there is strong erosion can be witnessed which is evident in the **Figure 34, Figure C35 and Figure C36**. In the Pre-Monsoon the siltation is 20% lesser than the Monsoon season. In the Post-Monsoon season the siltation is observed to be 30 % lesser than the same.

For the **Case II**, the siltation predicted during pre-monsoon, monsoon and post monsoon season for 2N-N cycle is represented in **Figure C37, Figure C38 and Figure C39**.Significant siltation observed in the jetty area near the river opening exactly in the northern part of the Narmada River Mouth in three seasons which is represented in the **Figure C40, Figure C41 and Figure 42.** In the Monsoon season siltation is in the range of 0.05-0.1m/2N-N cycle. Siltation

behaviour is observed near the proposed dam in the range of 0.06-0.16 m/2N-N cycle. The significant siltation around 0.09-0.15 m/2N-N cycle observed in the central region of the domain. In the Pre-monsoon and Post-Monsoon, the siltation is observed 15% and 20% decrease respectively.

In the extreme condition, the siltation in the **Case I** condition for 2N-N cycle is represented in the **Figure 43** .Significant siltation is observed in the river area which is closer to the jetty in the range of 0.08-0.18 m/2N-N. Near the dam the siltation is in the range of 0.01-0.08 m/2N-N.In the same area erosion can be witnessed also. In the central area of the domain the siltation is in the range of 0.04-0.08 m/2N-N. In the jetty area the siltation is in the range 0.004-0.08 m/2N-N which is represented in the **Figure 44**. Strong erosion can also be witnessed in that area.

The extreme condition, for the **Case II** for 2N-N cycle is represented in the **Figure 45**. Significant siltation is observed in the domain. Near the mouth of the river more erosion is persistent. Siltation in the range of 0.16-0.19 m/2N-N is present in the river. The siltation near the proposed dam is in the range of 0.04-0.17 m/2N-N.The siltation in the central area is in the range of 0.08-0.12 m/2N-N. In the jetty area the siltation is in the range 0.01-0.08 m/2N-N which is represented in the **Figure 46.**

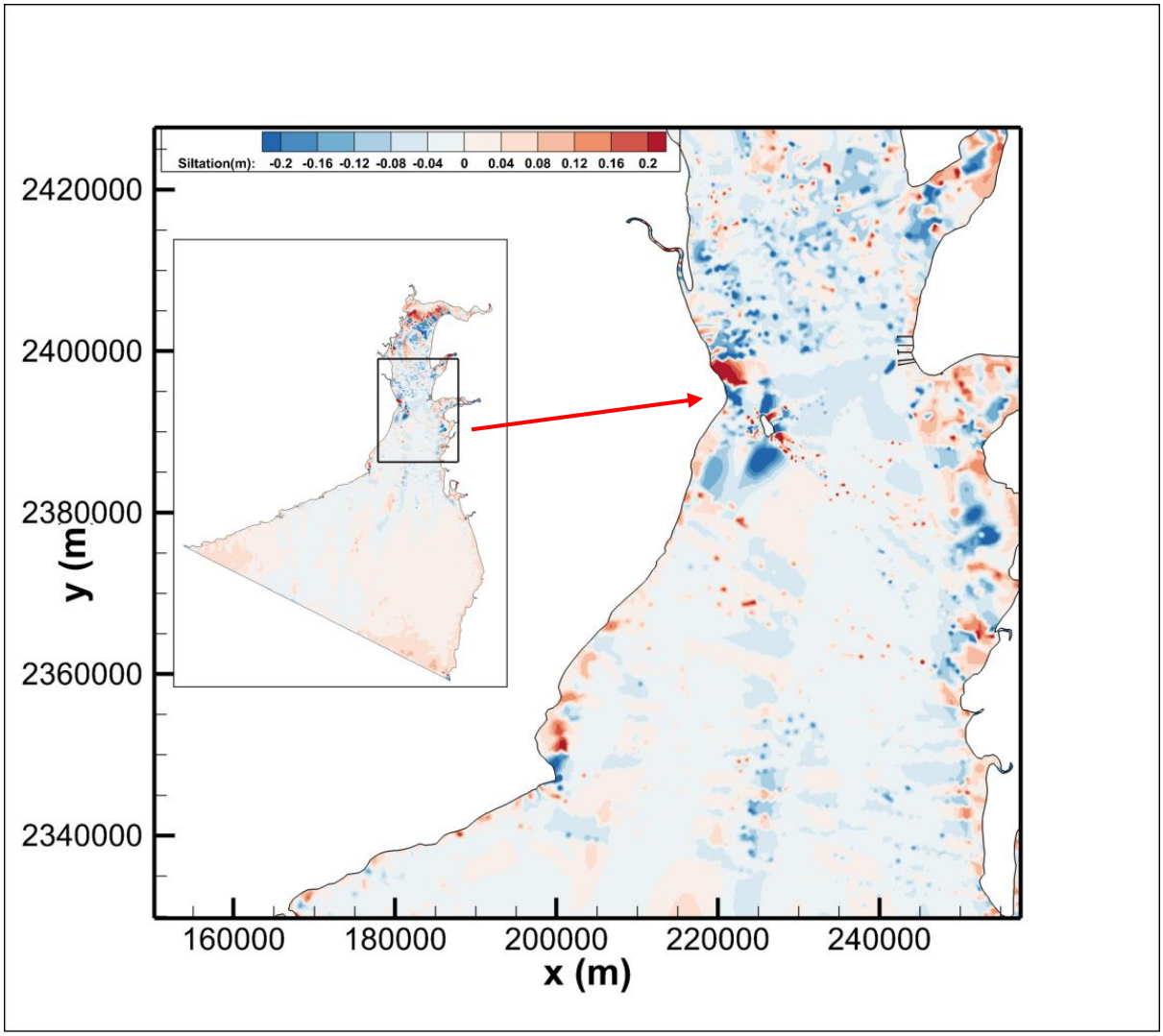

Figure C31: Bed level change at the end of 2N-N cycle simulation under Case I during pre - monsoon season

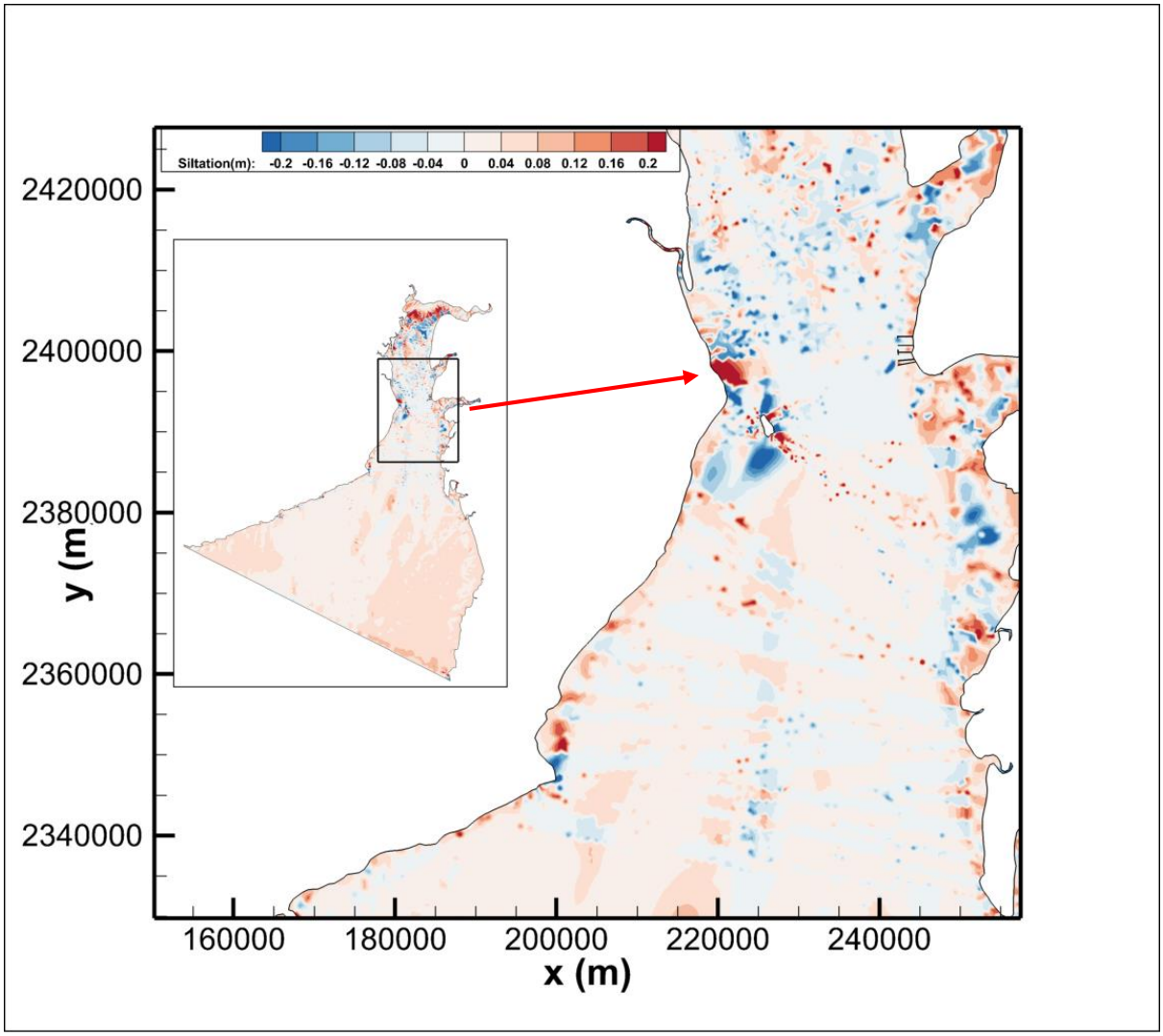

Figure C32: Bed level change at the end of 2N-N cycle simulation under Case I during monsoon season

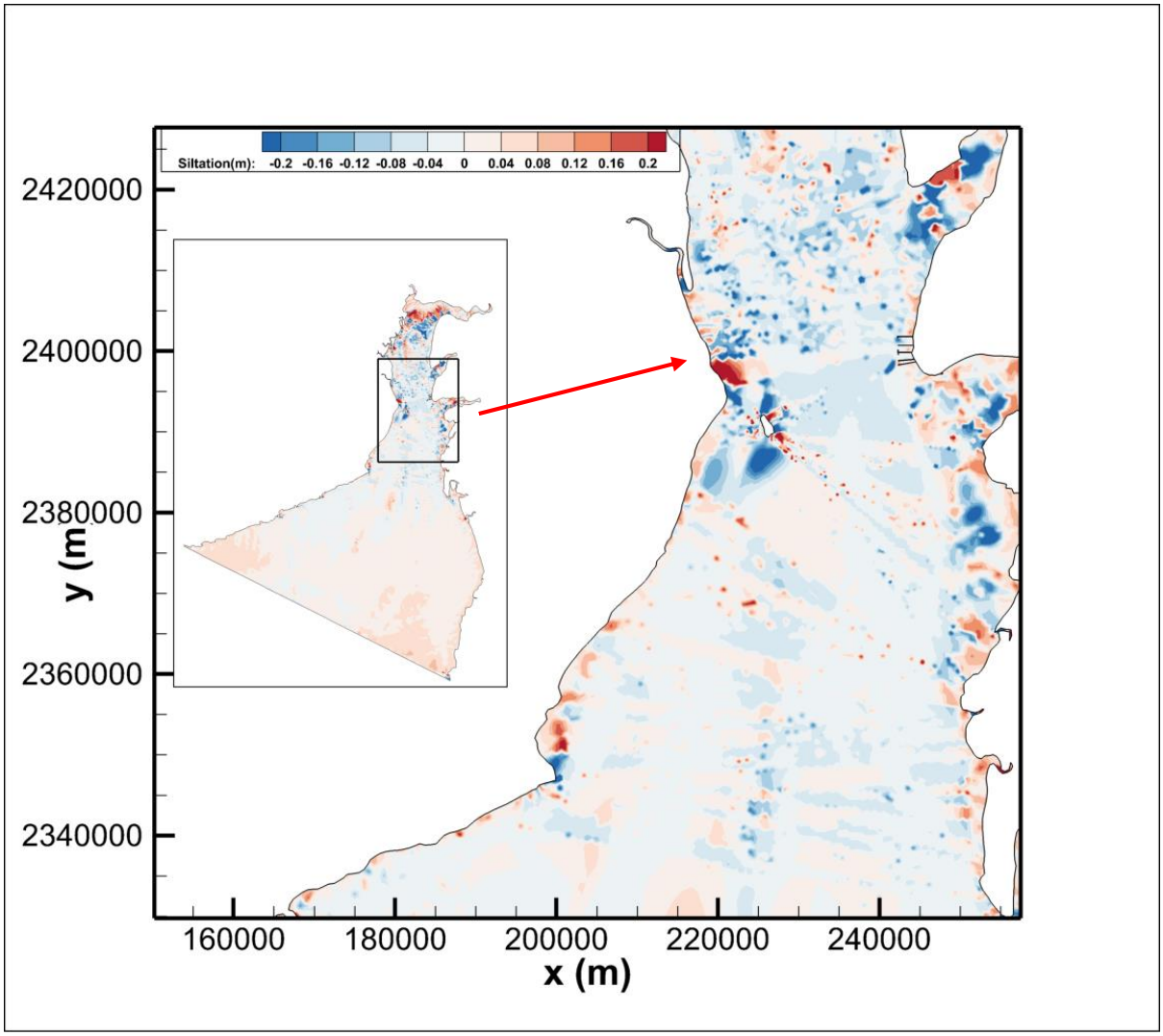

Figure C33: Bed level change at the end of 2N-N cycle simulation under Case I during post -monsoon season

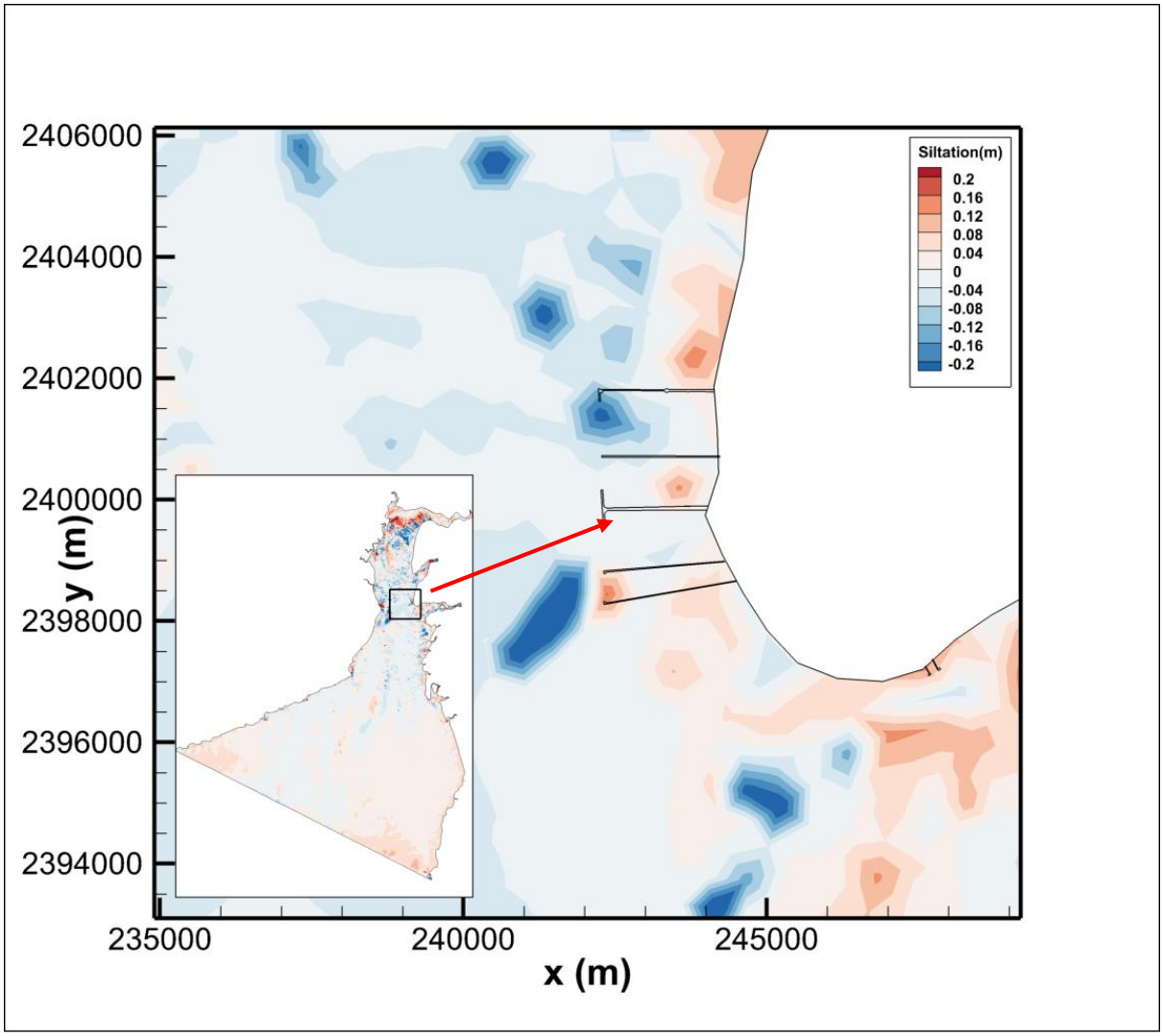

Figure C34: Bed level change at the end of 2N-N cycle simulation under Case I during pre-monsoon season in the jetty area

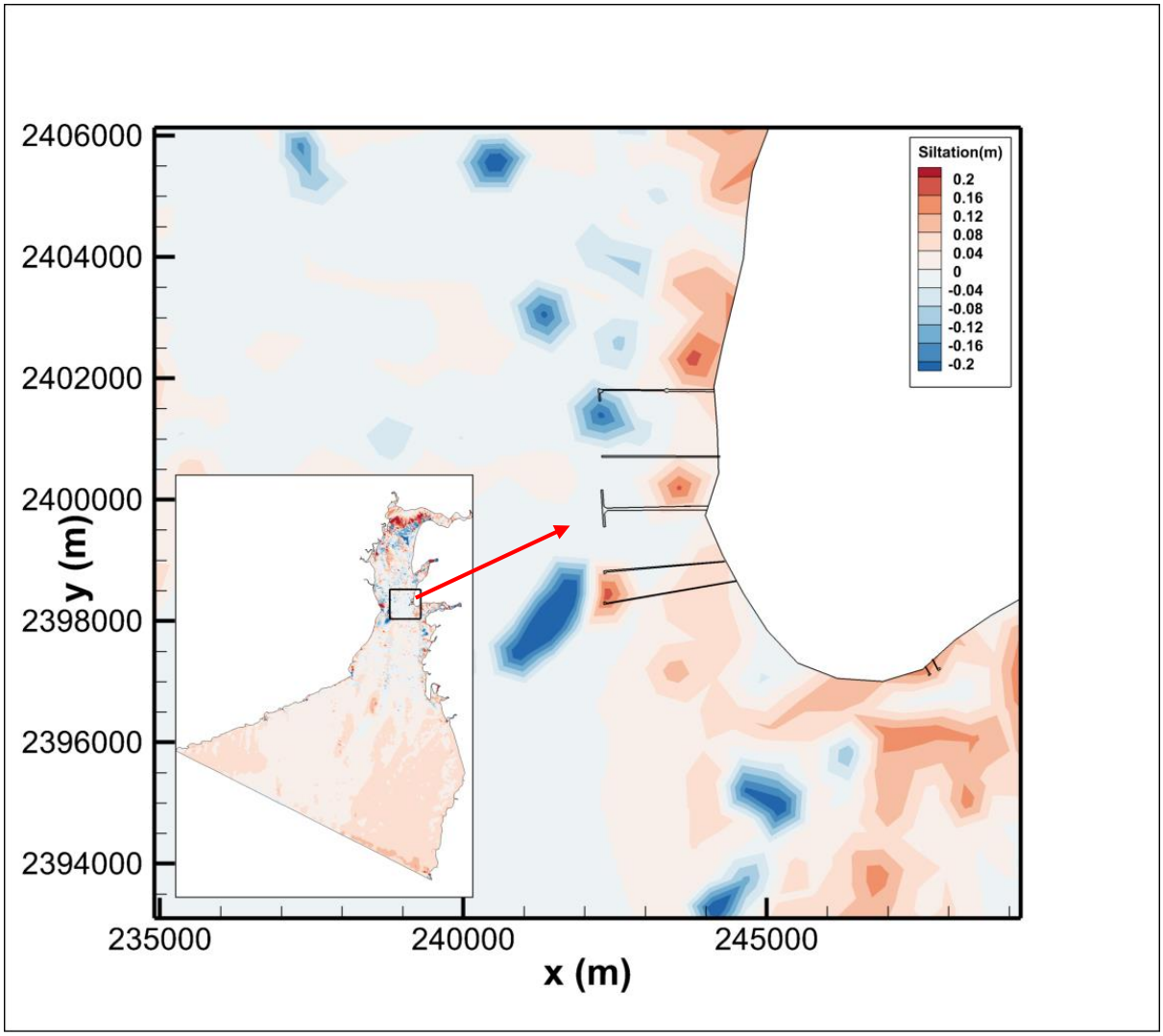

Figure C35: Bed level change at the end of 2N-N cycle simulation under Case I during monsoon season in the jetty area

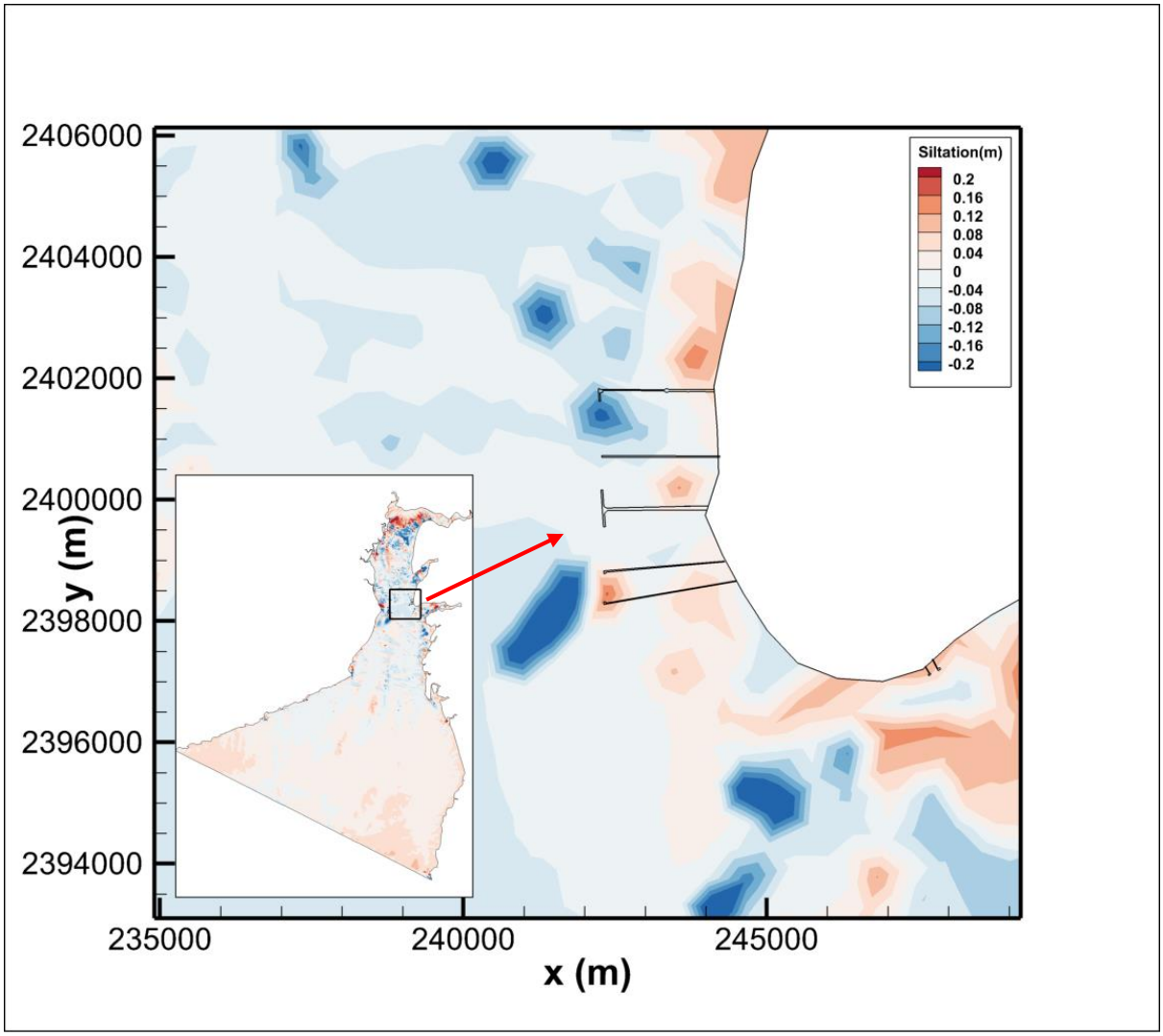

Figure C36: Bed level change at the end of 2N-N cycle simulation under Case I during post-monsoon season in the jetty area

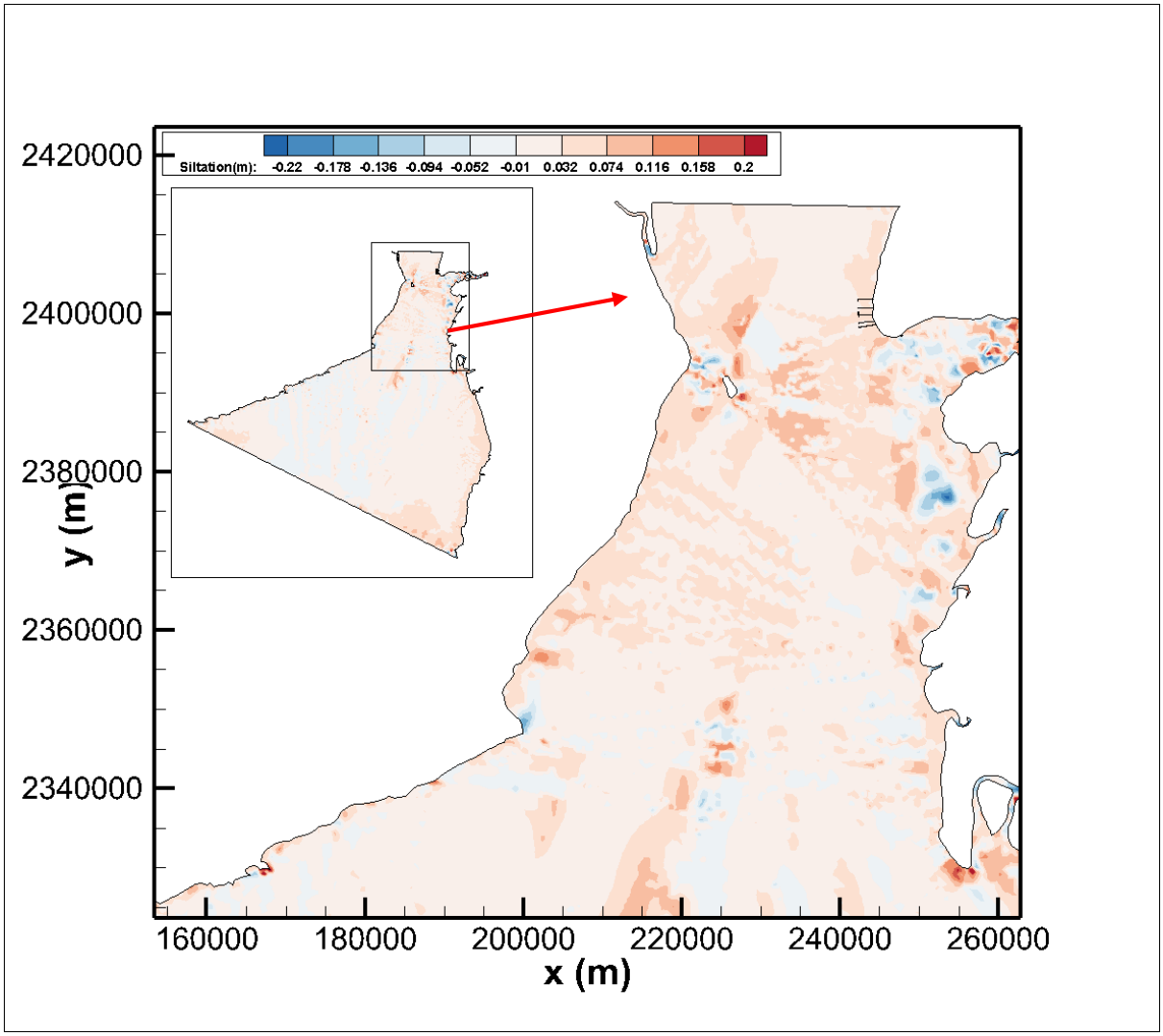

Figure C37: Bed level change at the end of 2N-N cycle simulation under Case II during pre -monsoon season

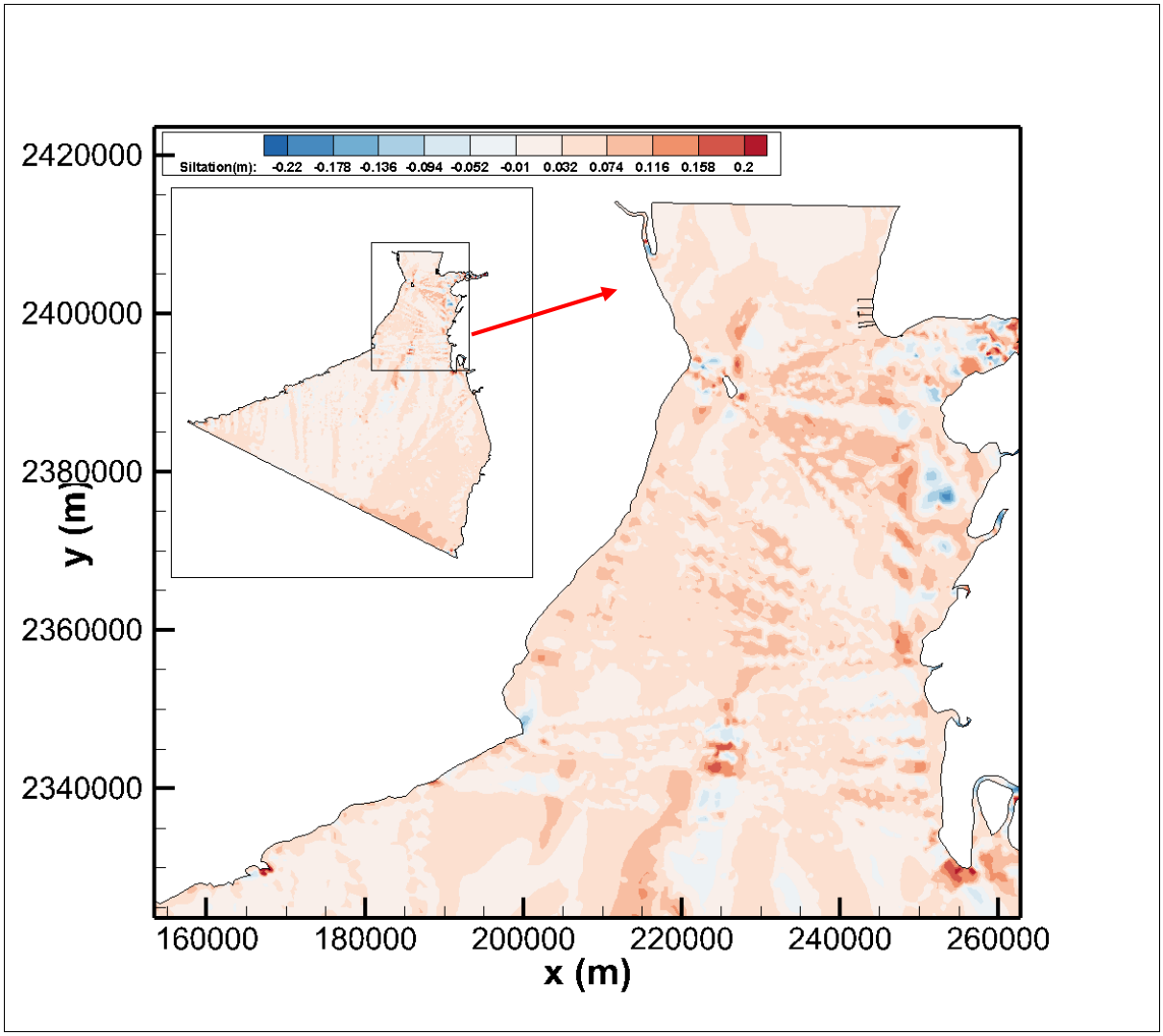

Figure C38: Bed level change at the end of 2N-N cycle simulation under Case II during monsoon season

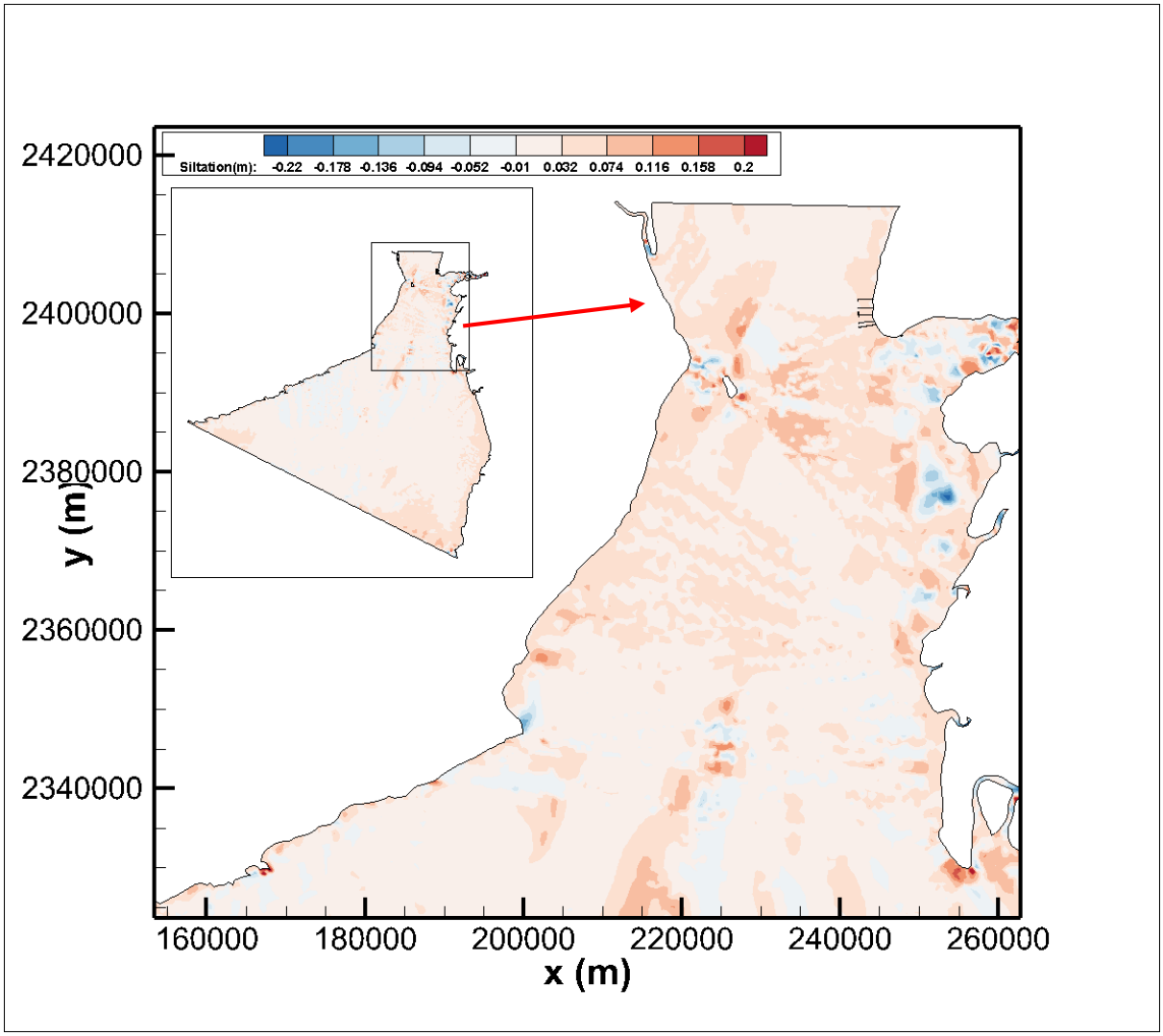

Figure C39: Bed level change at the end of 2N-N cycle simulation under Case II during post -monsoon season

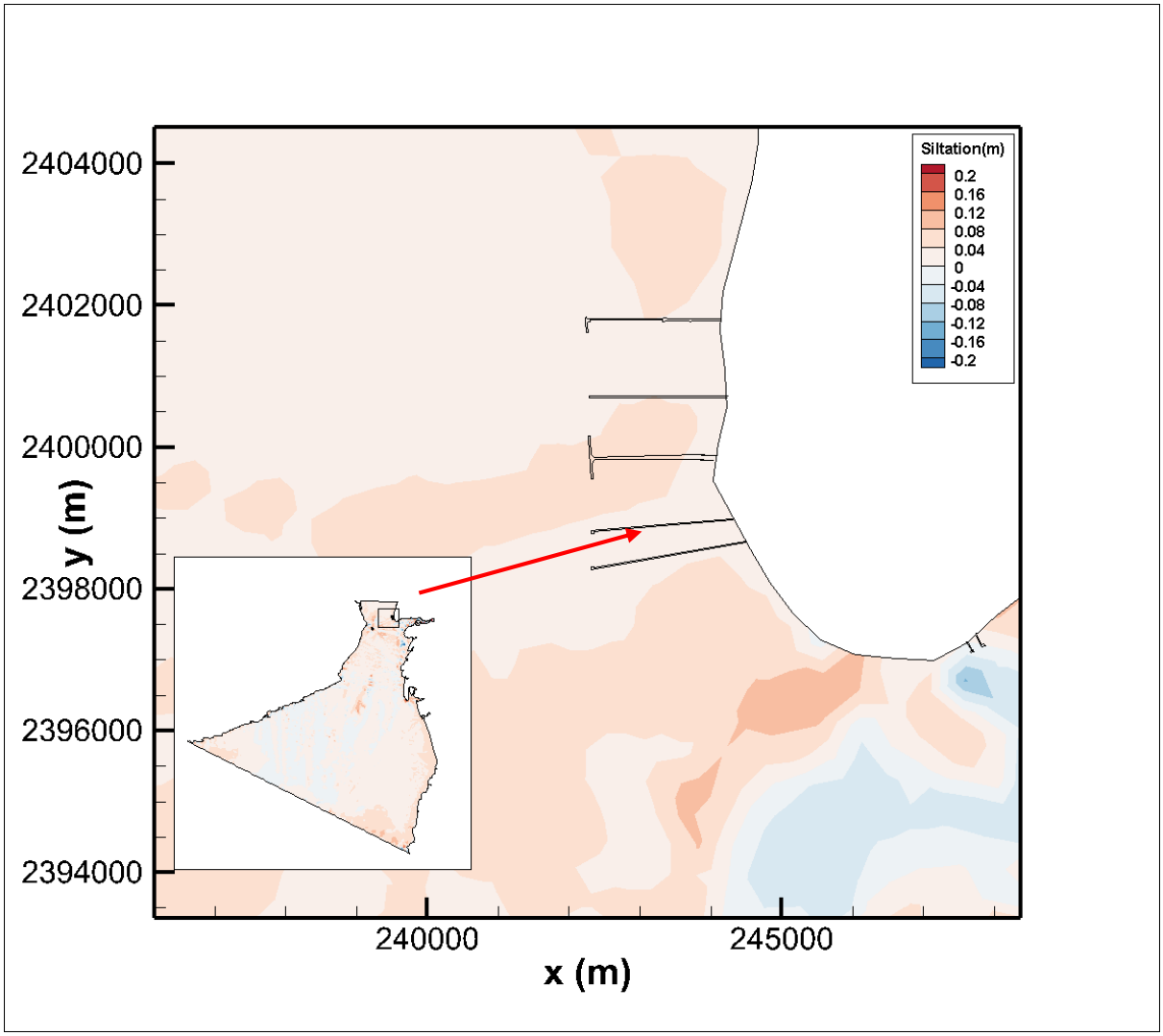

Figure C40: Bed level change at the end of 2N-N cycle simulation under Case II during pre- monsoon in the jetty area

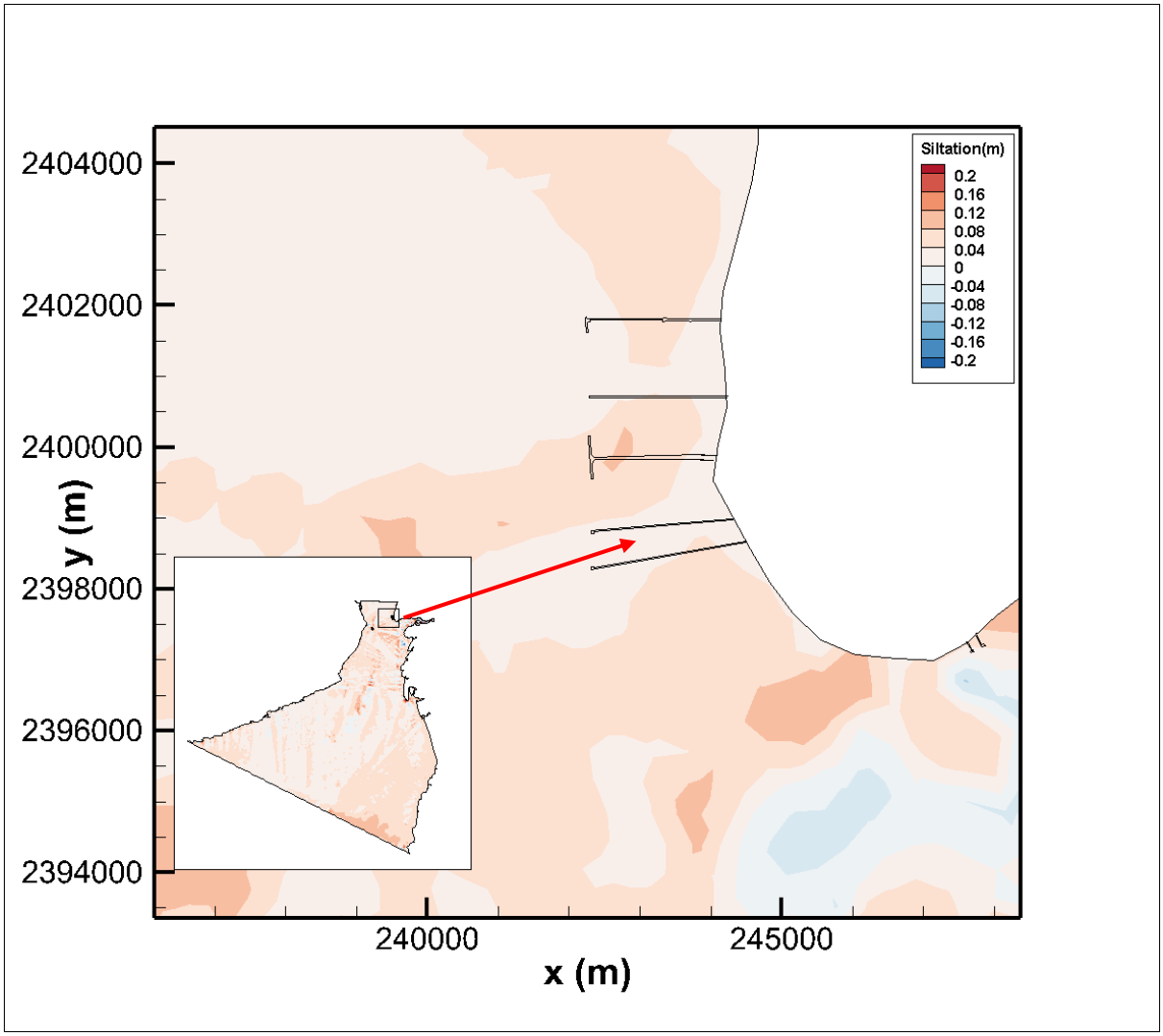

Figure C41: Bed level change at the end of 2N-N cycle simulation under Case II during monsoon in the jetty area

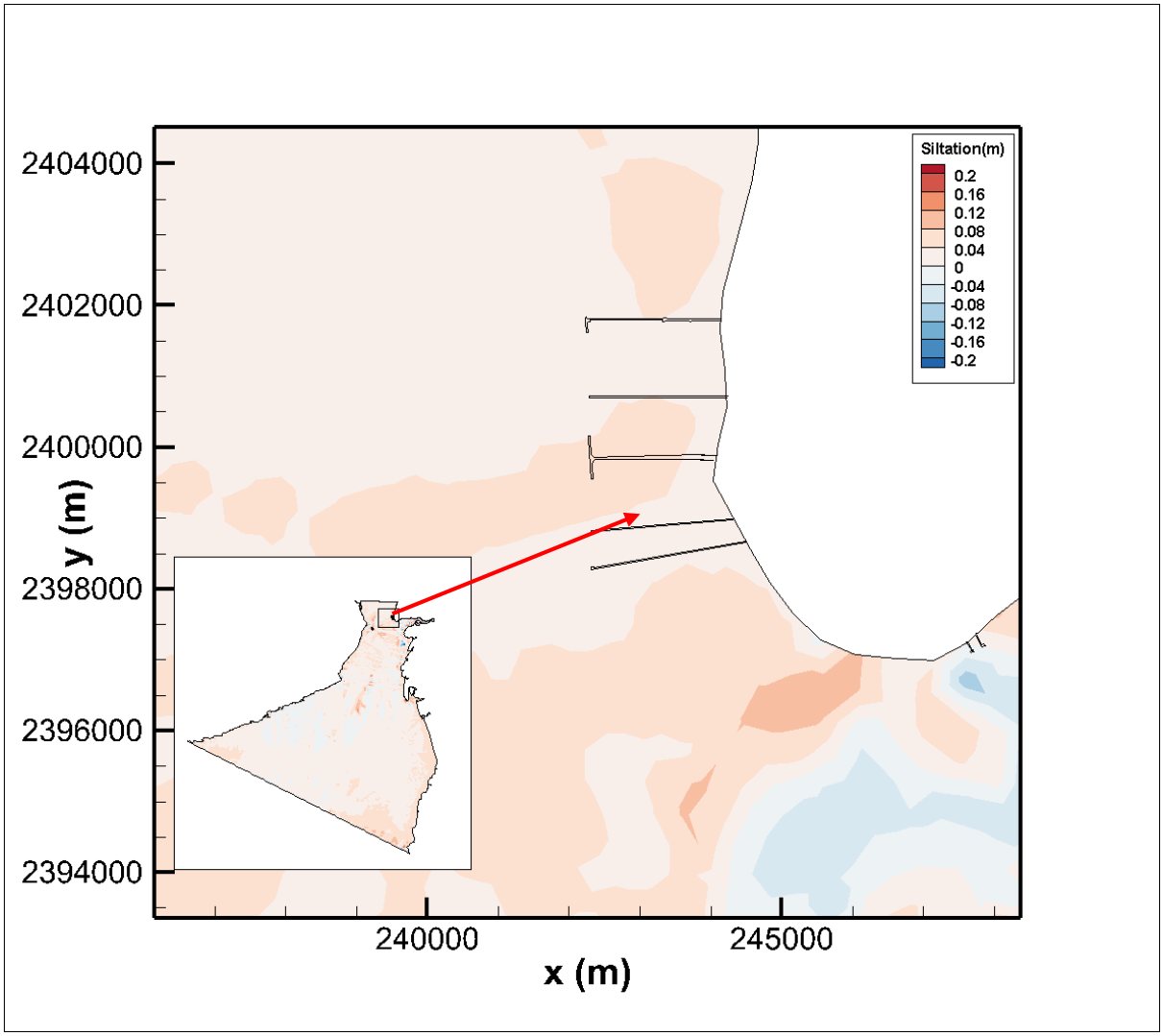

Figure C42: Bed level change at the end of 2N-N cycle simulation under Case II during post- monsoon in the jetty area

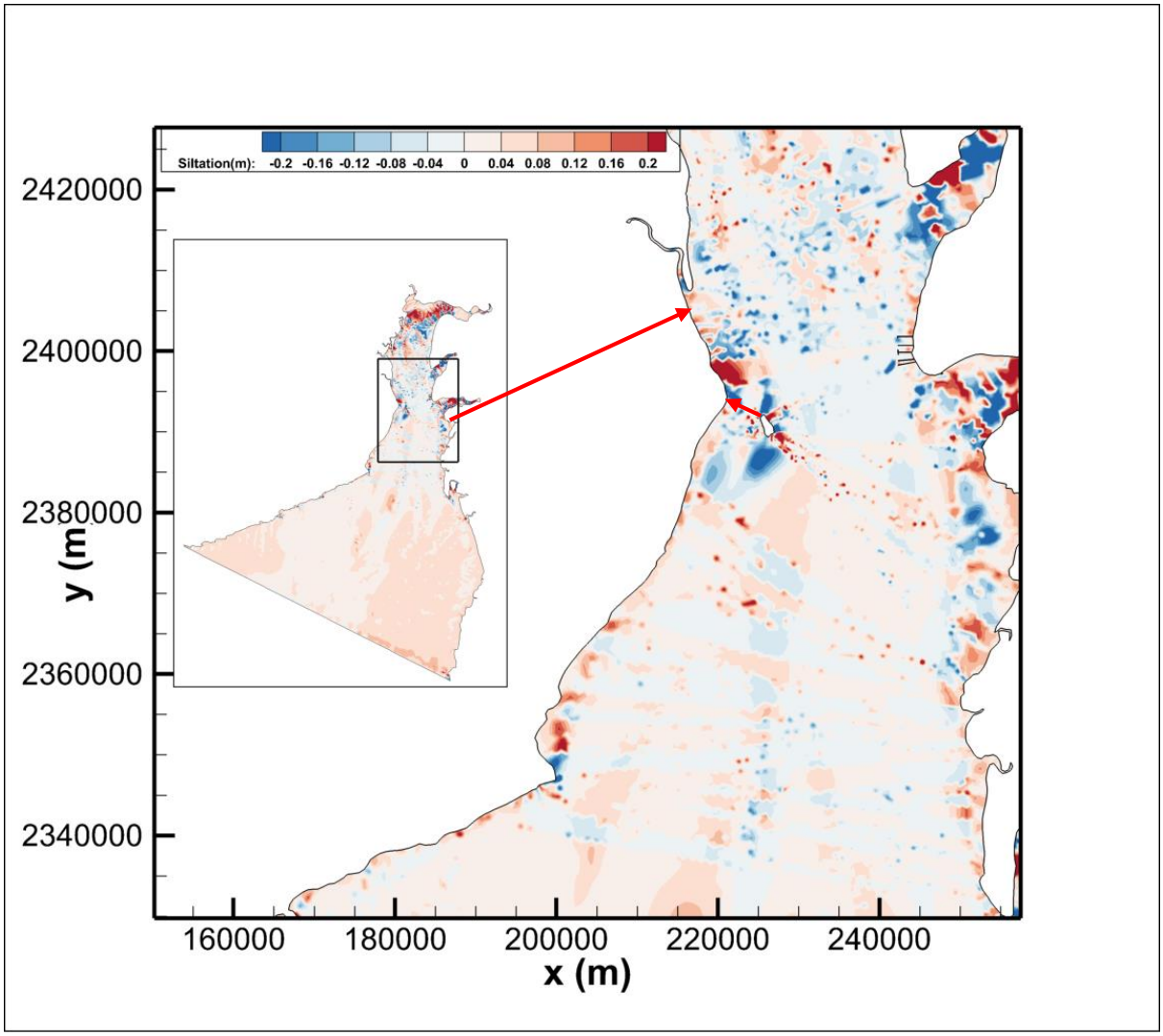

Figure C43: Bed level change at the end of 2N-N cycle simulation during extreme event in the domain for case I.

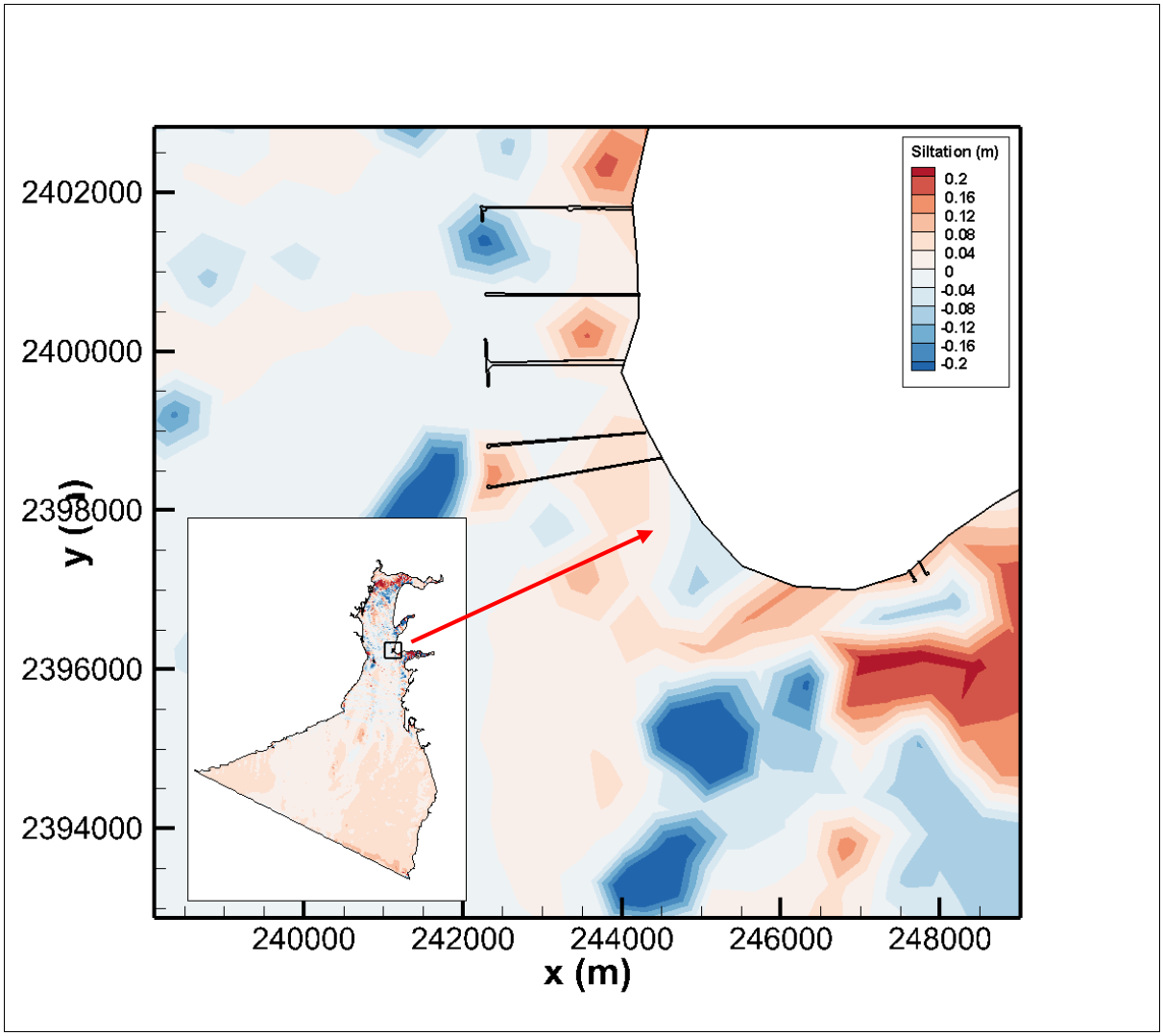

Figure C44: Bed level change at the end of 2N-N cycle simulation during extreme event in the jetty area for case I.

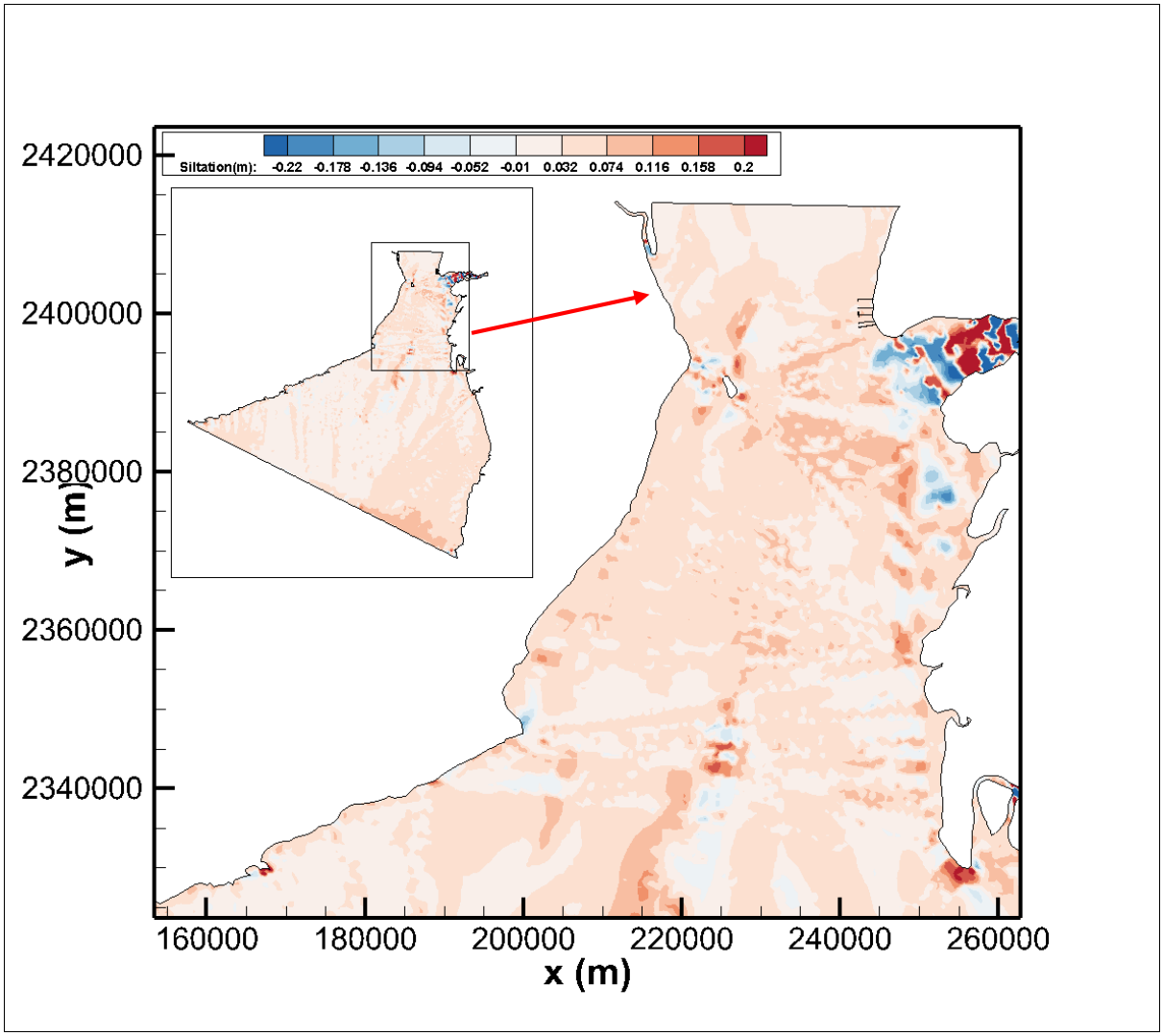

Figure C45: Bed level change at the end of 2N-N cycle simulation during extreme event in the domain for case II.

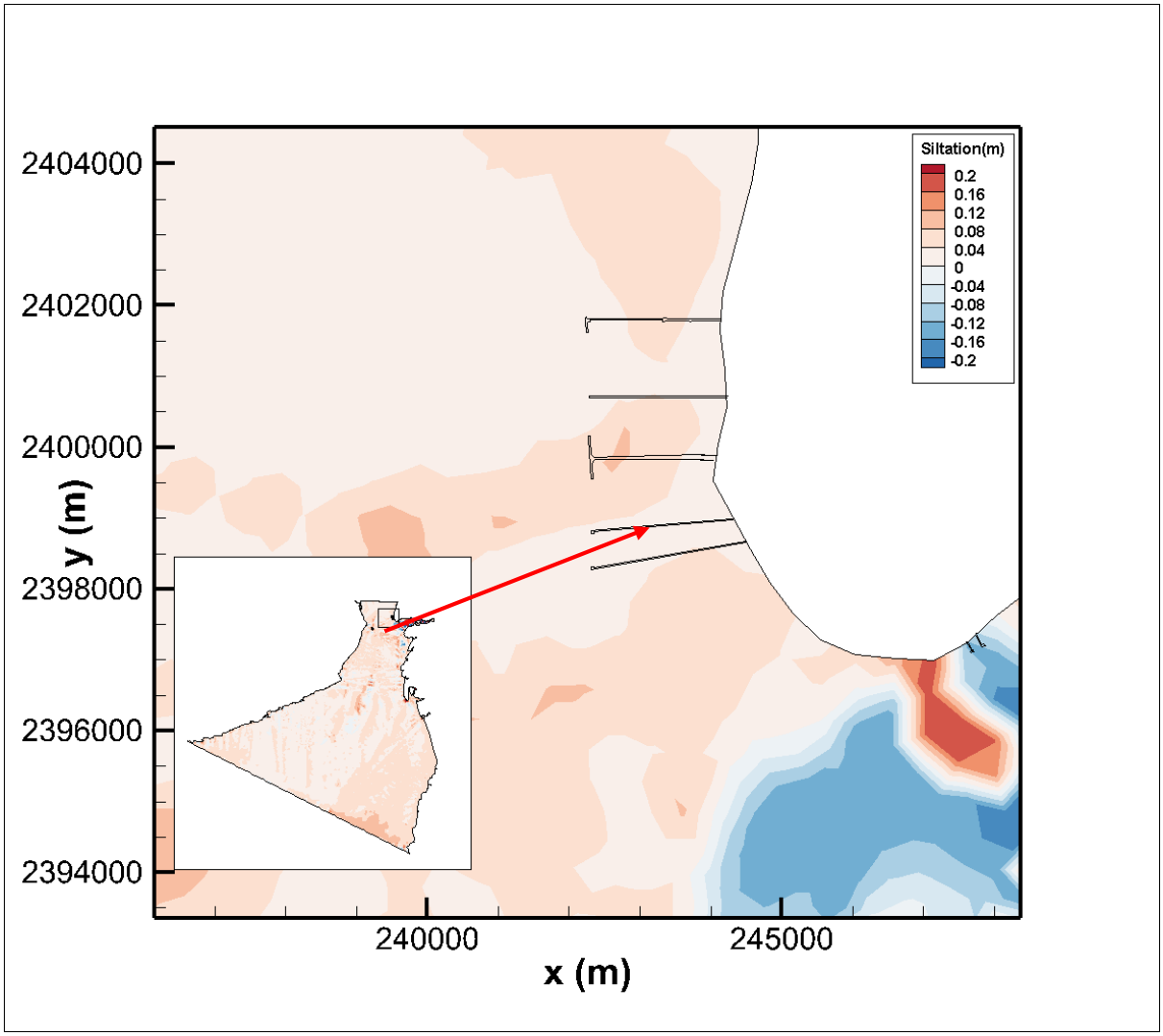

Figure C46: Bed level change at the end of 2N-N cycle simulation during extreme event in the jetty area for case II.

1.17 Local circulation and the siltation study in the reservoir area

1.17.1 Hydrodynamic study of the reservoir area

The flow pattern in the reservoir area is shown in the **Figure C47**. The local circulation involves the eddy in the area which is near to the proposed dam. The velocity in the area is in the range of 0.4 – 0.6 m/s averagely in the domain.

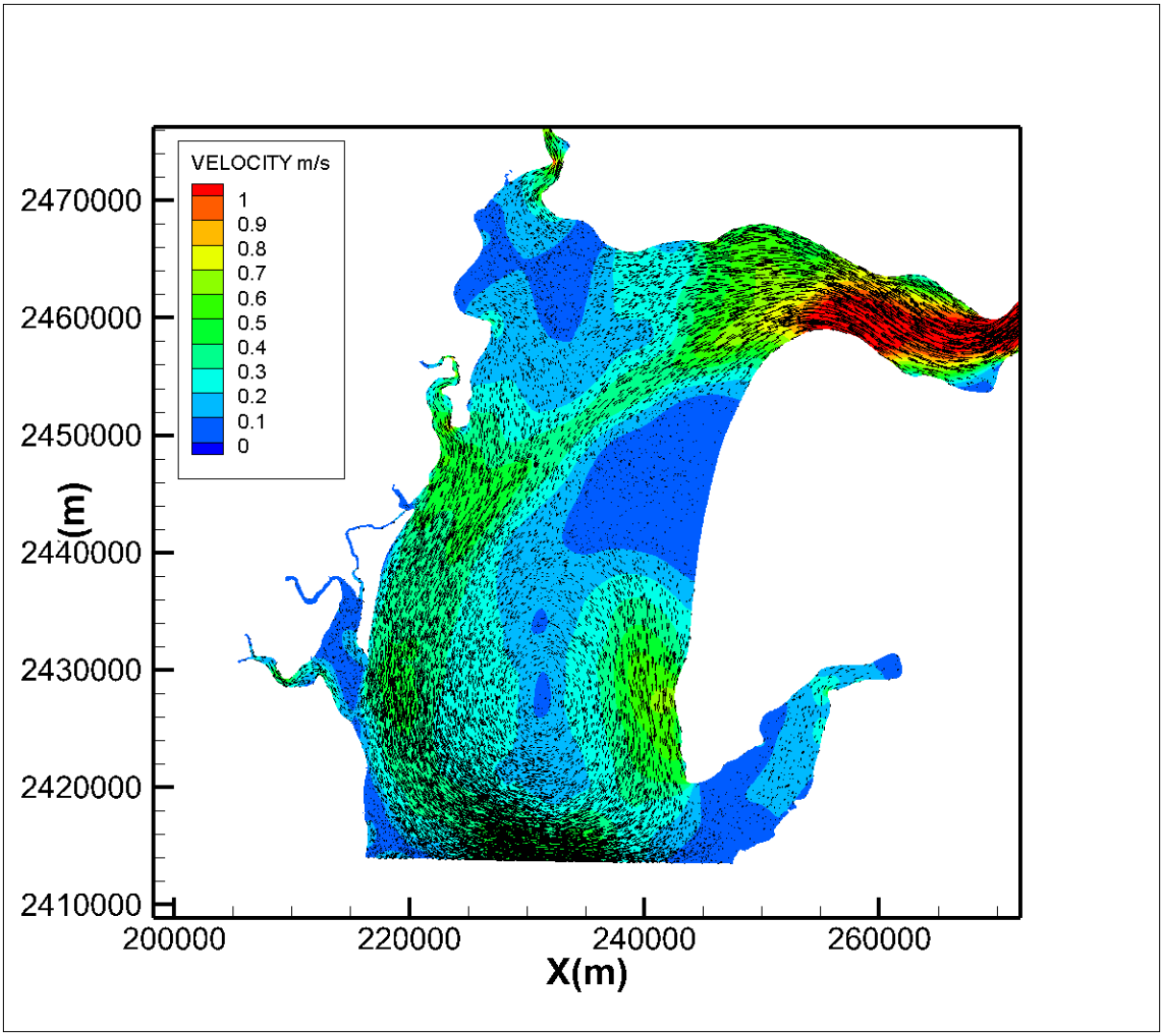

Figure C47: Local circulation in the reservoir area

1.17.2 Morphodynamic analysis in the reservoir area

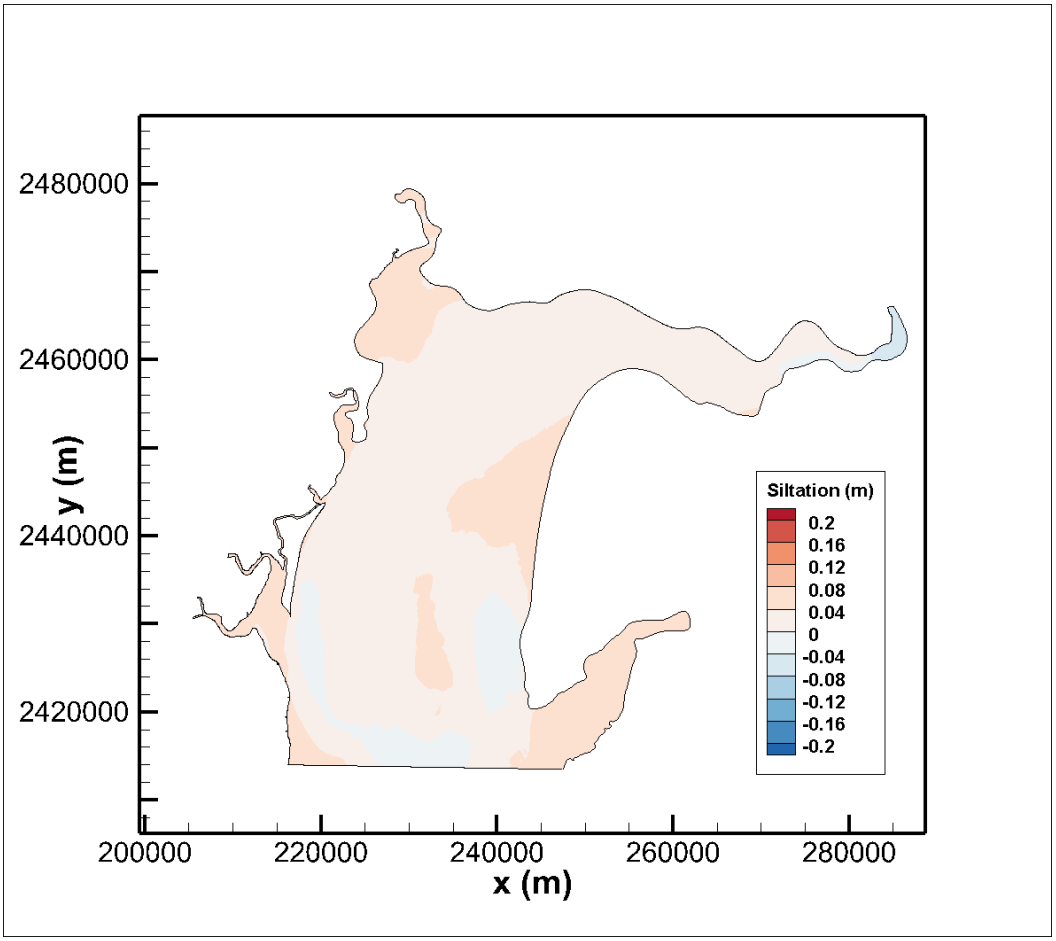

Figure C48: The morphodynamic analysis in the reservoir area

The average siltation rate in the area is 2-3 cm/N-N cycle which is shown in the **Figure C48**. With this siltation rate, an approximate volume of 18 Mm^3/14 days is predicted to be accumulating in the reservoir region. This may account for about an annual storage loss of around 1.5-3 % of the total capacity.

1.18 Concluding Remarks

1. Under the hydrodynamic study in the **Case I**, higher velocity observed in the domain with the maximum current speed in the order of 1.4 -3 m/s. less current speed is observed in the Ebbing period. The maximum current speed of 0.7 -1.4 m/s is observed in the offshore area. The maximum velocity during the ebbing is in the range of 1.4 m/s -2.1 m/s. Eddy formation is observed near the island in the north part of the domain during flooding. The increased velocity is due to the fact

that, in the absence of the proposed structure there is more flows occurring from the estuaries.

2. In the **Case I** the siltation behaviour is observed in the range of 0.01-0.09 m/2N-N cycle near the proposed dam area. Low amount of siltation in the range of 0.01-0.08 m/2N-N cycle is observed in the central area of the study domain. The less siltation happens because of the flushing from the rivers in the domain without any obstruction. In the Pre-Monsoon the siltation is 20% lesser than the Monsoon season. In the Post-Monsoon season the siltation is observed to be 30 % lesser than the same.
3. The hydrodynamic study in the **Case II** shows, an average of 0.3-2.4 m/s current speed is observed all over the considered domain during the flooding and less current speed is observed during the ebbing. The proposed dam will act as a wall which eliminate some circulation. The maximum current speed of 1 -1.5 m/s is observed in the offshore areas. During the ebbing the current velocity is in the range of 0.3-1.2 m/s near the study area. The proposed dam's south side has currents that range from 0.3 to 0.9 m/s
4. The Morphodynamic study under the **Case II** shows significant siltation observed in the jetty area near the river opening exactly in the northern part of the Narmada River Mouth in the range of 0.05-0.1m/2N-N cycle. Siltation behaviour is observed more near the proposed dam is in the range of 0.06-0.16 m/2N-N cycle. The significant siltation around 0.09-0.15 m/2N-N cycle observed in the central region of the domain. In the Pre-monsoon and Post-Monsoon, the siltation is observed 15% and 20% decrease respectively.
5. In the extreme event of the case I, near the river mouth, the current can be seen more frequently when there is flooding. Near the island, some eddy formations may be seen. When taking into account the study region, the domain’s average current speed is found to be in the range of 0.3-3.15 m/s. Near the island, a speed of 2.8 - 3.15 m/s has been recorded. The proposed dam's south side has currents that range from 1.4 to 2.8 m/s.
6. The siltation in the extreme event case I is between 0.08 and 0.18 m/2N-N in the river area closest to the jetty. The amount of siltation close to the dam is between 0.01-0.08 m/2N-N. Erosion is also visible in the same location. The siltation in the

domain's centre region ranges from 0.04-0.08 m/2N-N. The siltation in the vicinity of the jetty is between 0.004-0.08 m/2N-N.

7. In the extreme event case II. During the time of flooding, the current is observed more near the river mouth. The current speed in the order of 0.3-2.1 m/s is observed in the domain. The current speed of 1.2 -2.5 m/s is observed near the island. In the south side of the proposed dam the current has a range of 0.9-1.5 m/s. During ebbing the maximum current speed of 0.3 -2.1 m/s is observed in the domain. The southern side of the dam experience the velocity in the range of 0.3-0.9 m/s.
8. In the case II extreme event, more erosion persists close to the river's mouth. The river mouth contains silt with a range of 0.16-0.19 m/2N-N. The proposed dam is surrounded by siltation that ranges from 0.04-0.17 m/2N-N. The central region has siltation that ranges from 0.08 to 0.12 m/2N-N. The siltation in the jetty region ranges from 0.01 to 0.08 m/2N-N.
9. In the presence of the dam, the siltation rate is higher with the range of 0.06-0.16 m/2N-N cycle near the dam. The lack of flushing from the estuaries on the dam's northern side is the cause of the increased siltation. This causes significant siltation in the area, particularly near the Narmada river’s mouth at the Jetty and near to the proposed dam.
10. In Case I eroding patches are seen in the jetty area when compared with Case-II. As the range of siltation observed in case II seems to be slightly high compared to Case-I with the siltation rate of 0.05-0.1m/2N-N cycle.
11. In the vicinity of the proposed dam, eddy can be seen with the local circulation. The velocity in the area is between 0.4 and 0.6 m/s in average.
12. A volume of roughly 18 Mm/14 days is anticipated to accrue in the reservoir region as a result of the siltation. This can be the cause of a 1.5-3% annual storage capacity reduction, on average.

Annexure D

D-1 Details of the hydrodynamic model (TELEMAC2D)

D-1.1. General

The TELEMAC system is a set of finite element programs designed for the open channel flows which uses a string of common processes (digitization and graphics); it contains two and three dimension modules for the study of currents, sedimentation, waves and water quality. Forming the core of this system, TELEMAC-2D, the first module of this package, is a program for the solution of the two dimensional Saint-Venant equations. The water depth and the velocity averaged on the vertical are the main variables, but the transport of a passive tracer as well as turbulence can be taken into consideration. It uses triangular finite element discretization it can also work with quadrilateral elements.

TELEMAC-2D can be used for numerous studies in fluvial and maritime hydraulics, the test cases considered for the validation of the program give an idea of its fields of application. The present note describes the basic equations and the solution methods used.

D-1.2. The average of Navier-Stokes equations

Principle:

The Navier-Stokes equations (or Reynold's equations if we consider the turbulence) at constant density and with hydrostatic pressure will be averaged over the vertical by integrating from the bottom to the surface. Apart from the defined water depth, two new variables appear:

$$u = \frac{1}{h}\int_{Zf}^{Z} \mathrm{U1}\ \mathrm{dz} \text{and} v = \frac{1}{h}\int_{Zf}^{Z} \mathrm{U2}\ \mathrm{dz} \qquad (2)$$

These averages over the vertical of the horizontal components of the velocity vector will themselves be called velocity, or components of the velocity vector.

Average of the continuity equation:

The continuity equation becomes

$$\int_{Zf}^{Z}\left(\frac{\partial \mathrm{U1}}{\partial x}+\frac{\partial \mathrm{U2}}{\partial y}+\frac{\partial \mathrm{U3}}{\partial z}\right)\mathrm{dz} = 0 \qquad (3)$$

By using Leibnitz's rule, it follows:

$$\int_{Zf}^{Z}\left(\frac{\partial U1}{\partial x}+\frac{\partial U2}{\partial y}+\frac{\partial U3}{\partial z}\right)dz=\frac{\partial}{\partial x}\int_{Zf}^{Z}U1\,dz-U1\,(x,y,Z)\frac{\partial Z}{\partial x}+U1\,(x,y,Zf)\frac{\partial Zf}{\partial x}+\frac{\partial}{\check{Z}y}\int_{Zf}^{Z}U2\,dz-$$
$$U2\,(x,y,Z)\frac{\partial Z}{\partial y}+U2\,(x,y,Zf)\frac{\partial Zf}{\partial y}+U3\,(Z)-U3\,(Zf)=0 \qquad (4)$$

And, considering the conditions of impermeability:

$$\frac{\partial}{\partial x}(hu)+\frac{\partial}{\partial y}(hv)+\frac{\partial Z}{\partial t}-\frac{\partial Zf}{\partial t}=0 \qquad (5)$$

Or finally:

$$\frac{\partial h}{\partial t}+\frac{\partial}{\partial x}(hu)+\frac{\partial}{\partial y}(hv)=0 \text{ or} \frac{\partial h}{\partial t}+div\,(h\vec{u})=0 \qquad (6)$$

We remark straight away the analogy with the continuity equation of compressible fluids:

$$\frac{\partial \rho}{\partial t}+div\,(\rho\vec{u})=0 \qquad (7)$$

in the Saint-Venant equations the depth plays the role of the density.

Average of the momentum equation

We shall apply from the very beginning the hypothesis of hydrostatic pressure.

The equation of U_1, once developed, becomes:

$$\frac{\partial U_1}{\partial t}+\frac{\partial U_1^2}{\partial x}+\frac{\partial U_1U_2}{\partial y}+\frac{\partial U_1U_3}{\partial z}=-\frac{1}{\rho}\frac{\partial}{\partial x}[\rho g(Z-z)]$$
$$+\frac{1}{\rho}\left[\frac{\partial}{\partial x}(\tau_{11}+R_{11})+\frac{\partial}{\partial y}(\tau_{12}+R_{12})+\frac{\partial}{\partial z}(\tau_{13}+R_{13})\right]+F_x \qquad (8)$$

Let us detail the results from integrating each of these terms:

Time derivative:

$$\int_{zf}^{z}\frac{\partial U_1}{\partial t}dz=\frac{\partial(hu)}{\partial t}-U_1(Z)\frac{\partial Z}{\partial t}+U_1(Zf)\frac{\partial Zf}{\partial t} \qquad (9)$$

Advection terms:

$$\int_{zf}^{z} \frac{\partial U_1^2}{\partial x}\, dz = \frac{\partial}{\partial t}\int_{zf}^{z} U_1^2\, dz - U_1^2(Z)\frac{\partial Z}{\partial x} + U_1^2(Zf)\frac{\partial Zf}{\partial x} \qquad (10)$$

$$\int_{zf}^{z} \frac{\partial U_1 U_2}{\partial y}\, dz = \frac{\partial}{\partial y}\int_{zf}^{z} U_1 U_2\, dz - U_1(Z)U_2(Z)\frac{\partial Z}{\partial y} + U_1(Zf)U_2(Zf)\frac{\partial Zf}{\partial y} \qquad (11)$$

The last two terms produce non-linearity. Let us develop for example the expression in U_1U_2:

$$\frac{\partial}{\partial y}\int_{zf}^{z} U_1 U_2\, dz = \frac{\partial}{\partial y}\int_{zf}^{z} (u + U_1 - u)(v + U_2 - v)\, dz \qquad (12)$$

$$= \frac{\partial}{\partial y}\int_{zf}^{z} u\,v\, dz + \frac{\partial}{\partial y}\int_{zf}^{z} u(U_2 - v) + v(U_1 - u)\, dz + \frac{\partial}{\partial y}\int_{zf}^{z} (U_1 - u)(U_2 - v)\, dz$$

$$= \frac{\partial}{\partial y}(h\,u\,v) + \frac{\partial}{\partial y}\int_{zf}^{z} (U_1 - u)(U_2 - v)\, dz \qquad (13)$$

The term $\frac{\partial}{\partial y}\int_{zf}^{z} (U_1 - u)(U_2 - v)\, dz$ is not nil when there are heterogeneities in the velocity over the vertical. These terms, called those of dispersion, are generally interpreted as an additional diffusion. In fact, they take into account the fluctuations around the mean (here, spatial) and are analogous to Reynolds stress. In reality, these are advection terms arising from the fact that the movement of the water is due to a real current and not due to a current averaged over the vertical. Depending on the depth, all particles of water are not carried at the same velocity whereas in the Saint-Venant equations we choose an average current. We shall select here an approach with diffusion, with a tensor that shall add naturally to the Reynolds tensor.

Henceforth, ν_e shall include the molecular viscosity, the turbulence, and the dispersion.

$$\int_{zf}^{z} \frac{\partial U_1 U_3}{\partial z}\, dz = U_1(Z)U_3(Z) - U_1(Zf)U_3(Zf) \qquad (14)$$

Pressure gradient:

$$\int_{zf}^{z} -\frac{1}{\rho}\frac{\partial}{\partial x}\left[\rho g\left(Z-z\right)\right]dz = -hg\frac{\partial Z}{\partial x} \qquad (15)$$

This is true only if the density does not change over the horizontal.

Diffusion terms:

$$\frac{1}{\rho}\left[\frac{\partial}{\partial x}\left(\tau_{11}+R_{11}\right)+\frac{\partial}{\partial y}\left(\tau_{12}+R_{12}\right)+\frac{\partial}{\partial z}\left(\tau_{13}+R_{13}\right)\right]: \qquad (16)$$

Let us examine, for example, viscous term, written in the form $\frac{1}{\rho}div(\vec{\tau})$ where $\vec{\tau}$ is a vector with components (τ_{11}, τ_{12}, τ_{13}).

If we assume that the density does not vary over the vertical, it can be removed from within the integral and the formula of Leibnitz gives:

$$\frac{1}{\rho}\int_{zf}^{z} div(\vec{\tau})\,dz = \frac{1}{\rho}div(\int_{zf}^{z}\vec{\tau}\,dz) - \frac{1}{\rho}\vec{\tau}_{surface}.\vec{n}_{surface} + \frac{1}{\rho}\vec{\tau}_{fond}.\vec{n}_{fond} \qquad (17)$$

The last two terms of the last equation represent surface and bottom constraints caused, for example, by the wind or the friction at the bottom. These terms will be studied later along with source terms.

Remark on the way the term div ($\vec{\tau}$) is written:

According to Boussinesq's model, $\vec{\tau}$ is a vector in these components: $\begin{pmatrix} \mu_e\left(\frac{\partial U_1}{\partial x}+\frac{\partial U_1}{\partial x}\right) \\ \mu_e\left(\frac{\partial U_1}{\partial y}+\frac{\partial U_2}{\partial x}\right) \\ \mu_e\left(\frac{\partial U_1}{\partial z}+\frac{\partial U_3}{\partial x}\right) \end{pmatrix}$

where $\mu_e = \rho\nu_e$. Even though this is valid only when μ_e is constant in space (which is not the case with the turbulence model k-epsilon, and even less so when μ_e includes dispersion), we write $div(\vec{\tau})$ as $div\left(\mu_e\ \overrightarrow{grad}(U_1)\right)$. This approximation will avoid a coupling of the components of

the velocity in the final equations, and conserves, in spite of everything, a tensorial form of the viscosity terms. Tests with other programmes preceding TELEMAC (notably ULYSSE) have shown that this coupling of the velocity components could have been ignored. Knowing that the effective viscosity includes the dispersion terms, we can say that we have chosen a model rather than an approximation, the expression of $\vec{\tau}$ given by Boussinesq itself having been obtained from an analogy with molecular viscosity.

Before arriving at a final form of our diffusion terms, we shall have to make one more approximation. We have to consider that

$$\int_{zf}^{z} \overrightarrow{grad}(U_1)\, dz \quad \approx \quad h\, \overrightarrow{grad}(u)\,,$$

The term $\frac{1}{\rho} div(\int_{zf}^{z} \vec{\tau}\, dz)$ is finally written: $\frac{1}{\rho} div(h\, \mu\, \overrightarrow{grad}(u))$.

Assuming, in addition, that the density remains constant, the diffusion term is finally written as:

$div(h\, \nu_e\, \overrightarrow{grad}(u))$.

In this expression, ν_e is traditionally called turbulent diffusion. This is the key word VELOCITY DIFFUSIVITY. We have to remember that in the Saint-Venant equations, this term includes the dispersion. ν_e can then vary substantially, from less than 1 to more than 500m^2/s. This imposes a practical standardization on every application if the model of turbulence is not used.

Recapitulation:

The sum of these terms, many of which disappear in view of the impermeability of the bottom and of the free surface, gives the following equation:

$$\frac{\partial(hu)}{\partial t} + \frac{\partial}{\partial x}(huu) + \frac{\partial}{\partial y}(huv) = -h\, g \frac{\partial Z}{\partial x} + h\, F_x + div\left(h\, \nu_e\, \overrightarrow{grad}(u)\right) \qquad (18)$$

The U_2 equation gives,

$$\frac{\partial(hv)}{\partial t}+\frac{\partial}{\partial x}\left(huv\right)+\frac{\partial}{\partial y}\left(hvv\right)=-h\,g\,\frac{\partial Z}{\partial y}+h\,F_y+div\left(h\;v_e\,\overrightarrow{grad}(v)\right) \qquad (19)$$

Since the vertical velocity is assumed as insignificant, the U3 equation is not retained (it was already used in the hypothesis of hydrostaticity).

Along with the continuity equations, these equations form part of the bidimensional equations of BarrŽ de Saint-Venantin a form called conservative.

D-1.3. Different forms of equations

Conservative form

The equations obtained in the previous chapter are rewritten by taking: $Q_x = hu$, $Q_y = hv$. Q is the vector with Q_x and Q_y as components. The discharge Q is in fact expressed here in m^2/s.

Continuity:

$$\frac{\partial h}{\partial t}+div(\vec{Q})=0 \qquad (20)$$

Momentum:

$$\begin{aligned}\frac{\partial Q_x}{\partial t}+div(\vec{u}\,Q_x)&=-hg\,\frac{\partial Z}{\partial x}+h\,F_x+div\left(h\;v_e\overrightarrow{grad}\,u\right)\\ \frac{\partial Q_y}{\partial t}+div(\vec{u}\,Q_y)&=-hg\,\frac{\partial Z}{\partial y}+h\,F_y+div\left(h\;v_e\overrightarrow{grad}\,v\right)\end{aligned} \qquad (21)$$

Non-conservative form

In theory, only a rigorous application of conservative equations will lead to a good grasp of the problem considering the discontinuities that can arise in the solution (hydraulic jumps). Other reasons (stability of the model, use of the characteristics method) have led us to adopt a different formulation with variables h and u, called the depth-velocity formulation. This formulation is called non-conservative.

Using the conservative form of equations as a starting point, the derivatives of the products of functions are developed in the equations of momentum and of continuity.

The continuity equation becomes:

$$\frac{\partial h}{\partial t} + \vec{u}\,.\,\overrightarrow{grad}(h) + h\,div(\vec{u}) = Sce$$

and the equation of u:

$$h\frac{\partial u}{\partial t} + u\frac{\partial h}{\partial t} + u\frac{\partial hu}{\partial x} + hu\frac{\partial u}{\partial x} + u\frac{\partial hv}{\partial y} + hv\frac{\partial u}{\partial y} = -hg\frac{\partial Z}{\partial x} + h\,Fx + div(h \quad v_e\,\overrightarrow{grad}\,u) + u_{sce}\,Sce \quad (22)$$

And, using the continuity equation:

$$h\frac{\partial u}{\partial t} + hu\frac{\partial u}{\partial x} + hv\frac{\partial u}{\partial y} = -hg\frac{\partial Z}{\partial x} + h\,Fx + div(h \quad v_e\,\overrightarrow{grad}\,u) - u\,Sce + u_{sce}\,Sce \quad (23)$$

We divide both sides of the equation by h. And, working in the same manner for v, we arrive at:

$$\frac{\partial u}{\partial t} + u\frac{\partial u}{\partial x} + v\frac{\partial u}{\partial y} = -g\frac{\partial Z}{\partial x} + Fx + \frac{1}{h}div(h \quad v_e\,\overrightarrow{grad}\,u) + \frac{Sce}{h}(u_{sce} - u) \quad (24)$$

$$\frac{\partial v}{\partial t} + u\frac{\partial v}{\partial x} + v\frac{\partial v}{\partial y} = -g\frac{\partial Z}{\partial y} + Fy + \frac{1}{h}div(h \quad v_e\,\overrightarrow{grad}\,v) + \frac{Sce}{h}(v_{sce} - v) \quad (25)$$

The conservative and non-conservative forms of equations are not equivalent if discontinuities are present.

Remark

If there is a source at the bottom, the terms $\frac{(u_{sce} - u)Sce}{h}$ and $\frac{(v_{sce} - v)Sce}{h}$ have to be added to right hand sides. These terms are nil if the velocity of the source is the same as that of the current. We will henceforth include them in the expression F_x and F_y will not mention them explicitly.

Annexure - E

E-1. OCIRC

IIT Madras have developed an in-house computer code to implement the above equations. ***Ocirc 1.0*** has been used in several projects in the past for investigating tidal hydrodynamics and siltation, specifically to Cochin, Kandla, and Pradeep ports and to study Storm surge and Tsunami hydrodynamics for DoAE, MES, and DRDO etc. The model has also been applied in high tidal range basins such as Gulf of Kutch and Gulf of Khambhat. The model uses an unstructured mesh generation technique and solves the shallow water equations using a Finite Volume – Finite Element based method. The convective fluxes are estimated using Godunov's approach.

The numerical analysis is used to predict and estimate the morphological changes and also identify the location of erosion and accretion based on the hydrodynamic parameters that exist over the region of inspection. In order to pursue the mathematical model studies of hydrodynamics and siltation, the in-house developed hydrodynamic model used is **Ocirc**, the details of which are discussed. An unstructured meshing approach is being used in the OCIRC numerical model. The model predicts the tide induced flow around the berth and computes the changes in the bed levels due to the tidal flow using sediment load balance in the water column. The model domain can be discretized with triangular elements to obtain numerical solutions to the hydrodynamic equations. The final mesh has fine elements near the shallower water depths. The average mesh size is found to be about 20-100m which is very fine near the berth. The mesh is coarser near the offshore boundaries where the water depths are greater and finer in the channels and their confluence regions respectively. The bathymetry data used are the measured data and GEBCO 15 arc second data near the outer boundaries. The refined mesh is capable of capturing the details of the bathymetry significantly closer to reality. The details of boundary inputs and calibration details of the model are given below

E-1.1Model for Tidal Hydrodynamics and Morphodynamics

E-1.1.1Model formulation

Navier-Stokes equations (N-S equations) are the fundamental mathematical framework for any fluid dynamics process. In the context of tides, the N-S equations simplify to the well-known "vertically integrated shallow water equations (SWE)" that govern the ocean flow

field with main momentum transport occurring in the horizontal directions only. The SWE in a Cartesian co-ordinate frame fixed to the rotating earth and without lateral turbulent diffusion are,

$$q_{x,x} + q_{y,y} + \eta_{,t} = 0$$

$$q_{x,t} + \frac{q_x}{H} q_{x,x} + \frac{q_y}{H} q_{x,y} - f q_y = -\rho^{-1} H p_{a,x} - gH\eta_{,x} + \rho^{-1}\left(\tau_{ax} - \tau_{bx}\right)$$

$$q_{y,t} + \frac{q_y}{H} q_{y,z} + \frac{q_y}{H} q_{y,y} + f q_x = -\rho^{-1} H p_{a,y} - gH\eta_{,y} + \rho^{-1}\left(\tau_{ay} - \tau_{by}\right)$$

Here, the ea surface with 'z' measured positive upwards. *(qx, qy)* is the volume transport vector in the *(x, y)* plane and t is the time. The suffixes preceded by ',' indicate partial derivatives. $H = h + \eta$ is the total depth of water, h is the undisturbed depth of water at *z=0*, η is the sea surface elevation measured from the undisturbed sea surface, f is the Coriolis parameter, ρ is the density of water and g is the acceleration due to gravity. *(τax , τay) and (τbx , τby)* are the stresses at air-sea interface and bottom surface respectively. They are evaluated using the conventional quadratic law as follows:

$$\tau_a = K_a \rho_a |W| W, \qquad \tau_b = K_b \rho H^{-2} |q| q$$

where *Ka* and *Kb* are the wind and bottom stress coefficients respectively, *ρa* is the air density, *W* is the wind velocity measured 10m above the sea level and the volume transport $q \equiv (qx, qy)$. The effects of lateral eddy viscosity are added to the model for the purpose accounts for energy dissipation in lateral direction through standard eddy diffusivity term and using an Eddy viscosity formulation. Appropriate water levels and wind velocities have to be specified for this equation for simulation of tides. It has been observed (Chitra, 1998) that in long wave simulation studies, the initial conditions do not affect the numerical solution. Hence, the usual practice in tide simulation studies, is to assume the ocean to be initially at rest, before the introduction of the free surface perturbation or wind stress at the ocean free surface, i.e. $\eta, qx, qy = 0$ *for* $t \leq 0$. The conventional impermeable vertical side wall assumption may be made along the coastal boundary.

(a) Finite Volume Discretization

The FVM is chosen for the SWE as it will better conserve the mass and momentum in the truncated solution domain. To obtain a basic idea of the FVM, the reader is referred to Roache (1998). And for a detailed description of the method one should read Ashford (1996). The

FVM involves partitioning the domain into a set of non-overlapping control volumes. On each control volume, the integral form of the equations is required to hold. The solution unknowns are taken to be the cell-average quantities that interact through fluxes at the boundaries of the control volumes. Using the integral form of the equations guarantees that any discontinuities that arise in the solution will have the proper strengths (and speeds in an unsteady calculation). Several possible choices exist for the control volumes on an unstructured mesh. In this work, a cell-vertex method is used in which the unknowns are associated with the mesh vertices and the control volumes are taken to be the cells of the median dual mesh. The fluxes through the boundaries of the control volumes are computed using an upwind procedure based on Godunov's (Godonov, 1959) method.

(b) Time Stepping

For this purpose, an explicit multistage scheme is chosen. With the spatial discretization complete, the PDE reduce to a coupled system of ordinary differential equations that can be written as

$$\frac{dU}{dt} = R(U)$$

$$U(0) = U_0$$

Where U is the global conserved state vector containing all the unknowns, R(U) is an operator representing the spatial discretization and U_0 is the initial condition. A widely used explicit method for the above equations is the multistage scheme, where m is the stage, is

$$U^{(0)} = U^n$$

$$U^{(k)} = U^n + \alpha_k dt R(U^{(k-1)}), \quad k = 1,2,\ldots,m$$

$$U^{(n+1)} = U^{(m)}$$

where (n) and (n+1) refer to recent and new time levels respectively, and α_k are the stage coefficients. We have implemented a 1 and a 2-stage scheme with $\alpha_0 = 1.0$ for the 1 stage scheme and $\alpha_0=0.5$ and $\alpha_1=1.0$ for the 2-stage scheme.

(c) Initial condition

Generally, in coastal hydrodynamic modelling, the initial conditions do not play any crucial role. Hence the usual practice is to assume the ocean to be initially at rest, before the

introduction of boundary conditions on lateral boundaries and on the sea surface, i.e., ζ, qx, $qy = 0$; $t \leq 0$.

(d) Boundary conditions

The current solver could work with tide elevation boundary conditions alone. When elevation is provided at boundaries, velocity Sommerfeld radiation condition is satisfied at these boundaries. In cases, where velocity boundary condition shall be used, the solver would use the Sommerfeld condition to estimate the elevation at the boundary. It is also possible to run the model with Elevation and Velocity boundary conditions in case measurements are available.

(e) Mesh Generation

An unstructured mesh generation technique has been incorporated in the present model to produce high quality meshes suitable for shallow water equations. The mesh generation procedure is highlighted in **Fig.E1**. The mesh generation process begins with the construction of the boundary mesh. In this process, the domain boundaries are discretised considering a courant number criteria (C-criteria). The discretisation mainly aims at keeping the overall mesh courant number, required by the user, constant while it will also try to model the geometry as close as possible. This will produce high quality meshes in the estuary.

Morphodynamics Model

The mass balance of sediments at a given control volume and resulting change in volume of sediments is used to estimate change in bed level. This is same as MIKE21 ST module of MIKE 21 software. The bed level (h) equation as provided below is used to compute the siltation rates.

$$\frac{\partial h}{\partial t} + \frac{1}{1-n}\nabla_h \bullet (q_x, q_y) = 0$$

In the above, n is the porosity and q is the total sediment transport rate. The above approximation assumes that, under a balanced condition, the sediment entrainment and deposition rates are at equilibrium (Tambroni et al., 2010). In order to smooth out the bed level changes, a diffusion term could be added to the above equation. However, quantifying the diffusion coefficient will require lot of data. Hence, a Laplacian smoothing of the bed levels is carried out, with 3 cycles, for the purpose of mimicking the location specific diffusion of bed levels.

In order to compute the sediment fluxes, Ocirc employs the following approaches.

(a) Ackers and White formula: This formula is the most suitable one for the present situation as it directly computes the total load of sediment transport. It works very well when the flow conditions mostly shallow water, as that of the present case. It is applicable for a wide range of sediment size and water depths. Hence, this formula is expected to give more appropriate estimate of the sediment load.

(b) Van Rijn formula: This formula is another favoured formula in field by many engineers for total load estimates. However, the limitations of this approach (flow depth, h, >1.0m and D_{50}>0.5mm) is making this formula unusable for the present application.

(c) Bed & Suspended load estimates: Traditionally, the sediment transport has been considered to be of mainly 2 forms: Bed load and Suspended load. In this approach the load estimates will be combined to give the total load. It is usually observed that *(Coastal Engineering, 2004)* this formula will give the lower bounds of the total load.

E-1.2 Estimation of Total Load

According to Ackers and White formula, the sediment transport is related to,

$$Ggr = q_t\,(u^*/U)^n/UD = C[(Fgr/Agr)-1]^m$$

The above relationship is used to estimate q_t (m^3/m/s) from U (Mean flow), D (D35), u* (friction velocity), C (Chezy coefficient) and parameters n, m, Agr and Fgr. More information can be found in *Coastal Engineering (*2004*)*. The transport equation governing the bed level change is coupled with the hydrodynamic equation to estimate the rate of sedimentation in the estuary.

In the present study, the hydrodynamics and morphodynamics modules are coupled in time domain to provide the most sophisticated estimates of bed level change. After each hydrodynamic solution, the sediment rates are resolved in each cell and converted into siltation. The computed siltation is added to the bathymetry to provide a direct feedback of

bed change to velocity computation. Thus, the balance between sediment mobilizing and stabilizing stresses are continuously maintained during the computations.

E-1.3 Validation of Ocirc

The validation of Ocirc has been assessed by applying and comparing the results with the data (Murali et. al., 2002). The model is also validated by comparing its results with MIKE21 alternate wetting/ drying calculations in Gulf of Kutch where the effect of wetting and drying is much large. The details of this validation is provided pictorially in Fig.E2 to Fig.E7. Figs. E2 to E4 provide the details of the computational domain of Gulf of Kutch, unstructured mesh and bathymetry modeled respectively. Fig.E5 gives the details of tidal elevation at the offshore boundary as time series for 15 days. The comparison of computed velocities during the simulation period is provided between Ocirc and MIKE-21. **The comparison suggests a very good agreement between Ocirc and MIKE-21, thus validating the Ocirc.** Further details of simulations are provided in Fig.E6 and E7 in terms of simulated water levels and velocity vectors.

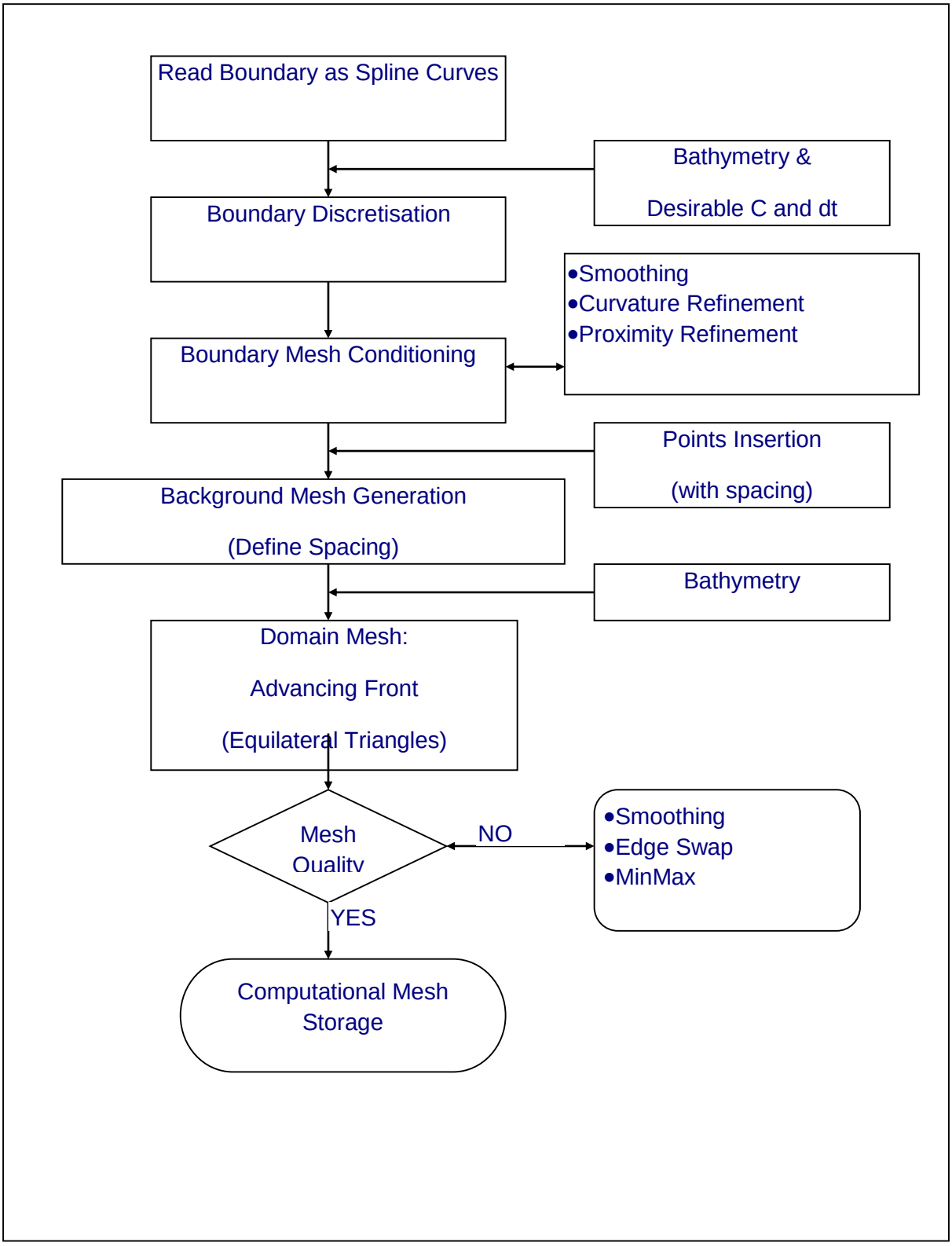
Read Boundary as Spline Curves
Bathymetry &
Desirable C and dt
Boundary Discretisation
•Smoothing
•Curvature Refinement
•Proximity Refinement
Boundary Mesh Conditioning
Points Insertion
(with spacing)
Background Mesh Generation
(Define Spacing)
Bathymetry
Domain Mesh:
Advancing Front
(Equilateral Triangles)
Mesh
Quality
NO
•Smoothing
•Edge Swap
•MinMax
YES
Computational Mesh
Storage

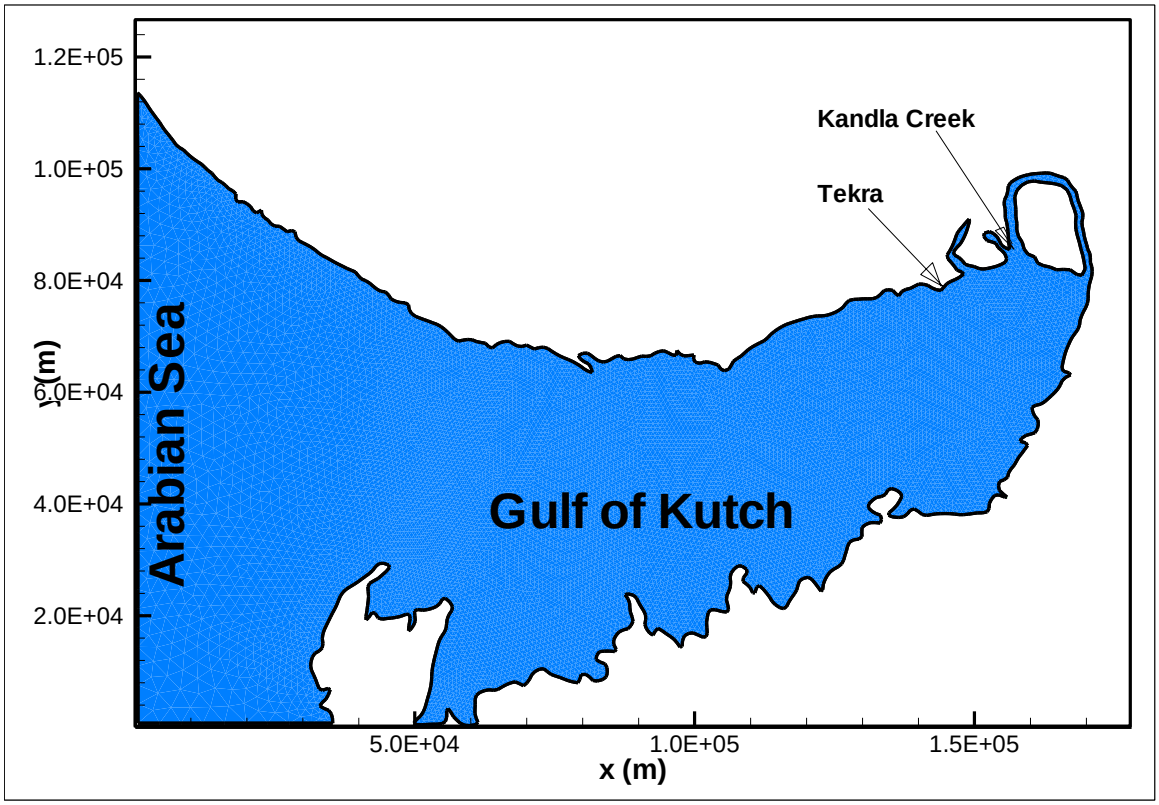

Figure E2 Boundary curve used for mesh generation for tidal model

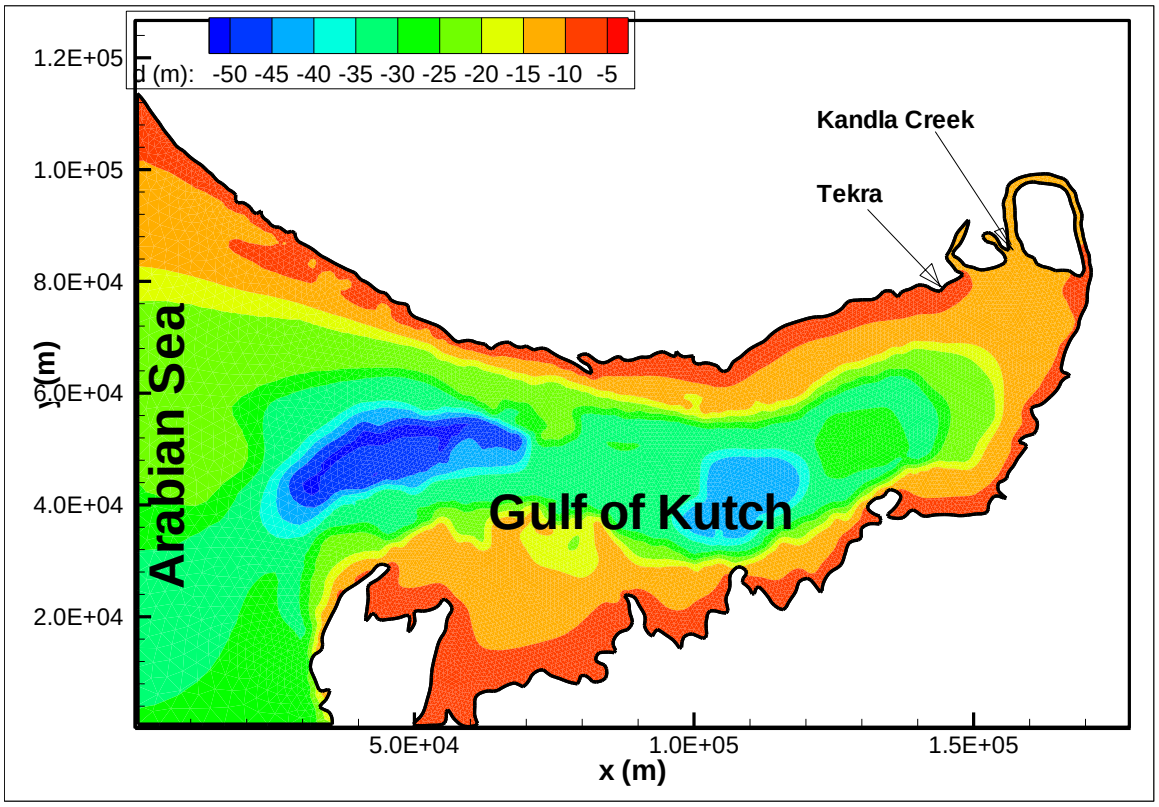

Figure E3 Sea bed levels represented in the computational mesh

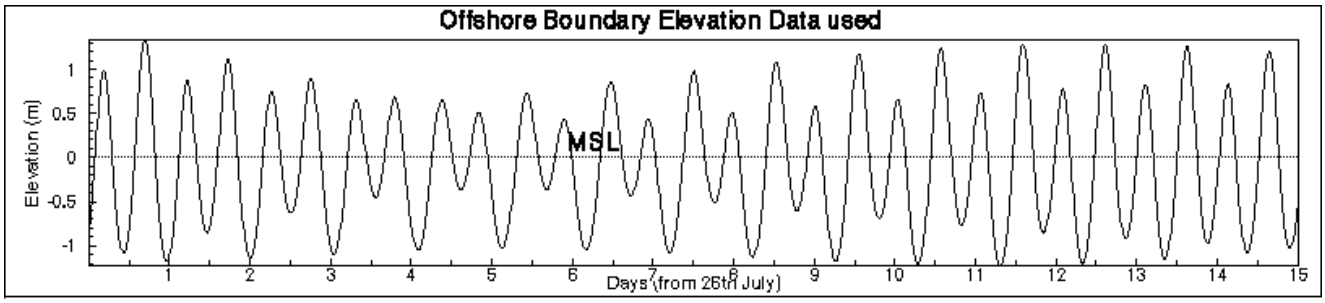

Figure E4 Tidal elevation boundary data used for the open boundary at Arabian Sea

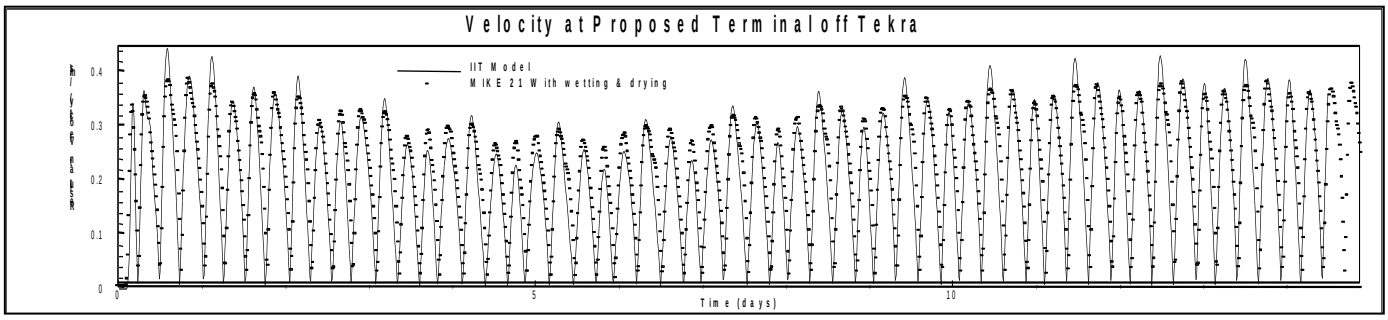

Figure E5 Comparison of present model results with wetting drying calculations.

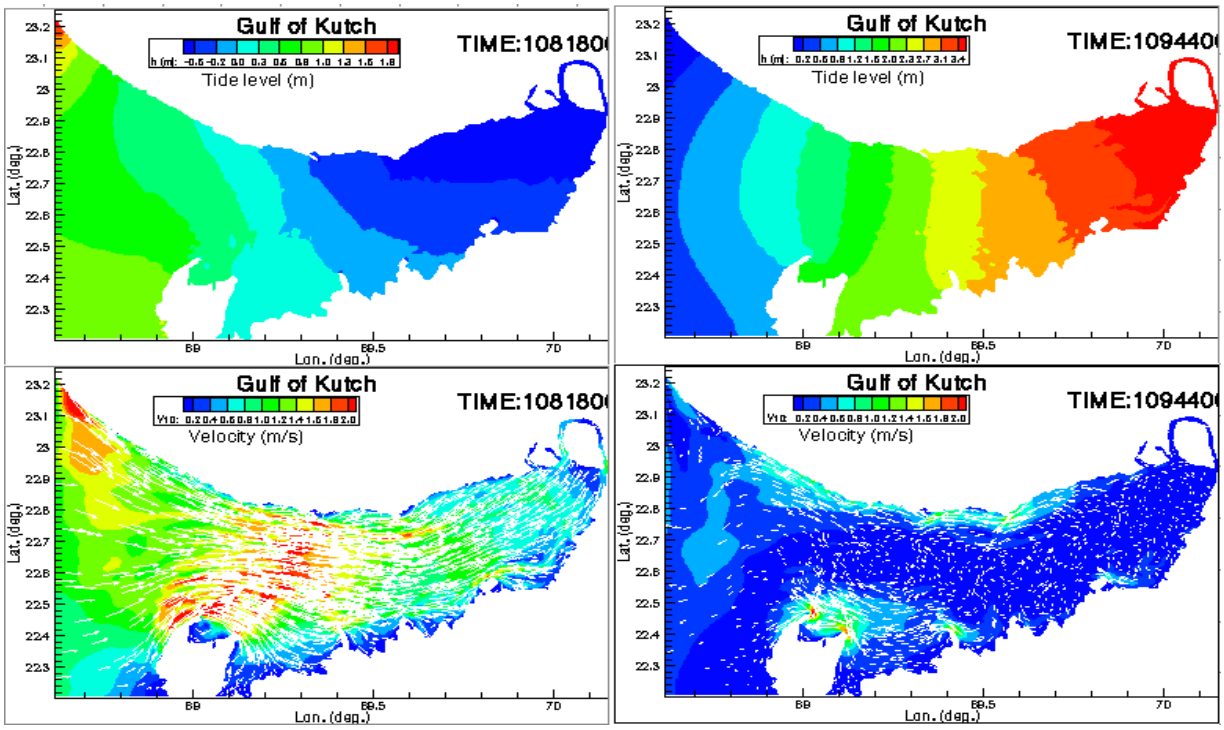

Figure E6 Simulated Tides and Current patterns in Gulf of Kutch calculations

(i) flooding and (ii) after flooding

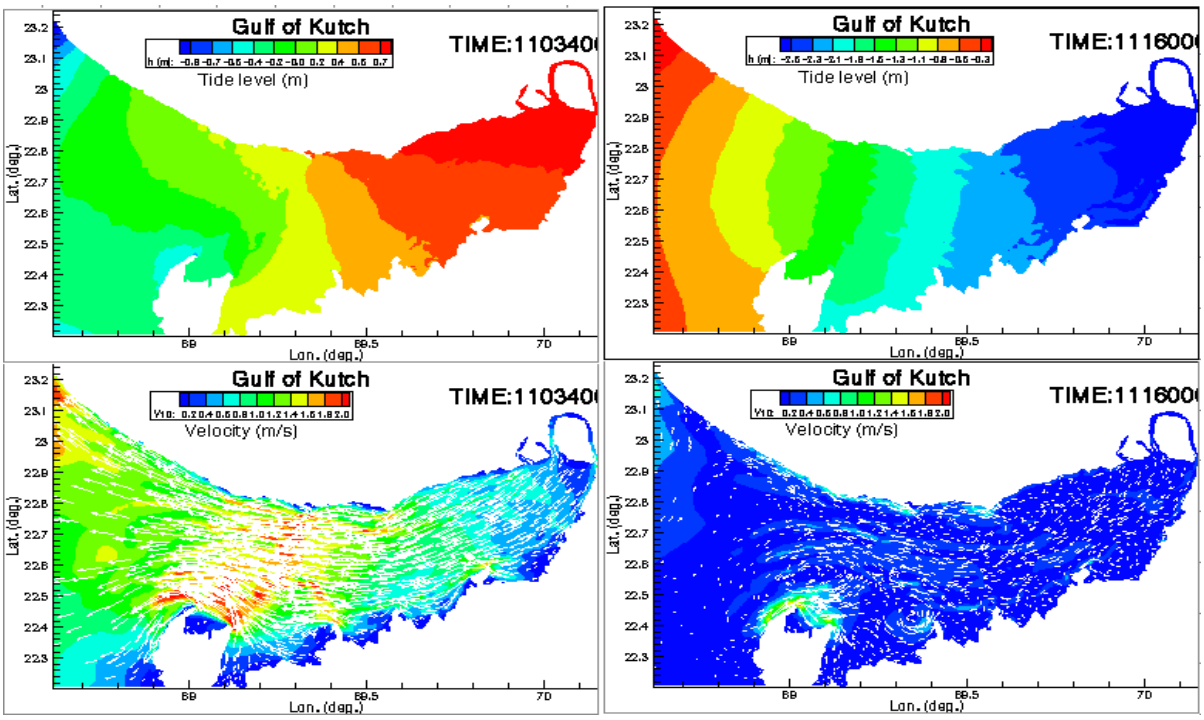

Figure E7 Simulated Tides and Current patterns in Gulf of Kutch calculations

ebbing and (ii) after ebbing.

References

1. Chitra.K, Murali.K and Mahadevan.R, (1996c), 'Simulation of storm surges along east coast of India using an explicit FEM', International Conference in Ocean Engineerong'96, Ocean Engineering Centre, IIT, Madras, India, Dec. 17-22, 1996.
2. Murali.K, Jing Lou and Kurichi Kumar. (2002). “An Unstructured model Simulations for Singapore Strait”. Maritime and Port Journal, Singapore, 2002.
3. Tambroni, N, C. Ferrarin and A. Canestrelli (2010). Benchmark on the numerical simulations of the hydrodynamic and morphodynamic evolution of tidal channels and tidal inlets, Continental Shelf Research 30 (2010).
4. Paulo Marcelo Vieira Ribeiro, Lineu José Pedroso (2017), Dynamic Response of Dam-Reservoir Systems: Review and a Semi-Analytical Proposal, http://dx.doi.org/10.1590/1679-78253500.